

University of Alberta

Derivation of surface pH-values based on mineral abundances over pyrite mining areas with airborne hyperspectral data (Hymap) of Sotiel-Migollas mine complex, Spain

by

Natalie Zabcic



A thesis submitted to the Faculty of Graduate Studies and Research
in partial fulfillment of the requirements for the degree of

Master of Science

Department of Earth and Atmospheric Sciences

Edmonton, Alberta

Fall 2008



Library and
Archives Canada

Bibliothèque et
Archives Canada

Published Heritage
Branch

Direction du
Patrimoine de l'édition

395 Wellington Street
Ottawa ON K1A 0N4
Canada

395, rue Wellington
Ottawa ON K1A 0N4
Canada

Your file *Votre référence*
ISBN: 978-0-494-47449-5
Our file *Notre référence*
ISBN: 978-0-494-47449-5

NOTICE:

The author has granted a non-exclusive license allowing Library and Archives Canada to reproduce, publish, archive, preserve, conserve, communicate to the public by telecommunication or on the Internet, loan, distribute and sell theses worldwide, for commercial or non-commercial purposes, in microform, paper, electronic and/or any other formats.

The author retains copyright ownership and moral rights in this thesis. Neither the thesis nor substantial extracts from it may be printed or otherwise reproduced without the author's permission.

AVIS:

L'auteur a accordé une licence non exclusive permettant à la Bibliothèque et Archives Canada de reproduire, publier, archiver, sauvegarder, conserver, transmettre au public par télécommunication ou par l'Internet, prêter, distribuer et vendre des thèses partout dans le monde, à des fins commerciales ou autres, sur support microforme, papier, électronique et/ou autres formats.

L'auteur conserve la propriété du droit d'auteur et des droits moraux qui protègent cette thèse. Ni la thèse ni des extraits substantiels de celle-ci ne doivent être imprimés ou autrement reproduits sans son autorisation.

In compliance with the Canadian Privacy Act some supporting forms may have been removed from this thesis.

Conformément à la loi canadienne sur la protection de la vie privée, quelques formulaires secondaires ont été enlevés de cette thèse.

While these forms may be included in the document page count, their removal does not represent any loss of content from the thesis.

Bien que ces formulaires aient inclus dans la pagination, il n'y aura aucun contenu manquant.


Canada

ABSTRACT

This research focused on identifying and characterizing sources of acid mine drainage (AMD) using imaging spectroscopy to support environmental assessments of mine tailings at the Sotiel-Migollas mine complex in Spain.

Monitoring of the study site was performed with Hymap imagery where predicted pH and AMD minerals were mapped using partial least squares analysis and iterative linear spectral unmixing analysis (ISMA), respectively.

The mineral maps provided spatial distributions of mineralogy where spatial patterns have been observed and found similar to other studies. Improvement in the details of the mapping was realized using the ISMA procedure over the Hourglass mapping method.

It was determined that a pH predictive spectral model developed at an unrelated mine site could not be properly transferred to the Sotiel-Migollas mine resulting in creation of a site-specific model.

This work showed that hyperspectral remote sensing is an effective means of quantitatively and qualitatively pinpointing sources of acidity.

ACKNOWLEDGEMENT

I would like to express my deep and sincere gratitude to my supervisor, Dr. Benoit Rivard, who kindly and patiently guided me through this thesis. His knowledge and logical way of thinking have been of great value to me over the years. His understanding, encouragement and personal guidance have provided a good basis to the present thesis. I also thank him for supporting my funding throughout my Master degree.

During this work I have collaborated with many colleagues for whom I have great regard, and I wish to extend my warmest thanks to all those who have helped me with my work at the German Aerospace Centre (DLR) and the University of Alberta.

My acknowledgment goes to DLR for providing the image data of this research and funding the fieldwork. I am grateful to Andreas Mueller, “mein Chef”, at DLR for teaching me some Bavarian (even though he knew I had no clue what he was saying), for all the beer/wine bottle opening tricks in the book, and most importantly (!), for the educational experience in imaging spectroscopy. Also, many thanks to Dr. Rolf Richter for teaching me all there is to know about atmospheric correction. It was a privilege to work with Dr. Richter. Many thanks to Stefanie Holzwarth for planning of the Hymap flightline collection and for the geometric correction. A special thanks to my colleagues and special friends at DLR Stefanie Holzwarth, Martin Bachmann, Wouter Dorigo and Martin Habermayer for sharing their knowledge in imaging spectroscopy, providing great help in programming and an enjoyable working environment. Many thanks for the encouragements and laughs shared during my time at DLR and in Munich. It was a pleasure working with you all.

Thanks to my field assistants and coaches: Claudia Laube, Martin Bachmann, Martin Habermayer, Andreas Mueller, Cindy Ong, and Dr. Asun Riaza. It was fun exploring the terrain with you despite the heat and walking with the awful smell of sulfur and oxidized iron. Dr. Riaza from the Geological Survey of Spain was of great help for providing access to the study site and providing valuable contacts for the research in Spain. Thanks to the locals of Calañas and Sotiel-Migollas, for preparing fantastic Tapas, good tips on places to visit and local stories about the mine. I especially liked the story

about locals making their dogs go into the Rio Odiel (pH of less than 3) to kill the lice and tics off their dogs.

I am deeply grateful to Cindy Ong and Thomas Cudahy from CSIRO for providing the fundamental research of this project. I would also like to thank Terry Cooks from HyVista for providing the high-quality remote-sensing Hymap data that are the centerpiece of this project.

I would like to express my gratitude to the Earth and Atmospheric Sciences Department staff. Also, many thanks to David Chesterman for providing laboratory instruments and space for some of my laboratory work. Thanks to Diane Caird who helped perform the X-Ray Diffraction measurements and analysis. I wish to thank Mei Mei Chong from EOSL for all her help in the laboratory and for being a good friend. My thanks also to Dr. Arturo Sanchez-Azofeifa for sharing his experiences and knowledge through his teaching and helpful guidance throughout the thesis.

My deep appreciation goes to my fellow classmates/colleagues at EOSL Jilu Feng, Jinkai Zhang and David Lyder who always had time in their tight schedules to discuss my work and gave very critical opinions to improve this work.

Most importantly, I am deeply grateful to my family - my mother, my father and my sister for their special moral support, offering good advices, and financial support throughout my full university studies. The end of this thesis would have never come without their support - Je vous aime! Special thanks to my uncle Branko for housing me during my stays in Germany and managing to comprehend my German and share amazing times in Munich (biking and sipping cappuccinos every morning and getting to know each other after waiting 24 years to finally meet).

Many thanks to my friends in Edmonton, who cheered up my days, encouraged me during my difficulties until I finished this thesis, made life in Edmonton enjoyable and made me feel at home.

TABLE OF CONTENTS

1. CHAPTER 1 - INTRODUCTION and LITERATURE REVIEW	1
1.1. Introduction	1
1.1.1. Introduction	1
1.1.2. Objectives of the study	1
1.1.3. Significance of the research	2
1.2. Acid mine drainage (AMD)	3
1.2.1. Geochemistry of AMD	3
1.2.1.1. Pyrite oxidation (AMD formation)	3
1.2.2. Spectral properties of AMD minerals	6
1.3. Remote mineral mapping of AMD minerals	13
1.3.1. Case studies and methods of mineral mapping of mine waste tailings ...	13
1.3.2. Key results in mineral mapping of tailings	15
1.3.3. Limitations and remaining challenges	16
1.4. Remote predictive mapping of pH	17
1.4.1. Previous studies	17
2. CHAPTER 2 – STUDY AREA	22
2.1. Geographic setting of the study site	22
2.1.1. Location of the Sotiel-Migollas mine complex	22
2.1.2. Odiel River watershed	24
2.1.3. Regional climate	24
2.2. Geological setting – Regional geology	24
2.2.1. Iberian Pyrite Belt (IPB)	24
2.2.2. Lithostratigraphic units of the IPB	26
2.2.2.1. Phyllite-Quartzite Group (Devonian)	26
2.2.2.2. Volcano-Sedimentary Complex	27
2.2.2.3. Culm Group	27
2.2.3. Mineralization in the IPB	28
2.2.4. Mining exploitation in the IPB and historical context	28

3.6. Characterization of sample suites	47
3.6.1. Labelling of field and laboratory spectra	47
3.6.1.1. Methods of spectra labelling	47
3.6.1.2. Results of spectra labelling	48
3.6.1.3. Discussion	49
3.6.2. Sample suites for the pH predictive modelling.....	49
4. CHAPTER 4 – MINERAL MAPPING	55
4.1. Introduction	55
4.2. Methods	55
4.2.1. Extraction of image endmembers and labelling	55
4.2.2. Generation of mineral maps	56
4.3. Results	57
4.3.1. Image endmember labelling	57
4.3.2. Mineral Maps	60
4.4. Analysis of mineral maps	65
4.4.1. Accuracy assessment of mineral maps	65
4.5. Discussion	68
4.6. Summary	72
5. CHAPTER 5- pH predictive Mapping	75
5.1. Introduction	75
5.2. Methods: PLS modeling	75
5.3. Evaluation of the Brukunga pH predictive model for spectral data of the Sotiel-Migollas mine complex	79
5.3.1. Preprocessing	79
5.3.2. Applying the Brukunga model to the Sotiel-Migollas Hymap images, laboratory and field spectra	81
5.3.3. Discussion	82
5.4. Predictive pH model specific to the Sotiel-Migollas Mine site	83

5.4.1. Calibration and validation datasets	83
5.4.1.1. Assignment of samples to calibration and validation datasets	83
5.4.1.2. Normality test for the calibration dataset	85
5.4.2. Calibration of the predictive models	86
5.4.3. Validation of the predictive pH models	97
5.4.4. Discussion	102
5.5. Application of the model to Hymap imagery	103
5.5.1. Results	103
5.5.2. Predictive pH maps	106
5.5.3. Discussion and links with the mineral maps	111
5.6. Comparison of the Brukunga and Sotiel-Migollas models	114
5.7. Summary	116
6. CONCLUSION	119
7. BIBLIOGRAPHY	122
8. APPENDICES	132
Appendix 3.1: UTM location of AMD mineral soil sampling sites	132
Appendix 3.2 Maps of the location and area of the sampling sites	133
a) Sampling sites of August 2004 field campaign	133
b) Sampling sites of June 2005 field campaign	135
Appendix 3.3: Calculation of absolute reflectance for field spectral measurements	138
Appendix 3.4: Hymap flight lines information	142
Appendix 3.5: XRD results for samples used in this study	143
Appendix 5.1: FRC and spectral reflectance of the mean calibration spectrum for the Brukunga model resampled to Hymap resolutions of Sotiel-Migollas imagery	146
Appendix 5.2: Calibration models using the full spectrum of all 40 samples (Set 1 – group 1)	147

Appendix 5.3: Calibration models using the VNIR of all 40 samples (Set 1 – group 2)	148
Appendix 5.4: Calibration models using the full spectrum and removing parameter outliers from the first model (Set 2 – group 1)	149
Appendix 5.5: Calibration models using the full spectrum and removing parameter and spectral outliers from the first model (Set 2 – group 2)	150
Appendix 5.6: Calibration model using the VNIR and removing parameter outliers from the first model (Set 2 – group 3)	151
Appendix 5.7: Calibration model using the VNIR and removing parameter and spectral outliers from the first model (Set 2 – group4)	152
Appendix 5.8: Actual pH and predicted pH when applying model pls-36sp-6fc-540ch to the Hymap imagery	153
Appendix 5.9: Actual pH and predicted pH when applying model pls-35sp-7fc-28ch to the Hymap imagery	153
Appendix 5.10: Actual pH and predicted pH when applying model pls-35sp-7fc-62ch to the Hymap imagery	154
Appendix 5.11: Actual pH and predicted pH when applying model pls-36sp-8fc-126ch to the Hymap imagery	154

LIST OF TABLES

Table 1.1: Absorption features of Fe-bearing minerals	12
Table 3.1: Mineral categories and number of samples of waste-rock collected at the Sotiel-Migollas mine complex	35
Table 3.2: Description and coordinates (in UTM European Mean 1950, zone 29 North) of each calibration site	35
Table 3.3: Description of ASD FieldSpec Pro spectroradiometers	36
Table 3.4: Location of spectral discontinuities of ASD instruments	38
Table 3.5: Summary of the Hymap system technical specifications	39
Table 3.6: Atmospheric parameters for the ATCOR4 atmospheric correction of all HyMap images	42
Table 3.7: Percentage error of at-surface images compared to ground validation sites ..	44
Table 3.8: pH values of bulk and coating of samples used for the pH modeling of Sotiel-Migollas and the evaluation of the Brukunga pH model	46
Table 3.9: Identification of acid mine drainage mineral samples of August 2004 and June 2005	48
Table 3.10: Samples of AMD minerals and efflorescent salts of August 2004 and June 2005	50
Table 3.11: Coating and bulk samples of the AMD minerals (A04 and J05 samples) ...	50
Table 3.12: Results of the tests for equality of variances and means	51
Table 3.13: Descriptive statistics for the August 2004 (A04) and June 2005 (J05) samples	51
Table 3.14: Merged dataset (N=58) from the AMD minerals coating and bulk samples	54
Table 4.1: Mineral mixture labels for the endmembers	58
Table 4.2: Comparison of image classification and that of spectra for samples of corresponding field locations	67
Table 5.1: Actual pH and pH predicted by applying the Brukunga model to the Sotiel-Migollas' images and ASD laboratory and field spectra	80

Table 5.2: Summary of the results of the application of the Brukunga PLS model to the Sotiel-Migollas data	82
Table 5.3: Comparison of the dominant mineral of samples found at the Brukunga and the Sotiel-Migollas mine sites	83
Table 5.4: Sampling sites indiscernible (N=19) and discernible (N=39) on images	84
Table 5.5: Calibration (N=40) and validation (N=18) datasets	85
Table 5.6: Descriptive statistics and normality test results of the calibration pH dataset	86
Table 5.7: Summary of parameters used for the model calibrations for the two sets	88
Table 5.8: Summary of predicted and actual pH values and residuals of calibration models from set 1 (all 40 samples used)	91
Table 5.9: Descriptive statistics of pH of the samples for the calibration set after removing outliers	92
Table 5.10: Summary of predicted and actual pH and residuals of calibration models from set 2	96
Table 5.11: Parameter and spectral outliers detected in the calibration set	97
Table 5.12: Descriptive statistics of pH of the samples for the validation set before (N=18) and after removing the outlier (N=17)	98
Table 5.13: Actual and predicted pH from the validation of all calibration models with their parameter residuals	101
Table 5.14: Shapiro-Wilk normality test results of the parameter residuals from the validation of all models after removing outlier A04-36	101
Table 5.15: Summary of calibration and validation results of the different PLS models for Sotiel-Migollas	102
Table 5.16: Summary of the calibration and validation results of models applied to the Hymap imagery	106
Table 5.17: Spectral regions of high FRC values for Brukunga and Sotiel-Migollas models with a description of spectral features related to wavelength positions	116

LIST OF FIGURES

Figure 1.1: Model of the formation of secondary sulphate-minerals from oxidation of pyrite in mine-waste environments	4
Figure 1.2: Modelling of the cyclic reactions of pyrite oxidation.....	6
Figure 1.3: Spectra of iron oxide, iron hydroxide, iron sulphate and sulphide minerals related to pyrite oxidation	10
Figure 1.4: Scatter plots of band centre positions of major absorptions	11
Figure 1.5: Spectral angle differences of samples as a function of source water pH	18
Figure 1.6: Absorption band centre positions (${}^4T_1 \leftarrow 6A_1$) as a function of the source water pH of the sediment samples	19
Figure 1.7: Predicted pH derived from spectral data versus measured pH	21
Figure 1.8: Final regression coefficients for the Brukunga predictive pH model	21
Figure 2.1: General location of study site	22
Figure 2.2: Local maps of the study site – including tailings, processing plant, towns, and Odiel River	23
Figure 2.3: Location of the Iberian Pyrite Belt (IPB)	25
Figure 2.4: Location of deposits in the Spanish part of the Iberian Pyrite Belt	25
Figure 2.5: Lithostratigraphic column of the Iberian Pyrite Belt	26
Figure 2.6: Lithostratigraphical units of the IPB present at the Sotiel-Migollas site	30
Figure 2.7: Cross-section of the lithostratigraphical and structural interpretation of the Sotiel-Migollas mine complex	31
Figure 3.1: Workflow diagram summarizing the thesis data collection and manipulation of the datasets	32
Figure 3.2: Location of flightlines with corresponding flightline number over the Sotiel-Migollas mine (UTM European Mean 1950, zone 29 North) for campaigns of 2004 and 2005	40
Figure 3.3: Apparent surface reflectance of a ground invariant target (Basketball court), after applying the radiative transfer model for each Hymap datasets (May 2004, August 2004, and June 2005)	42

Figure 3.4: Multiplicative factor obtained from the mean of three invariant target spectra for each Hymap datasets (May 2004, August 2004, and June 2005)	43
Figure 3.5: At-surface reflectance of the ground validation site (Basketball court) in comparison to the absolute field reflectance and the apparent surface reflectance for the three Hymap imagery datasets	44
Figure 3.6: Frequency histograms of pH values for AMD mineral samples of August 2004.....	52
Figure 3.7: Frequency histograms of pH values for AMD mineral samples of June 2005	52
Figure 3.8: Frequency histogram of pH from August 2004 and June 2005, bulk and coating samples grouped together (Final dataset for the predictive pH modelling of Sotiel-Migollas mine).	53
Figure 3.9: Flow chart presenting the different groupings of datasets done with the statistical analysis	54
Figure 4.1: Spectra of image endmembers grouped by predominant minerals.....	59
Figure 4.2: Overview of the mine waste sites mineral maps.....	61
Figure 4.3: Mineral map of tailing ponds.	62
Figure 4.4: Mineral maps of mine waste surrounding the processing plant	62
Figure 4.5: Mineral maps of distal waste rock tailings.....	63
Figure 4.6: Mineral maps of mine waste along the Odiel River.....	64
Figure 4.7: Mineral map of mine waste sites shown on figure 4.1 draped over a digital elevation model	65
Figure 5.1: Scatter plot of predicted pH versus actual pH when applying the Brukunga model to the Sotiel-Migollas Hymap imagery	81
Figure 5.2: Scatter plot of predicted pH versus actual pH when applying the Brukunga model to the Sotiel-Migollas laboratory and field spectra	82
Figure 5.3: Frequency histogram of pH values for the calibration dataset (N=40)	86
Figure 5.4: Results of the best calibration models from SET 1.....	90
Figure 5.5: Frequency histograms of sample pH for the calibration set after removing outliers	93

Figure 5.6: Results of the best calibration models from SET 2	95
Figure 5.7: Frequency histogram of pH values for the validation dataset	98
Figure 5.8: Control chart of the pH values for the validation set (N=18)	98
Figure 5.9: Validation results for calibration models from sets 1 and 2	100
Figure 5.10: Results of the predicted pH versus actual pH when applying the models to the Hymap imagery of August 2004 and June 2005	105
Figure 5.11: Overview of the pH predictive maps for the mine waste sites	106
Figure 5.12: pH predictive map of tailings ponds	108
Figure 5.13: pH predictive map for the mine waste surrounding the processing plant..	108
Figure 5.14: pH predictive maps of distal waste rock tailings.....	109
Figure 5.15: pH predictive maps of mine waste along the Odiel River	110
Figure 5.16: pH predictive maps of mine waste sites shown on figure 5.13 and draped over a digital elevation model	111
Figure 5.17: FRC for Brukunga model (resampled to Hymap resolution) and Sotiel-Migollas model using the ASD spectral resolution	115

LIST OF ACRONYMS

AMD	Acid mine drainage
ASD	Analytical Spectral Devices
AVIRIS	Airborne Visible/Infrared Imaging Spectrometer
CEM	Constrained Energy Minimization
CSIRO	Australian Commonwealth Scientific and Research Organisation
CV	Cross-Validation
DFD	The German Remote Sensing Data Centre
DLR	German Aerospace Centre
DN	Digital number
EM	Endmember
EOSL	Earth Observation Systems Laboratory
FOV	Field of View
FRC	Final Regression Coefficients
GPS	Global Position Systems
IFOV	Instantaneous Field of View
IMF	The Remote Sensing Technology Institute
IPB	Iberian Pyrite Belt
ISMA	Iterative Spectral Unmixing Analysis
JCPDS	Joint Committee on Powder Diffraction Standards
MESMA	Multiple Endmember Spectral Mixture Analysis
MNF	Minimum Noise Fraction
NDVI	Normalized Difference Vegetation Index
NIR	Near-Infrared
PLS	Partial Least Squares
PPI	Pixel Purity Index
PQ	Phyllite-Quartzite
PRESS	Prediction Residual Error Sum of Squares
REP	Relative Error of Prediction
RGB	Red, Green, Blue
RMSD	Root Mean Square Difference

RMSE	Root Mean Square Error
SAM	Spectral Angle Mapper
SEC	Standard Error of Calibration
SEP	Standard Error of Prediction
SFF	Spectral Feature Fitting
SSEE	Spatial-Spectral Endmember Extraction
SWIR	Shortwave-Infrared
UofA	University of Alberta
USGS	United-States Geological Survey
UTC	Coordinate Universal Time
UTM	Universal Transverse Mercator
UV	Ultraviolet
VIS	Visible
VMS	Volcanogenic Massive Sulphide
VNIR	Visible and Near-Infrared
VSC	Volcano-Sedimentary Complex
XRD	X-Ray Diffraction

1. CHAPTER 1 - INTRODUCTION and LITERATURE REVIEW

1.1. Introduction

1.1.1. Introduction

Environmental impacts have become a primary item on industries' agendas where efforts are made to prevent or reduce pollution related to their production activities. In this regard, mining industries are faced with increasing environmental pressures and regulatory controls with demands for cost-effective tools to acquire environmental data.

Acid mine drainage (AMD) is a key concern of mining industries due to its impacts on the quality of water and soils surrounding mine waste deposits. With the advancement of high-resolution remotely sensed imagery, new methods and monitoring techniques have evolved and the technology has been found to be suitable for long-term monitoring of mine waste impacts.

The primary goal of this research was to develop remote sensing methodologies to monitor the mining environment with quantitative (e.g. pH) and qualitative data (mineral maps) at a regional scale to pinpoint major sources of AMD. This effort will help decision makers understand the spatial extent of the high-risk areas of pollution and better define and prioritize possible remediation efforts.

1.1.2. Objectives of the study

This M.Sc. research focuses, in a first instance, on creating mineral maps of AMD found at the Sotiel-Migollas mine complex located in Spain, through hyperspectral remote sensing. The mineral maps provide a qualitative spatial distribution of the AMD minerals from the tailing at this site.

In a study by Ong and Cudahy (2002) and Ong et al. (2003a) pH levels of pyrite mine tailings in Brukunga, Australia were predicted from airborne hyperspectral imagery. The second objective of this thesis aims to evaluate if this model can be applied to another pyrite mine site, namely the abandoned Sotiel-Migollas mine. In 2004 the tailings of this site were examined with spectroscopic measurements revealing that the tailings were of comparable mineralogy to that of Brukunga and the Leadville mines (Ong and Cudahy, 2002; Ong et al., 2003a) of Colorado. The initial aim was to test whether the pH predictive model of Ong was applicable to this site. If the model were not applicable to the Sotiel-Migollas mine, a new predictive model was to be developed for this site using field samples of the tailings.

1.1.3. Significance of the research

Quantitative measurements are key data in evaluating mining environments. Traditional quantification of mine waste requires intensive collection of mineral samples and subsequent laboratory analysis. To obtain the large amount of data and conduct the analysis is time-consuming and expensive if it is desired to cover the whole mine and providing an understanding of the continuous spatial distribution of the waste. Reflectance spectroscopy techniques provide an alternative approach to traditional laboratory methods of mineral analysis. These techniques require less sample preparation and are fast, non-destructive, non-hazardous, and in limited cases, cost-effective. For example, Swayze et al. (2000) showed the cost-effectiveness aspect by using AVIRIS (Airborne Visible/Infrared Imaging Spectrometer) airborne imagery data at the California Gulch Superfund site at Leadville, CO, where an estimated minimum of \$2 million were saved in investigation costs by accelerating remediation efforts by two years.

This research will provide valuable information about the Sotiel-Migollas mine, where the mineralogy of the mine tailings has not been characterised nor mapped. In addition, this research will determine the applicability of the Ong et al. (2003a) predictive pH model to an independent site. Should this model apply to any other pyrite mine site, it

will allow any user to monitor such mining environment and to derive quantitative environmental measurements.

1.2. Acid mine drainage (AMD)

AMD derives from the oxidation of metal sulphides, e.g. pyrite, that are exposed to oxygen and water. Pyrite can be found within the waste rocks dumps, ore stock piles and tailings of many mines. During the production of AMD both iron and sulphur from the pyrite are oxidized resulting in the generation of sulphuric acid. The acidity is capable of releasing heavy metals contained in the waste rock affecting the purity of the waters and leading to metal enrichment in sediments. This phenomenon is amplified through mining activities because oxygen has greater accessibility to the pyrite when the surface area of the material is increased by the rock crushing and grinding process. Anthropogenic activities are not the only cause of acid mine drainage – this process also occurs naturally when outcrops are exposed to the weathering environment.

1.2.1. Geochemistry of AMD

1.2.1.1. Pyrite oxidation (AMD formation)

AMD is formed through a series of four geochemical and microbial reactions (Kleinmann et al., 1981), which follows a cyclic form until either ferric iron or pyrite (FeS_2) is exhausted:

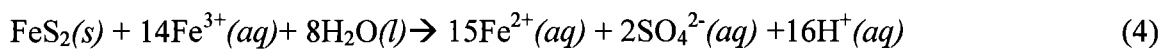
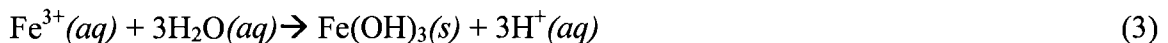
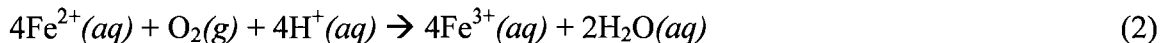
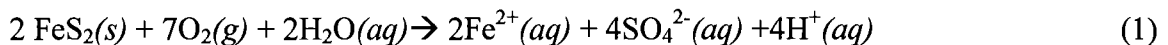


Figure 1.1 illustrates the possible reaction pathways from the oxidation of pyrite (FeS_2) to the formation of secondary sulphate minerals and presents the different pH conditions under which they precipitate.

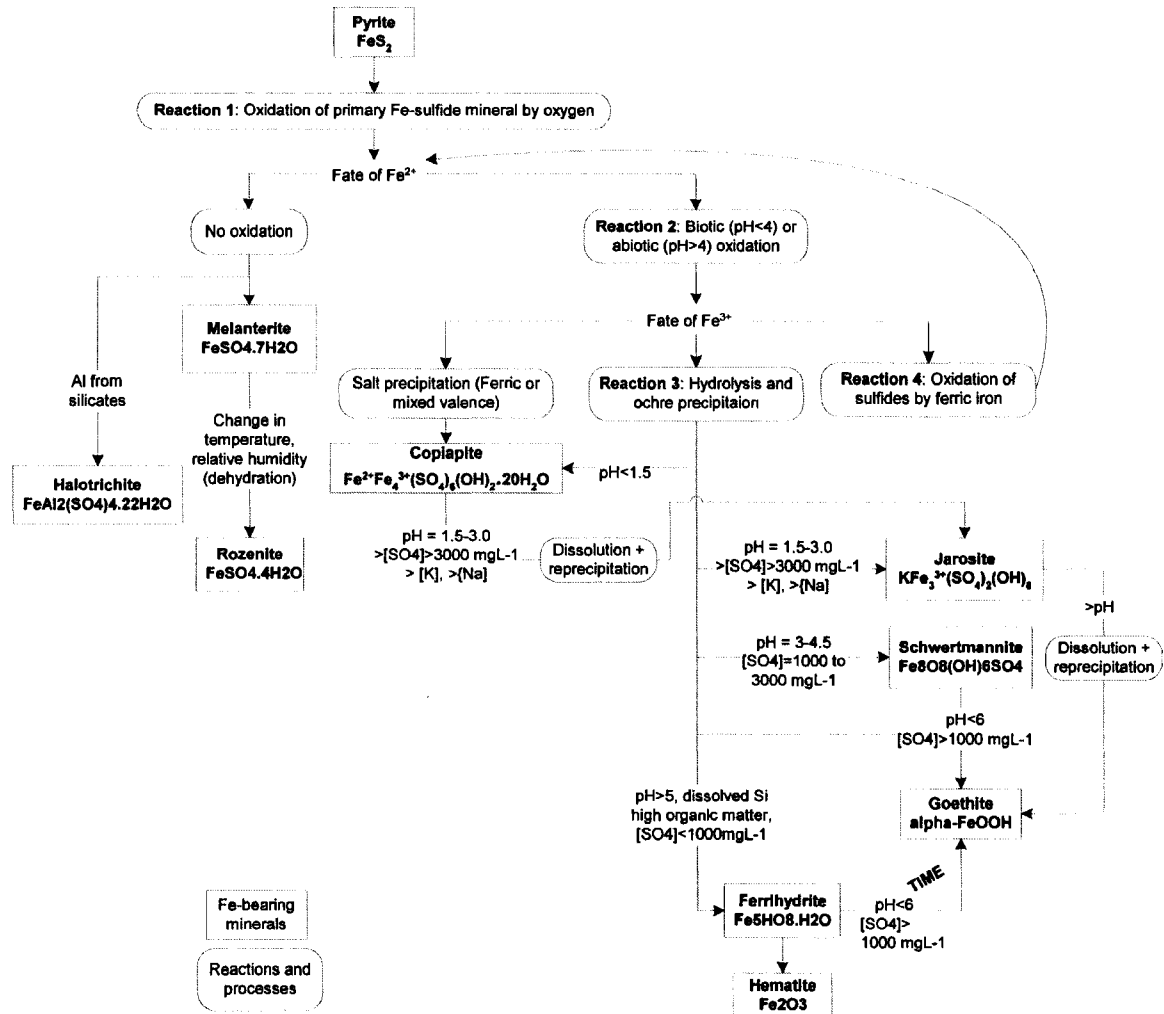


Figure 1.1: Model of the formation of secondary sulphate-minerals from oxidation of pyrite in mine-waste environments. Merged models from Hammarstrom et al. (2005); Montero S. et al. (2005) model originally from Bigham (1994) where additional data came from Alpers et al. (1994) and Nordstrom et al. (1978).

Initially, when pyrite comes into contact with oxygen and water, a spontaneous oxidation reaction occurs releasing ferrous iron (Fe^{2+}) and converting sulphur to sulphate, which also produces sulphuric acid (H_2SO_4) and ferrous sulphate (FeSO_4) (reaction 1). In this first reaction, one mole of pyrite generates two moles of acidity. The rate of oxidation for this first reaction is dependent on oxygen and water, but also can be catalyzed by the presence of bacteria (e.g. *Thiobacillus ferrooxidans*) (Belzile et al., 2004).

The ferrous iron released during the initial oxidation stage is available for oxidation into ferric iron (Fe^{3+}) (reaction 2) or can be grouped with the sulphate (SO_4^{2-}) (no oxidation) to produce soluble sulphate minerals such as melanterite ($\text{FeSO}_4 \cdot 7\text{H}_2\text{O}$), rozenite ($\text{FeSO}_4 \cdot 4\text{H}_2\text{O}$) or szomolnokite ($\text{FeSO}_4 \cdot \text{H}_2\text{O}$) (Hammarstrom et al., 2005). The conversion of Fe^{2+} to Fe^{3+} requires one mole of acidity for every Fe^{2+} transformed to Fe^{3+} . The rate of oxidation in an abiotic system is a function of pH, i.e., when pH levels are greater than 4.5 the process is extremely slow; at pH levels lower than 3.5 the reaction is independent of the pH level and mostly determined by the presence of microorganisms in acid mine drainage (e.g. *Thiobacillus ferrooxidans*) where the rate of the reaction can be accelerated by several orders of magnitude (Murad and Rojik, 2003; Nordstrom and Southam, 1997; Silverman and Ehrlich, 1964). This reaction is referred to as the rate determining step by Singer and Stumm (1970) in the overall series of acid producing reactions, thus is the stage that needs to be controlled to effectively prevent pollution by AMD (Singer and Stumm, 1970).

Reaction 3 is the hydrolysis of iron, which tears the water molecule and forms ferric hydroxides (ochre precipitation). The $\text{Fe}(\text{OH})_3$ is a precipitate product that colours the acidic runoff orange or red. A greater concentration of hydrogen ions is released into the aquatic environment, therefore further reducing the pH. At this stage, the precipitation of ferric hydroxides is pH dependant and at pH levels lower than 2.5, the reaction is only determined by bacterial oxidation (Salomons, 1995). Fe-bearing minerals precipitated at this stage can be jarosite (pH~1.5 to 3), schwertmannite (pH~3 to 4), ferrihydrite (pH>5), or goethite (pH 3 to 6). In addition, mixtures of minerals are often observed, e.g. mixtures of schwertmannite and ferrihydrite at pH 4.5 to 6.5 and mixtures of ferrihydrite and goethite at higher pH levels (Bigham et al., 1996a; Bigham et al., 1996b).

The release of Fe^{3+} seen in reaction 2 allows precipitation of ferric hydroxides ($\text{Fe}(\text{OH})_3$) as seen in reaction 3 (hydrolysis and ochre precipitation) to produce the hydrated sulphate minerals. These minerals are salt precipitations of ferric or mixed valence Fe, e.g. copiapite ($\text{Fe}^{2+}\text{Fe}_4^{3+}(\text{SO}_4)_6(\text{OH})_2 \cdot 20\text{H}_2\text{O}$). Alternately, the Fe^{3+} can act as an oxidant agent for further pyrite oxidation when acting as an electron acceptor

(reaction 4). During reaction 4, the pH level is very low since more hydrogen ions are released. The rate of oxidation is controlled by the concentration of Fe^{3+} , more so than oxygen since Fe^{3+} is the major oxidant of iron pyrite (Singer and Stumm, 1970). This reaction is obviously the key stage of acid production where one mole of pyrite produces 16 moles of acidity, in addition to sulphate and Fe^{2+} . When ferric iron plays the role of oxidant agent at this stage, a cyclic series of the reactions begins. The cycle continues until exhaustion of ferric iron or pyrite. Stumm and Morgan (1981) suggested a diagram illustrating the pathway for pyrite oxidation and shown in figure 1.2.

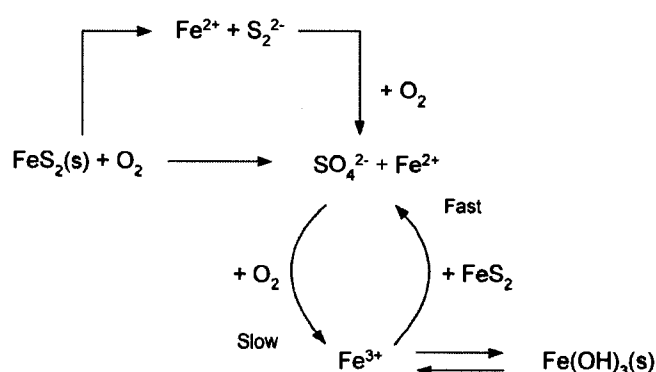
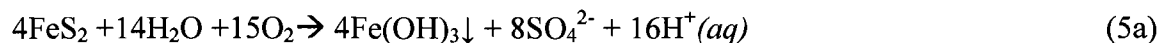


Figure 1.2: Modelling of the cyclic reactions of pyrite oxidation by Stumm and Morgan (1981) and Arnesen (1993); figure from Banks et al. (1997).

The overall series of reactions indicates that this process leads to an abundant release of sulphuric acid and the formation of ochreous Fe^{3+} -bearing minerals as summarized in reaction 5:



Or



1.2.2. Spectral properties of AMD minerals

Spectroscopy is an efficient and accurate tool for identifying secondary iron-bearing minerals because they present diagnostic absorption features in the visible to short wave infrared region (0.4 to 2.5 μm) of the electromagnetic spectrum (Cloutis et al.,

2006; Crowley et al., 2003; Montero S. et al., 2005). The direct detection of pyrite by spectral absorption features is less evident than the secondary iron-bearing minerals because of its low reflectance level, its saturated Fe-absorptions, and its usual opaque coating of oxidation products (Swayze et al., 1996). Therefore, the focus here is to detect the secondary iron-bearing minerals in order to indirectly localize the oxidizing pyrite.

Infrared absorption features in minerals are due to electronic and vibrational processes. Feature bands produced by these two types of processes can be distinguished from each other based on their appearance and on their location in the electromagnetic spectrum (Hunt and Salisbury, 1970). The electronic processes are observed in the visible near infrared (VNIR) spectral range (0.4 to 1.5 μm) and the vibrational processes are seen in the shortwave infrared (SWIR) spectral range (1.5 to 2.5 μm). Thus the mineral spectra can be partitioned into two classes for spectral identification: the electronic and the vibrational regions. These processes are produced by the interaction of electromagnetic energy with the atoms and bonds within the minerals.

In the VNIR spectral range, the electrical processes observed are due to crystal field effects, charge transfer absorptions, conduction bands, and colour centres (Clark, 1999). Crystal field transitions are known as energy level changes in the valence electrons due to unfilled *d* orbital electron shells of transition metals (e.g. Fe, Cr, Co, Ni). For ferric iron-bearing minerals, crystal field transitions commonly occur between 0.750 and 0.950 μm as a broad band, 0.550 and 0.650 μm and a narrower band near 0.450 μm (Hunt and Ashley, 1979). Examples of such crystal field effects are seen in goethite with absorption bands found at 0.480, 0.674, and 0.939 μm and jarosite with absorption features at 0.437 and 0.911 μm and a weak shoulder at 0.650 μm (figure 1.3). In ferrous iron-bearing minerals, crystal field transitions are found between 0.900 and 1.100 μm (Hunt and Ashley, 1979), for example, rozenite with Fe^{2+} -related crystal field absorption at 0.432, 0.978 and 1.170 μm (figure 1.3). In some instances, mixed valence can occur, such as in copiapite where both Fe^{2+} and Fe^{3+} ions are present causing intense crystal field absorptions for Fe^{3+} at bands 0.431, 0.541, 0.868 μm , and weak Fe^{2+} bands at 0.947 and 1.170 μm where Fe^{2+} is coordinated by H_2O (Cloutis et al., 2006). Charge transfer

processes involve electron transfer between the same metal ion in different valence states (e.g. Fe^{2+} and Fe^{3+}) or between metal ions and ligands (e.g. O-H^- , H-O-H , and O^{2-}) due to the absorption of a photon. These charge transfer processes cause intense absorptions in the ultraviolet (UV) extending into the visible region (e.g. $<0.4 \mu\text{m}$ in hematite and goethite) and result in the reddish coloration of the minerals. Examples of ligand-metal charge are presented in melanterite and paracoquimbite with a small absorption band at 0.434 and $0.429 \mu\text{m}$, respectively, and are superimposed on a sharp falloff towards the UV which can be related to a $\text{Fe}^{3+}\text{-O}$ charge transfer feature for melanterite and Fe-O for paracoquimbite (figure 1.3).

The vibrational processes observed in the SWIR spectral region consist of combinations and overtones of fundamental vibrations due to symmetric and asymmetric stretching and symmetric and asymmetric bending motions of the covalent bonds (Clark et al., 1990; Herzberg, 1945). The absorptions are caused by OH^- , H_2O . The water molecule in minerals has three fundamental vibration modes: the symmetric OH stretch (ν_1), the H-O-H bend (ν_2), and the asymmetric OH stretch (ν_3) (Hunt and Salisbury, 1970). The hydroxyl molecule only has one fundamental vibrational mode, the OH stretch (ν_{OH}), and displays OH stretching overtones ($2\nu_{\text{OH}}$) (Hunt and Salisbury, 1970) located at $1.4 \mu\text{m}$. Most secondary iron-bearing minerals viewed in this research produce absorption features near $1.4 \mu\text{m}$ due to the first overtones of the water O-H stretching fundamentals ($2\nu_3$) and near $1.9 \mu\text{m}$, due to the combination of water O-H stretching with the H-O-H bending vibrations ($\nu_2 + \nu_3$) (Hunt and Salisbury, 1970). For example, H_2O - and OH-bearing minerals, such as fibroferrite and copiapite present both 1.4 and $1.9 \mu\text{m}$ absorption features due to OH stretching overtones and H_2O overtones and combinations (table 1.1) H_2O -bearing minerals such as rhomboclase, coquimbite, rozenite, szmolnokite, pickeringite, melanterite have absorption features at 1.4 and $1.9 \mu\text{m}$ due to the H_2O overtones and combinations and present no OH stretching overtones (table 1.1) (Cloutis et al., 2006). Minerals that are only OH-bearing such as jarosite only present the $1.4 \mu\text{m}$ absorption features due to the OH stretching overtones, with two absorption bands in the $1.4 \mu\text{m}$ region attributed to first-order overtones of ν_{OH} (table 1.1).

Table 1.1 summarizes the positions of absorption bands for the identification and discrimination of Fe-bearing minerals from pyrite. Band positions are presented by separating the absorption features of the VNIR and SWIR regions; the features due to Fe³⁺- and Fe²⁺; the H₂O- and OH-bands and the combination and overtone bands of OH- or H₂O-bending, stretching, and rotational or S-O bending.

In addition, figure 1.4 illustrates in scatter plots the positions of absorption band centres for the different Fe-oxide and sulphate minerals viewed in this section. Some minerals, however, are more difficult to distinguish, such as fibroferrite, ferricopiapite, and copiapite, because they have similar band positions following continuum-removal, as shown in figure 1.4a. They can be distinguished from their absorption depth at bands 0.850 µm and 0.550 µm (figure 1.3). Other minerals difficult to differentiate on figure 1.4 include ferrihydrite and schwertmannite where neither possess a feature at 0.550 µm, thus the absorption edge position in the visible region can help to discern them (figure 1.4c). Between schwertmannite and goethite, the position of the maxima reflectance in the visible region is the main distinguishing feature, where goethite's maximum reflectance at 0.764 µm differs from that of schwertmannite's at 0.738 µm (figure 1.4d) and goethite has a 0.550 µm feature absent in schwertmannite. The difference between rozenite and halotrichite is the position of the reflectance maximum with values of 0.603 and 0.679 µm respectively.

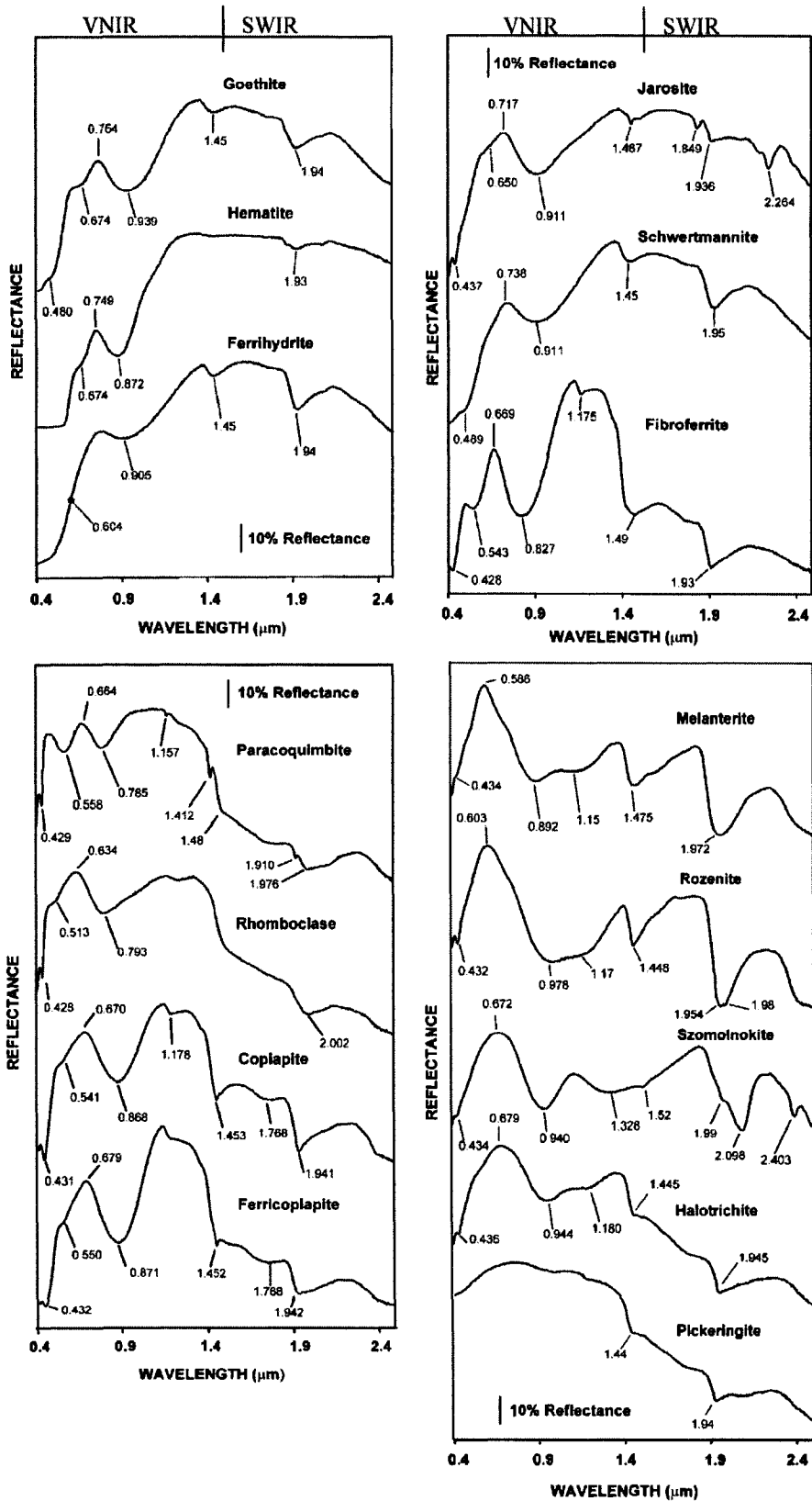


Figure 1.3: Spectra of iron oxide, iron hydroxide, iron sulphate and sulphide minerals related to pyrite oxidation (Crowley et al., 2003).

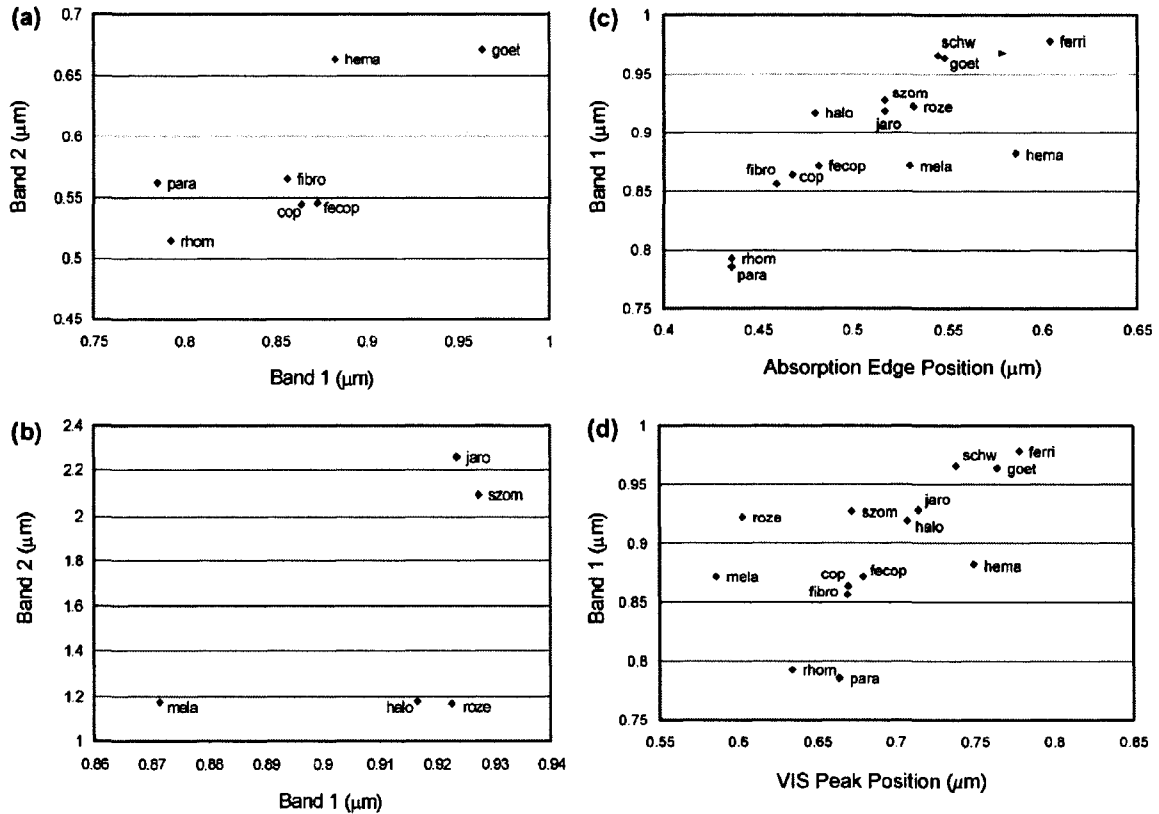


Figure 1.4: Scatter plots of band centre positions of major absorptions: (a) continuum-removed absorption band centre near $0.9 \mu\text{m}$ versus band centre near $0.55 \mu\text{m}$. (b) continuum-removed $0.9 \mu\text{m}$ absorption band centre versus longer wavelength crystal field and vibrational band centre (c) visible wavelength region absorption edge versus the position of crystal field absorption band centre near $0.9 \mu\text{m}$ for all the minerals except pickeringite and (d) visible wavelength region reflectance maxima versus the position of the $0.9 \mu\text{m}$ absorption band centre for all minerals except pickeringite. Key to mineral names: cop=copiapite; fecop=ferricopiapite; ferri=ferrhydrite; fibro=fibroferrite; goet=goethite; halo=halotrichite; hema=hematite; jaro=jarosite; mela=melantherite; para=paracoquimbite; rhom=rhomboclase; roze=rozenite; schw=schwertmannite; szom=szomolnokite, (Crowley et al., 2003).

Table 1.1: Absorption features of Fe-bearing minerals (modified from Cloutis et al. (2006) with additional data from Bishop and Murad (1996) and Crowley et al. (2003)).

Mineral		VNIR (0.4-1.5 μm)						SWIR (1.5-2.5 μm)					Source of data	
		Wvl position (in μm) of Fe ³⁺ - absorption band minima for Fe ³⁺ - bearing minerals			Wvl position of Fe ²⁺ absorption band minima for Fe ²⁺ -bearing minerals.			Wvl position of minima of H ₂ O- and OH-associated abs. bands in the 1.4 and 1.9 μm regions			Wvl position of band minima for combinations of OH- or H ₂ O-bending, stretching, and rotational fundamentals or S-O bending overtones			
					Type of Fe ²⁺ coordination	Band position (μm)		OH stretching overtones (1.4 μm region)	H ₂ O overtones/combinations (1.4 μm region)	H ₂ O combinations (1.9 μm region)	1.7-1.8 μm region	2.0-2.7 μm region		
Rhombochase (H ₃ O)Fe ²⁺ (SO ₄) ₂ •3H ₂ O	H ₂ O-bearing	0.429	0.530 ^a	0.785									1	
		0.428	0.513	0.793						2.002				2
Coquimbite Fe ₂ ³⁺ (SO ₄) ₃ •9H ₂ O	H ₂ O-bearing	0.423-0.433	0.530-0.558	0.865									1	
Rozenite FeSO ₄ •4H ₂ O	H ₂ O-bearing				SO ₄ and H ₂ O	0.920 ^b	1.170							1
						0.432	0.978	1.170		1.450, 1.500 ^d	1.950, 1.980	1.750 ^f	2.440 ^{d,c} , 2.530 ^b	2
Szomolnokite FeSO ₄ •H ₂ O	H ₂ O-bearing				SO ₄ and H ₂ O	0.900								1
						0.434	0.940	1.328		1.448	1.954, 1.980	1.980 ^e	2.100 ^e , 2.410 ^{d,c} , 2.550 ^b	2
Pickeringite MgAl ₂ (SO ₄) ₄ •22H ₂ O	H ₂ O-bearing													1
										1.440 ^d	1.942, 2.050 ^d	1.750 ^{f,d}	2.100 ^d , 2.550 ^{d,b}	2
Melanterite FeSO ₄ •7H ₂ O	H ₂ O-bearing				H ₂ O	0.920 ^b	1.170							1
						0.434	0.892	1.150		1.440	1.940			2
Jarosite KFe ₃ ³⁺ (SO ₄) ₂ (OH) ₆	OH-bearing	0.430-0.436	0.500 ^a , 0.630 ^a	0.910-0.922										1
										1.465-1.468, 1.510-1.520			1.840-1.850	2.080 ^{d,A} , 2.210 ^B , 2.270 ^B , 2.300 ^C , 2.401 ^C , 2.460 ^C , 2.510 ^B , 2.590 ^{d,B} , 2.610 ^B
Fibroferrite Fe ³⁺ (SO ₄)(OH)•5H ₂ O	H ₂ O- and OH-bearing	0.437	0.650	0.911										1
		0.427	0.550 ^a	0.844						1.467	1.936	1.849	2.264	2
Copiapite Fe ³⁺ Fe ₃ ³⁺ (SO ₄) ₆ (OH) ₂ •20H ₂ O	H ₂ O- and OH-bearing	0.428	0.543	0.827										1
		0.430	0.55 ^a	0.850-0.866	H ₂ O	0.947 ^e	1.170 ^e	1.360	1.452, 1.48 ^d	1.490	1.934	1.780 ^f	2.400 ^{d,A} , 2.470 ^{d,B} , 2.550 ^{d,B}	2
Ferricopiapite Fe ₂₃ ³⁺ Fe ₄ ³⁺ (SO ₄) ₆ (OH) ₂ •20H ₂ O	H ₂ O- and OH-bearing													1
		0.431	0.542	0.868			1.178		1.490	1.930				2
Schwertmannite Fe ₈ O ₈ (OH) ₆ SO ₄	Fe-oxide H ₂ O-bearing	0.431	0.550 ^a	0.860-0.873										1
		0.430 ^a	0.500 ^a , 0.600 ^a	0.910-0.918										3
Ferrihydrate Fe ₈ HO ₈ •4H ₂ O	Fe-oxide			0.911										2
				0.900						1.450	1.950			2
Hematite Fe ₂ O ₃	Fe-oxide	0.480	0.674	0.872										2
		0.480	0.674	0.939						1.450	1.940			2
Goethite α-FeOOH	Fe-oxide													2
										1.450	1.930			2
Paracomquimbite Fe ₂₃ (SO ₄) ₃ •9H ₂ O	H ₂ O-bearing	0.429	0.558	0.785										2
										1.157, 1.412, 1.480	1.910, 1.976			2
Halotrichite FeAl ₂ (SO ₄) ₂ •22H ₂ O	H ₂ O-bearing					0.436	0.944	1.180						2

^a Shoulder, band position approximate.

^b Band may be due to Fe³⁺ and/or consist of overlapping Fe³⁺ and Fe²⁺ bands.

^c Weak bands may be present but obscured by other bands.

^d Shoulder on a more intense absorption band, wavelength position approximate.

^e Broad band, wavelength position approximate.

^f Weak band, wavelength position approximate.

A 3ν₃ S-O.

B ν_{OH}ν_{SO} + γ/δ_{OH}ν_{SO}

C 3ν₃ S-O or OH/H₂O combinations and/or overtones

Source of data: 1. Cloutis et al. (2006); 2. Crowley et al. (2003); 3. Bishop and Murad (1996).

1.3. Remote mineral mapping of AMD minerals

Mapping mine waste using traditional methods (i.e. ground surveys) is a challenge due to their extent and the large volume of mine waste. However, multiple studies have shown that hyperspectral remote sensing is an accurate and efficient tool to characterize mine tailings in a continuous spatial form. Imaging spectroscopy is a non-invasive technique for locating areas of mine waste and identifying minerals that generate acid mine drainage.

1.3.1. Case studies and methods of mineral mapping of mine waste tailings

The mapping of minerals in mine tailings has been performed through imaging spectroscopy for already more than a decade (Dalton et al., 2000; Farrand and Harsanyi, 1997; Ferrier, 1999; Kemper and Sommer, 2002; King et al., 1995; Lopez-Pamo et al., 1999; Montero S. et al., 2005; Ong and Cudahy, 2002; Ong et al., 2003a; Ong et al., 2003b; Rockwell et al., 2005; Sares et al., 2004; Shang et al., 2002; Swayze et al., 1996; Swayze et al., 2000; Williams et al., 2002).

Several methods are available for characterizing mine waste tailings. King et al. (1995) and Swayze et al. (1996) began mapping waste rock piles to localize sources of acid mine drainage and map Fe-bearing mineral distribution using the Tricorder algorithm developed by Clark et al. (1990). Further advancement in this algorithm led to the development of Tetracorder algorithm (Clark et al., 2003), which consists of a modified least-squares shape-matching method using more than 250 laboratory spectra of endmember minerals and mineral mixtures to match with unknown spectra. This tool is frequently used for mapping mine waste (Dalton et al., 2000; Ong et al., 2003a; Rockwell et al., 2005; Swayze et al., 2000). Swayze et al. (2000) have shown the ability to use imaging spectroscopy to map acid mine drainage and waste using the spectral properties of Fe-bearing minerals and AVIRIS airborne images. They mapped iron-bearing products such as jarosite, goethite, and hematite from mine waste. Dalton et al. (2000) accurately mapped sources of acid-generating and acid-neutralizing minerals from pyrite

mineralization, also through AVIRIS imagery. Ong et al. (2003a) used Hymap airborne imagery to map key minerals and mineral mixtures related to acid mine drainage on a multitemporal basis at the Brukunga pyrite mine. The matching of spectra to map minerals was performed against a reference spectral library of key minerals and mixtures of minerals of AMD produced synthetically in the laboratory. Results showed the ability of Tetracorder to consistently map similar minerals over different dates. In the VNIR, coarse grain jarosite, fine grain jarosite, mixtures of jarosite and goethite, and goethite were mapped. Another technique used for mapping is the constrained energy minimization (CEM) (Farrand and Harsanyi, 1997; Harsanyi, 1993) where Farrand and Harsanyi (1997) mapped the distribution of tailings and ferruginous sediments at a silver and base metal mine using the technique and AVIRIS imagery. This technique enhances the spectral response of the target's signature (the foreground signature) and suppresses the response of undesired background signatures (i.e. noise and non-related material). As a result, unambiguous mapping of ferruginous sediments were provided. Partially constrained linear unmixing was used by Shang et al. (2002) to map zones of oxidation and different minerals of the Copper Cliff mine tailings in Sudbury, Ontario. A selection of pure endmembers from a spectral library was used for the unmixing of Hymap airborne data. The endmembers were determined based on minerals identified from ground samples through X-ray diffraction (XRD) and consisted of pyrite, pyrrhotite, gypsum, hematite, dolomite, jarosite, and goethite, among others. This method showed that the scene-derived endmembers could be replaced by library mineral samples in order to unmix the Hymap image spectra. Crowley et al. (2003) showed in their experiments that other Fe-secondary minerals, such as the soluble iron sulphates, could be identified through spectroscopic analysis. The identification of the spectral data was performed using the continuum-removal procedure (Clark, 1999; Clark and Roush, 1984).

Frequently, reflectance data are analyzed separately for the VNIR and SWIR (Crosta and Souza F., 1998; Dalton et al., 2000; Farrand and Harsanyi, 1997; McCubbin and Lang, 1999; Montero S. et al., 2005; Swayze et al., 1996; Swayze et al., 2000, among others). The VNIR spectral range presents diagnostic features for the iron-bearing minerals, whereas the SWIR region includes features of clays, sulphates, micas, and

carbonates. Only jarosite has diagnostic features in both but in many cases the SWIR features can be dominated by clay minerals, thus it is preferred to use the VNIR to facilitate the identification of Fe-bearing minerals. Rockwell et al. (2005) found that the VNIR region was more reliable for identifying jarosite in comparison to the SWIR, since the crystal field absorption feature of jarosite is commonly present regardless whether the Fe-OH absorption feature at 2.27 μm in the SWIR is detectable or not. Since the VNIR spectral region is sufficient to detect iron-bearing minerals, this method reduces the dimensionality of the data and reduces computation time during analysis.

1.3.2. Key results in mineral mapping of tailings

Patterns in the spatial distribution of minerals from tailings have been commonly observed at different sites and by different authors. Swayze et al. (1996) and Swayze et al. (2000) show concentric mineral zones where the zones fan out downslope of the piles and occasionally circular patterns with the centre composed of jarosite and surrounded progressively by a mixture of jarosite and goethite, then by a larger zone of goethite and finally, by the domination of hematite at the edges of the goethite zones. Similarly, Montero S. et al. (2005) have mapped patterns of accumulation of Fe-bearing minerals where copiapite and jarosite form a central unit that is surrounded by goethite and hematite. Also, Rockwell et al. (2005) have identified zonation patterns of iron-bearing sulphates, hydroxides, and oxides, through interpretation of AVIRIS images. The pattern consists of a pyrite rich centred area that grades into fine-grained jarosite, mixtures of jarosite and goethite, goethite, generic Fe^{3+} , and hematite. The patterns presented by these studies represent the evolution of the oxidation of pyrite where the iron-bearing minerals reflect the pH of the water from which they have precipitated, thus presenting an outward transition from a central zone of pyrite of low pH to minerals formed in gradually more neutral pH conditions (i.e. hematite) (Rockwell et al., 2000; Rockwell et al., 1999; Swayze et al., 2000). This common zonation pattern suggests a decrease of potential acid mine drainage as a function of the distance from the centre zone that consists of the ore zone. Thus, a predictive pattern is provided which represents the mineralization and alteration zoning around the pyrite and can be potentially expected in this study.

Studies of the accuracy of the mineral maps include laboratory or field spectral analyses as well as X-ray Diffraction (XRD) analysis of samples of Fe-bearing rocks collected in the field for most studies. For Rockwell et al. (2005), the iron mineral distribution maps derived from the analysis of AVIRIS imagery were accurate in identifying medium-grained goethite, coarse-grained goethite, medium- to coarse-grained goethite with traces of jarosite, and mixtures of goethite and jarosite. Rockwell et al (2005) and Swayze et al. (2000) consider XRD is generally unreliable in identifying amorphous iron minerals even though iron is present in high abundance and consider spectroscopy as an accurate and efficient tool for locating and identifying iron-bearing minerals. On another hand, King et al. (1995) rely on Mössbauer spectroscopy for the identification of amorphous iron oxides.

The most common Fe-bearing minerals identified throughout these studies are copiapite, jarosite, schwertmannite, ferrihydrite, goethite, and hematite. In some instances, pyrite was mapped if it was concentrated in coarse grains, such as mapped by AVIRIS data in the Oregon Gulch tailings by Swayze et al. (1996) and at the Bauer Mill site near Stockton, Utah (Rockwell et al., 2005) because it weathered more slowly than finer grained pyrite and was present in sufficient abundance to be detected.

1.3.3. Limitations and remaining challenges

One of the main limitations of remotely derived mineralogical information for tailings and mine waste is the presence of intimate mineral mixtures because their spectra consist of non-linear mixtures (Nash and Conel, 1974; Singer, 1981) of mineral spectra. In these circumstances, absorption features of some minerals may be obscured by other minerals. In many studies, linear unmixing techniques are used as an approximation to estimate the abundance of minerals from spectra and seem to work well in many situations (Kemper et al., 2000; McCubbin and Lang, 1999; Shang et al., 2002). However, linear techniques are not as accurate in determining the abundances of minerals from spectra as those determined using non-linear techniques. Thus non-linear unmixing models are necessary to fully determine the exact mineral make up of the spectra.

Montero S. et al. (2005) did not use unmixing and correlation of spectral depth to mineral abundance because of intimate mixtures of mineral grains on the surface of the waste piles. Instead, they identified the spectrally dominant mineral by comparing continuum-removed absorption bands of the unknown spectra with those in a reference library.

1.4. Remote predictive mapping of pH

Predicting leachate pH through imaging spectroscopy is a new application where limited studies have been realized by Ong and Cudahy (2002), Ong et al. (2003a), Sares et al. (2004), Swayze et al. (2000) and Williams et al. (2002). As part of this thesis, efforts are devoted to progress the predictive mapping of pH of pyritic mine tailings in order to provide tools for generating direct quantitative pH mapping in addition to qualitative mineral mapping, where leachate pH can be estimated by knowing the mineral precipitation environment.

1.4.1. Previous studies

Sares et al. (2004) indirectly determined the pH of stream water using hyperspectral data by identifying the precipitated minerals on the streambed. The precipitated minerals are related to each mineral's pH stability range, i.e., the pH at the time of the deposition: jarosite pH=2; ferrihydrite+schwertmannite pH=3; schwertmannite pH=3-4; ferrihydrite pH=4-5. The predicted pHs were assessed using water analysis and field spectrometry of mineral precipitate along the streambed alluvium.

Williams et al. (2002) used reflected light to estimate pH of stream waters associated with coal mine drainage in the Anthracite region of eastern Pennsylvania. The pH values were estimated from sediment colour and spectral reflectance in the VNIR for mine drainage precipitates (Fe-oxides such as schwertmannite, goethite, and ferrihydrite). The Red-Green-Blue (RGB) sediment colour values were calculated from L*a*b colour parameters obtained with a Minolta CR-300 Chroma Meter that analyses the reflective colours of material. The spectral angle difference technique (SAM; Kruse et al. (1993))

was applied with vectors of 3 dimensions from the RGB values. The angle between the reference RGB spectrum (of synthetic goethite) and the sediment sample's RGB spectrum was calculated by the SAM technique in order to determine which samples had a similar colour to the reference sample. As a result, sediment samples with similar colour to the reference (low theta angle) consisted of goethite and/or schwertmannite that were formed in low pH drainage water. Samples of ferrihydrite presented higher theta values when compared to the reference samples, thus were different colours and were produced at different pH values than the reference, i.e. in near neutral pH source waters. The relationship between the sediment colour differences against the referenced goethite (theta angles) and source water pH is shown in figure 1.5 with an r^2 of 0.76 (Williams et al. 2002). The pHs associated to the minerals are as follow: ferrihydrite: pH=6-7; goethite: pH=3-5.8; and schwertmannite: pH=3.8-5.8. However, this study does not present a validation of the accuracy of the modelled linear equation and is only limited to three types of Fe-oxides (schwertmannite, goethite, and ferrihydrite).

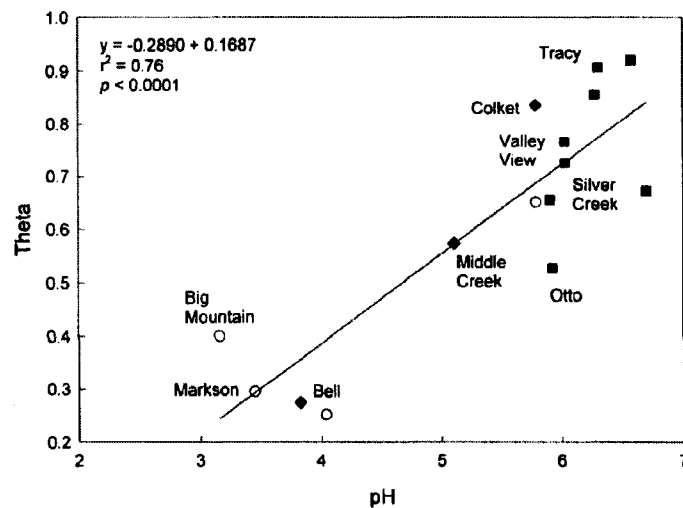


Figure 1.5: Spectral angle differences of samples as a function of source water pH: ■ -ferrihydrite, ○ -goethite, ◆ -schwertmannite (Williams et al., 2002).

Williams et al. (2002) also used VNIR reflectance data of the samples to predict their pH. Through continuum-removal, the crystal field band centres (${}^4T_1 \leftarrow 6A_1$) between 0.900 and 1.000 μm were isolated for comparison with a reference synthetic spectrum of goethite. The pH values of the samples were plotted against the band centre

positions resulting in an r^2 of 0.87 as seen in figure 1.6 (Williams et al., 2002). In this experiment the pHs associated to the minerals are: ferrihydrite: pH=5.6-6.8; goethite: 3-5.8; and schwertmannite: pH=3.4-5.7. Again no validation of the modelled equation was performed. Correlation of pH with values of bandwidth and band depth of the crystal field absorption features of the samples were also examined, but the band centre presented the best correlation.

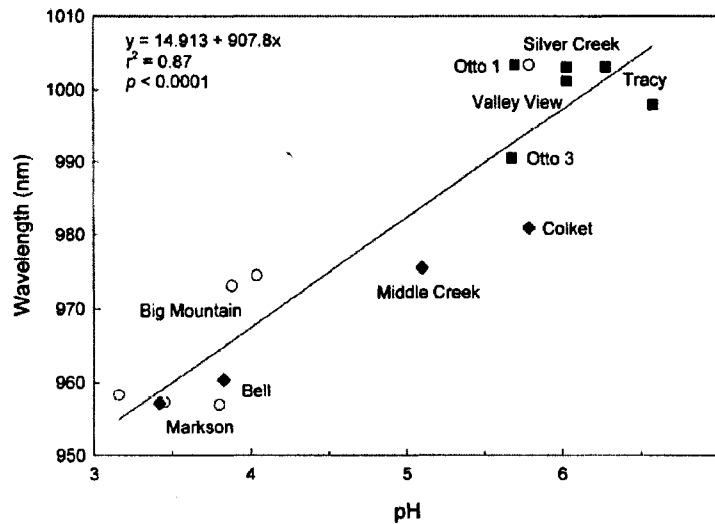


Figure 1.6: Absorption band centre positions (${}^4T_1 \leftarrow 6A_1$) as a function of the source water pH of the sediment samples: ■-ferrihydrite, ○-goethite, ◆-schwertmannite (Williams et al., 2002).

Swayze et al. (2000) have shown excellent correlation between leachate pH and spectral zone mineralogy. The leachate pH was measured in laboratory from field samples collected in each spectral zone. The spectral zones they have identified formed a concentric pattern and each spectral zone had its own distinct leachate pH range: for jarosite zone, pH between 2.3-2.6; for jarosite+goethite zone, pH between 2.9-3.5; and for goethite zone, pH between 4.5-6.1. Thus, their findings showed through mineral maps a chemical gradient from highly acidic, metal-rich water formed in close proximity to the waste, to more neutral, less metal-rich water further away from the waste piles. They have associated the pH to the mineralogy and found that the pH decrease outwards from the central zone of jarosite to the exterior ring of goethite.

Ong and Cudahy (2002) and Ong et al. (2003a) established a relationship between hyperspectral data and pH measurements for data collected at the Brukunga Pyrite Mine

located in the Mount Lofty Ranges in South Australia. They extended this application by developing a spectral predictive model of surface pH based on airborne hyperspectral imagery and demonstrated quantitative multi-annual monitoring capabilities for the Brukunga mine. The Brukunga mine was in operation from the 1950's and was closed in 1972 (Ong et al., 2003a). The mine produced pyrite as a source of sulphur for superphosphate fertilizer (Ong et al., 2003a). The mining operations have left large surfaces of waste dumps and outcrops exposed to oxidation and leaching of heavy metals. Ong et al. (2003a) collected laboratory spectra of Brukunga samples using an Analytical Spectral Devices spectrometer and a PIMA-SP spectrometer that respectively cover the 0.350-2.500 μm and 1.300-2.500 μm regions of the electromagnetic spectrum. In addition, pH measurements were made in the laboratory. XRD analyses were performed to identify the mineralogy of the samples. The predictive pH model was calibrated using Partial Least Square analysis (PLS) (Haaland and Thomas, 1988) applied to 52 samples collected from 43 locations within the Brukunga mine site. Figure 1.7 presents a comparison of the predicted and measured pH for these samples (the calibration model). The final regression coefficients (FRC) obtained during the calibration of the Brukunga pH model are plotted on figure 1.8 against spectra of goethite and jarosite. Spectral bands with high regression coefficient values (positive or negative) correspond to significant absorption features located near 0.400, 0.580, 0.910, and 2.260 μm . Ong et al. (2003a) labelled these bands as ferric iron charge transfer absorptions and ferric iron crystal field absorptions and concluded that spectral features of secondary iron minerals contribute highly to the relationship between observed pH and pH predicted from spectral data. The validation of the predictions obtained from applying the model to the Hymap imagery was performed by comparing 2 sampling sites averaged laboratory pH to the average predicted pH obtained from the imagery. The first validation-sampling site was a transect of samples where laboratory pH gave a mean value of 4.05 +/- 0.51. The second validation-sampling site presented a laboratory mean pH of 2.4. Respectively, these two sites presented a mean predicted pH from the imagery of 4.9 +/- 0.45 and 2.3. In this case, the pHs obtained were not associated to the mineralogy of the site.

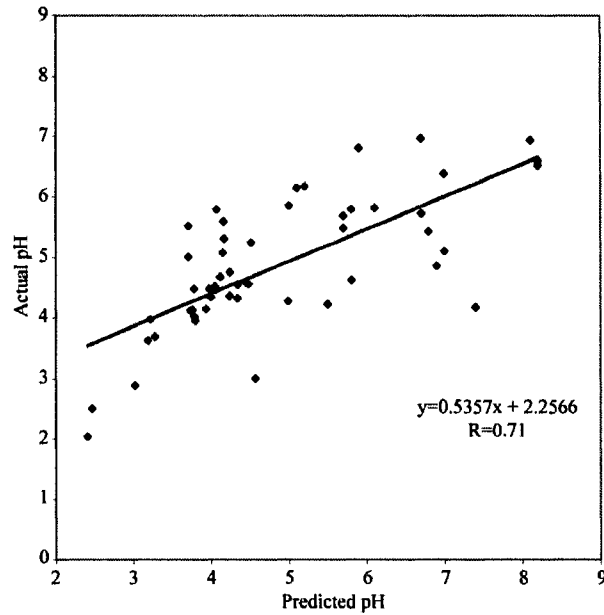


Figure 1.7: Predicted pH derived from spectral data versus measured pH (Ong et al., 2003a).

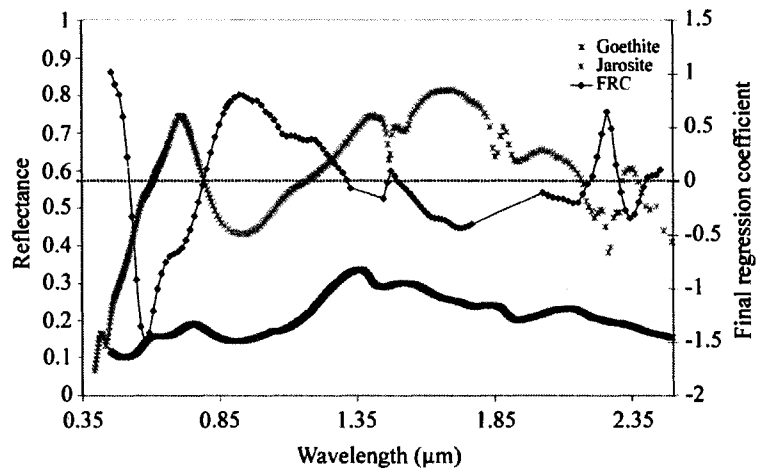


Figure 1.8: Final regression coefficient for the Brukunga predictive pH model (Ong et al., 2003a).

2. CHAPTER 2 – STUDY AREA

2.1. Geographic setting of the study site

2.1.1. Location of the Sotiel-Migollas mine complex

The Sotiel-Migollas mine complex is located in the vicinity of the towns of Sotiel de Coronada and Calañas in the region of Andévalo, province of Andalusia, South-West of Spain (figure 2.1). The mine complex includes the processing plant, two ponds tailings, three major waste rock tailings, and various minor areas of rock waste or tailings (figure 2.2).

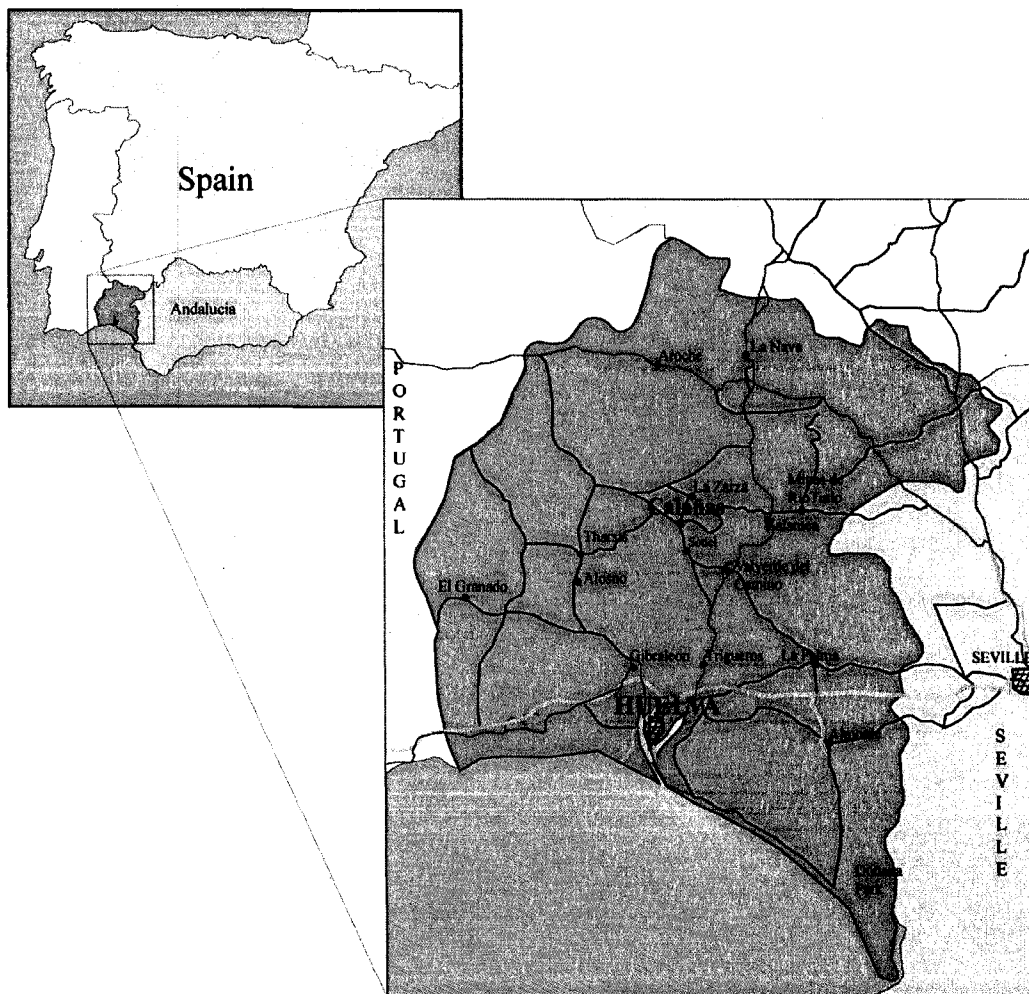


Figure 2.1: General location of study site.

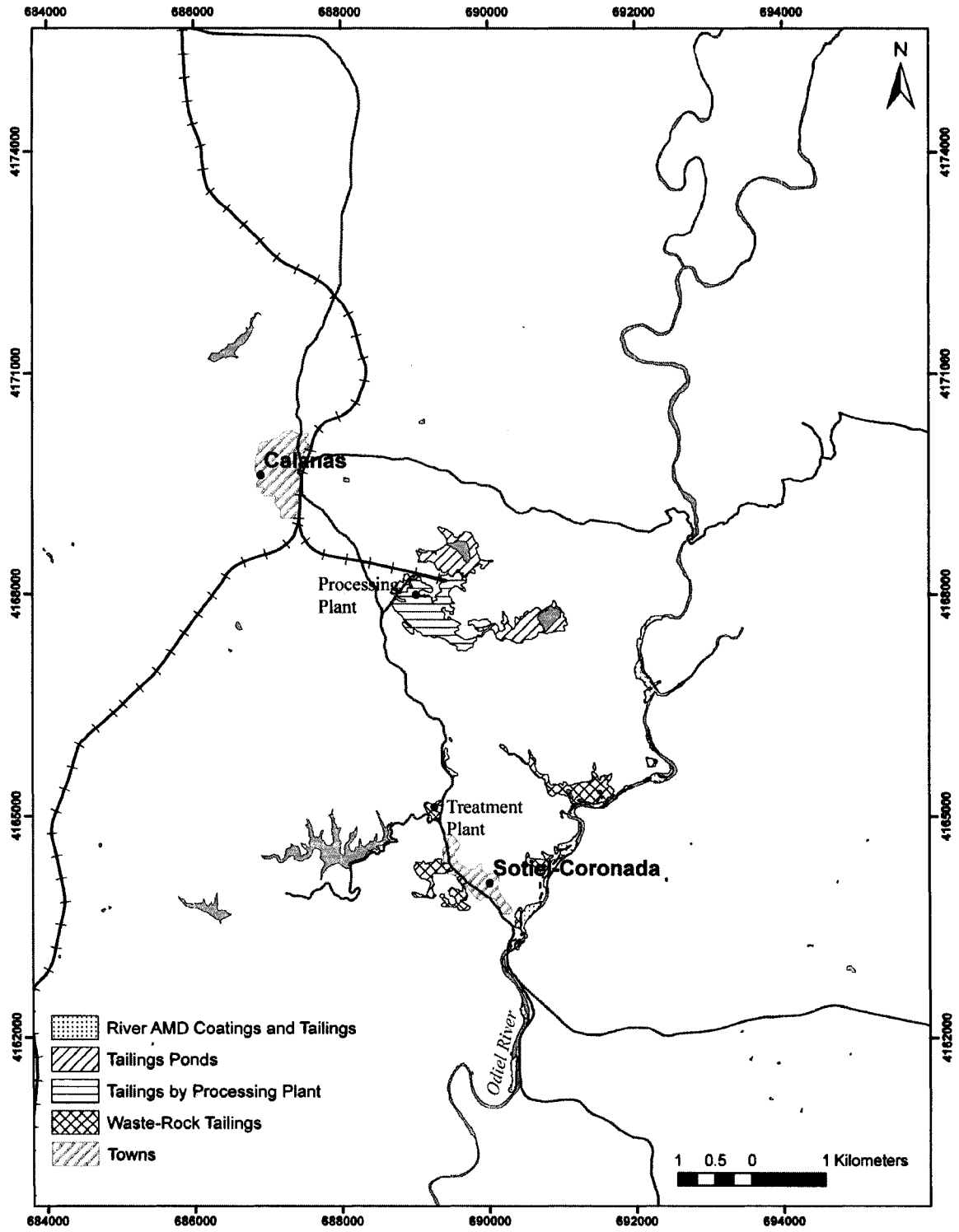


Figure 2.2: Local maps of the study site – including tailings, processing plant, towns, and Odiel River.

2.1.2. Odiel River watershed

The mine complex lies within the Odiel watershed. The watershed covers an area of 2333 km² and hosts the Odiel River approximately 140 km in length with a mean annual discharge of approximately 15 m³/s (Braungardt et al., 2003). The source of the river is in the Sierra de Aracena y Picos de Aroche Natural Park, Southwest Spain. The river then crosses a rich and ancient mining region known as the Iberian Pyrite Belt, finally passing through the Las Marismas del Odiel Natural Area just before discharging into the Atlantic Ocean in Huelva, Spain (figure 2.1).

2.1.3. Regional climate

The climate of the region is Mediterranean, characterized by long, dry summers and short, mild winters. The average rainfall varies between 600 mm in the lower part of the basin to 1000 mm in the upper northern hills (Olías et al., 2004). Nearly half of the annual rainfall occurs in the fall and winter between November and January, with some occurring in April, and virtually none during the summer months (Olías et al., 2004).

2.2. Geological setting – Regional geology

2.2.1. Iberian Pyrite Belt (IPB)

The study site is situated in the Iberian Pyrite Belt (IPB), which is considered the largest volcanogenic massive sulphide (VMS) deposit in the world. The IPB has an extent of 250 km from Seville in southern Spain to the south-western coast of Portugal (figure 2.3) and has a width varying from 30 to 50 km (Munha et al., 1986; Sainz et al., 2003).

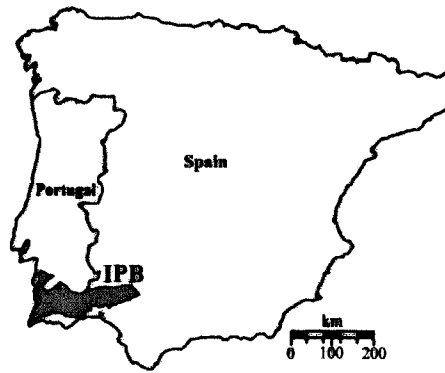


Figure 2.3: Location of the Iberian Pyrite Belt (IPB).

The massive sulphide deposits were formed by precipitation from hydrothermal fluids during intense seabed volcanic activity in the early Carboniferous, about 300-350 Ma (Boulter, 1993; Moreno, 1993). The distribution of over 1700 Mt of massive sulphide ore and 250 Mt of stockwork ore resulted from the uplifting and compression of the deposits defining the IPB region (Tornos, 2006). Figure 2.4 presents the location of deposits and the geological context of the IPB that is further discussed below.

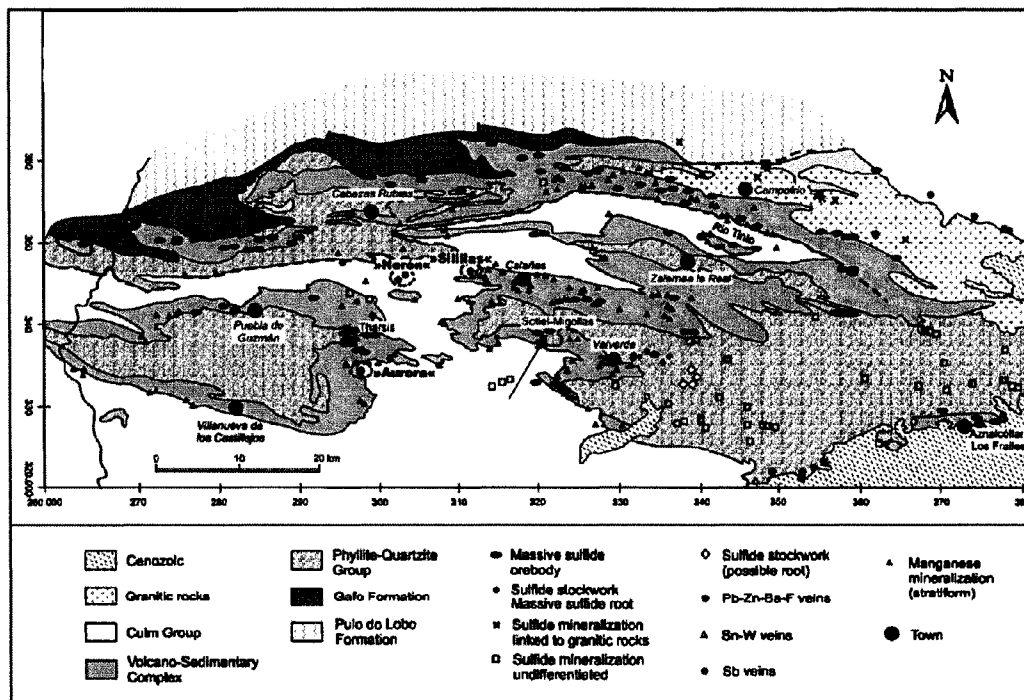


Figure 2.4: Location of deposits in the Spanish part of the Iberian Pyrite Belt (modified after Leistel et al. (1998). The arrow points to the study site.

2.2.2. Lithostratigraphic units of the IPB

The IPB is composed of Late Devonian to Middle Carboniferous rocks (Leistel et al., 1998) divided into three major lithostratigraphic units (Schermerhorn, 1971). They consist of the Phyllite-Quartzite Group (PQ) overlain by the Volcano-Sedimentary Complex (VSC), itself overlain by the Culm Group (Schermerhorn, 1971), (figure 2.5).

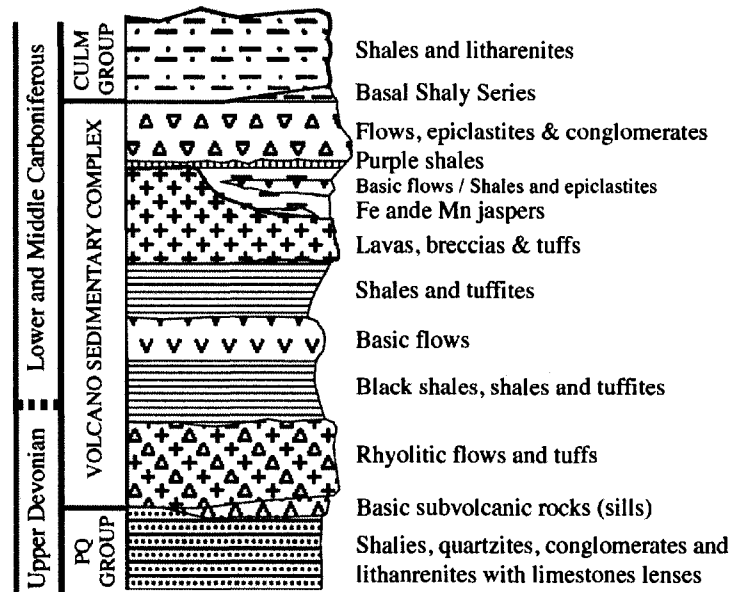


Figure 2.5: Lithostratigraphic column of the Iberian Pyrite Belt (Saez et al., 1999; Tornos, 2006).

2.2.2.1. Phyllite-Quartzite Group (Devonian)

The Phyllite-Quartzite Group is a thick layer of 2000 m that is comprised of a homogeneous detrital sequence of alternating metamorphosed shales and quartz sandstones from the Late Devonian (Almodovar et al., 1998; Gonzalez et al., 2006; Leistel et al., 1998; Moreno et al., 1996; Saez et al., 1999; Tornos, 2006). At the top of the sequence lies a 30 m thick sequence of carbonate lenses and nodules, as well as rare quartzitic conglomeratic units (Leistel et al., 1998; Van den Boogaard, 1967). Fan deltas, near-shore sandstone bars and sedimentary deposits of mega debris-flows occur at the top of the PQ (Moreno et al., 1996) indicating a high-energy environment (Leistel et al.,

1998; Saez et al., 1999; Tornos, 2006). Within the PQ group, hydrothermal alteration or stockwork zones are significantly present (Tornos, 2006).

2.2.2.2. Volcano-Sedimentary Complex

The VSC is composed of Late Faménian (Upper Devonian) to Middle Viséan (Lower Carboniferous) sequences of mafic and felsic volcanic rocks representing 20% and 60% of the complex, respectively. These rocks are interbedded with black shales and chemical sediments. The complex also includes greywacke, quartzwacke, impure quartzite, jasper, radiolarite, and limestone lenses and nodules (Davis, 2001). The felsic rocks that compose the VSC are pyroclastic rocks with submarine dacitic ashflow tuffs with smaller amounts of rhyolite (Davis, 2001; Thieblemont et al., 1998). The mafic rocks are mainly diabase and pillow lavas (Davis, 2001). At the boundary between the PQ Group and the VSC is an anoxic sequence of organic black shales of Late Devonian and can also present volcanic rocks. The sulphide mineralization is hosted by the anoxic sequence, either directly in the black shales or resting on the acidic volcanic facies. Above the anoxic sequence, the VSC presents diverse Lower Carboniferous volcanic sedimentary and volcanoclastic rocks. At the boundary between the VSC and the Culm group is an Upper Viséan volcanodetrital and shaly sequence that comprises reworked material from the Upper VSC, presenting the first manifestations of the post-volcanic turbiditic activity. The exposure of the VSC is distributed into several independent areas in a discontinuous way (figure 2.4) and represents only 25% of the entire IPB outcrops.

2.2.2.3. Culm Group

The Culm Group is a turbidite formation of up to 3000 m thick, dating from Late Viséan to Late Bashkirian (Lower Carboniferous). It consists of flysch sediments (Schermerhorn, 1971) composed of greywacke and shale with litharenites and rare conglomerates containing clasts of the mafic and felsic volcanic rocks of the VSC (Barriga et al., 1997; Carvalho et al., 1999; Strauss et al., 1977).

2.2.3. Mineralization in the IPB

The volcanic massive sulphide mineralization (VMS) of the IPB contains high proportions of pyrite, chalcopyrite and other Cu ores (Leistel et al., 1998; Strauss et al., 1977), and common occurrences of sphalerite, galena, tetrahedrite, arsenopyrite, and pyrrhothite (Mitsuno et al., 1988; Routhier, 1980; Strauss, 1970). The most common minor mineral phases are Bi-Sb-Pb-As sulphosalts, stannite, cassiterite, magnetite, electrum, and cobaltite (Aye and Picot, 1976; Mitsuno et al., 1988; Routhier, 1980; Sierra, 1984; Strauss, 1970). The VMS are enriched in a variety of elements including Fe, Zn, Cu, Pb, Ag, Sb, Bi, Au, and Sn (Leistel et al., 1998; Strauss et al., 1977). The VMS host trace amounts of Cd, Co, Hg, and Se (Pauwels et al., 2002).

2.2.4. Mining exploitation in the IPB and historical context

The ore deposits from the volcanic massive sulphides of the IPB have been exploited since 4500 B.C. during the Iberian, Phoenician, and Roman times. During these periods mainly silver, gold and copper deposits were mined extensively (Blanco Freijero and Rothenberg, 1981; Ferrero, 1988) and since 2500 yr B.C., zinc, copper, and lead mineralization have been mined continuously (Rothenberg and Blanco Freijero, 1980). It has been estimated through remains of slag deposits, that the Romans mined approximately 25 Mt of sulphide ore from the IPB during the 4th century AD (Strauss et al., 1977). Regardless of the extensive mining of metals during the past 5000 years, remarkably large reserves remain in the region, though the near-surface deposits are almost all exhausted forcing exploration of deeper orebodies (Leistel et al., 1998).

In the middle of the 19th century, intensive mining resumed due to high demand for copper and sulphuric acid (van Geen et al., 1997), with a peak in pyrite production between 1875 and 1930 (Ruiz et al., 1998). From the mid-19th century to the late 1970's, more than 250 Mt of sulphide ore were extracted and the activities were mainly limited to the Tinto and Odiel watersheds (van Geen et al., 1997). During the 20th century, pyrite for the production of sulphuric acid, copper and base metals as well as gold and silver were

the main mining products in the IPB (Saez et al., 1999). During the last 100 years, over 80 mines were in operation but only a few are still active, namely Aznalcollar-Los Frailes (Zn, Cu, Pb, Ag), Rio Tinto (Au and Ag), Tharsis (pyrite), Neves-Corvo (Cu and Sn) (Saez et al., 1999) and the recently closed Sotiel-Migollas mine (Cu, Pb, Zn, S, and Ag (Saez et al., 1999)). Many mines closed because pyrite was no longer used as a raw material for the production of sulphuric acid and the base-metal content of the deposits were somewhat poor (Leistel et al., 1998). More than 80 mines have extracted 300 million tonnes of polymetallic ores (Strauss and Madel, 1974) in the IPB.

2.3. Sotiel-Migollas Complex

2.3.1. Local Geology

All three lithostratigraphical units of the IPB are represented at the Sotiel-Migollas Mine complex (Gonzalez et al., 2006), (figures 2.6 and 2.7). The PQ Group is intersected by mafic sills and veins of the feeding stockwork mineralization and the top layers exhibit various conglomerate levels of gravity-flow deposits and scattered carbonate lenses of small size. The VSC contains at its base a thick layer of felsic volcanic and coarse- to fine-grained volcanoclastic (Va_1). On top of this volcanic layer is an anoxic sequence containing black shales that host several ore bodies followed by basic rocks and tuffs, felsic volcanic and volcanoclastic rocks and tuffs (Va_2). Purple shales and a succession of volcanic breccias and reworked tuffs (Va_3) complete the VSC unit. The top stratigraphic unit is the Culm group characterized by shales and greywackes (figure 2.6).

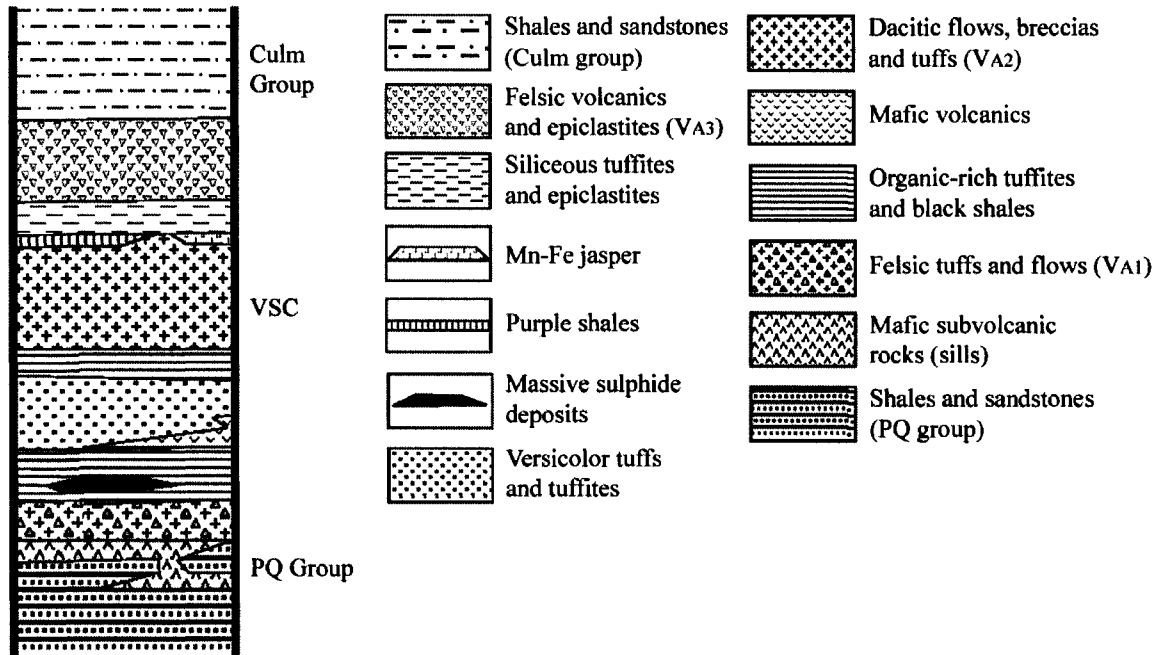


Figure 2.6: Lithostratigraphical units of the IPB present at the Sotiel-Migollas site (modified from Saez et al. (1999)).

2.3.2. Description of ore bodies

The massive sulphide deposit at the Sotiel-Migollas mine consists of three major lenses, namely the Sotiel, Sotiel-East and Migollas (figure 2.7). The Sotiel deposit is found directly within the VSC in the black shale unit between the dacitic sills and the PQ Group (Tornos, 2006). The Migollas deposit is located within the PQ Group. The resources estimated for the Sotiel-Migollas complex exceeds 130 Mt of massive sulphides and an unknown amount of mineralization from the stockwork (Gonzalez et al, 2006). On average, the grades of the mineralization are approximately 0.7% Cu, 1.24% Pb, and 2.76% Zn (Santos et al., 1993).

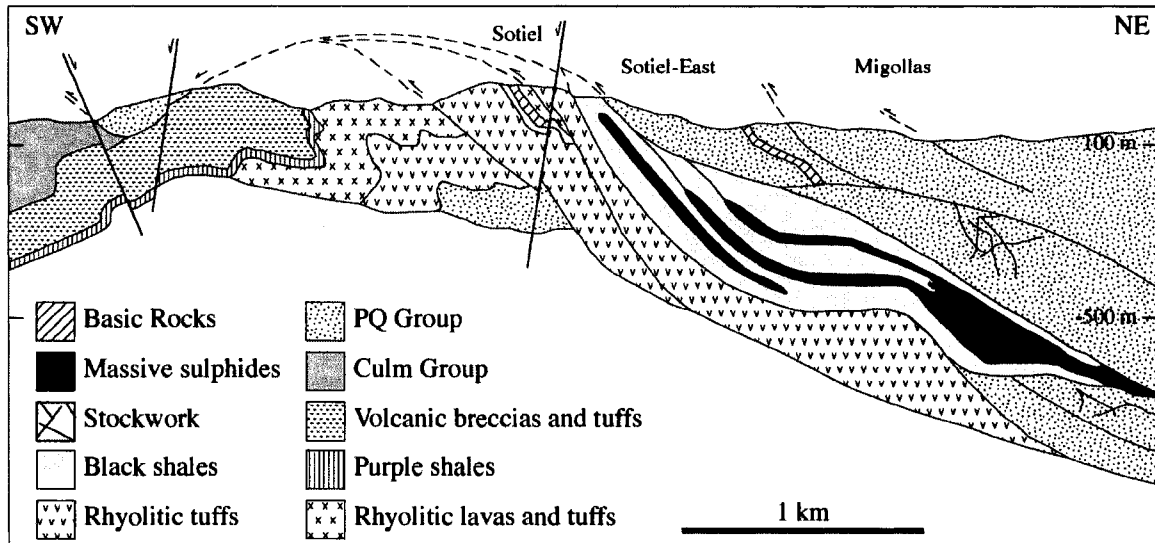


Figure 2.7: Cross-section of the lithostratigraphical and structural interpretation of the Sotiel-Migollas mine complex (modified from Santos et al. (1993) and Gonzalez et al. (2006)).

2.3.3. History of mining at the study area – mining operation

Evidence of metallurgical activities in the vicinity of the Odiel and Tinto Rivers date from 2500 yr B.C. (Briard, 1976; Rothenberg and Blanco Freijero, 1980). More recent mining of the Sotiel deposit started in 1984 and was operated by Almagrera S.A. The mine was extracting mainly copper, lead, and zinc by differential flotation with contents of 0.6%, 1.13%, and 4.5% respectively (Morales, 1999). In addition to the treatment of polymetallic sulphides, pyrite was mined to obtain sulphur of 42% content for the production of sulphuric acid (Morales, 1999). The products of the mining process are metal concentrates of copper, lead, and zinc, sulphuric acid and oleum (a solution of sulphur trioxide in sulphuric acid) that resulted from the roasting of residual pyrite at the Sulfuric Acid Plant on site. The Migollas deposit was discovered in 1989 and was mined for copper and silver. The Migollas Copper Mine was controlled and owned by Navan Mining plc. The Sotiel-Migollas mine has been abandoned since 2002.

3. CHAPTER 3 – DATA ACQUISITION and SAMPLE SUITES

3.1. Introduction

This chapter presents the datasets acquired in the field and laboratory to carry out the objectives of this thesis. Figure 3.1 presents a workflow diagram of the thesis for a full visual understanding of the different type of data collected, the different data processing and analyses performed, as well as the directions of the intermediate and end products of this work. All data presented in this chapter are subsequently used for the mineral mapping and predictive pH mapping of the mine waste tailings, presented in chapters 4 and 5.

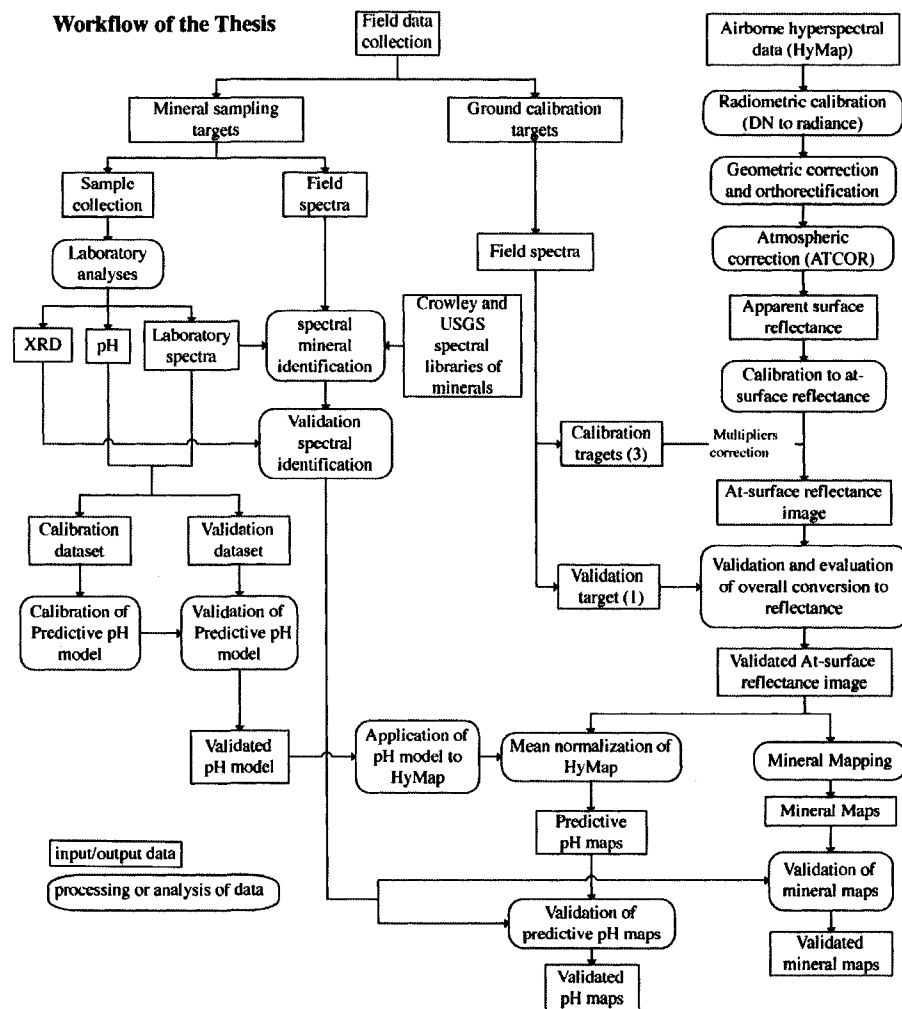


Figure 3.1: Workflow diagram summarizing the thesis data collection and manipulation of the datasets.

3.2. Field datasets, criteria and methods of site selection

3.2.1. Field datasets

Three field campaigns have occurred that coincide with the acquisition of airborne data (section 3.3) in May 2004 (M04), August 2004 (A04), and June 2005 (J05). During these field campaigns, two categories of field sites were selected. The first category served to support the development and validation of predictive pH models and for the validation of the mineral maps derived from imagery (campaigns of A04 and J05). The second category was used to calibrate the airborne hyperspectral imagery to surface reflectance and for the assessment of this calibration (campaigns of M04 and J05). For the first category, reflectance spectra were acquired in the field during the collection of mineral soil samples. The samples were then taken to the laboratory for pH measurements, X-ray diffraction analysis (XRD) and further spectral measurement. Spectra and pH measurements were used for the calibration and validation of the pH model and the validation of the pH maps. XRD data supported the mineral identification conducted from the analysis of laboratory and field spectra. The field and laboratory spectra were also used for the assessment of the mineral maps derived from remote sensing.

3.2.2. Criteria for the selection of field sites

Several criteria guided the selection of mineral soil sampling sites and image calibration sites (Che, 1992). In order to support the development of predictive mineral maps and pH models, the mineral soil sampling sites should span the spectrum of dominant minerals typically found in acid mine drainage environments and the range of soil pH values encountered at the site. The image calibration is conducted using a multiplier correction method that compares the at-sensor and field reflectance values of a suite of sites to generate a multiplier spectrum. Thus the sites should span a wide range of spectral reflectance values to properly constrain the regression of image and field reflectance values across multiple sites. For both categories of sites, it is important to find

flat and homogeneous areas, i.e. uniform in reflectance and bare of vegetation. In addition, the site area should exceed three times the size of the airborne imagery pixel (i.e. at least 15 x 15 meters or 225 m² area). Finally, all sites should be encompassed by the image.

3.2.3. Selection of field sites

3.2.3.1. Selection of mineral soil sampling sites

Images acquired in May 2004 were analyzed to support the selection of sampling sites for the August 2004 field campaign. For the field campaign of June 2005, the selection of sites was guided by mineral maps created from analysis of the August 2004 imagery. The mineral maps were created using the Spectral Hourglass method embedded in the ENVI imagery software package (ITT, Boulder, Colorado, www.itvis.com/envi). This method involves using the Minimum Noise Fraction (MNF) transform to reduce noise in the imagery, a Pixel Purity Index (PPI) to select the purest pixels that may adequately capture the signature of known endmember mineral occurrences, and the Spectral Angle Mapper (SAM) to detect and map the distribution of these endmembers. From these images, large areas of predicted mineral occurrences related to acid mine drainage environments were chosen as sampling sites. The research then led to a revised methodology for the creation of the mineral maps described in chapter 5.

During field work additional acid mine drainage minerals were found and sampled. These areas represented interesting endmembers that could be used for the validation of the mineral map and for the calibration of the predictive pH model.

The total number of sites visited in August 2004 and June 2005 for mineral sampling was 41 and 56 respectively. At every site, a sediment sample was collected for further analyses in the laboratory. Samples were grouped into three mineral categories (table 3.1) including: 1) acid mine drainage minerals (AMD) (ferric oxyhydroxides, ferric oxides, ferric oxyhydrates, ferric iron-bearing hydroxyl-sulphates and hydroxyl-sulphate-

hydrite), used for the calibration and validation of the predictive pH model and the assessment of the mineral maps; 2) efflorescent salt minerals (ferric sulphate-hydrate, mixed ferrous-ferric sulphate-hydrate and ferrous sulphate-hydrates); and 3) other minerals to support the assessment of the mineral maps. Appendix 3.1 gives the location coordinates of the sampling sites for the August 2004 (A04) and June 2005 (J05) field campaigns as well as the mineral category for each sample. Appendix 3.2 presents maps of the location and area of the sampling sites visible on the Hymap imagery.

Table 3.1: Mineral categories and number of samples of waste-rock collected at the Sotiel-Migollas mine complex.

Mineral categories	August 2004 campaign	June 2005 campaign
AMD minerals	16	38
Efflorescent salt minerals	7	13
Other minerals	18	5

3.2.3.2. Selection of ground calibration targets

The ground calibration sites were selected from hyperspectral imagery acquired in May 1999 prior to the first field campaign of May 2004. The sites include a football field, a parking lot near the processing plant, and a concrete school ground. A basketball court was selected for the validation of the atmospheric correction. All sites met the aforementioned criteria (section 3.1.2). The school ground and the parking at the processing plant are darker sites than the football court. Table 3.2 gives a description of each site.

Table 3.2: Description and coordinates (in UTM European Mean 1950, zone 29 North) of each calibration site.

Site	Approximate Area (m²)	X	Y	Description
Football field	4337	687381	4169220	Iron coating of fine gravel – Bright target
School Ground	910	687496	4169891	Paved surface – Concrete
Parking at Processing Plant	2014	688939	4168205	Iron coating gravel – gentle slope of 5°
Basketball court	728	687336	4169207	Artificial - red painted concrete surface

Coordinates are projected to UTM European Mean 1950 zone 29N.

3.3. Field and laboratory spectral measurements

3.3.1. Instrumentation

Reflectance spectra were collected in the field and laboratory using an Analytical Spectral Devices (ASD) FieldSpec Pro portable spectroradiometer. The ASD spectroradiometer is composed of three detectors covering the 350 nm to 2500 nm wavelength range with a sampling interval of 1 to 2 nm and spectral resolution of 3 or 10 to 12nm (table 3.3). The ASD FieldSpec Pro measures directly the relative reflectance (R_{relative}), equation 3.1, which consists of a ratio between the light reflected by the sample (I_{target}) and the light reflected by a white Spectralon reference ($I_{\text{reference standard}}$) panel (Clark et al., 2002).

$$R_{\text{relative}} = I_{\text{target}} / I_{\text{reference standard}} \quad (3.1)$$

Table 3.3: Description of ASD FieldSpec Pro spectroradiometers (Analytical Spectral Devices, 2000).

Spectrometer	Bandwidth (sampling interval)	Spectral resolution
VNIR (350-1050 nm)	1.4 nm	3 nm at 700 nm
SWIR 1 (900-1850 nm)	2 nm	10 to 12 nm
SWIR 2 (1700-2500 nm)	2 nm	10 to 12 nm

3.3.2. Acquisition methods

3.3.2.1. Field spectral measurements

Field spectral measurements were acquired for the ground calibration sites and the mineral sampling sites. The spectral measurements should be acquired as close as possible to the acquisition time of the airborne imagery. Thus, ground calibration sites were measured during the overflight, i.e. at solar noon \pm 2 hours; whereas the mineral sampling sites were measured within days of the flight acquisition again near solar noon under similar atmospheric conditions. For all field spectral measurements, the

spectrometer was positioned at nadir at approximately 1 meter above the target giving a field-of-view footprint of approximately 45 cm.

Between 43 and 51 spectra were collected over the entire area of each calibration site following a five meter grid sampling scheme. For the mineral sampling sites, between 5 and 35 spectra were acquired per site depending on the size of the sampling area and were collected following a grid sampling scheme when possible. Georeferenced data (GPS), photographs and descriptions of the sites and sky conditions were documented for all spectral measurements.

3.3.2.2. Laboratory spectral measurements

Laboratory spectra were collected for all samples since not all sites could be measured in the field due to poor atmospheric conditions.

The viewing and illumination geometry in the laboratory were carefully controlled and similar to that of the airborne data acquisition. For each seasonal set of samples, the illumination provided by an external Halogen Lamp (JC14.5V-50 WC) was at a zenith angle corresponding to that of the sun at the time of the flight acquisition (i.e. for samples collected in May 2004, August 2004 and June 2005, the laboratory illumination was set to a zenith angle of 30°, 35° and 15° respectively). The field-of-view did not exceed 4.4 cm in diameter, but depended on the sample size. The samples were measured in a grid pattern to sample the entire specimen; and between 4 and 119 spectral measurements were taken per sample. The ASD instrument configuration was set to collect respectively 10, 25, and 20 samples of the spectrum, dark current and white reference.

3.3.3. Processing of spectra

A number of pre-processing steps were conducted prior to analysis. The first step was one of data quality assessment involving the removal of corrupted measurements

from the dataset. Corrupted spectra included oversaturated measurements and/or errors in measurement in the laboratory and in the field. Subsequently, a correction was performed to remove sudden amplitude discontinuities observed between 1000 and 1001 nm and 1830 and 1831 nm that correspond to transitions in detectors. The correction involved applying gain factors for data from the first (VIS) and third (SWIR2) spectrometers to match data from the second (SWIR1) spectrometer, which remained constant. Table 3.4 documents the wavelength location of the breaks observed for the three different ASD instruments used in this study.

Table 3.4: Location of spectral discontinuities of ASD instruments.

ASD instrument	First step	Second step
ASD DFD-DLR (2005)	Bands 651-652 (1.000 to 1.001 μm)	No step
ASD IMF-DLR (2004)	Bands 651-652 (1.000 to 1.001 μm)	No step
ASD UofA – EOSL	Bands 651-652 (1.000 to 1.001 μm)	Bands 1481-1482 (1.830 to 1.831 μm)

The ASD from IMF-DLR and DFD-DLR were used for the 2004 and 2005 field campaign respectively. The ASD from the EOSL-UofA was used for all laboratory spectral measurements.

The reference panel used in the field contained traces of impurities (or dirt) which caused the field spectra to show residual reflectance. In order to correct for these artefacts, the field reference panel needed to be calibrated against a clean laboratory panel. The laboratory calibrated spectrum is the absolute reflectance of the field reference panel, i.e. the ratio between the reflectance of the field reference standard and that of the laboratory reference standard (equation 3.2), which was provided by DLR for both field campaigns. With the laboratory calibrated spectrum, it is possible to correct the relative field reflectance (equation 3.1) of the targets to absolute reflectance (equation 3.3).

$$\text{Laboratory calibrated spectrum} = (I_{\text{field reference standard}}/I_{\text{laboratory reference standard}}) \quad (3.2)$$

$$R_{\text{abs}} = R_{\text{relative}} * \text{Laboratory calibrated spectrum} \quad (3.3)$$

It is important to note that the laboratory calibrated spectrum provided for the Spectralon used in the summer of 2004 was very noisy, therefore it was necessary to cross-calibrate it with the calibration spectrum of the Spectralon used in the summer of 2005. Further details on the calculations of absolute reflectance for field spectra of 2004 and 2005 are presented in appendix 3.3.

Once the jumps were removed from all the spectra and the absolute reflectance was calculated for the field spectra, statistics were calculated to obtain the mean, minimum, maximum and standard deviation of the reflectance spectra for each sample.

3.4. Airborne spectral measurements

3.4.1. Airborne hyperspectral survey parameters

Airborne hyperspectral data were acquired with the Hymap sensor over the Sotiel-Migollas mine. Hymap is a whiskbroom imaging spectrometer and has 126 spectral bands covering the 0.45 – 2.5 μm visible to short wave infrared region with contiguous spectral coverage (except in the atmospheric water vapour bands) and with bandwidths between 10 and 20 nm (Cocks et al., 1998). Table 3.5 presents a summary of the Hymap system spatial and spectral configurations. The German Aerospace Center (DLR) and HyVista Corp. jointly provided the acquisition of the data. The Hymap flights were carried out on May 6 1999, May 19 2004, August 14 2004 and June 17 2005 to allow multi-temporal analysis (in future work). Appendix 3.4 provides details of the flight lines over the study sites during the four overflights. The acquisition covered a maximum area of approximately 163 km^2 between Northing 4151550 and 4173316 and Easting 680906 and 696357 (figure 3.2) for each of the flight campaigns of 2004 and 2005.

Table 3.5: Summary of the Hymap system technical specifications (Cocks, et al. 1998).

Typical Operational Parameters			
Platform	Light, twin engine aircraft (Dornier Do 228)		
Altitudes	2000-5000 m above ground level		
Ground Speed	110-180 knots		
Spatial Configurations			
IFOV	2.5 mrad along track 2.0 mrad across track		
FOV	61.3 degrees (512 pixels)		
Swath	2.3 km at 5m IFOV (along track) 4.6 km at 10m IFOV (along track)		
Typical Spectral Configurations			
Module	Spectral range	Bandwidth across module	FWHM
VIS	0.45-0.89 μm	15-16 nm	15 nm
NIR	0.89-1.35 μm	15-16 nm	15 nm
SWIR1	1.40-1.80 μm	15-16 nm	13 nm
SWIR2	1.95-2.48 μm	18-20 nm	17 nm

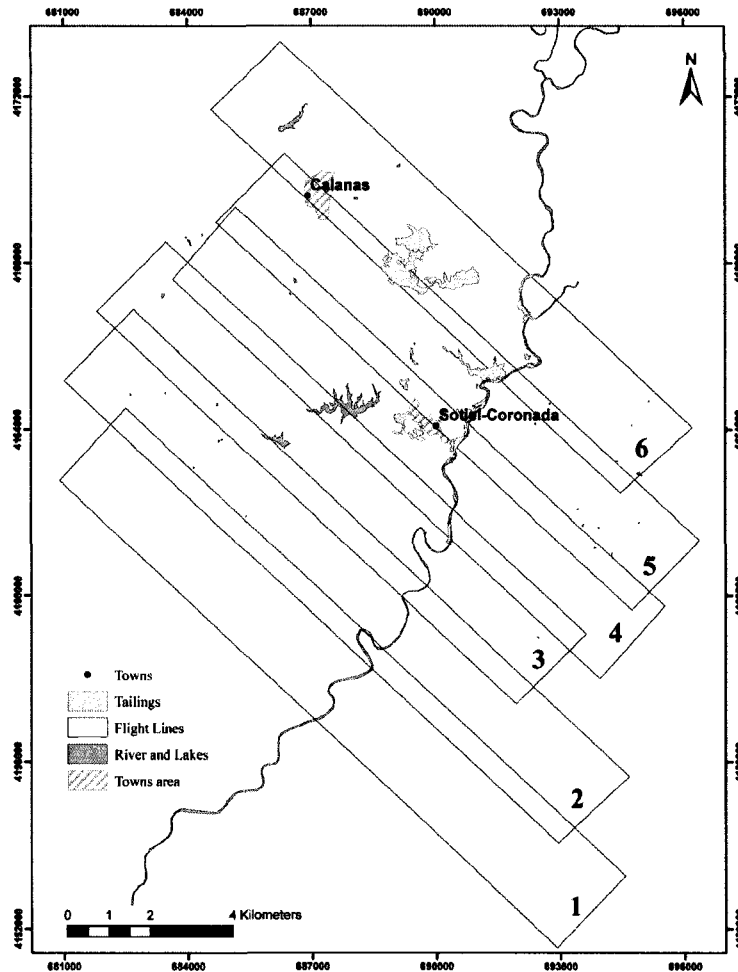


Figure 3.2: Location of flightlines with corresponding flightline number over the Sotiel-Migollas mine (UTM European Mean 1950, zone 29 North) for campaigns of 2004 and 2005.

3.4.2. Pre-processing of the airborne hyperspectral images

Pre-processing of the Hymap images involves several steps to obtain calibrated at-surface reflectance. These steps consist of a radiometric calibration, a geometric correction and orthorectification, an atmospheric correction using a radiative transfer model, and a calibration using ground calibration sites. Following the pre-processing steps, an evaluation is conducted to verify the accuracy of the overall conversion to at-surface reflectance.

3.4.2.1. Radiometric calibration: DN to at-sensor radiance

During the flight, the radiometric data is recorded in digital number (DN). This raw data is then corrected for dark current/electronic offsets using an on-board calibration lamp. Then, the DN is converted to at-sensor radiance $L(k)$ (in units of $\text{mW}/\text{cm}^2/\text{sr}/\text{nm}$), using pre-flight calibration coefficients, i.e. gains ($c_1(k)$) and offsets ($c_0(k)$) calculated from the laboratory radiometric calibration through standard procedures (Cocks et al. 1998). The calibration coefficients for each band (k) were used in the conversion as illustrated in equation 3.4:

$$L(k) = c_0(k) + c_1(k)DN(k) \quad (3.4)$$

3.4.2.2. Geometric correction and orthorectification

The next step consists of performing a geometric correction and an orthorectification using the parametric algorithm PARGE (Schlaepfer, 2002). This process is based on parameters obtained during the recording of the image and includes sensor-specific parameters, a digital terrain model and flight parameters, such as sensor position (i.e. latitude, longitude and height) and attitude (i.e. roll, pitch and heading). The output of the application of the PARGE algorithm is an at-sensor radiance image free of distortions introduced by sensor movement.

3.4.2.3. Atmospheric correction using a radiative transfer model

Once the radiance image is geocoded and orthorectified, the correction for atmospheric effects is performed using the airborne Atmospheric and Topographic Correction Model (ATCOR4), (Richter, 2002). ATCOR4 transforms the at-sensor radiance information to apparent surface reflectance by simultaneously correcting the effects of varying illumination related to topography and atmospheric effects using the MODTRAN4 radiative transfer algorithm (Berk, 1998). The atmospheric parameters chosen through the ATCOR4 software were a standard rural aerosol type over the entire

scenes and a visibility (aerosol optical depth) of 25 km (table 3.6). The water vapour was calculated as an average of the land water vapours from spectral bands 0.94 μm and 1.13 μm and was retrieved on a per pixel basis. Details of the flight acquisition parameters used for the atmospheric correction parameters are provided in appendix 3.4.

Table 3.6: Atmospheric parameters for the ATCOR4 atmospheric correction of all Hymap images.

Atmospheric parameters	
Aerosol type	Rural
Adjacency range	1 km
Visibility	25 km
Regions for water vapour algorithm	0.94 μm and 1.13 μm

The apparent surface reflectance obtained after applying the radiative transfer model holds residuals, which correspond to atmospheric absorptions that were not removed by ATCOR or represent errors in the sensor’s radiometric calibration (figure 3.3).

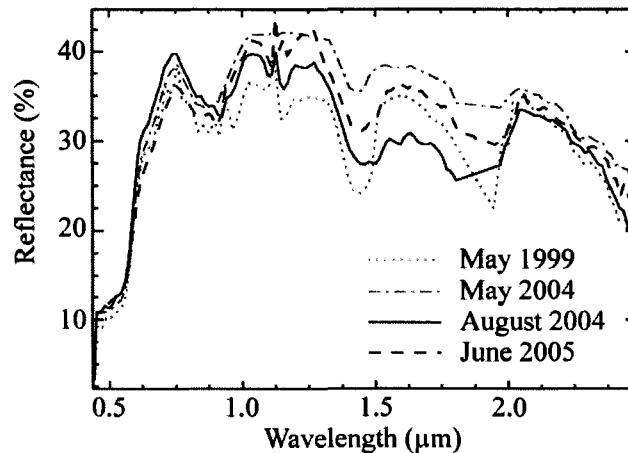


Figure 3.3: Apparent surface reflectance of a ground invariant target (Basketball court), after applying the radiative transfer model for each Hymap datasets (May 2004, August 2004, and June 2005).

3.4.2.4. Calibration to at-surface reflectance using ground calibration sites

To minimize residual artefacts from the output of the radiative transfer model, a multiplier correction is applied to the images based on a comparison of field spectra at

ground calibration sites with corresponding spectra from the Hymap data (offset spectrum) (Clark et al. 2002). This comparison gives a multiplicative factor (or gain) for each spectral channel. It can be applied to every at-sensor reflectance spectrum in the Hymap dataset to obtain a final at-surface reflectance image. The outcome of this process delivers polished spectra and facilitates the comparison of image data with field measurements.

Thus, three of four invariant sites (football ground, school ground, and the parking lot at the processing plant) were compared to the Hymap imagery for each dataset, giving a ratio of ASD field spectra to Hymap spectra. The three ratio values were averaged to give one multiplicative factor per dataset (figure 3.4), which was then applied to every spectrum of the Hymap image. Because field spectra were not acquired in August 2004, the gain factor calculated for May of the same year were utilized.

No field spectra is available for the May 1999 images, therefore only the standard calibration file is used for the radiative transfer model during the atmospheric correction.

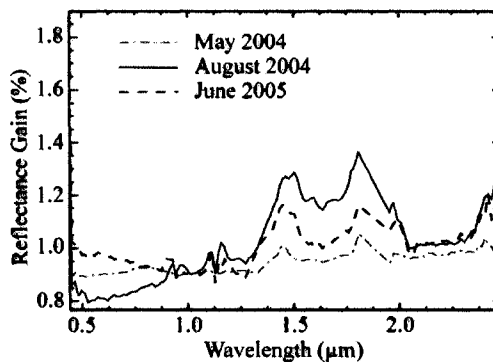


Figure 3.4: Multiplicative factor obtained from the mean of three invariant target spectra for each Hymap datasets (May 2004, August 2004, and June 2005).

3.4.3. Evaluation of calibration to at-surface reflectance

The accuracy of the conversion of imagery to at-surface reflectance was examined by comparing the at-surface reflectance spectra of a separate ground calibration site (Basketball court) with that measured in the field (figure 3.5).

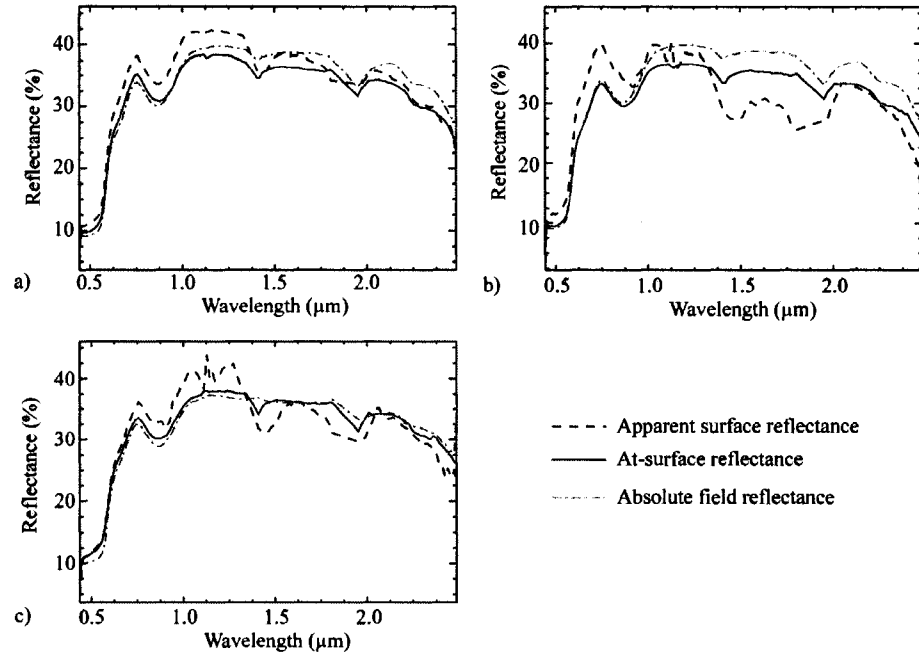


Figure 3.5: At-surface reflectance of the ground validation site (Basketball court) in comparison to the absolute field reflectance and the apparent surface reflectance for the three Hymap imagery datasets: a) May 2004; b) August 2004; and c) June 2005. The absolute field reflectance was measured in the field in May 2004 and June 2005. The spectra of May 2004 were used for comparison with the Hymap August 2004 data.

An absolute mean error of -1.097% is observed for the three image datasets (table 3.7). The absolute error is the difference between the at-surface reflectance and the field absolute reflectance over all wavelengths. The highest absolute error is observed for the August 2004 imagery and is likely due to the absence of ground measurements of the calibration sites for that field campaign. The low absolute error indicates that the overall conversion is suitable for further analyses of the hyperspectral imagery.

Table 3.7: Percentage error of at-surface images compared to ground validation sites. May 1999 has no field spectral measurement to evaluate the atmospheric correction.

Hymap image datasets	Reflectance error (%) = Apparent – absolute reflectance of ground validation site (Basketball court) over all wavelengths
May 1999*	N/A
May 2004	-1.267
August 2004	-2.345
June 2005	0.320
Absolute Mean error (%)	-1.097

3.5. Other measurements

In addition to spectral measurements acquired from samples in the laboratory, pH measurements and X-Ray Diffraction analyses (XRD) were completed on separate powders of sample bulk material and sample coating. When possible the top few millimetres of material coating was removed (scraped) from samples. Both the coating and bulk material were crushed using a mortar and pestle to generate approximately 20 grams. The two categories of material are analyzed to examine potential differences in pH and in mineralogy between them. This represents valuable information for the interpretation of reflectance measurements that sample only the top few tens of microns of the surface (Swayze et al., 2000).

3.5.1. pH

The pH analyses are used for the calibration and validation of the pH predictive model. The analyses were performed separately on the coatings and bulk material of the samples that were used for the pH predictive modeling. The pH analysis was performed with the same methods employed by Ong et al. (2003a) for consistency. A solution of 1:5 mass-volume of powdered sample to deionised water was prepared for the pH analysis. The solution was mixed on a Gyrotory Shaker-Model G2 for four hours, and then left to settle out for approximately one hour. At this point, the solution was measured using an Orion pH meter (Model 290A), which was calibrated before hand with four buffer solutions (pH 2, 4, 7, and 10). Table 3.8 presents the pH measurements for the bulk and coating material for the samples collected during the two field campaigns of August 2004 and June 2005. Only the samples used for the calibration and validation of the predictive pH model of the Sotiel-Migollas mine and the evaluation of the Brukunga's model are given. The pH values of the coating samples range from 1.43 to 6.43 and that of the bulk samples from 1.63 to 8.29.

Table 3.8: pH values of bulk and coating of samples used for the pH modeling of Sotiel-Migollas and the evaluation of the Brukunga pH model.

August 2004 samples			June 2005 samples		
Sample	pH (coating)	pH (bulk)	Sample	pH (coating)	pH (bulk)
A04-07	2.629	5.27	J05-01	-	2.564
A04-08	-	4.506 (thick coat)	J05-02	3.257	3.383
A04-09	3.735	4.446	J05-04	-	6.089 (thick coat)
A04-14	4.491	5.109	J05-05	3.37	3.734
A04-18	2.631	3.587	J05-06	2.813	-
A04-20	-	2.097	J05-08	-	2.66
A04-21	2.891	2.248	J05-09	-	7.943 (thick coat)
A04-22	-	2.433	J05-10	-	7.816
A04-27	4.101	6.732	J05-14	-	3.536
A04-29	-	2.441	J05-15	-	2.557
A04-31	-	2.486	J05-19	-	2.502
A04-31	-	5.985	J05-20	2.699	2.782
A04-33	-	5.983	J05-21	-	2.625
A04-34	-	5.334	J05-22	-	2.619
A04-36	-	7.832 (thick coat)	J05-23	2.838	2.849
A04-37	-	7.621 (thick coat)	J05-24	3.387	3.287
A04-43	5.221	6.248	J05-25	4.7	4.857
	4.893		J05-30	3.102	2.528
A04-44	6.365	7.65	J05-32	4.011	4.111
	6.435		J05-35	2.869	2.386
A04-47	3.269	5.79	J05-37	3.643	6.929
			J05-38	2.973	3.304
			J05-39	3.278	3.414
			J05-40	2.608	-
			J05-41	-	8.248 (thick coat)
			J05-42	2.221	2.259
			J05-43	3.666	3.121
			J05-44	1.765	1.766
			J05-45	1.73	1.662
			J05-46	2.892	2.393
			J05-47	1.431	1.629
			J05-49	3.219	2.998
			J05-51	3.744	3.842
			J05-52	4.144	4.163
			J05-53	3.663	3.651
			J05-54	2.043	2.05
			J05-55	3.364	3.504
			J05-56	3.872	3.331
			J05-57	4.008	4.06
			J05-58	2.074	2.016

3.5.2. X-Ray Diffraction

The X-Ray Diffraction analyses were conducted on the powdered minerals of bulk and coating material to help support the mineral identification from the spectra. The XRD instrument is a Rigaku Geigerflex Power Diffractometer with a Co tube and a graphite monochromator. The identification of the minerals was conducted by matching the observed diffraction patterns with that in the JCPDS database. Hematite, goethite, ferrihydrite, were the main oxides and hydroxides detected in the samples. Calcite, dolomite and ankerite represented the carbonates detected. The main silicate minerals identified were albite, clinocllore, illite, kaolinite, montmorillonite, muscovite,

orthoclase, and quartz, among several others. The common sulphates identified were copiapite, coquimbite, ferricopiapite, gypsum, halotrichite, jarosite, melanterite, kalinite, pickeringite, rhomboclase, rozenite, and szomolnokite. A compilation of the XRD results for the coating and bulk material is presented in appendix 3.5 . According to Lapakko (2002), amorphous minerals commonly associated with acid mine drainage, e.g., oxyhydroxides of iron, aluminum, and aluminosilicates, cannot be identified with XRD analysis.

3.6. Characterization of sample suites

3.6.1. Labelling of field and laboratory spectra

Field and laboratory spectra collected from the sediment samples consist of nonlinear mixtures of different minerals, i.e., intimate mixtures in which the minerals are distributed homogeneously. We know of no robust nonlinear unmixing code that could determine the type of minerals in a mixture and their corresponding fractional abundances. Therefore, the spectra were subjected to linear unmixing methods to identify the type and provide an approximation of abundances of the material and as a guide to determine the most abundant minerals in the mixture.

3.6.1.1. Methods of spectra labelling

The mineral identification of the sediment sample spectra was performed by comparison with a spectral library of secondary Fe-oxide, Fe-hydroxide, and Fe-sulphate-hydrate minerals related to acid mine drainage and published by Crowley et al. (2003). The pyrite1 spectra of the USGS spectral library available in the ENVI software package was also used. The comparison was performed using an unconstrained linear unmixing method provided by DLR (Bachmann, 2007). The linear unmixing consists of a multiple endmember spectral mixture analysis (MESMA). Also, different spectral analyses were performed which consist of Spectral Angle Mapper (SAM) and spectral feature fitting (SFF) (Clark et al., 1992; Clark et al., 1990; Clark and Swayze, 1995;

Clark et al., 1991) in order to compare results with the MESMA unmixing. A thorough visual inspection of the compared spectra was made to avoid false-positive labelling. X-ray diffraction analysis results also guided the labelling of the spectra.

3.6.1.2. Results of spectra labelling

Table 3.9 presents the final identification of each sample in the August 2004 and June 2005 datasets.

Table 3.9: Identification of acid mine drainage mineral samples of August 2004 and June 2005.

Sample	Label of laboratory spectra	Sample	Label of laboratory spectra	Sample	Label of laboratory spectra
A04-07	SCH gt	J05-01	HE	J05-32	GT-FERR he
A04-08	GT-HE	J05-02	FERR/SCH-GT	J05-33	ME
A04-09	JR-FERR	J05-04	GT-HE sch/ferr	J05-35	GT-HE jr
A04-14	GT-FERR-PK jr	J05-05	SCH/FERR gt	J05-37	GT-JR-FERR
A04-16	PY	J05-06	SCH jr-gt	J05-38	JR-HE
A04-17	PY	J05-08	SCH-GT	J05-39	HE-FERR jr
A04-18	HE jr	J05-09	GT-FERR/sch	J05-40	GT-FERR sch
A04-19	CO	J05-10	SCH/FERR-JR	J05-41	SCH-GT
A04-20	HE	J05-12	HA-PK	J05-42	HE
A04-21	GT-JR	J05-13	RH-HA-pk	J05-43	JR py
A04-22	HE jr gt	J05-14	HE-SCH ferr	J05-44	HE
A04-23	PK-PY-qz	J05-15	SCH-JR	J05-45	HE co
A04-24	PY	J05-19	HE	J05-46	JR-GT-HE-FERR
A04-25	RZ-ME-pyr-sz	J05-20	FERR/SCH-HE jr	J05-47	HE par jr
A04-26	PY RZ ha sz	J05-21	HE	J05-48	PY qz
A04-27	GT-FERR	J05-22	HE-FERR	J05-49	HE jr
A04-29	JR-FERR/SCH gt	J05-23	HE	J05-50	RZ-HA
A04-30	PY RZ	J05-24	HE FERR-PK	J05-51	GT-FERR he
A04-31	GT-FERR	J05-25	FERR/SCH-GT	J05-52	SCH-HE
A04-33	GT-FERR others	J05-26	PY	J05-53	SCH jr-he
A04-34	SCH-GT ferr	J05-27	CO-HA-rh	J05-54	HE
A04-36	GT- SCH/ferr	J05-27b	SZ	J05-55	SCH jr he
A04-37	GT sch/ferr	J05-28	ME-RZ	J05-56	HE jr
A04-43	FERR/SCH he	J05-29	PY sz	J05-57	GT-JR
A04-44	FERR/SCH-HE	J05-30	GT-JR-FERR	J05-58	HE
A04-47	JR-GT	J05-31	ME	J05-59	HA-PK-SZ

DOMINANT: usually >60%; **CO-DOMINANT:** two or more components appear to be present in approximately equal amounts; **SUB-DOMINANT:** usually between ~20% and 60%; **minor:** concentrations between ~ 5% and 20%; *trace:* levels below 5%. Abbreviations: Gt: Goethite; Jr: jarosite; He: hematite; Sch: Schwertmannite; Ferr: Ferrihydrite Py: Pyrite; cop: Copiapite; Pk Pickeringite. A04: samples of August 2004; J05: samples of June 2005

3.6.1.3. Discussion

The mineral identification and abundance estimation from spectra remains a qualitative process subject to misinterpretations because of the nature of intimate mixtures of mineral grains. The unmixing method used helped to guide the identification of the most dominant mineral in the mixtures. Inferring the presence of certain minerals based on the presence of specific absorption features does not imply an accurate identification of minerals. In many instances there can be more than one mineral sharing an absorption feature at the same wavelength location introducing uncertainty in the mineral identification process. In addition absorption features of a given mineral can be obscured or attenuated by that of other minerals in the sample also introducing difficulties in the labelling of the sample. The identification of minerals from mixture spectra thus remains a continuous challenge and requires the educated use of ancillary data such as field observations and XRD results.

3.6.2. Sample suites for the pH predictive modelling

Prior to the conception of the Sotiel-Migollas pH predictive model, all samples collected in the field during the August 2004 and June 2005 field campaign (A04 and J05 in table 3.10) were sorted in two categories:

- 1- Acid Mine drainage related minerals (including goethite, hematite, schwertmannite, jarosite, etc.), N=58;
- 2- Efflorescent salt minerals (including copiapite, rosenite, szomolnokite, melanterite, etc.), N=20.

For each AMD mineral sample, the coating (N=38) and/or the bulk (N=56) (table 3.11) of the sample was analyzed in the laboratory for pH and XRD. Other samples were removed from the dataset since they were not relevant to this study, hence the gap in the numbering of the sample identification number.

Table 3.10: Samples of AMD minerals and efflorescent salts of August 2004 and June 2005.

AMD Minerals		Efflorescent salts
A04-07	J05-04	J05-39
A04-08	J05-05	J05-40
A04-09	J05-06	J05-41
A04-14	J05-08	J05-42
A04-18	J05-09	J05-43
A04-20	J05-10	J05-44
A04-21	J05-14	J05-45
A04-22	J05-15	J05-46
A04-27	J05-19	J05-47
A04-29	J05-20	J05-49
A04-31	J05-21	J05-51
A04-33	J05-22	J05-52
A04-34	J05-23	J05-53
A04-36	J05-24	J05-54
A04-37	J05-25	J05-55
A04-43	J05-30	J05-56
A04-44	J05-32	J05-57
A04-47	J05-35	J05-58
J05-01	J05-37	J05-48
J05-02	J05-38	J05-50
		J05-59

Table 3.11: Coating and bulk samples of the AMD minerals (A04 and J05 samples).

COATINGS		BULKS	
A04-07	J05-37	A04-07	J05-01
A04-09	J05-38	A04-08	J05-02
A04-14	J05-39	A04-09	J05-04
A04-18	J05-40	A04-14	J05-05
A04-21	J05-42	A04-18	J05-08
A04-27	J05-43	A04-20	J05-09
A04-43	J05-44	A04-21	J05-10
A04-44	J05-45	A04-22	J05-14
A04-47	J05-46	A04-27	J05-15
J05-02	J05-47	A04-29	J05-19
J05-05	J05-49	A04-31	J05-20
J05-06	J05-51	A04-33	J05-21
J05-20	J05-52	A04-34	J05-22
J05-23	J05-53	A04-36	J05-23
J05-24	J05-54	A04-37	J05-24
J05-25	J05-55	A04-43	J05-25
J05-30	J05-56	A04-44	J05-30
J05-32	J05-57	A04-47	J05-32
J05-35	J05-58		J05-35

A statistical analysis was then conducted to create a common dataset from the August 2004 coating samples (A04 coating), August 2004 bulk samples (A04 bulk), June 2005 coating samples (J05 coating), and June 2005 bulk samples (J05 bulk). The means and variances of separate datasets should be comparable if they are to be merged. The analysis evaluated the relation between independent qualitative variables (years - A04 and J05) or surface groups (coating and bulk) and dependant quantitative variables (means and variances of pH). Means were compared with the z-test if $n > 30$ or the t-test if

$n < 30$ (n being the number of samples). The variances were compared using the Fisher test (Levene's test as shown in table 3.12). These tests apply to assumed normally distributed populations thus the normality of the distributions was examined with the Shapiro-Wilk W test (table 3.13). However, the distributions of the samples are not necessarily expected to fit a normal distribution since pH ranges can vary considerably depending on the mineralogy present at the study site. The null-hypothesis (H_0) stipulates: if p -values > 0.05 then the distribution is normal. Results of the descriptive statistics and tests are presented in table 3.12 and 3.13 respectively, for each datasets. The corresponding histogram of normal distribution for each group are presented in figures 3.6, 3.7, and 3.8.

Table 3.12: Results of the tests for equality of variances and means.

		Levene's Test for Equality of Variances		t-test for Equality of Means						
		F	Sig.	t	df	Sig. (2-tailed)	Mean Difference	Std. Error Difference	95% Confidence Interval of the Difference	
									Lower	Upper
A04-Coat vs A04-Bulk	Equal variances assumed	1.977	0.172	-1.663	25	0.109	-1.16261	0.69925	-2.60275	0.27753
	Equal variances not assumed			-1.901	22.667	0.070	-1.16261	0.61156	-2.42874	0.10352
J05-Coat vs J05-Bulk	Equal variances assumed	5.810	0.019	-1.385	65	0.171	-0.47485	0.34278	-1.15943	0.20974
	Equal variances not assumed			-1.513	55.022	0.136	-0.47485	0.31384	-1.10379	0.15410
A04-CoatBulk vs J05CoatBulk	Equal variances assumed	2.233	0.141	-2.040	56	0.046	-0.950814	0.466040	-1.884405	-0.017223
	Equal variances not assumed			-1.928	28.882	0.064	-0.950814	0.493235	-1.959771	0.058144

Table 3.13: Descriptive statistics for the August 2004 (A04) and June 2005 (J05) samples.

	A04-coat AMD	A04-bulk AMD	A04-coat/bulk AMD	J05-coat AMD	J05-bulk AMD	J05-coat/bulk AMD	A04/J05-coat/bulk AMD
Descriptive Statistics							
N	9	18	18	29	38	40	58
Mean	3.91	5.07	4.41	3.08	3.56	3.46	3.76
Std. Deviation	1.26	1.89	1.81	0.79	1.71	1.56	1.69
Minimum	2.63	2.10	2.10	1.43	1.63	1.43	1.43
Maximum	6.40	7.83	7.83	4.70	8.25	8.25	8.25
Normality test							
Shapiro-Wilk Statistic	0.92	0.93	0.93	0.98	0.80	0.78	0.86
Shapiro-Wilk p-value	0.36	0.19	0.18	0.75	<0.0001	<0.0001	<0.0001

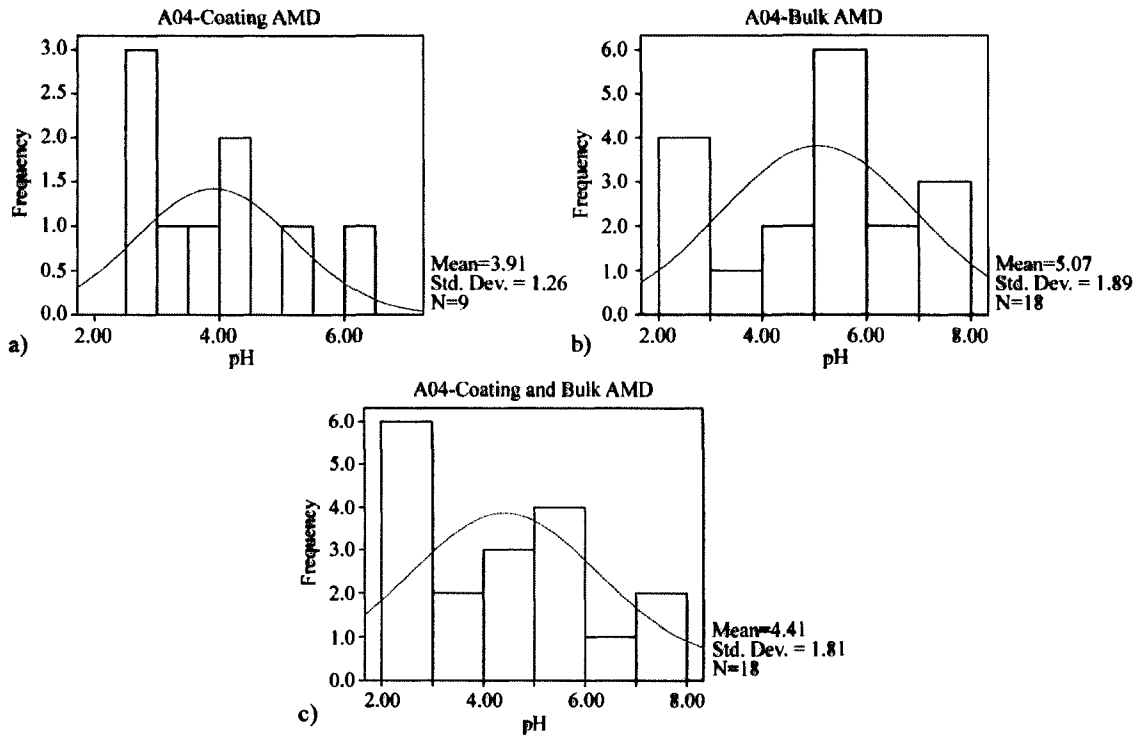


Figure 3.6: Frequency histograms of pH values for AMD mineral samples of August 2004: a) Coating samples b) Bulk samples c) Bulk and coating samples grouped together. The red curve represents the Normal Fit Distribution of the data.

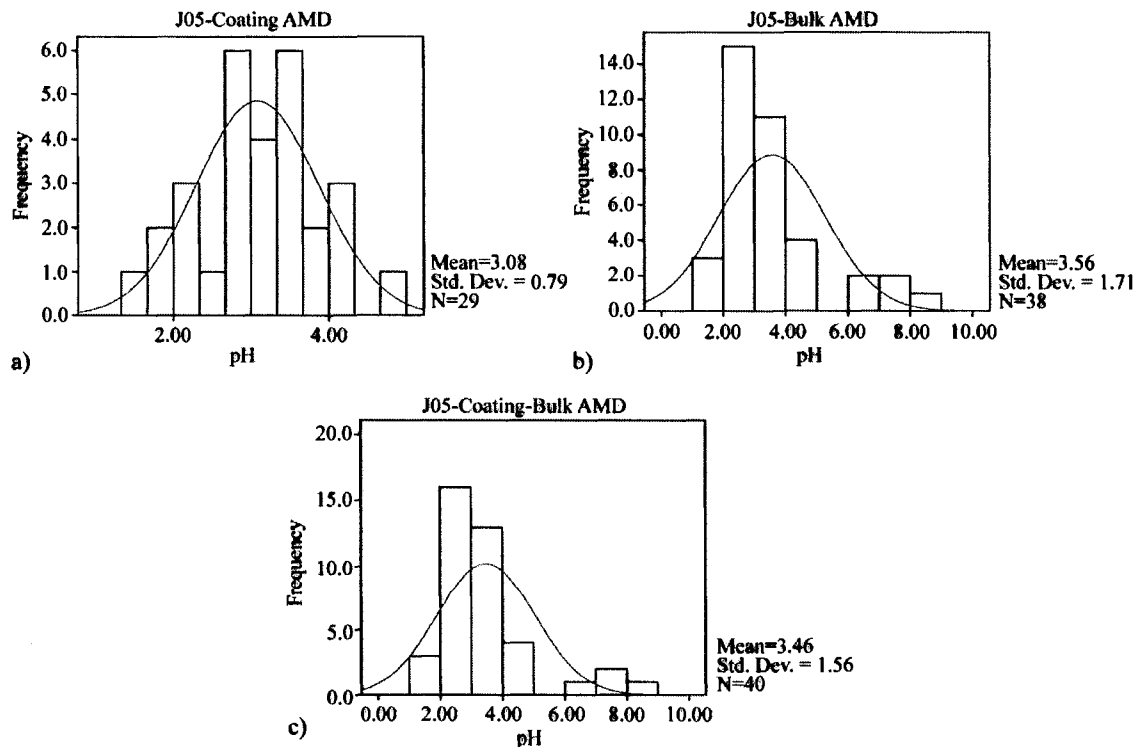


Figure 3.7: Frequency histograms of pH values for AMD mineral samples of June 2005: a) Coating samples b) Bulk samples c) Bulk and coating samples grouped together. The red curve represents the Normal Fit Distribution of the data.

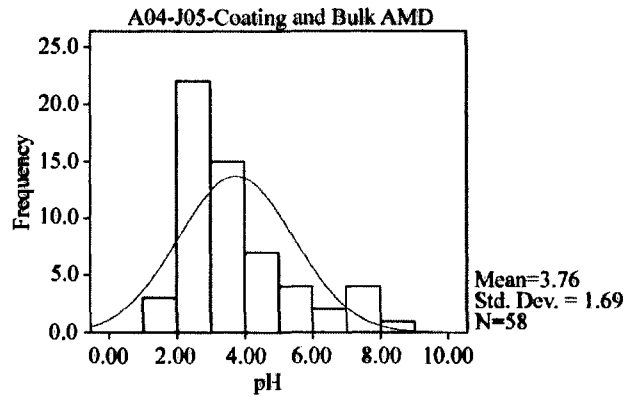


Figure 3.8: Frequency histogram of pH from August 2004 and June 2005, bulk and coating samples grouped together (Final dataset for the predictive pH modeling of Sotiel-Migollas mine). The red curve represents the Normal Fit Distribution of the data.

Figure 3.9 presents the flow chart describing the assessment leading to the merger of the different datasets. The A04-coating and A04-bulk sample sets present equal means and variances and form a group A04-CoatBulk of 18 samples. The J05-bulk dataset shows a bimodal distribution of pH values. The J05-coating and J05-bulk have equal means but different variances and were merged. This new group has a bimodal distribution of pH values. Both 2004 and 2005 groups were then compared and have equal means and equal variances and were merged (table 3.14, A04/J05-Coating/bulk, where N=58). This final dataset is slightly skewed towards low pH values due to the high pH values of the J05 dataset. When merging the bulks to the coatings, if both coating and bulk material are available for one sample, only the coating was chosen. If only a bulk was available for a sample then it was retained in the grouping.

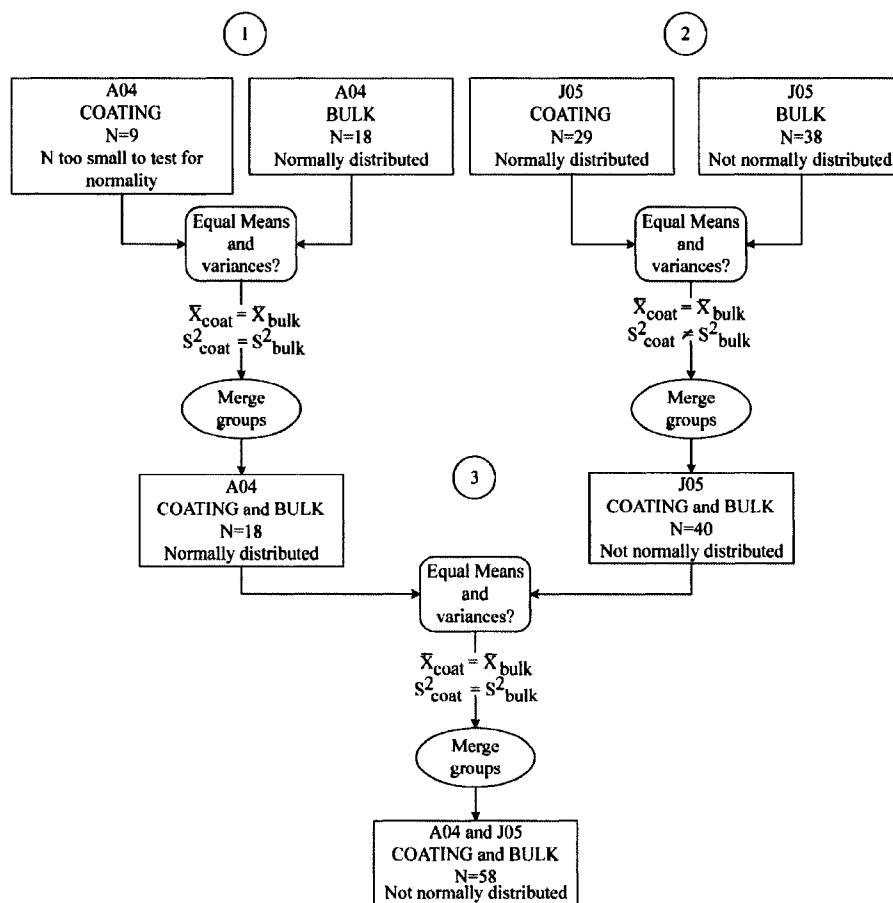


Figure 3.9: Flow chart presenting the different groupings of datasets done with the statistical analysis.

Table 3.14: Merged dataset (N=58) from the AMD minerals coating and bulk samples.

AMD Mineral	Surface	AMD mineral	Surface	AMD mineral	Surface
A04-07	Coat	J05-04	Bulk	J05-39	Coat
A04-08	Bulk	J05-05	Coat	J05-40	Coat
A04-09	Coat	J05-06	Coat	J05-41	Bulk
A04-14	Coat	J05-08	Bulk	J05-42	Coat
A04-18	Coat	J05-09	Bulk	J05-43	Coat
A04-20	Bulk	J05-10	Bulk	J05-44	Coat
A04-21	Coat	J05-14	Bulk	J05-45	Coat
A04-22	Bulk	J05-15	Bulk	J05-46	Coat
A04-27	Coat	J05-19	Bulk	J05-47	Coat
A04-29	Bulk	J05-20	Coat	J05-49	Coat
A04-31	Bulk	J05-21	Bulk	J05-51	Coat
A04-33	Bulk	J05-22	Bulk	J05-52	Coat
A04-34	Bulk	J05-23	Coat	J05-53	Coat
A04-36	Bulk	J05-24	Coat	J05-54	Coat
A04-37	Bulk	J05-25	Coat	J05-55	Coat
A04-43	Coat	J05-30	Coat	J05-56	Coat
A04-44	Coat	J05-32	Coat	J05-57	Coat
A04-47	Coat	J05-35	Coat	J05-58	Coat
J05-01	Bulk	J05-37	Coat		
J05-02	Coat	J05-38	Coat		

A04: August 2004; J05: June 2005; Coat: Coating.

4. CHAPTER 4 – MINERAL MAPPING

4.1. Introduction

This chapter describes the analysis of the Hymap imagery to produce mineral maps that describe for each pixel in the scene the distribution of the dominant iron-bearing minerals related to acid mine drainage in mine tailings. The spatial patterns of mineralogy can be used to monitor the impact of mine waste over time, prioritize remedial efforts, and help detect contamination in the surrounding environment through filtration, spillover or runoff that cannot always be detected on the ground. Such instances are detected in this study.

4.2. Methods

The generation of mineral maps first involved the extraction of spectral endmembers from the Hymap at-surface reflectance images, which were then used for spectral unmixing. Sections 4.2.1 and 4.2.2 provide a description of these two processing steps.

4.2.1. Extraction of image endmembers and labelling

The spectral endmembers were extracted using the spatial-spectral endmember extraction (SSEE) tool of Rogge et al. (2007), which makes use of the spectral and spatial characteristics of image pixels to locate the purest (e.g. most unique) spectral endmembers. This technique was developed to improve the detection in imagery of spectrally similar endmembers.

Endmember extraction was performed on subset images that contained the mine tailings and waste rock piles found throughout the study area. Pixels occupied by vegetation were removed from the image subsets by calculating the normalized difference vegetation index (NDVI) and using a minimum threshold of 0.3 for masking pixels with

vegetation. From the remaining data, SSEE found a large number of endmembers and those representing mine waste material were retained. Spectra representing other materials (e.g. water, soils, infrastructure, remaining vegetation, and noisy spectra) were used to identify and discard pixels occupied by these materials. These pixels were identified by performing a SAM classification with the endmembers and the thresholds for the SAM classification were based on field knowledge and a visual comparison of the spectra of the classified pixel and the endmembers. The resulting masked images only contained pixels with mine tailing material as inputs to the final mineral map classification.

From the 275 candidate AMD mineral(s)-image endmembers, 26 were obtained by grouping similar endmember spectra and averaging them, thus avoiding redundancy. The labelling of the 26 image endmembers was guided with spectra of sediment samples collected in the field, measured in the laboratory, and labelled using an unmixing procedure (Bachmann, 2007) supported with SAM and SFF spectral analyses, as well as XRD results as described in chapter 3. Spectra from spectral libraries of the USGS and Crowley et al. (2003) also served to guide the labelling of image endmembers.

4.2.2. Generation of mineral maps

The mineral mapping of the images was performed using the iterative linear spectral unmixing analysis (ISMA) of Rogge et al. (2006). ISMA is an unmixing method performed in two steps to find the most favourable endmember sets on a per-pixel basis. First, an iterative unconstrained unmixing was performed using the 26 available endmembers and at each of the 26 iterations one endmember was removed. Then an analysis of the root mean square error as a function of iteration was performed to locate the critical iteration that uses too few endmembers, characterizing the optimal endmember set for the pixel. In addition to determining the optimal per pixel endmember set, ISMA produces images for each endmember describing their per pixel fractional abundance, and includes a shade endmember in the unmixing procedure since each mixture contains some amount of shadowing. To generate the mineral maps, each pixel

was assigned the label of the most abundant endmember predicted by the ISMA unmixing process.

4.3. Results

4.3.1. Image endmember labelling

The image endmembers resulting from the SSEE analysis represent mostly mineral mixtures, since the mine tailings of this study are intimate mixtures of minerals. Table 4.1 lists the 26 endmembers and their respective mineralogical label. The minerals dominating the mixtures include goethite, schwertmannite, hematite, jarosite, rozenite, halotrichite, copiapite, pickeringite, szomolnokite and pyrite. These are also mixed with rhomboclase, melanterite, gypsum, muscovite, alunite, and albite, consistent with the spectra and XRD results of sediment samples of the study site.

Figure 4.1 presents the endmember spectra and outlines spectral features related to infrared active minerals. Based on the most dominant mineral there are 11 groups of mineral mixtures with slight variations of mineral mixtures observed in each group. The groupings include: goethites, schwertmannite, jarosite, hematite, copiapite, halotrichite, rozenite, szomolnokite, pyrite, pickeringite, and soils dominated by goethite and/or schwertmannite and ferrihydrite.

Table 4.1: Mineral mixture labels for the endmembers.

EM	Label	EM	Label
1	GT , mu, al	14	HA , rz
2	GT-SCH , mu, al	15	RZ
3	GT-JR , mu, al	16	SZ-HA , py
4	Soils-with SCH/FERR , gt, mu, al	17	PK-HA-SZ
5	SCH-JR , al, mu	18	CO , jr, sch
6	Soils with GT-FERR	19	CO , me, sch
7	SCH , gt cl, qz, mu, and/or al	20	HA-CO
8	GT , al	21	JR-SCH , ferr, al, mu, qz
9	JR-GT mu, al	22	SCH-JR , al and/or mu
10	HA , sch, al, alu, gp	23	HE , mu, al
11	HA , rh	24	HE
12	HA , jr	25	HE , cl
13	RZ-HA	26	PY-SZ

DOMINANT: usually >60%; **CO-DOMINANT:** two or more components appear to be present in approximately equal amounts; **SUB-DOMINANT:** typically ~20% - 60%; **minor:** concentrations <20%.
 Abbreviations: Al: Albite; Alu: Alunite; Cl: Clinocllore; Co: Copiapite; Ferr: Ferrihydrite; Gt: Goethite; Gp: Gypsum; Ha: Halotrichite; He: Hematite; Jr: Jarosite; Me: Melanterite; Mu: Muscovite; Pk: Pickeringite; Py: Pyrite; Qz: Quartz; Rh: Rhomboclase; Rz: Rozenite; Sch: Schwertmannite; Sz: Szomolnokite.

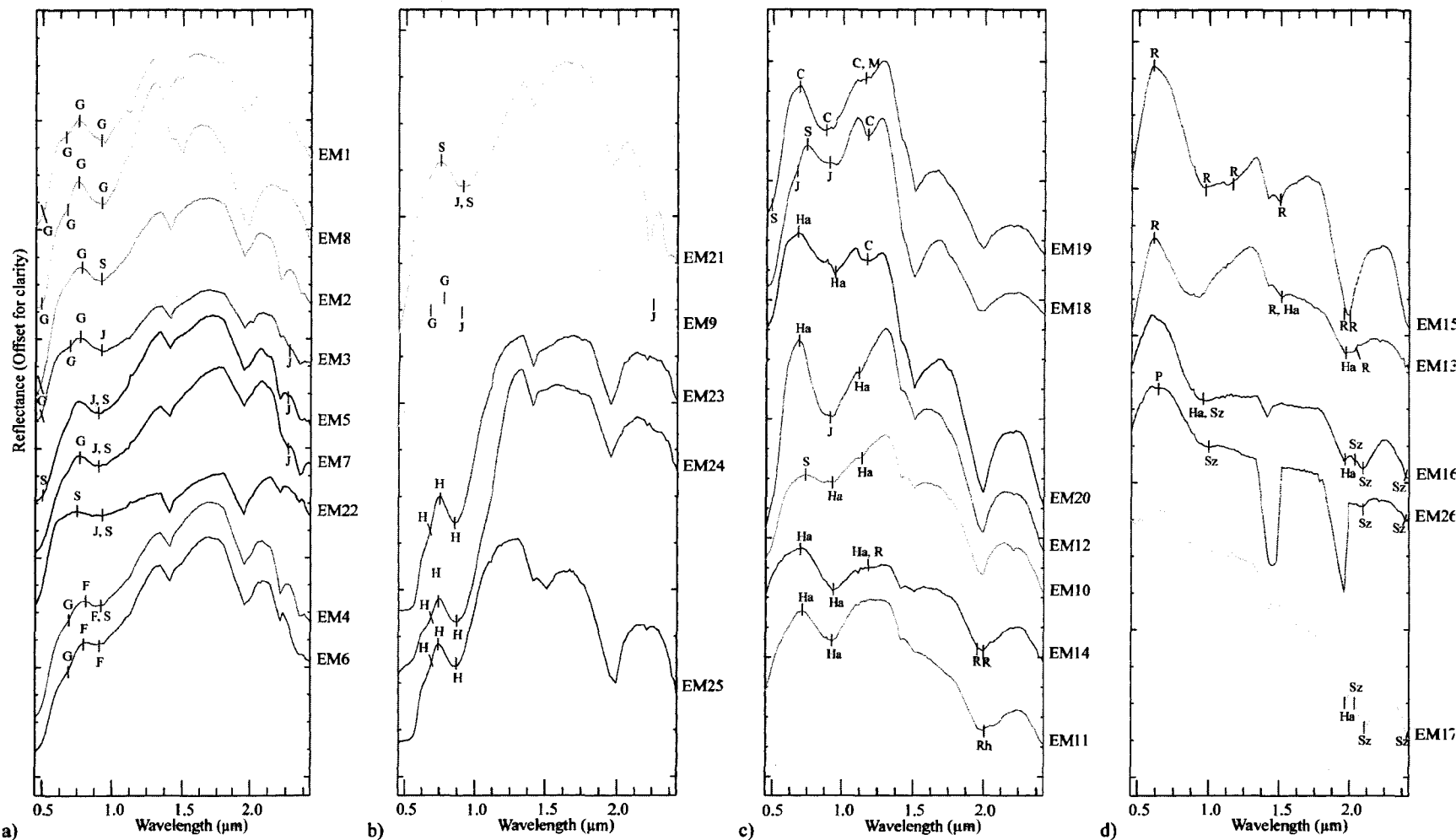


Figure 4.1: Spectra of image endmembers grouped by predominant minerals. Within each of the 11 groups, the mineralogical variation is shown using minor colour variations. a) goethite (oranges), schwertmannite (blue) and soils dominated by goethite and/or schwertmannite, ferrihydrite (maroon); b) jarosite (yellow) and hematite (purple); c) copiapite (magenta) and halotrichite (sienna and red); d) rozenite (green, EM13 and 15), szomolnokite (cyan, EM16), pyrite (sea green, EM26), and pickeringite (tistle, EM17). C: Copiapite; F: Ferrihydrite; G: Goethite; H: Hematite; Ha: Halotrichite; J: Jarosite; M: Melanterite; R: Rozenite; Rh: Rhomboclase; S: Schwertmannite; Sz: Szomolnokite. The colors given to these endmember spectra are the same colors of the corresponding image endmember classification colors for the mineral maps.

4.3.2. Mineral Maps

The mineral maps of the tailings and waste sites in and around the town of Sotiel-Coronada and along the Odiel River are displayed in figure 4.2. Within this study area, two tailings ponds (A and B) are located beside the processing plant (Sulphuric Acid plant/flotation plant) (C). Two other more distal mine waste-rock tailing sites are found along the Odiel River, the main waste-rock tailings (D) and a smaller one (E). Along the river, several bed plains of rocks are coated with AMD minerals: river north of Sotiel-Coronada (F), river at Sotiel-Coronada (G), and river south of Sotiel-Coronada (H). Within the town, two other sites of mine waste are present (I and J). Each of these sites is shown in enlargement in the subsequent figures (Figures 4.3 to 4.6). Figure 4.7 presents the tailings on a backdrop of Hymap imagery draped over a digital elevation model to visualize the spatial distribution of the waste in the context of the drainage network of the area.

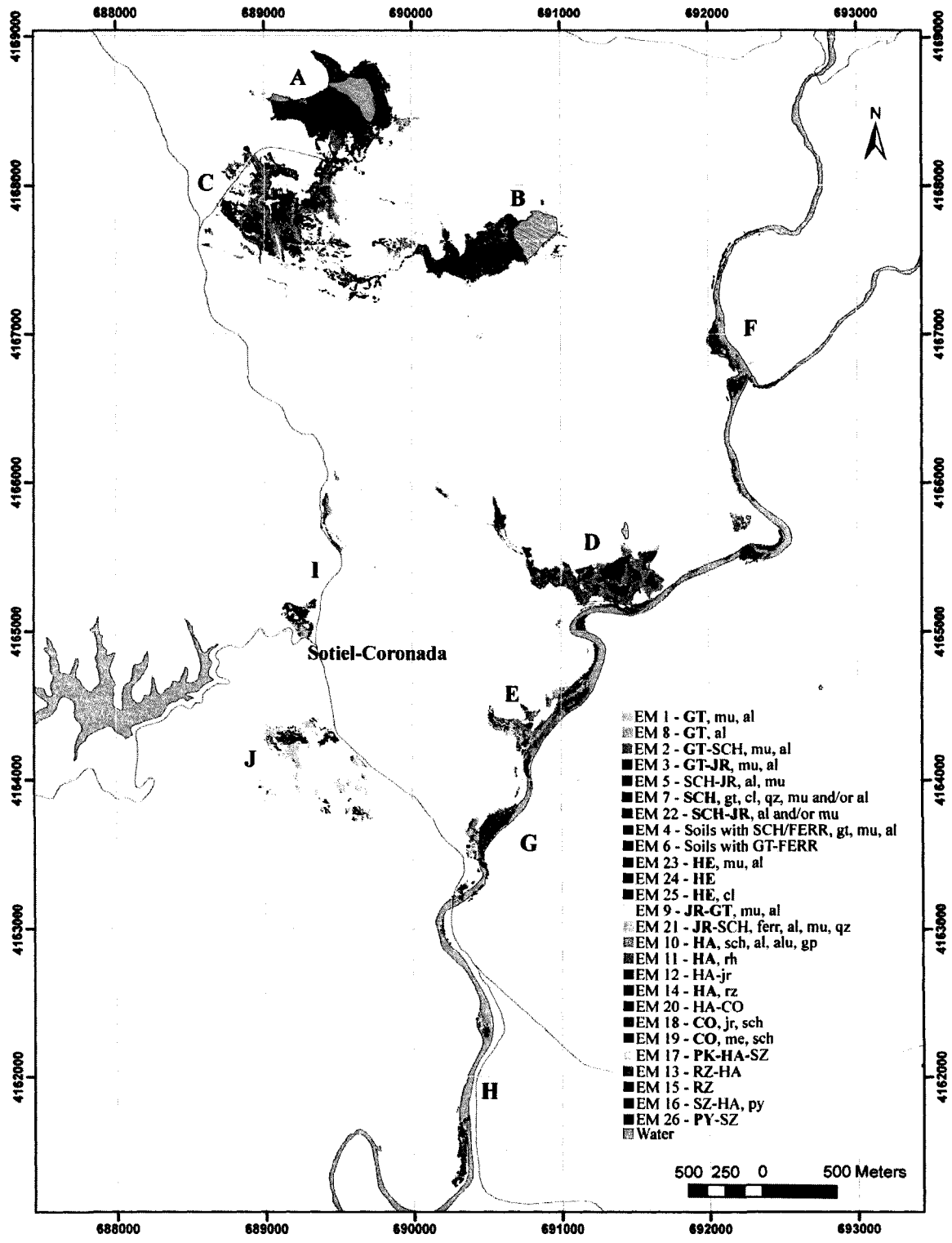


Figure 4.2: Overview of the mine waste sites mineral maps. The endmember spectra are shown on figure 4.1.

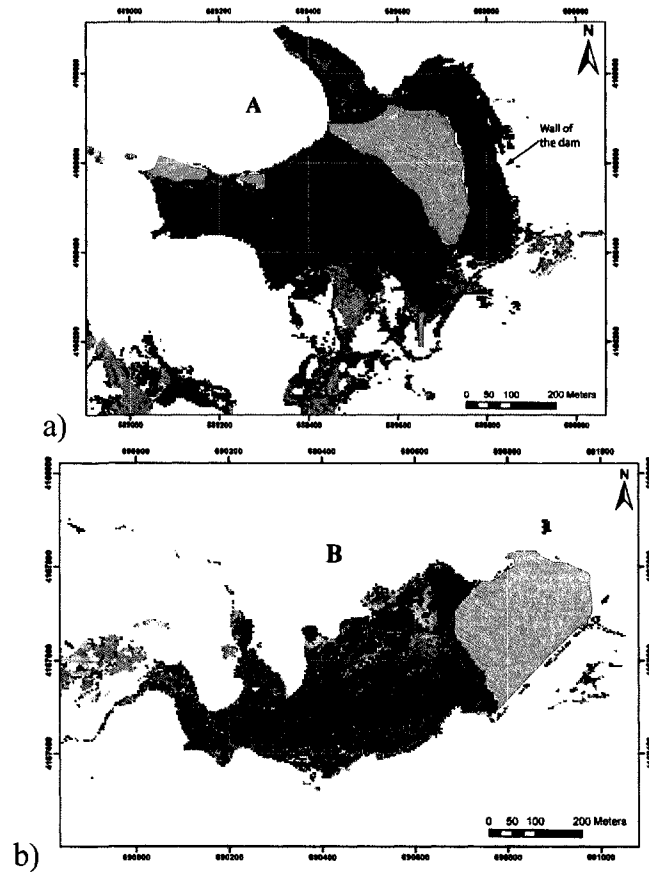


Figure 4.3: Mineral map of tailings ponds: a) tailings pond on the northeast side of the processing plant; b) tailings pond of the east side of the processing plant. Colour table shown on figure 4.2.

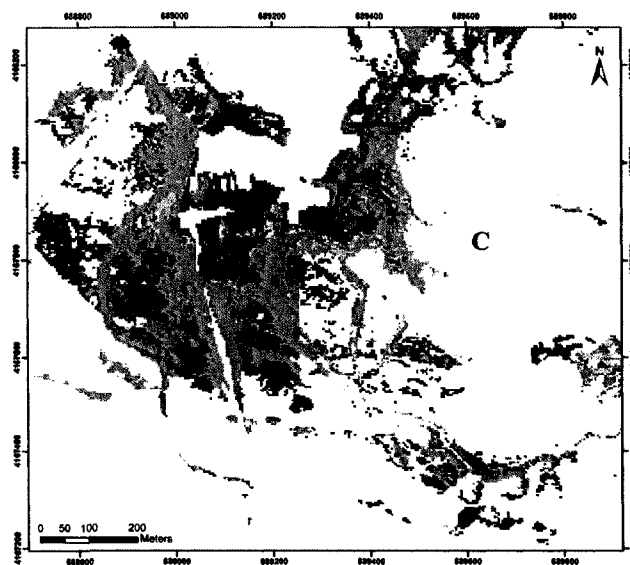


Figure 4.4: Mineral maps of mine waste surrounding the processing plant. Colour table shown on figure 4.2.

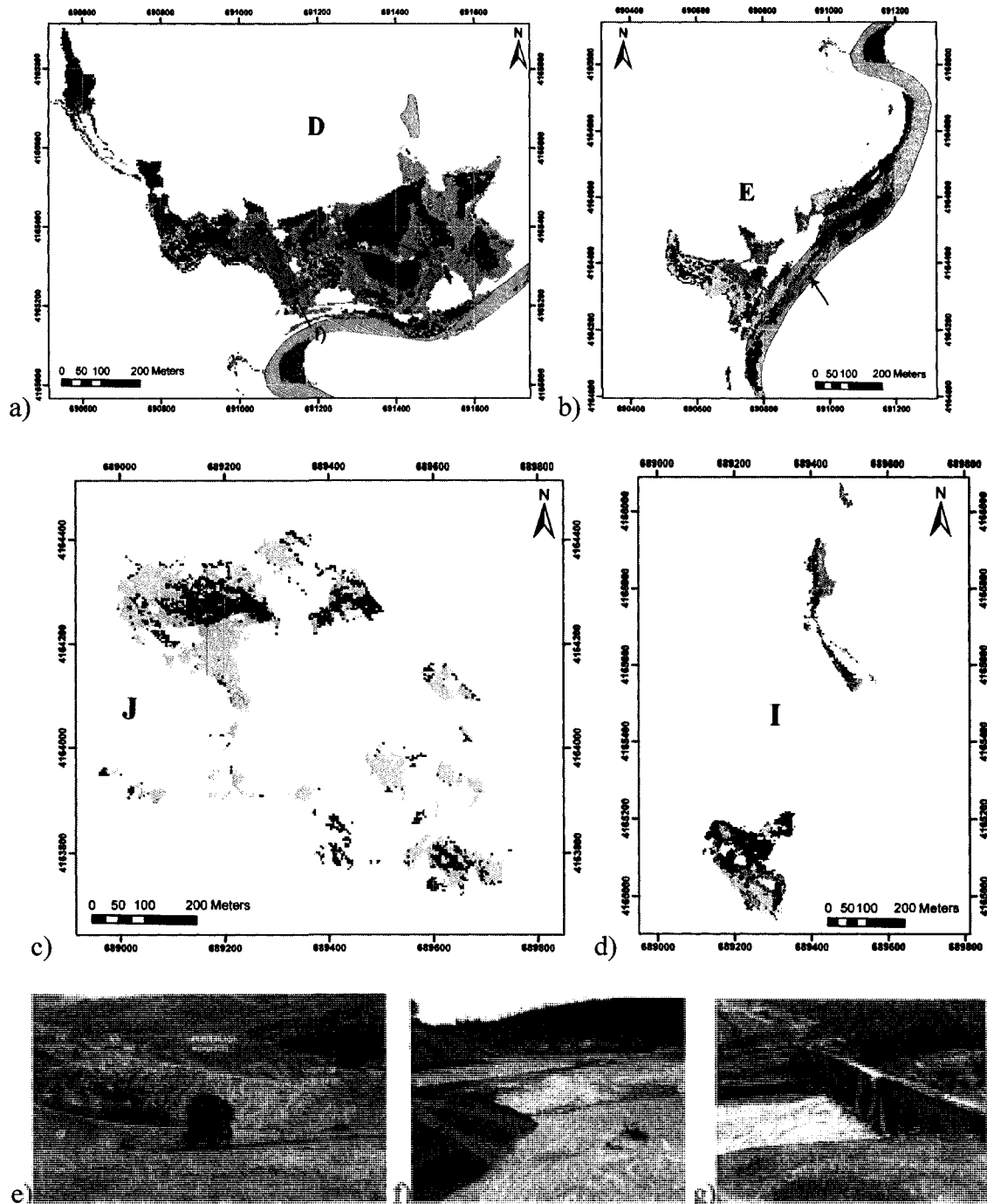


Figure 4.5: Mineral maps of distal waste rock tailings: a) main mine waste tailings located southeast of the processing plant; b) mine waste tailings along the Odiel River, south of the main tailings; c) Mine waste in Sotiel-Coronada; d) Mine waste at the Almagrera S.A. Mines' Treatment Plant; e) photos of tailings at the main waste-rock tailings site (area D) showing plateau of hematite with slope of goethite; f) and g) Halotrichite deposits in runoff zones of the tailings (area D). Also shown is the riverbed area, which may not reflect the water level during the acquisition of the imagery. Colour table shown on figure 4.2.

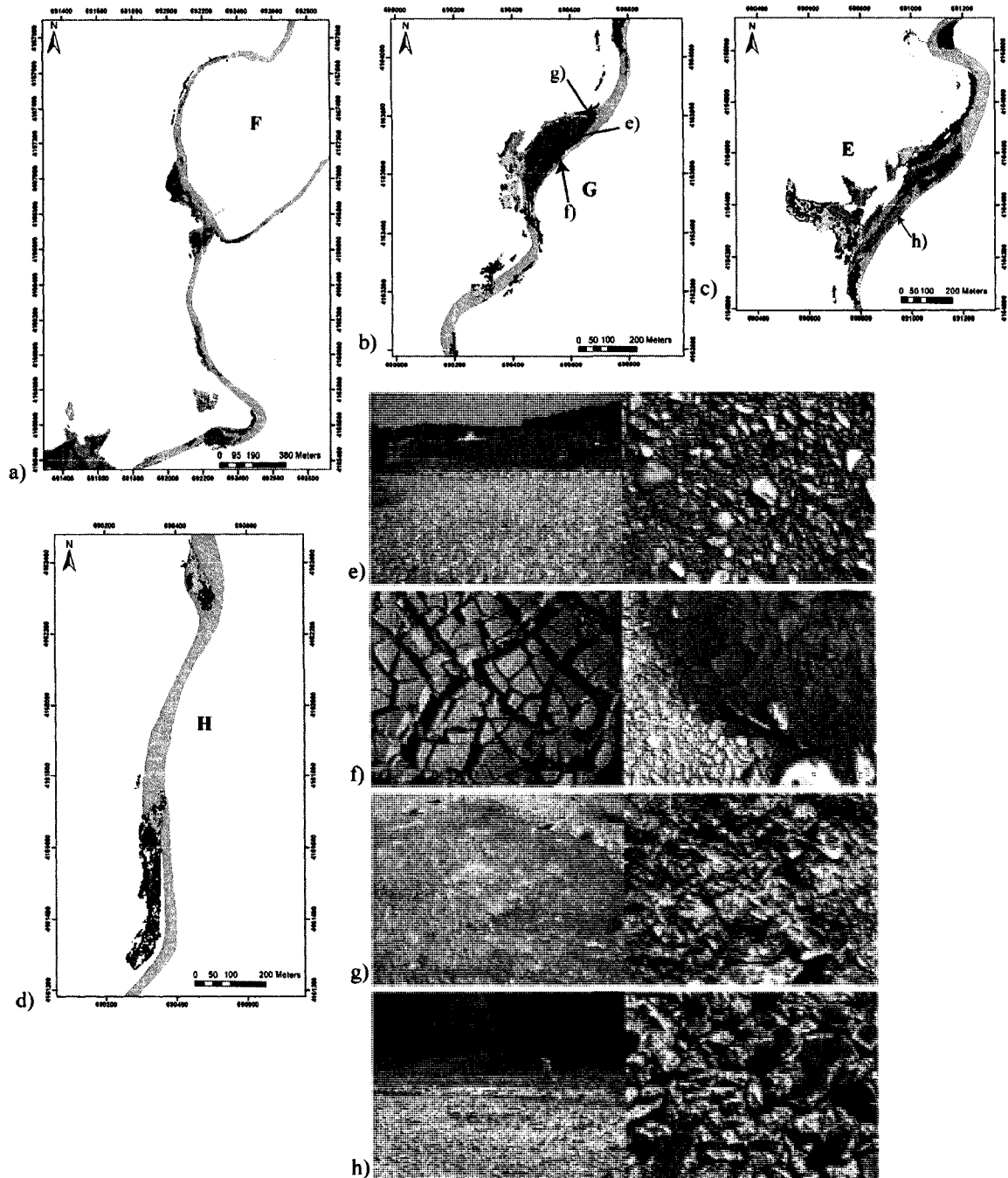


Figure 4.6: Mineral maps of mine waste along the Odiel River: a) bed plains northeast of Sotiel-Coronada; b) bed plains at Sotiel-Coronada; c) bed plains near the small waste-rock tailings by the Odiel River; d) bed plains south of Sotiel-Coronada; e) example of coarse pebbles coated principally with a mixture of goethite and jarosite (area G); f) example of mud cracks dominated by schwertmannite and jarosite minerals (area G); g) example of coarse pebbles cemented with thick coating of goethite (area G); h) example of halotrichite coating (area E). Also shown is the riverbed area, which may not reflect the water level during the acquisition of the imagery. Colour table shown on figure 4.2.

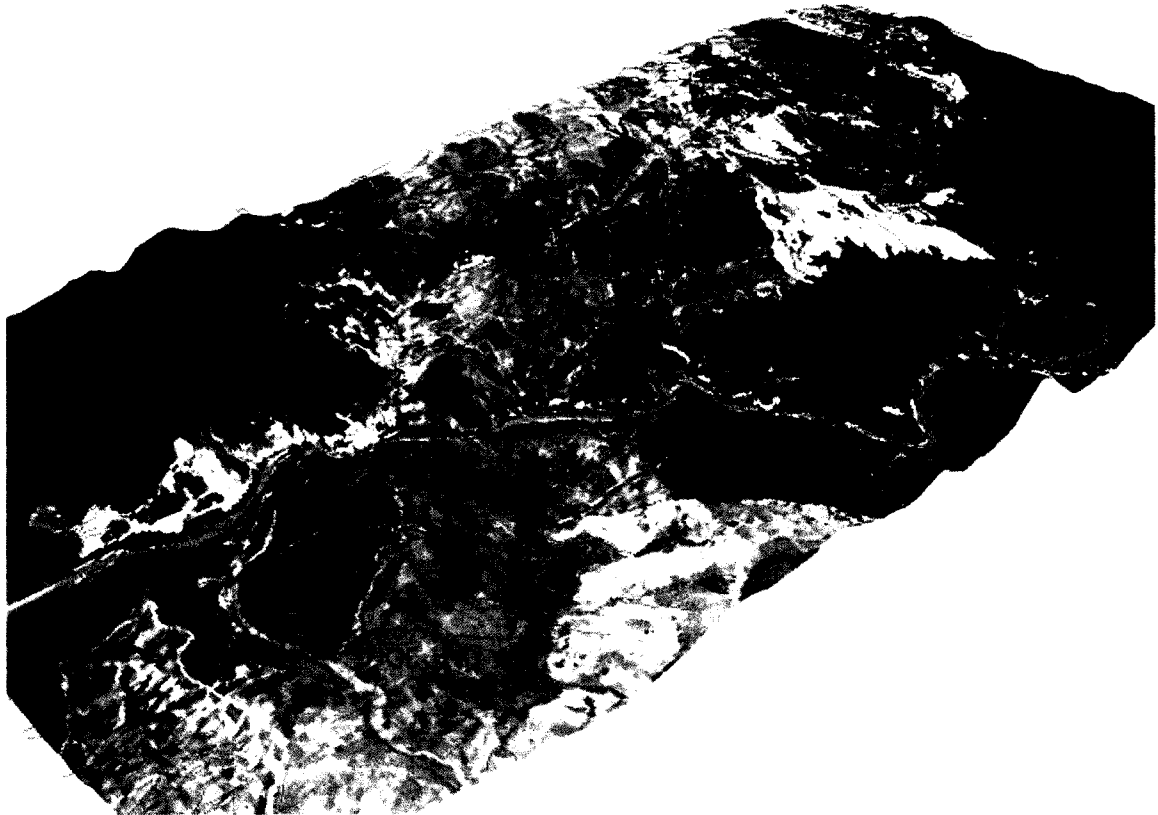


Figure 4.7: Mineral map of mine waste sites shown on figure 4.1 draped over a digital elevation model. Backdrop image mosaic of Hymap strips 4, 5, and 6 (RGB bands, respectively 0.6335 μm , 0.5568 μm , and 0.4644 μm ; shown in black and white (stretch 0-255). Maximum relief, vertical exaggeration of 1.5.

4.4. Analysis of mineral maps

4.4.1. Accuracy assessment of mineral maps

The assessment of the mineral maps is performed by comparing the image classification with that of laboratory spectra for sediment samples collected from corresponding field locations in and around the tailings. As seen in table 4.2, the field sites encompass multiple pixels and are mapped by multiple image endmembers even within a given sampling area. This is likely the consequence of the site selection process and coarseness of the preliminary maps that were used to guide the site selection process. Sampling sites used for the assessment were selected early in the research based on preliminary mineral maps created using the Hourglass method as described in section 3.2.3.1. This method gave image endmembers that represented broad areas with a coarse

labelling of the mineral mixtures. By comparison, the SSEE image endmember extraction provided greater detail and diversity of mineral endmembers and that were used for the final maps. This situation leads to a comparison of results at different spatial scales. Thus, when comparing the image classification results from the unmixing to the laboratory spectra of samples collected with the coarser representation, it is difficult to assess the finest details of the mapping. Nonetheless, it is possible to qualitatively show the mineralogical agreement between ground samples and the image classifications. In most cases some of the pixels classified at a site represent mineral mixtures that are part of the label for the field reference spectrum and thus the classification seems generally accurate. In order to obtain a viable statistical accuracy assessment, ground samples would have to be collected using the final unmixing mineral maps which would have required an additional field campaign. Such a campaign was beyond the scope of this study.

Table 4.2: Comparison of image classification and that of spectra for samples of corresponding field locations.

Laboratory sample spectrum	Laboratory sample spectrum label	Image classification for pixels of the sampling sites	Laboratory sample spectrum	Laboratory sample spectrum label	Image classification for pixels of the sampling sites
J05-01	HE	12 pixels EM23: HE , mu, al	J05-42	HE	9 pixels EM24: HE 3 pixels EM23: HE , mu, al
J05-02	FERR/SCH-GT	4 pixels EM2: GT-SCH , mu, al 3 pixels EM10: HA-JR , al, alu, gp 1 pixel EM8: GT , al	J05-43	JR py	3 pixels EM2: GT-SCH , mu, al 2 pixels EM1: GT , mu, al 1 pixel EM21: JR-SCH , ferr, al
J05-04	GT-HE-sch/ferr	1 pixel EM3: GT-JR , mu, al 8 pixels EM3: GT-JR , mu, al 7 pixels EM1: GT , mu, al 2 pixels EM2: GT-SCH , mu, al 2 pixels EM22: SCH-JR , al/mu 2 pixels EM5: SCH-JR , al, mu 1 pixel EM8: GT , al	J05-45	HE cop	12 pixels EM24: HE 3 pixels EM23: HE , mu, al
J05-05	SCH/FERR gt	14 pixels EM22: SCH-JR al, mu 3 pixels EM3: GT-JR , mu, al	J05-46	JR-GT-HE-FERR	7 pixels EM2: GT-SCH , mu, al 1 pixel EM1: GT , mu, al
J05-09	GT-FERR/sch	5 pixels EM1: GT , mu, al 2 pixels EM8: GT , al 1 pixel EM7: SCH , gt, cl, qz, mu, a	J05-47	HE par jr	12 pixels EM 23: HE , mu, al
J05-19	HE	9 pixels EM23: HE , mu, al	J05-48	PY+qz	6 pixels EM22: SCH-JR al, mu 1 pixel EM17: PK-HA-SZ 1 pixel EM16: SZ-HA , py 1 pixel EM26: PY-RZ 10 pixels EM23: HE , mu, al
J05-20	FERR/SCH-HE, jr	8 pixels EM22: SCH-JR , al, mu 1 pixel EM7: SCH , gt, cl, qz, mu, al	J05-49	HE jr	
J05-22	HE-FERR	5 pixels EM23: HE , mu, al 1 pixel EM22: SCH-JR al, mu	J05-50	RZ+HA	3 pixels EM15: RZ 2 pixels EM17: PK-HA-SZ 2 pixels EM14: HA , rz 1 pixels EM11: HA-rh 9 pixels EM1: GT , mu, al 1 pixel EM8: GT , al 1 pixel EM2: GT-SCH , mu, al 1 pixel EM16: SZ-HA , py 13 pixels EM2: GT-SCH , mu, al 2 pixels EM22: SCH-JR al, mu
J05-24	HE-FERR-PK	11 pixels EM23: HE , mu, al 3 pixels EM22: SCH-JR al, mu 1 pixel EM25: HE , cl	J05-51	GT-FERR he	
J05-25	FERR/SCH-GT	3 pixels: EM6: soils GT-FERR 1 pixel EM2: GT-SCH , mu, al 1 pixel EM22: SCH-JR al, mu 1 pixel EM25: HE , cl	J05-52	SCH-HE	
J05-28	ME-RZ	5 pixels EM16: SZ-HA , py 1 pixel EM14: HA , rz	J05-53	SCH jr-he	21 pixels EM2: GT-SCH , mu, al 5 pixels EM23: HE , mu, al 1 pixel EM3: GT-JR , mu, al 12 pixels EM24: HE 9 pixels EM23: HE , mu, al 10 pixels EM2: GT-SCH , mu, al
J05-29	PY, sz	4 pixels EM16: SZ-HA , py	J05-54	HE	
J05-35	GT-HE jr	2 pixels EM1: GT , mu, al 2 pixels EM22: SCH-JR al, mu	J05-55	SCH jr he	
J05-37	GT-JR-FERR	14 pixels EM1: GT-SCH , mu 3 pixels EM2: GT-SCH , mu, al 3 pixels EM22: SCH-JR al, mu	J05-56	HE jr	10 pixels EM23: HE , mu, al 8 pixels EM24: HE
J05-38	JR-HE	5 pixels EM22: SCH-JR al, mu 2 pixels EM2: GT-SCH , mu, al 1 pixel EM1: GT , mu, al	J05-57	GT-JR	15 pixels EM2: GT-SCH , mu, al
J05-39	HE-FERR jr	6 pixels EM2: GT-SCH , mu, al	J05-58	HE	65 pixels EM24: HE 8 pixels EM14: HA , rz 4 pixels EM11: HA , rh
J05-40	GT-FERR-sch	15 pixels EM8: GT , al	J05-59	HA+PK+SZ	
J05-41	SCH-GT	7 pixels EM2: GT-SCH , mu, al 6 pixels EM3: GT-JR , mu, al 1 pixel EM10: HA , sch, al, alu, gp 1 pixel EM1: GT , mu, al			

DOMINANT: usually >60%; **CO-DOMINANT:** two or more components appear to be present in approximately equal amounts; **SUB-DOMINANT:** typically ~20% - 60%; **minor:** concentrations <20%.

4.5. Discussion

Tailings ponds:

The tailings ponds are often used as mine waste storage to avoid exposure to air and water and consequential oxidative dissolution of the sulphide minerals (Johnson and Hallberg, 2003). Portions of the tailings that are submerged (figures 4.3a and b) cannot be sensed with Hymap imagery but a greater proportion is exposed and it is important to monitor because the sulphide oxidation rate may be high due to the direct contact with oxygen and runoff. The exposed tailings outlined in figure 4.3a are mostly dry but those presented in figure 4.3b are moist and muddy. Both areas show great differences in their mineralogical content, and thus represent different stages of pyrite oxidation. The tailings ponds on the northeast side of the processing plant (figure 4.3a) are essentially composed of mineral mixtures dominated by hematite with some albite, muscovite, and clinocllore (EM23 and EM24). In addition, some patches are dominated by both schwermannite and jarosite with some albite and muscovite (EM22). The dominance of hematite shows that these tailings are far advanced in the oxidation process and more stable, since hematite is observed at the last stage of the pyrite oxidation cycle (figure 1.1).

In contrast, the other tailings pond (figure 4.3b) is mainly composed of rozenite (EM15) and presents a much greater diversity in mineralogy, especially near the open water. The extensive presence of rozenite indicates that at the time of acquisition of the imagery, the pond was dryer in the areas where rozenite dominates, i.e., contained lower relative humidity. Melanterite transforms into rozenite during high temperature periods and days of low relative humidity. Thus, the absence of melanterite in areas dominated by rozenite indicates dryer tailings. The tailings closer to the exposed water are comprised of mineral mixtures dominated by copiapite with some jarosite and schwermannite (EM18) or with some melanterite and schwermannite (EM19). The areas closest to the water, on the east end of the pond, are composed of mixtures dominated by halotrichite-copiapite, schwermannite-jarosite, and goethite-schwermannite. The presence of these minerals indicates that the oxidation of pyrite is still in progress and the tailings are not as stable as

the northern tailings pond, dominated by the most stable and latest phase of oxidation, hematite. The tailings ponds on the southeast site would require greater attention during monitoring because of the dominance of efflorescent salts and jarosite mineral mixtures. These metal-rich salts produce an instant source of acid and metals when dissolved.

Tailings at the processing plant:

The tailings around the processing plant (figure 4.4) are characterized by a dominance of efflorescent salts and numerous piles with very fine-grained materials left from the crushing and roasting ashes. This site shows a distinctive zonation pattern around the plant. Closest to the plant is a mixture of szomolnokite and halotrichite with a high content of fine-grained pyrite (EM16 in cyan) seen in the samples collected in the field. Interlocking this mineral assemblage are patches of a mixture of schwertmannite and jarosite (EM22) and patches of rozenite (EM15). On the north side of the plant an extensive area of EM16 (cyan) includes small patches of EM 17 (a mixture of pickeringite, halotrichite and szomolnokite) interfingering, the only area around the processing plant where this endmember is found. Surrounding the large patches of szomolnokite (EM16) are patches of jarosite (EM21), in turn surrounded by large patches of goethite mixed with schwertmannite (EM2). The EM2 is then surrounded by EM22 comprised of schwertmannite mixed with jarosite. The latter two endmembers, in addition with EM16, are the three most spatially abundant mineral mixtures present around the processing plant. Adjacent patches of soils rich in schwertmannite and ferrihydrite (EM4), and goethite are mapped between the spectrally dominant goethite and schwertmannite (EM2). Further out, small zones of hematite (EM23) are present. The zonation pattern seen around the processing plant resembles greatly one described by Swayze et al. (2000) for the California Gulch Superfund Site near Leadville, Colorado (described in section 1.3.2).

On the east side of the processing plant are numerous patches dominated with halotrichite (EMS 10, 11, 12, 14, where halotrichite is mixed jarosite and gypsum, jarosite, rhomboclase, and rozenite, respectively). This section also contains patches of hematite (EM23), schwertmannite and jarosite (EM22), jarosite and schwertmannite

(EM21) and goethite and jarosite (EM3) characterizing the area as having a very diverse mineralogy.

Waste-rock tailings:

The waste-rock tailings present similarities. The largest waste-rock tailings (Figure 4.5a) show an obvious pattern of hematite surrounded by goethite. In fact, these tailings are big dump piles with plateaus mainly composed of hematite, and slopes composed of goethite as shown in the photographs of figure 4.5e. This trend is also observed in one small patch of the smaller waste-rock tailings (figure 4.5b).

Another pattern observed at the California Gulch Superfund Site near Leadville, Colorado by Swayze et al. (2000) is observed in the waste-rock tailings. It consists of jarosite (EM21) and rozenite-halotrichite (EM13) mineral surfaces surrounded by schwertmannite (EM22), and then by goethite (EMs 1 and 2), and finally by hematite (EMs 23 and 24). This pattern is seen at the main waste-rock tailings (figure 4.5a) and a similar pattern is found at the waste-rock tailings in the Sotiel-Coronada town (figure 4.5c). However, this second site does not show the presence of hematite surrounding the goethite, suggesting that this site is at an earlier phase of oxidation than that of the main waste-rock tailings (figure 4.5a). In addition, this site shows large patches of szomolnokite surrounded by rozenite, schwertmannite and goethite and has a high concentration of efflorescent salt minerals, such as rozenite, szomolnokite, and halotrichite. Some jarosite is observed in the centre of the site at a lower elevation than the surrounding slopes of goethite and schwertmannite.

Runoffs from the tailings drain into the lower levels of the tailings. The accumulation of AMD in these pools eventually leads to the precipitation of large amounts of efflorescent salts, rich in heavy metals as seen in two major areas in the largest waste-rock tailings of figure 4.5a, as indicated by arrows. Photographs of these two sites are seen in figures 4.5f and 4.5g. These two sites were mapped as halotrichite mixed with rhomboclase (EM11) and few patches of halotrichite mixed with rozenite (EM14) and jarosite (EM10). Both areas drain toward the Odiel River, where walls were

built to prevent drainage into the river. However, during heavy rainfalls, spillage over the walls may occur, thus making this site an important area to monitor during high rainfall given the high availability of AMD.

Riverbed deposits:

Mineral mapping of the riverbeds along the Odiel River (figure 4.6) shows the occurrence of goethite, jarosite and schwertmannite mixtures and in certain areas mixtures dominated by halotrichite. The Odiel River is a meandering river with point bars accumulating coarse pebbles. The coarse pebbles are mainly mapped as having a coating of goethite and jarosite with clay minerals (EM3, figure 4.6e). On the edges of these point bars lie muddy sediments (figure 4.6f) mapped as mixtures of schwertmannite and jarosite with more minor albite and muscovite (EM22). Several parts of the riverbanks are characterized by coarse pebbles coated with a thick layer of goethite (EM1 or 8) and strongly cemented, as shown in figure 4.6g. These banks were mapped as goethite. Near the smaller waste-rock tailings along the Odiel River (figure 4.5b) halotrichite-jarosite mixtures (EM10) have been detected on a dry surface (corresponding photograph - figure 4.5h). There are no significant differences between the mineralogy of AMD found upstream and downstream from the Sotiel-Migollas mine tailings because several other mining sites are found upstream from this site along the Odiel River.

Implications for monitoring:

From the observation of the mineral maps, it was found that several areas would need immediate attention. The most important sites to concentrate remedial efforts consist of tailings surrounding the processing plant, lower elevation areas of tailings where runoff accumulate efflorescent salts, such as seen in the waste-rock tailings around the mine complex, and in dry areas along the Odiel River. Areas containing abundant efflorescent salts need important monitoring or control because when dissolved, these salts can release high levels of metals such as Cu, Zn, As, etc. Also, areas containing jarosite have high acid generating capacity, which makes them important sources of acid water and heavy metals. Areas containing mainly hematite and goethite remain important to monitor, but are not as critical as the jarosite-rich areas, since heavy metals are not

believed to be mobile in the absence of low pH waters (Swayze et al., 1996). Attention should also be drawn to all channels that drain the tailings directly into the Odiel River – several are found in the two important waste-rock tailings in proximity to the Odiel River, where a high concentration of efflorescent salts and jarosite are observed. These runoffs should have high occurrence of acidic water and be taken into account when examining the watershed context. In addition to providing the location of sources of acidity, the mineral maps may be useful in directing the collection of ground samples for further analyses, such as measurements of heavy metal content, and other chemical analyses. Lastly the mineral maps display spectral evidence of acid generating minerals on the shores of the Odiel River, indicating that runoff from the tailings is not confined to the mine sites and propagates downstream. This would be important information to take into consideration in future plans to improve the structures confining the acidic waters generated by the tailings.

The observations made from the mineral maps show that topography plays an important role in the distribution of certain secondary minerals as it influences the flow of surface runoff.

4.6. Summary

This chapter illustrated the ability to map the mineralogy of the mine waste tailings at the Sotiel-Migollas mine complex. Mineral maps produced for the study site provide an in-depth knowledge of the distribution and spatial patterns of the mineralogy of oxidizing sulphide products. The key minerals identified include hematite, goethite, schwertmannite, hematite, ferrihydrite, jarosite and several areas containing abundant efflorescent salts.

Twenty-six endmembers were extracted using the SSEE method and used to generate the mineral maps. The endmembers were labelled via a comparison with spectral libraries of Crowley et al. (2003), USGS, and field and laboratory spectra of ground samples as well as XRD results. The mineral maps were generated using the ISMA unmixing

procedure. The image classification displays the most abundant mineral assemblage for each pixel. The methods used in this research gave a more refined classification than using the Hourglass method and SAM classification, often used in other mineral mapping projects. Also, the SSEE endmember extraction tool presented a fast and non-subjective method for endmember selection, as opposed to the Hourglass method.

The qualitative assessment of the mineral maps using samples collected in the field suggested that the classification showed an agreement between the mineralogical labels of ground samples and that of the classified image.

The advantages of presenting mineral maps to site evaluators is to locate rapidly the most important minerals susceptible of producing high levels of AMD and provide information to prioritize field sampling of mine wastes for further investigations. These maps also provide previously unavailable information on the oxidation state of the entire site, which may give an insight on changes that could occur during climate or weather variations (e.g. during heavy rain falls). Also, the mineral maps allow the identification of more sensitive areas for potential future remediation efforts. In this case, such areas are mainly located around the processing plant, in topographically low areas of the waste-rock tailings where runoff accumulates and evaporates to produce high quantities of efflorescent salts, the tailings ponds where halotrichite, copiapite, rozenite are located, and finally along the Odiel River where several areas of halotrichite were found.

A key challenge remaining in the production of mineral maps is the labelling of the minerals from the spectral endmembers. The intimate mixture of the minerals in the tailings brings an enormous challenge in the labelling. XRD analysis does not always give accurate identification of the mineralogy of the samples, thus an alternative method of labelling the spectral endmembers is to use reference spectral libraries (e.g. Crowley et al. 2003 and USGS). However, in some cases the XRD analysis did help guide the spectral identification. Careful visual inspection of the spectra and comparison with reference spectra was important to obtain the best labelling of the spectra but this method remains very subjective. In this study the mapping procedure developed to generate the

mineral maps gave classified maps that are consistent with field observations and interpretation of sample spectra.

5. CHAPTER 5- pH predictive Mapping

5.1. Introduction

This chapter examines the relationship between the spectral response of AMD tailings and their leachate pH using a full-spectrum analytical method, partial least squares (PLS) regression. The aim is to generate a model to estimate soil pH from spectral data.

The first section of this chapter examines the applicability of the predictive pH model generated for the Brukunga mine (Ong and Cudahy, 2002; Ong et al., 2003) to an independent test site, the Sotiel-Migollas mine complex, in Southwest Spain. The next section examines a new predictive pH model developed specifically for the Sotiel-Migollas mine complex. The last section presents maps resulting from the application of this model to Hymap imagery of the Sotiel-Migollas mine site.

5.2. Methods: PLS modeling

The development of predictive models is based on the multivariate calibration technique of Partial Least Squares (PLS) analysis (Haaland, 1988; Martens, 1989). In this work, the PLS calibration focuses on developing a relationship between the reflectance spectrum (a large set of independent variables) and the known pH (dependent variable) of mineral soil samples to build a pH predictive model. PLS decomposes the original independent and dependent variables into a smaller set of orthogonal variables called factors (or latent variables), where the covariance between the two is maximized. The first factors contain the most relevant information present in the reflectance measurements to predict the dependent variable (Haaland, 1988). The last factors represent random noise in the data and need to be discarded in the modeling.

When running the PLS process, an optimal number of factors must be chosen. The optimal number of factors is determined by the prediction residual error sum of squares

(PRESS) from the one-out cross validation approach. The one-out cross validation consist of building a model with the calibration samples and leaving one sample out at a time (Wold, 1978). That single sample is used to validate the calibration model. This process is repeated until all observations are used to validate the calibration model. The choice for the optimal number of factors is usually presented with the first lowest value of PRESS. To help determine the factors with the lowest PRESS, an F-statistical test is performed with a default cut off probability of 0.75 ($\alpha=0.25$). During the PLS calibration, it is important to select the correct optimal number of factors in order to avoid sub- or over-fitting the model caused by too many factors.

Pre-processing of the spectra consist of normalizing the spectra to standardize the spectral information so that the mean spectrum of the dataset is equal to 1, also known as mean centering, as shown in equations 5.1 to 5.5:

$$y = [R_1, \dots, R_n] \quad (5.1)$$

$$y_{mean} = \sum_{i=1}^n \frac{R_i}{n} \quad (5.2)$$

$$N_i = \frac{R_i}{y_{mean}} \quad (5.3)$$

$$x = [N_1, \dots, N_n] \quad (5.4)$$

$$x_{mean} = \sum_{i=1}^n \frac{N_i}{n} = 1 \quad (5.5)$$

From these equations, y is the sampled spectrum associated with a given pixel or sediment sample; R is the reflectance value for band i of spectrum y ; n is the total number of bands in the spectrum; and x is the normalized reflectance spectrum associated with y and has a mean (x_{mean}) equal to 1. The spectrum x was calculated using y_{mean} , being the mean reflectance value of the sample spectrum y . The normalization is implemented in the setup module of the calibration model in the Xspectra software (Mason, 1998) used for the PLS analysis. Therefore, all spectra are automatically normalized during the calibration and the validation of the model.

The final outcome of the PLS modeling is a weight or factor for each spectral band giving a final regression coefficient (FRC) for each band. These FRCs are applied to each spectrum giving a transformed spectrum with predicted values of pH, as presented in equation 5.6:

$$pH_{pred} = \sum_{i=1}^n [(R_{mean_norm_i} - R_{cal_mean_i}) \times FRC_i] + pH_{ave} \quad (5.6)$$

where R_{mean_norm} is the normalized reflectance for each band i of the spectrum with a mean equal to 1; R_{cal_mean} is an average reflectance for each band i of the mean spectrum calculated from the calibration spectra; FRC is the final regression coefficient given from the PLS model for each band i ; and pH_{ave} is the average pH of the calibration samples. The FRC values give the importance of each spectral channel in the prediction, most of which can be related to the important absorption features of the mineral spectrum (i.e., greatest positive or negative FRC values).

As the calibration models are built, Xspectra detects parameter and spectral outliers by using parameter and spectral residuals calculated from the cross-validation pass. Xspectra uses a F-statistic test to evaluate outliers with a high F cutoff probability of 0.9. For each sample the parameter residual (Rp) is known as the difference between the actual (p_{actual}) and the predicted ($p_{predicted}$) pH:

$$Rp = (p_{actual} - p_{predicted}) \quad (5.7)$$

A given parameter residual is flagged as an outlier if its $(Rp_i)^2$ is atypically large which is assessed with the F-ratio described in equation 5.8:

$$F - ratio_{i_param} = \frac{(n-1)Rp_i^2}{\sum_{j \neq i} (Rp_j)^2} \quad (5.8)$$

where i is the number of the sample being tested and n is the number of samples in the training set. The critical cutoff value $F_{(\alpha; v_1; v_2)}$ is found in the F-statistic table with an F

cutoff probability of 0.90 ($\alpha=0.10$) and degrees of freedom of one (1) for the numerator (v_1) and ($n-1$) for the denominator (v_2).

Spectral residuals (Rs) are known as the sum of the squares of the difference between the original and the modeled spectrum:

$$Rs = \sum_{k=1}^p (S_{original_k} - S_{modeled_k})^2 \quad (5.9)$$

where p is the number of bands in the spectrum; $S_{original}$ is the original spectrum reflectances; and $S_{modeled}$ is the modeled spectrum. The modeled spectrum is calculated during the cross-validation pass by the PLS algorithm. Again, the F-statistic test is used to determine the outlier spectral samples in the same manner as for the parameter outliers. The F-ratio used is described in equation 5.10:

$$F - ratio_{i\ spect} = \frac{Rs_i^2}{\sum_{j \neq i} (Rs_j)^2} \quad (5.10)$$

The F cutoff probability used is 0.90 with degrees of freedom of 1 for the numerator (v_1) and ($n-f-1$) for the denominator (v_2), where f is the number of factors in the model.

Several statistical parameters are used to evaluate the performance of the calibration model. Among them are the r^2 value between the predicted pH ($p_{predicted}$) resulting from the cross-validation procedure and the actual pH (p_{actual}); the standard error of calibration and prediction (SEC and SEP); the root mean square error (RMSE) also known as the root mean square difference (RMSD), the average error index in the analysis; and the relative error of prediction (REP), an error average percentage in the set of samples. The REP is evaluated for the predictions of the calibration and the validation sets of samples.

$$RMSE = \sqrt{\frac{\sum_{i=1}^n (p_{actual} - p_{predicted})^2}{n}} \quad (5.11)$$

$$SEC(P) = \sqrt{\frac{\sum_{i=1}^n (p_{actual} - p_{predicted})^2}{n-1}} \quad (5.12)$$

$$REP(\%) = \frac{100}{\bar{p}} \sqrt{\frac{\sum_{i=1}^n (p_{actual} - p_{predicted})^2}{n}} \quad (5.13)$$

5.3. Evaluation of the Brukunga pH predictive model for spectral data of the Sotiel-Migollas mine complex

5.3.1. Preprocessing

The Brukunga model was applied to field and laboratory spectra and Hymap images acquired over the Sotiel-Migollas mine site during the flight and field campaigns of August 2004 and June 2005. The model was provided by C. Ong for 126 bands emulating bands of the 1999, 2004 Hymap system, and one version of 108 bands emulating bands of the 2005 system. These versions of the model could thus be readily applied to imagery of the corresponding year. The ASD field and laboratory spectra were resampled, from 2151 bands to the Hymap 1999 resolution of 126 bands and the 1999 model was then applied. Appendix 5.1 presents the Brukunga model's FRC and calibration mean spectrum for the three years. In the software ENVI, an IDL program was created with IDL variables defining the FRC, the mean calibration spectrum (R_{cal_mean}), and average calibration pH (pH_{ave}) (c.f. equation 5.6). The mean centering (c.f. equations 5.1 to 5.5) of the spectral data was performed followed by the application of the models to the images, field and laboratory spectra.

Table 5.1 lists the spectral data available to compare actual pH with the pH predicted from the model. Forty one field sites were indiscernible on the imagery and for each site the predicted pH value is a mean value for the pixels encompassed by the site area. Fifty eight spectra of samples returned to the laboratory and thirty three spectra collected in the field were also available.

Table 5.1: Actual pH and pH predicted by applying the Brukunga model to the Sotiel-Migollas' images and ASD laboratory and field spectra

Sample	Actual pH	Predicted pH after applying the Brukunga model			
		ASD laboratory spectra resampled to 1999 Hymap resolution	ASD field spectra resampled to 1999 Hymap resolution	August 2004	Hymap images June 2005
A04-07	2.63	5.73	-	6.15	-
A04-08	4.51	4.99	-	5.03	-
A04-09	3.74	4.67	-	4.22	-
A04-14	4.49	6.34	-	indiscernible	-
A04-18	2.63	8.49	-	7.83	-
A04-20	2.10	7.33	-	6.84	-
A04-21	2.92	4.97	-	4.43	-
A04-22	2.43	6.76	-	6.48	-
A04-27	4.10	6.30	-	indiscernible	-
A04-29	2.46	5.61	-	indiscernible	-
A04-31	5.99	6.37	-	indiscernible	-
A04-33	5.98	5.82	-	indiscernible	-
A04-34	5.33	6.27	-	indiscernible	-
A04-36	7.83	5.70	-	6.99	-
A04-37	7.62	5.90	-	5.44	-
A04-43	5.06	6.18	-	5.72	-
A04-44	6.40	4.40	-	7.16	-
A04-47	3.27	4.43	-	4.34	-
A04-47	3.27	4.43	-	4.50	-
J05-01	2.56	5.92	7.18	-	3.93
J05-02	3.26	4.64	5.66	-	8.16
J05-04	6.09	5.69	4.95	-	4.77
J05-05	3.37	5.27	4.65	-	3.34
J05-06	2.81	8.26	13.42	-	indiscernible
J05-08	2.66	5.93	13.06	-	indiscernible
J05-09	7.94	8.09	6.97	-	5.22
J05-10	7.82	5.03	2.707	-	indiscernible
J05-14	3.54	9.97	12.36	-	indiscernible
J05-15	2.56	8.19	11.42	-	indiscernible
J05-19	2.50	5.90	6.97	-	4.32
J05-20	2.70	5.43	5.37	-	4.26
J05-21	2.63	8.28	6.80	-	indiscernible
J05-22	2.62	7.41	10.04	-	7.79
J05-23	2.84	8.12	7.126	-	indiscernible
J05-24	3.39	10.03	10.61	-	8.06
J05-25	4.70	3.89	4.00	-	6.34
J05-30	3.10	6.39	6.85	-	indiscernible
J05-32	4.01	7.28	6.05	-	indiscernible
J05-35	2.87	4.57	5.08	-	indiscernible
J05-37	3.64	4.07	5.14	-	4.36
J05-38	2.97	8.23	6.86	-	indiscernible
J05-39	3.28	7.41	7.88	-	6.33
J05-40	2.61	6.94	8.23	-	8.27
J05-41	8.25	4.19	4.41	-	5.00
J05-42	2.22	6.79	7.13	-	3.85
J05-43	3.67	6.62	6.39	-	6.63
J05-44	1.77	7.40	6.22	-	indiscernible
J05-45	1.73	8.39	-	-	5.81
J05-46	2.89	5.60	11.07	-	7.90
J05-47	1.43	9.71	4.98	-	5.15
J05-49	3.22	8.23	7.89	-	5.80
J05-51	3.74	6.40	5.32	-	4.57
J05-52	4.14	5.93	5.84	-	5.17
J05-53	3.66	6.19	-	-	4.69
J05-54	2.04	7.00	-	-	3.47
J05-55	3.36	6.58	-	-	5.83
J05-56	3.87	6.78	-	-	4.25
J05-57	4.01	4.99	-	-	3.91
J05-58	2.07	6.91	-	-	4.58

5.3.2. Applying the Brukunga model to the Sotiel-Migollas Hymap images, laboratory and field spectra

The evaluation of the applicability of the Brukunga model to the Sotiel-Migollas data is made by comparing the predicted pH against laboratory pH measurements (actual pH) of the samples collected at the Sotiel-Migollas site during these overflights. Of the 41 field sites visible in imagery, thirteen are in 2004 Hymap imagery while 28 were in 2005 imagery. The model is also applied separately to the laboratory and field spectra of samples collected from both field campaigns. The laboratory spectra are more numerous (N=58) and give a better representation of the sampled population.

The Brukunga model is evaluated with the root mean square error (RMSE) and the coefficient of determination (r^2). These values are compiled in table 5.2.

Figures 5.1 and 5.2 display actual pH against pH predicted for imagery, laboratory and field spectra. In all instances the correlation between predicted and observed pH is poor and the largest r^2 is 0.15. In addition, for all cases the correlation is negative, thus there appears to be no correlation between actual pH and predicted pH when the Brukunga model is applied to the Sotiel-Migollas mine site.

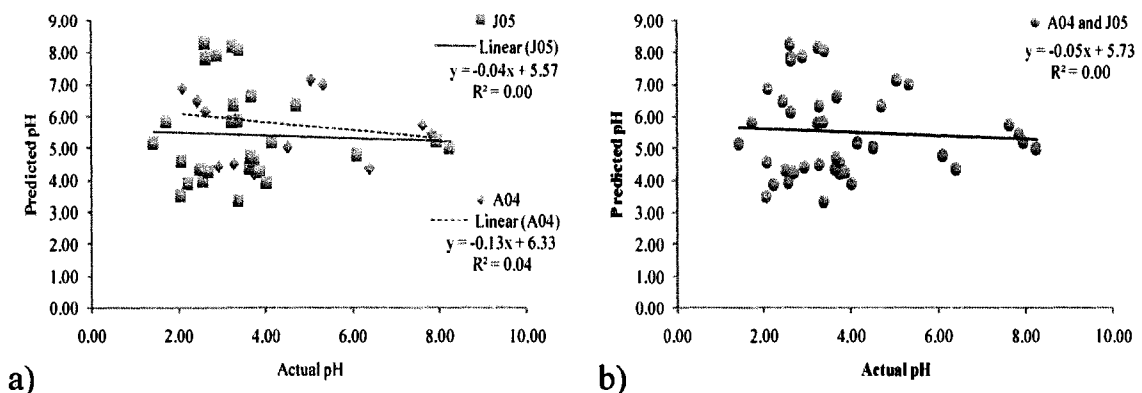


Figure 5.1: Scatter plot of predicted pH versus actual pH when applying the Brukunga model to the Sotiel-Migollas Hymap imagery: a) A04 (lozenges) N=10 and J05 (squares) N=28; b) A04 and J05 merged N=38. A04 for August 2004 and J05 for June 2005.

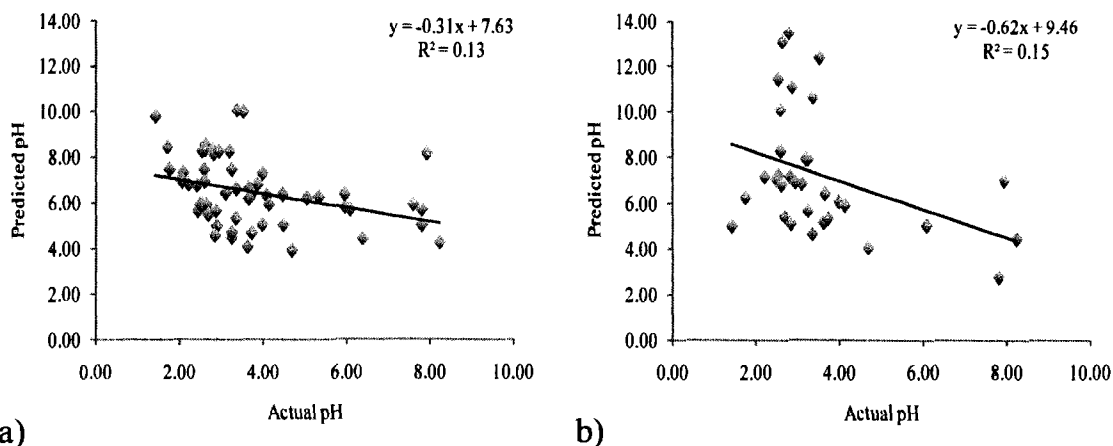


Figure 5.2: Scatter plot of predicted pH versus actual pH when applying the Brukunga model to the Sotiel-Migollas laboratory and field spectra: a) laboratory spectra (A04 and J05 merged) N=58; b) field spectra J05 N=33.

Table 5.2: Summary of the results of the application of the Brukunga PLS model to the Sotiel-Migollas data.

	Results for imagery			Results for laboratory spectra	Results for field spectra
	August 2004 (A04)	June 2005 (J05)	A04 and J05 merged	A04 and J05 merged	J05
N	13	28	41	58	33
RMSE	2.82	2.90	2.87	3.73	5.14
R	-0.20	-0.04	0.00	-0.36	0.38
R²	0.04	0.00	0.00	0.13	0.15
Y=mx+b	Y=-0.13x+6.33	Y=-0.04x+5.57	Y=-0.05x+5.73	y=-0.31x + 7.63	y=-0.62x+9.46

5.3.3. Discussion

Why does the Brukunga model fail when applied to the Sotiel-Migollas dataset? Table 5.3 shows the number of samples per dominant mineral group at Brukunga and Sotiel-Migollas. The number of samples per dominant mineral group is greatly different for both sites, showing a majority of samples of jarosite (N=28), schwertmannite (N=19), and goethite (N=7) at the Brukunga site. In contrast, the Sotiel-Migollas site is dominated by hematite (N=19) and goethite (N=17), followed by schwertmannite (N=10). At Sotiel-Migollas, only 6 samples are dominated by jarosite. Brukunga has no samples containing a majority of hematite or ferrihydrite. This disparity in the dominant mineralogy of samples suggests that a model specific to one site may not be applied to a separate site if

the dominant mineralogy of samples of both sites are not represented in the calibration model.

Table 5.3: Comparison of the dominant mineral of samples found at the Brukunga and the Sotiel-Migollas mine sites.

Dominant mineral in samples	Number of samples represented at Brukunga	Number of samples represented at Sotiel
Hematite	0	19
Goethite	7	17
Schwertmannite	19	10
Jarosite	28	6
Ferrihydrite	0	5
Pyrite	1	0
Halotrichite	1	0
AMD-bearing soils	2	0

5.4. Predictive pH model specific to the Sotiel-Migollas Mine site

This section presents the results of the site-specific pH model for the Sotiel-Migollas mine and the application of this model to hyperspectral images and laboratory spectral measurements.

5.4.1. Calibration and validation datasets

5.4.1.1. Assignment of samples to calibration and validation datasets

The data were grouped into a calibration set of 40 samples and a validation set of 18 samples giving an approximate 2:1 proportion. Samples collected from sites clearly discernible on the Hymap images (table 5.4) were initially assigned to the validation set. This initial selection resulted in 39 samples for validation and 19 for calibration. However, an ideal repartition of the samples would have more samples in the calibration set than the validation set. Thus, half of the samples from sites visible on the images were transferred to the calibration set. This was performed first by grouping these samples according to the most dominant mineral within the samples and then selecting for transfer the samples with minimum and maximum pH value per mineral group. Thus the sample

pH values of the validation set were within the minimum-maximum pH range of the calibration set. Any additional sample transfer was made by ensuring a representation of each mineral group, generating a ranking order of sample pH within each mineral group and selecting alternating samples based on pH value (table 5.5).

Table 5.4: Sampling sites indiscernible (N=19) and discernible (N=39) on images.

Samples from sites indiscernible on images			Samples from sites discernible on images					
Dominant mineral group	Sample	pH	Dominant mineral group	Sample	pH	Dominant mineral group	Sample	pH
Gt	J05-35	2.87	Gt	J05-40	2.61	Jr	J05-46	2.89
	J05-30	3.10		A04-21	2.92		A04-47	3.27
	J05-32	4.01		J05-37	3.64		J05-43	3.67
	A04-27	4.10		J05-51	3.74		A04-09	3.735
	A04-14	4.49		J05-57	4.01	A04-07	2.63	
	A04-33	5.98		A04-08	4.51	J05-55	3.36	
	A04-31	5.985		A04-37	7.62	J05-05	3.37	
J05-04	6.09	A04-36	7.83	Sch	J05-53	3.66		
J05-44	1.765	J05-09	7.94		J05-52	4.14		
J05-22	2.62	J05-47	1.43		A04-34	5.33		
J05-21	2.625	J05-45	1.73		J05-41	8.25		
He	J05-23	2.84	J05-54	2.04	Ferr	J05-20	2.70	
	J05-14	3.54	J05-58	2.07		J05-02	3.26	
	A04-29	2.46	A04-20	2.10		J05-25	4.70	
Jr	J05-38	2.97	J05-42	2.22	A04-43	5.06		
	J05-08	2.66	A04-22	2.43		A04-44	6.40	
Sch	J05-06	2.81	He	J05-19	2.50			
	J05-10	7.82		J05-01	2.56			
	J05-15	2.58		A04-18	2.63			
				J05-49	3.21			
			J05-39	3.28				
			J05-24	3.39				
			J05-56	3.87				

Dominant mineral groups: based on most dominant mineral of the sample. Abbreviations: Gt: Goethite; Jr: jarosite; He: hematite; Sch: Schwertmannite; Ferr: Ferrihydrate Py: Pyrite; cop: Copiapite; Pk Pickeringite. A04: samples of August 2004; J05: samples of June 2005.

Table 5.5: Calibration (N=40) and validation (N=18) datasets.

CALIBRATION			VALIDATION					
Dominant mineral group	Samples	pH	Dominant mineral group	Samples	pH	Dominant mineral group	Samples	pH
Gt	J05-40	2.61	Jr	A04-29	2.46	Ferr	J05-02	3.26
	J05-35	2.87		J05-38	2.97		A04-43	5.06
	J05-30	3.10		A04-47	3.27		A04-21	2.92
	J05-51	3.74		A04-09	3.73	J05-37	3.64	
	J05-32	4.01	J05-20	2.70	Gt	J05-57	4.01	
	A04-27	4.10	J05-25	4.70	A04-08	4.51		
	A04-14	4.49	A04-44	6.40	A04-36	7.83		
	A04-33	5.98	A04-07	2.63	J05-45	1.73		
	A04-31	5.985	J05-08	2.66	J05-58	2.07		
	J05-04	6.09	J05-06	2.81	He	J05-42	2.22	
A04-37	7.62	J05-05	3.37	J05-19	2.50			
J05-09	7.94	J05-52	4.14	A04-18	2.63			
He	J05-47	1.43	J05-10	7.82	J05-39	3.28		
	J05-44	1.765	J05-41	8.25	Jr	J05-46	2.89	
	J05-54	2.04	J05-15	2.56		J05-43	3.67	
	A04-20	2.10	Sch	J05-05	J05-55	3.36		
	A04-22	2.43			J05-53	3.66		
	J05-01	2.56			A04-34	5.33		
	J05-22	2.62						
	J05-21	2.625						
	J05-23	2.84						
	J05-49	3.22						
J05-24	3.39							
J05-14	3.54							
J05-56	3.87							

Dominant mineral groups: based on most dominant mineral of the sample. Abbreviations: Gt: Goethite; Jr: jarosite; He: hematite; Sch: Schwertmannite; Ferr: Ferrihydrate Py: Pyrite; cop: Copiapite; Pk Pickeringite. A04: samples of August 2004; J05: samples of June 2005.

5.4.1.2. Normality test for the calibration dataset

In regards to partial least squares analysis, it is important that the data be normally distributed because the results are sensitive to outlying observations, i.e., non-normally distributed data (Reimann and Filzmoser, 1999) and PLS assumes a normal distribution of the response variable (Bajwa and Tian, 2005). Thus, before calibrating the new pH model, the Shapiro-Wilk normality test (test used for N<2000) was performed on the calibration set. Figure 5.3 shows the frequency histogram of the pH values with the normal curve modeled to fit the pH variable in the calibration set. Table 5.6 presents a summary of the descriptive statistics of the set and the results of the normality test.

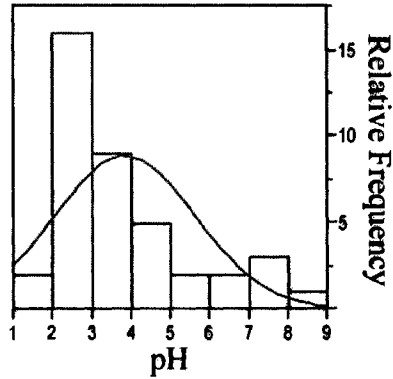


Figure 5.3: Frequency histogram of pH values for the calibration dataset (N=40). The red curve represents the Normal Fit Distribution of the data.

Table 5.6: Descriptive statistics and normality test results of the calibration pH dataset.

Descriptive Statistics	pH from Calibration set
N of Cases	40
Minimum	1.431
Maximum	8.248
Arithmetic Mean	3.836
Standard Deviation	1.799
Normality test	pH from Calibration set
Shapiro-Wilk Statistic	0.849
Shapiro-Wilk p-value	0.000

According to the p-values obtained from the Shapiro-Wilk test, the calibration set does not follow a normal distribution because the null-hypothesis (H_0) stipulates that if the p-value > 0.05 then the distribution is normal. Since the p-value is lower than 0.05 the null-hypothesis of a normal distribution is rejected. In the next section, a PLS calibration is first conducted while assuming the set has a normal distribution. Then outliers are assessed and removed, and another normality test is performed.

5.4.2. Calibration of the predictive models

The calibration of the models was examined in two sets. The first set of models used all calibration samples (N=40) without removal of outliers. The second set of models involved the removal of parameter and spectral residual outliers detected by Xspectra. In addition, for each set one group of models was created with the full spectrum range of 1869 bands (listed in appendices 5.2, 5.4, and 5.6) and a second group with the VNIR spectral range of 1000 bands (listed in appendices 5.3, 5.5, and 5.7).

For each set a number of models were obtained by varying the number of initial bands retained for the model. To achieve an optimal subset of bands, thresholds were set for a minimum final regression coefficients (FRC) value, where channels with high absolute |FRC values| were kept. When a new threshold (x) is set, bands corresponding to FRC values between $-x$ and $+x$ are eliminated and a new model is calibrated. For all models, careful attention was given to the RMSE and the r^2 values to determine the best calibration model. Table 5.7 presents a summary of all the models built including the start parameters for the start-off model and the parameters of the final model with lowest RMSE and highest r^2 . Detailed information on these models, i.e., the parameters modified, is given in tables in appendices 5.2 to 5.7 for both sets.

Table 5.7: Summary of parameters used for the model calibrations for the two sets.

ASD resolution, 40 spectra samples Full spectrum, No H2O vapor bands Calibration - Normalization MEAN=1

S E T	number of selected spectra (samples)	Number of channels	CV Number of factors After AUTO	Optimal #factor after running CV	F prob	Outlier F prob	Removed Outlier samples	Minimum FRC	Measured vs predicted Correl. (R)	Measured vs predicted RMS error	Param Outliers detected	Spec Outliers detected	score scatterplots RAW data outliers	score scatterplots Mahalanobis distance outliers	Model name	
1	Start	40	1869	39	9	0.25	0.9	-	-	0.758	1.190	32, 39	14	none	none	pls-40sp-9fc-1869ch
	Final	40	785	39	8	4.77E-14	0.9	-	0.15 ^a	0.801	1.077	10, 32, 39	1, 14, 33	none	none	pls-40sp-8fc-785ch
	Start	40	1000	26	7	0.25	0.9	-	-	0.712	1.262	31, 36, 39, 40	13, 14	none	none	pls-40sp-7fc-1000ch
	Final	40	169	18	6	0.003875	0.9	-	0.75 ^b	0.786	1.112	31, 36, 39, 40	14, 15	19	19	pls-40sp-6fc-169ch
2	Start	40	1869	39	9	0.25	0.9	-	-	0.758	1.190	32, 39	14	none	none	pls-40sp-9fc-1869ch
	Final	38	883	37	12	0.25	0.9	32, 39	0.12 ^c	0.900	0.752537	10, 11, 34, 36	20, 33	none	none	pls-38sp-12fc-883ch
	Start	40	1869	39	9	0.25	0.9	-	-	0.758	1.190	32, 39	14	none	none	pls-40sp-9fc-1869ch
	Final	37	948	36	8	0.25	0.9	14, 32, 39	0.14 ^d	0.875	0.824	6, 9, 10, 13, 34	1, 25, 33	25	25	pls-37sp-8fc-948ch
	Start	40	1000	26	7	0.25	0.9	-	-	0.712	1.262	31, 36, 39, 40	13, 14	none	none	pls-40sp-7fc-1000ch
	Final	36	540	26	8	0.25	0.9	31, 36, 39, 40	0.225 ^e	0.895	0.701	9, 10, 32, 33, 34	3, 33	15	15	pls-36sp-8fc-540ch
	Start	40	1000	26	7	0.25	0.9	-	-	0.712	1.262	31, 36, 39, 40	13, 14	none	none	pls-40sp-7fc-1000ch
	Final	34	297	20	7	0.25	0.9	13, 14, 31, 36, 39, 40	0.5 ^f	0.860	0.705	7, 9, 10, 32, 33, 34	15, 28	15	15	pls-34sp-7fc-297ch

CV: Cross-validation

a. FRC increments of 0.025; b FRC increments of 0.025; c. FRC increments of 0.01; d. FRC increments of 0.01; e. FRC increments of 0.25; f. FRC increments of 0.025.

FIRST SET: models built with all calibration samples

The initial model created using the full spectral range presented an r^2 of 0.58 with a RMSE of 1.19. From this calibration, removal of bands was determined by an initial minimum FRC threshold set at 0.025 and further calibrations were performed by increasing the threshold by increments of 0.025 until a calibration presented the best r^2 and RMSE. The best model from this dataset (model pls-40sp-8fc-785ch) occurred at a minimum threshold of 0.75, with a r^2 of 0.64 and a RMSE of 1.08. The optimal number of factors was 8 and 785 bands were retained. Figure 5.4a displays the actual and predicted pH values for this model. The final FRC values and bands of this calibration are plotted in figure 5.4b. Intermediate models created between the first and final model for this first group are presented in a table of appendix 5.2.

The initial model using the VNIR range presented an r^2 of 0.50 with a RMSE of 1.26. From this calibration, a FRC threshold was set at 0.025 and was increased in increments of 0.025. The best model from this dataset (model pls-40sp-9fc-169ch) also occurred at a minimum threshold of 0.75, with an r^2 of 0.62 and a RMSE of 1.11. The optimal number of factors was 6 and 169 bands remained. The actual and predicted pH values of this model are plotted in figure 5.4c and the final FRC values of this calibration are plotted in figure 5.4d. Models built between the first and best model of this group are presented in a table of appendix 5.3.

Both models (pls-40sp-8fc-785ch and pls-40sp-9fc-169ch) present reasonable and similar r^2 but the RMSE is high. Table 5.8 shows the sample residual for each model and figure 5.4 gives the frequency histograms of the residuals for both models.

For the first model, samples 32 and 39 (J05-25 and J05-10) present the highest residuals and Xspectra detected these as parameter residual outliers. Xspectra also detected one spectral residual outlier (sample 14 – J05-47). For the second model three samples are highly under estimated (samples 36, 39, and 40 – J05-06, J05-10 and J05-41) and one sample is highly over estimated (sample 31 – J05-20), all of which were detected

as parameter residual outliers by Xspectra. The next section presents models in set 2 that were built by removing the outliers identified by Xspectra, to evaluate any improvement in r^2 and RMSE.

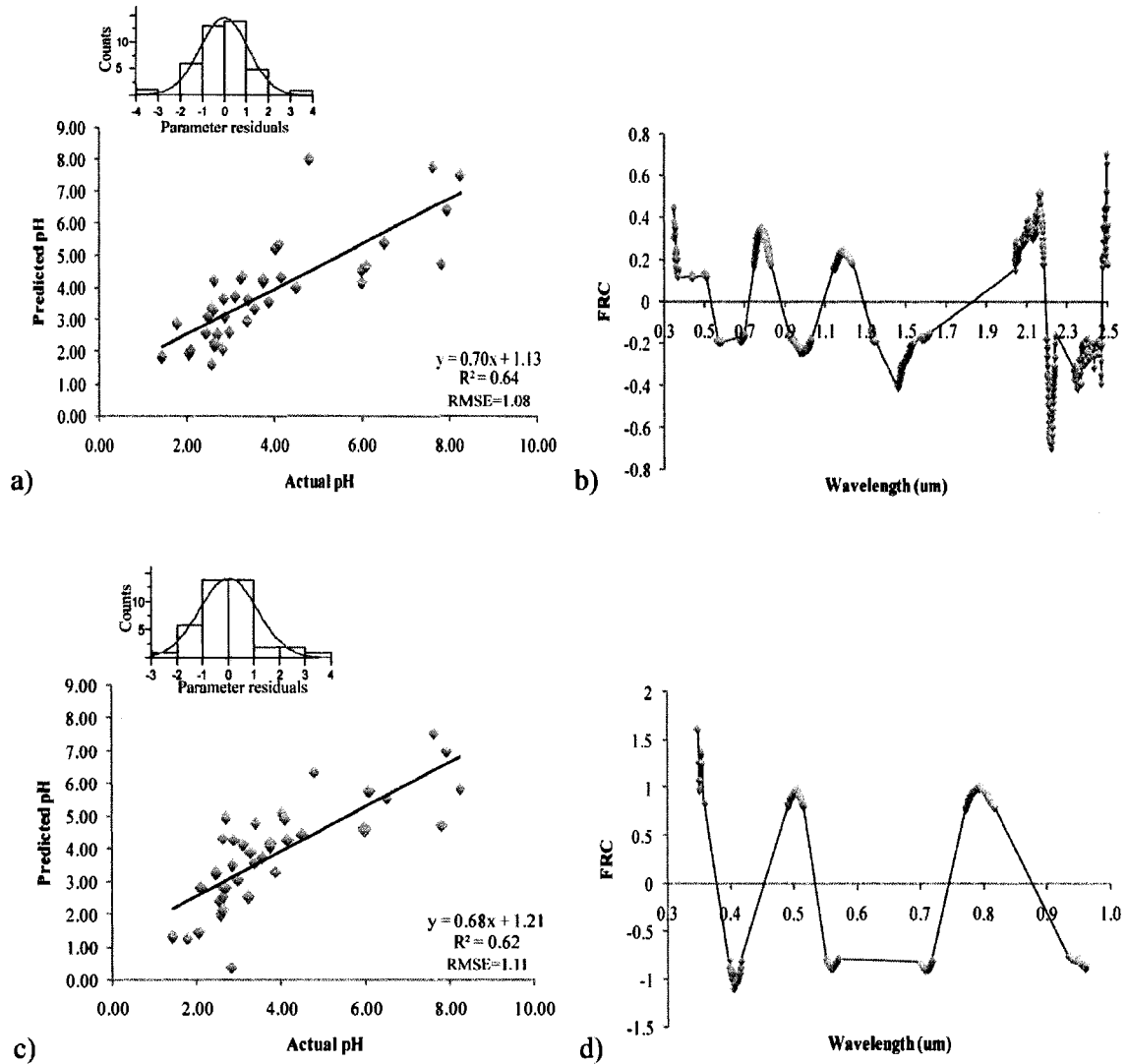


Figure 5.4: Results of the best calibration models from SET 1: a) Actual versus predicted pH from calibration model pls-40sp-8fc-785ch; b) FRC from calibration model pls-40sp-8fc-785ch; c) Actual versus predicted pH from calibration model pls-40sp-6fc-169ch; d) FRC from calibration model pls-40sp-6fc-169ch. Histograms of parameter residuals shown in inset. The red curve represents the Normal Fit Distribution of the data.

Table 5.8: Summary of predicted and actual pH values and residuals of calibration models from set 1 (all 40 samples used).

Sample	Sample # in Xspectra	Actual pH	Pls-40sp-8fc-785ch		Pls-40so-6fc-169ch	
			Predicted pH	Parameter residual	Predicted pH	Parameter residual
J05-15	1	2.56	3.36	-0.80	2.39	0.17
J05-40	2	2.61	3.30	-0.69	2.53	0.08
J05-35	3	2.87	3.09	-0.22	4.28	-1.41
J05-30	4	3.10	3.71	-0.61	4.13	-1.03
J05-51	5	3.74	4.19	-0.44	4.17	-0.42
J05-32	6	4.01	5.20	-1.18	5.10	-1.09
A04-27	7	4.10	5.35	-1.25	4.90	-0.80
A04-14	8	4.49	3.99	0.50	4.44	0.05
A04-33	9	5.98	4.53	1.45	4.66	1.33
A04-31	10	5.99	4.14	1.85	4.57	1.41
J05-04	11	6.09	4.68	1.41	5.76	0.33
A04-37	12	7.62	7.73	-0.11	7.54	0.08
J05-09	13	7.94	6.39	1.55	6.98	0.97
J05-47	14	1.43	1.81	-0.38	1.32	0.11
J05-44	15	1.77	2.86	-1.10	1.25	0.51
J05-54	16	2.04	1.93	0.12	1.45	0.59
A04-20	17	2.10	2.01	0.09	2.80	-0.70
A04-22	18	2.43	2.55	-0.12	3.25	-0.82
J05-01	19	2.56	1.61	0.95	2.00	0.57
J05-22	20	2.62	2.15	0.47	2.86	-0.24
J05-21	21	2.63	2.29	0.34	2.12	0.50
J05-23	22	2.84	3.66	-0.82	3.48	-0.64
J05-49	23	3.22	4.29	-1.07	2.53	0.68
J05-24	24	3.39	3.63	-0.24	4.77	-1.38
J05-14	25	3.54	3.32	0.21	3.73	-0.19
J05-56	26	3.87	3.55	0.32	3.29	0.58
A04-29	27	2.46	3.09	-0.63	3.24	-0.78
J05-38	28	2.97	2.57	0.40	3.03	-0.06
A04-47	29	3.27	4.36	-1.09	3.89	-0.62
A04-09	30	3.74	4.27	-0.53	4.06	-0.33
J05-20	31	2.70	2.53	0.17	4.95	-2.25
J05-25	32	4.80	7.99	-3.19	6.35	-1.55
A04-44	33	6.50	5.39	1.11	5.53	0.97
A04-07	34	2.63	4.21	-1.58	4.32	-1.69
J05-08	35	2.67	2.22	0.45	2.82	-0.16
J05-06	36	2.81	2.05	0.76	0.37	2.44
J05-05	37	3.37	2.93	0.44	3.57	-0.20
J05-52	38	4.14	4.31	-0.17	4.25	-0.11
J05-10	39	7.82	4.76	3.06	4.70	3.11
J05-41	40	8.25	7.51	0.74	5.81	2.43

Bold: detected as parameter residual outliers by Xspectra, based on F-test (0.9) after the model built

SECOND SET: models built after removal of parameter and spectral residual outliers detected by Xspectra

Four groups of models (table 5.7) were created in this set by:

- i. Removing only parameter outliers detected when starting with the full spectral region and all 40 samples;
- ii. Removing parameter and spectral outliers detected when starting with the full spectral region and all 40 samples;
- iii. Removing only parameter outliers detected when starting with the VNIR spectral region and all 40 samples;
- iv. Removing parameter and spectral outliers detected when starting with the VNIR spectral region and all 40 samples.

After removing the outlier samples, the frequency distribution of sample pH in the reduced calibration suites was evaluated for normality (figure 5.5). Table 5.9 summarizes the descriptive statistics of the Shapiro-Wilk test. The p-values for normality are <0.0001, <0.0001, 0.0008, and 0.0010 for models with N=38, N=37, N=36, and N=34, respectively. Even after removing outliers, the distributions do not fit normality since the p-values are not greater than 0.05, but do approach normality as more outliers are removed.

Table 5.9: Descriptive statistics of pH of the samples for the calibration set after removing outliers.

Groups of calibration from set 2	Descriptive statistics					Shapiro-Wilk Normality test	
	N	Mean	Min	Max	s.d.	W	p-value
i.	38	3.709	1.431	8.248	1.717	0.838343	<0.0001
ii.	37	3.770	1.765	8.248	1.697	0.820360	<0.0001
iii.	36	3.663	1.431	7.943	1.581	0.876733	0.0008
iv.	34	3.603	1.765	7.621	1.394	0.873870	0.0010

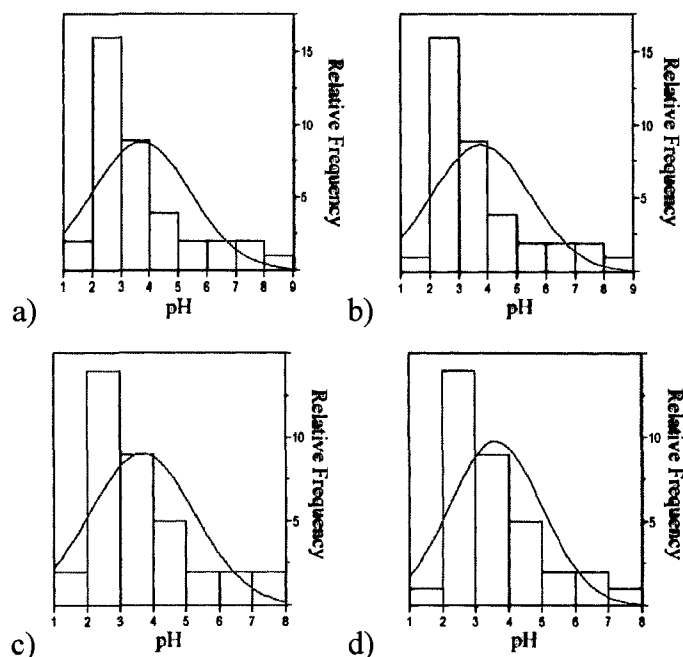


Figure 5.5: Frequency histograms of sample pH for the calibration set after removing outliers: a) N=38; b) N=37; c) N=36; d) N=34. The red curve represents the Normal Fit Distribution of the data.

The first group of models (i) was based on removing parameter residual outliers 32 and 39 (J05-25 and J05-10) when using all 40 samples and 1869 bands (model pls-40sp-9fc-1869ch). Then bands with low FRC values were removed (by incrementing the minimum FRC threshold by 0.01 between each calibration) until the best r^2 and RMSE were obtained. The best and final model (model pls-38sp-12fc-883ch) had an r^2 of 0.81 and RMSE of 0.75. The optimal number of factor was 12 and 883 bands remained at a minimum FRC value of 0.12. The actual and predicted pHs of this model are presented in figure 5.6a and the FRCs and remaining bands in figure 5.6b. The intermediate models built between the first and final model of this group are given in a table in appendix 5.4.

The second group of models (ii) were created by removing the spectral residual outlier 14 (J05-47) in addition to the parameter residual outliers 32 and 39. Then bands having low FRC values were removed by increasing the minimum FRC values by increments of 0.01 ending with a minimum FRC value of 0.14 for the best model. The final model built in this group has an r^2 of 0.77 with an RMSE of 0.82, using 948 spectral bands and an optimal number of factors of 8 (model pls-37sp-8fc-948ch). Intermediate

models created in this group are presented in appendix 5.5. The actual versus predicted pH of this calibration are plotted in figure 5.6c and the FRCs and remaining bands in figure 5.6d.

The third group of models (iii) were calibrated starting with the VNIR spectral range and all 40 samples. The parameter residual outliers detected in the set 1 model were removed namely samples 31, 36, 39, and 40 (J05-20, J05-06, J05-10, and J05-41). Then new calibration models were obtained by removing bands with low FRC values, by increments of 0.25, leading to a final model (model pls-36sp-8fc-540ch) with a minimum FRC value of 0.225. This model had an r^2 of 0.80, a RMSE of 0.70, and 540 bands after removal of bands with low FRC and using an optimal number of factors of 8. The actual versus predicted pH of this calibration are plotted in figure 5.6e and the FRCs in figure 5.6f. Models created between the first and the final models are presented in appendix 5.6.

The last group of models (iv) was built by removing both the parameter residual outliers (31, 36, 39 and 40 – respectively J05-20, J05-06, J05-10 and J05-41) and spectral residual outliers 13 and 14 (J05-09 and J05-47), with the 40 calibration samples and the 1000 bands of the VNIR. Bands were then removed again by setting minimum thresholds to the FRC eliminating those with low FRC values by increasing the threshold in increments of 0.025. The best model obtained from this group (model pls-34sp-7fc-297ch) had an r^2 of 0.74, a RMSE of 0.71 and a minimum FRC value threshold of 0.225. Figure 5.6g plots the actual and predicted pH of this calibration model and figure 5.6h presents the FRCs and remaining bands. Appendix 5.7 presents the in-between models calibrated from this group.

Another type of outliers that may be considered for removal are the score outliers, but none were detected in the initial models of this set.

Table 5.10 gives the actual and predicted pH of the calibration models considered in the second set with residuals for each sample. Figure 5.6 also presents the frequency histograms of residuals for each model in set 2. Models pls-36sp-8fc-540ch and pls-34sp-

7fc-297ch (figure 5.6e, 5.6g) present the best results of RMSE and r^2 of all models built in set 1 and 2.

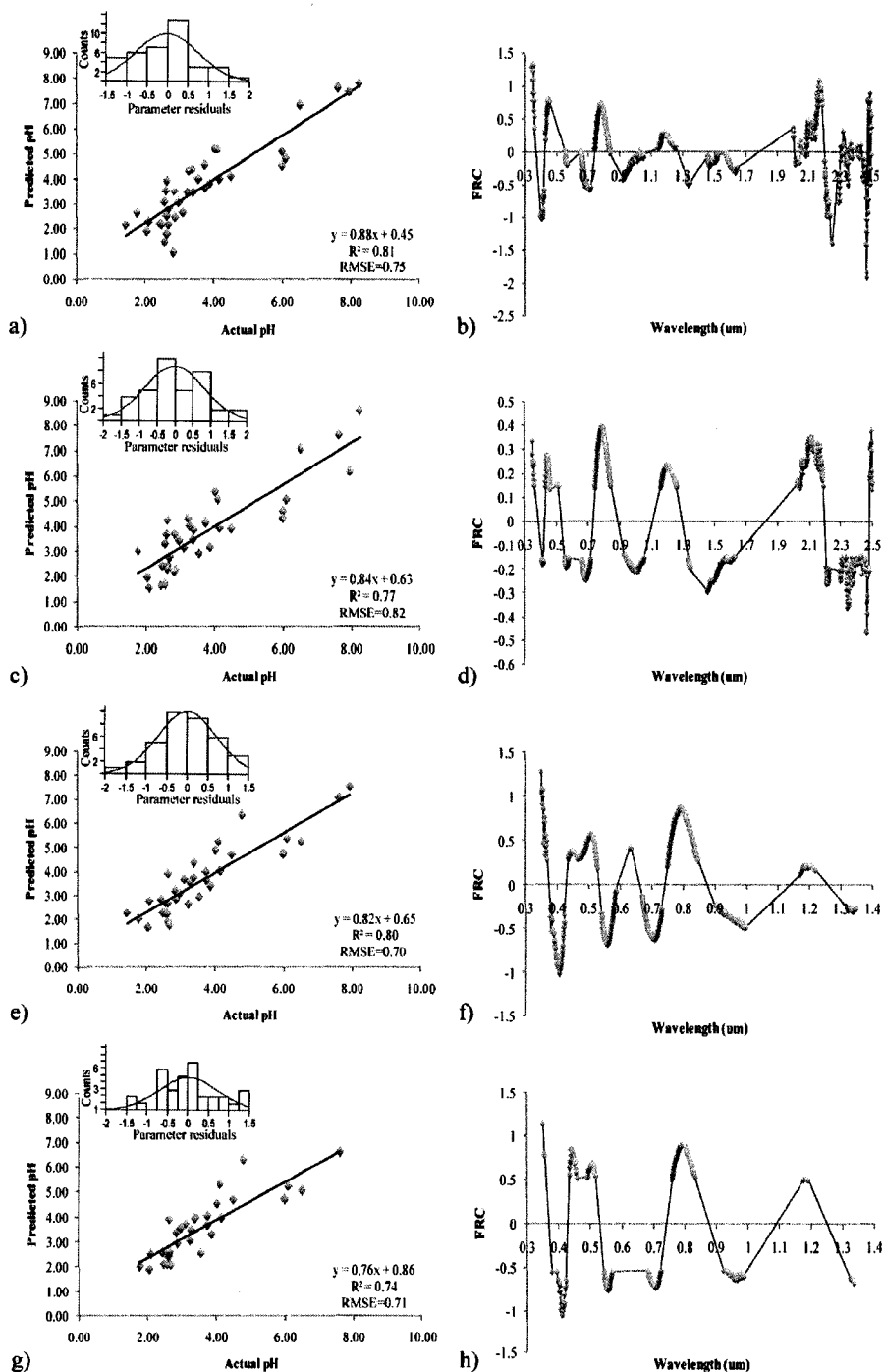


Figure 5.6: Results of the best calibration model from SET 2: a) Actual versus predicted pH model pls-38sp-12fc-883ch; b) FRC pls-38sp-12fc-883ch; c) Actual versus predicted pH for model pls-37sp-8fc-948ch; d) FRC Model pls-37sp-8fc-948ch; e) Actual versus predicted pH for model pls-36sp-8fc-540ch; f) FRC for model pls-36sp-8fc-540ch; g) Actual versus predicted pH for model pls-34sp-7fc-297ch; h) FRC for model pls-34sp-7fc-297ch. Frequency histograms of parameter residuals are shown in inset. The red curve represents the Normal Fit Distribution of the data.

Table 5.10: Summary of predicted and actual pH and residuals of calibration models from set 2.

Sample	Sample no.	Actual pH	Pls-38sp-12fc-883ch		Pls-37sp-8fc-948ch		Pls-36sp-8fc-540ch		Pls-34sp-7fc-297ch	
			Predicted pH	Residual	Predicted pH	Residual	Predicted pH	Residual	Predicted pH	Residual
J05-15	1	2.56	3.08	-0.52	3.30	-0.74	2.24	0.31	2.10	0.46
J05-40	2	2.61	3.49	-0.88	3.65	-1.04	2.24	0.36	2.42	0.18
J05-35	3	2.87	2.46	0.41	2.28	0.59	2.83	0.04	2.94	-0.07
J05-30	4	3.10	2.61	0.49	3.14	-0.04	3.69	-0.58	3.71	-0.61
J05-51	5	3.74	4.57	-0.82	4.18	-0.44	4.00	-0.25	4.04	-0.29
J05-32	6	4.01	5.19	-1.18	5.37	-1.36	4.89	-0.88	4.54	-0.53
A04-27	7	4.10	5.16	-1.06	5.07	-0.97	5.23	-1.13	5.31	-1.21
A04-14	8	4.49	4.09	0.40	3.88	0.61	4.71	-0.22	4.71	-0.22
A04-33	9	5.98	5.10	0.89	4.60	1.38	4.70	1.29	4.69	1.29
A04-31	10	5.99	4.51	1.47	4.33	1.65	4.77	1.21	4.74	1.25
J05-04	11	6.09	4.80	1.29	5.06	1.03	5.36	0.73	5.23	0.86
A04-37	12	7.62	7.63	0.00	7.63	-0.01	7.07	0.55	6.62	1.00
J05-09	13	7.94	7.51	0.43	6.20	1.75	-	0.43	-	-
J05-47	14	1.43	2.12	-0.69	-	-	-	-0.84	-	-
J05-44	15	1.77	2.63	-0.86	3.03	-1.26	7.52	-0.27	2.03	-0.26
J05-54	16	2.04	1.89	0.16	1.97	0.07	2.27	0.38	1.87	0.18
A04-20	17	2.10	2.26	-0.16	1.54	0.55	2.04	-0.68	2.52	-0.42
A04-22	18	2.43	2.20	0.23	1.63	0.80	1.67	-0.42	2.58	-0.15
J05-01	19	2.56	1.44	1.12	1.69	0.88	2.78	-0.14	2.61	-0.04
J05-22	20	2.62	2.51	0.10	2.44	0.18	2.85	-0.06	2.54	0.08
J05-21	21	2.63	1.77	0.86	2.27	0.35	2.70	0.75	2.61	0.02
J05-23	22	2.84	3.50	-0.66	3.67	-0.83	2.68	-0.36	3.37	-0.54
J05-49	23	3.22	3.49	-0.27	4.33	-1.11	1.88	0.61	3.05	0.17
J05-24	24	3.39	3.47	-0.08	3.87	-0.48	3.20	-0.95	4.01	-0.63
J05-14	25	3.54	4.01	-0.48	2.90	0.64	2.61	0.61	2.55	0.98
J05-56	26	3.87	3.83	0.04	3.17	0.70	4.34	0.46	3.30	0.57
A04-29	27	2.46	2.18	0.29	2.40	0.06	2.93	0.18	2.11	0.36
J05-38	28	2.97	3.06	-0.09	3.45	-0.48	3.42	-0.09	3.55	-0.57
A04-47	29	3.27	4.31	-1.04	4.00	-0.73	2.28	-0.26	3.48	-0.21
A04-09	30	3.74	3.66	0.07	4.14	-0.41	3.07	0.10	3.70	0.04
J05-20	31	2.70	2.79	-0.09	2.78	-0.08	3.53	-	-	-
J05-25	32	4.80	-	-	-	-	-	-1.53	6.30	-1.50
A04-44	33	6.50	6.92	-0.42	7.07	-0.57	3.63	1.27	5.07	1.43
A04-07	34	2.63	3.95	-1.32	4.24	-1.61	6.33	-1.26	3.91	-1.28
J05-08	35	2.67	2.17	0.50	2.75	-0.09	5.23	0.92	2.08	0.59
J05-06	36	2.81	1.02	1.79	2.15	0.66	3.89	-	-	-
J05-05	37	3.37	4.40	-1.03	3.49	-0.11	1.75	-0.38	3.92	-0.55
J05-52	38	4.14	4.01	0.14	3.93	0.21	3.75	0.12	3.95	0.19
J05-10	39	7.82	-	-	-	-	-	-	-	-
J05-41	40	8.25	7.80	0.44	8.62	-0.37	4.02	-	-	-

Bold: detected as parameter residual outliers by Xspectra, based on F-test (0.9) after the model built

Outliers detected in the second set of models are listed in table 5.11 with a brief description of the samples and suggestions of why they are outliers. The parameter outlier samples show measured pHs that are either too low or too high based on the theoretical pH value of the dominant mineral in the samples. Also, some samples had thick coatings and in these cases it was difficult to remove only the first few millimetres of coating, thus presenting other minerals from the core of the sample which could have influenced the pH.

Table 5.11: Parameter and spectral outliers detected in the calibration set.

Parameter residual outliers		
Object	Sample	Description
31	J05-20	Dominated by Ferrihydrite. Theoretical pH should be >5. Measured pH (2.70) is too low for presence of ferrihydrite.
32	J05-25	Dominated by Ferrihydrite. Theoretical pH should be >5. Measured pH (4.70) is too low for presence of ferrihydrite.
36	J05-06	Dominated by Schwertmannite. Theoretical pH should be 3-4.5. Measured pH (2.81) is too low for presence of schwertmannite
39	J05-10	Dominated by Schwertmannite. Theoretical pH should be 3-4.5. Measured pH (7.82) is too high for presence of schwertmannite
40	J05-41	Dominated by Schwertmannite. Theoretical pH should be 3-4.5. Measured pH (8.25) is too high for presence of schwertmannite
Spectral residual outliers		
Object	Sample	Description
13	J05-09	Thick coating from riverbed
14	J05-47	Sample spectrum is dominated by Hematite. Theoretical pH should be >5. Contains jarosite and is located in area of drainage susceptible of containing more jarosite and efflorescent salts – reducing pH considerably

5.4.3. Validation of the predictive pH models

Each calibration model created in the previous section is evaluated with a set of independent laboratory spectral samples, i.e. the validation dataset (N=18). Table 5.12 presents a summary of the descriptive statistics and the Shapiro-Wilk normality test results for the validation set. The p-value indicates that the set does not fit a normal distribution as can be seen in the frequency histogram in figure 5.7a. The distributions appears skewed to high pH due to sample A04-36 that has a pH of 7.832. According to Haaland and Thomas (1988), parameter residual outliers in the validation set cannot be detected based on F-ratio since the parameter matrix residuals do not exist in the validation step. Instead, a control chart was used to detect whether this sample is an outlier or not based on the 3-sigma control chart (figure 5.8). If the sample has a pH value higher or lower then 3-sigma to the mean pH of the validation set it becomes an outlier and is removed from the dataset to improve the quality of the data. As shown in figure 5.8, sample A04-36 is an outlier and once removed, the data fits a normal distribution (figure 5.7b) and the p-value (0.795) confirms its normality.

Table 5.12: Descriptive statistics of pH of the samples for the validation set before (N=18) and after removing the outlier (N=17).

Descriptive Statistics		pH from Validation set	
N of Cases		18	17
Minimum		1.730	1.730
Maximum		7.832	5.334
Arithmetic Mean		3.587	3.338
Standard Deviation		1.438	1.002
Normality test		pH from Validation set	
Shapiro-Wilk Statistic		0.881	0.969
Shapiro-Wilk p-value		0.027	0.795

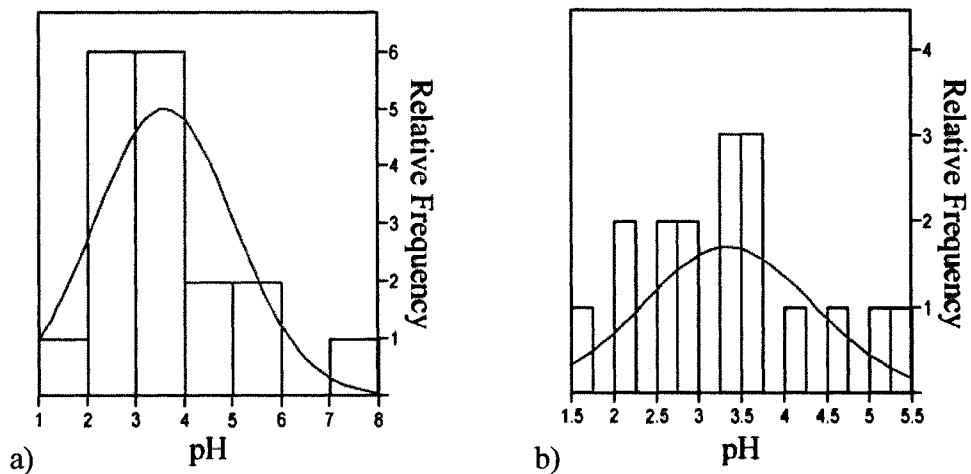


Figure 5.7: Frequency histogram of pH values for the validation dataset: a) N=18; b) N=17 after removing outlier sample A04-36. The red curve represents the Normal Fit Distribution of the data.

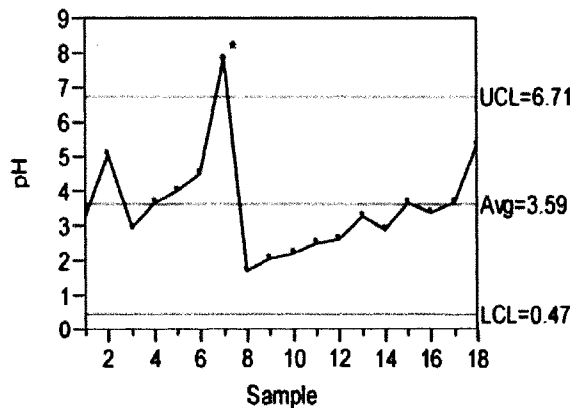


Figure 5.8: Control chart of the pH values for the validation dataset (N=18). The centre line is the average pH of the 18 validation samples and the upper and lower lines are 3-sigma limits (three times the standard deviation from the mean). Sample 7 (A04-36) exceeds the upper limit, and is thus considered an outlier.

Figure 5.9 compiles scatter plots of the actual versus predicted pH of the validation set (without the A04-36 sample, N=17). The predicted values were obtained for each model from sets 1 and 2. Predicted and actual pH, and residual for each sample in each model are shown in table 5.13 along with the r^2 and RMSE for each model. For the first set, model pls-40sp-6fc-169 created from the VNIR spectral range gave the best r^2 (0.68) and RMSE (0.92) for the validation dataset. For the second set, models pls-36sp-6fc-540 and pls-34sp-7fc-297ch, both built from the VNIR spectral range, gave the best validation results with an r^2 of 0.71 and 0.68 and RMSE values of 0.74 and 0.75.

Table 5.14 presents the Shapiro-Wilk normality test results of the parameter residuals from the validation for all models. The frequency histogram of the residuals for each model is included in figure 5.9. The residuals for all models fit a normal distribution since their p-values are higher than 0.05.

Table 5.15 gives a summary of the calibration and validation results for all models tested. Statistical parameters were calculated from the calibration and validation sets in order to evaluate the prediction capabilities of the PLS models and determine the optimal model.

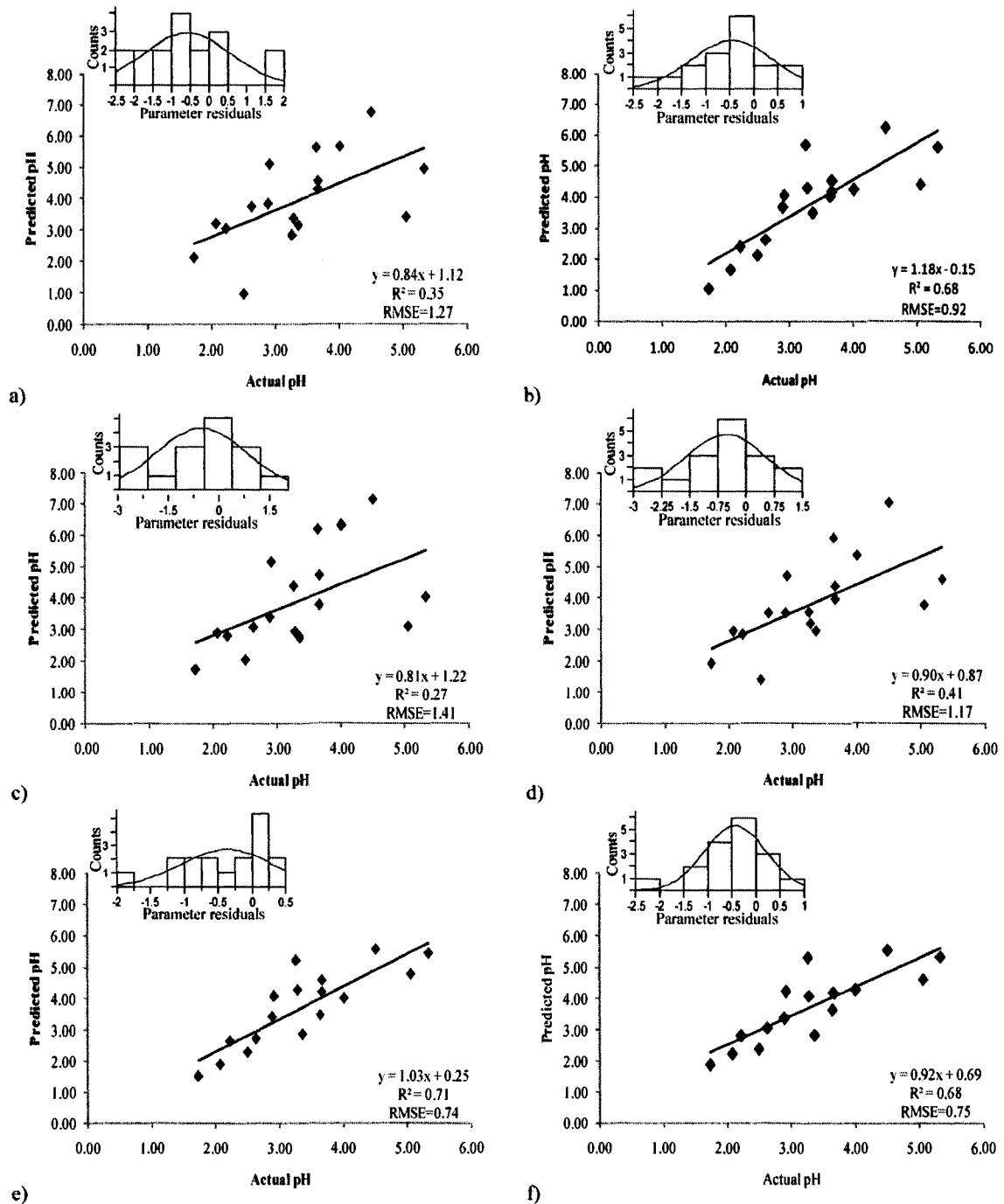


Figure 5.9: Validation results for calibration models from sets 1 and 2: Actual versus predicted pH for the validation dataset (N=17). SET 1: a) model pls40sp-8fc-785ch; b) model pls-40sp-6fc-169ch; SET 2: c) model pls-38sp-12fc-883ch; d) model pls-37sp-8fc-948ch; e) model pls-36sp-6fc-540ch; f) model pls-34sp-7fc-297ch. Frequency histograms of parameter residuals shown in inset. The red curve represents the Normal Fit Distribution of the data.

Table 5.13: Actual and predicted pH from the validation of all calibration models with their parameter residuals.

Sample	Actual pH	Sample no	VALIDATION RESULTS											
			SET 1				SET 2							
			A: pls-40sp-8fc-785ch		B: pls-40sp-6fc-169ch		C: pls-38sp-12fc-883ch		D: pls-37sp-8fc-948ch		E: pls-36sp-6fc-540ch		F: pls-34sp-7fc-297ch	
Predicted pH	Residual	Predicted pH	Residual	Predicted pH	Residual	Predicted pH	Residual	Predicted pH	Residual	Predicted pH	Residual			
J05-02	3.26	1	2.83	0.42	5.69	-2.44	4.38	-1.12	3.55	-0.29	5.21	-1.96	5.30	-2.04
A04-43	5.06	2	3.40	1.66	4.43	0.63	3.09	1.96	3.77	1.28	4.77	0.29	4.61	0.44
A04-21	2.92	3	5.09	-2.17	4.07	-1.16	5.14	-2.23	4.70	-1.78	4.09	-1.17	4.23	-1.32
J05-37	3.64	4	5.63	-1.99	4.05	-0.40	6.20	-2.56	5.91	-2.27	3.47	0.17	3.62	0.02
J05-57	4.01	5	5.65	-1.64	4.25	-0.24	6.32	-2.31	5.38	-1.37	4.00	0.00	4.29	-0.29
A04-08	4.51	6	6.77	-2.26	6.24	-1.74	7.14	-2.63	7.05	-2.54	5.57	-1.06	5.56	-1.05
J05-45	1.73	8	2.12	-0.39	1.04	0.69	1.75	-0.02	1.92	-0.19	1.53	0.20	1.88	-0.15
J05-58	2.07	9	3.20	-1.13	1.65	0.43	2.89	-0.82	2.96	-0.88	1.90	0.18	2.22	-0.15
J05-42	2.22	10	3.07	-0.85	2.42	-0.20	2.81	-0.59	2.86	-0.63	2.65	-0.43	2.81	-0.59
J05-19	2.50	11	0.94	1.56	2.12	0.38	2.04	0.47	1.41	1.10	2.30	0.20	2.37	0.13
A04-18	2.63	12	3.74	-1.11	2.64	-0.01	3.08	-0.44	3.52	-0.89	2.73	-0.10	3.08	-0.45
J05-39	3.28	13	3.37	-0.10	4.29	-1.01	2.93	0.35	3.19	0.09	4.27	-0.99	4.08	-0.81
J05-47	2.89	14	3.85	-0.96	3.69	-0.79	3.41	-0.52	3.53	-0.64	3.43	-0.54	3.39	-0.49
J05-43	3.67	15	4.31	-0.65	4.52	-0.86	3.79	-0.12	3.97	-0.30	4.58	-0.92	4.18	-0.52
J05-55	3.36	16	3.14	0.22	3.49	-0.13	2.76	0.61	2.95	0.41	2.87	0.49	2.83	0.53
J05-53	3.66	17	4.57	-0.91	4.18	-0.51	4.71	-1.05	4.38	-0.72	4.21	-0.55	4.21	-0.55
A04-34	5.33	18	4.94	0.40	5.63	-0.30	4.02	1.31	4.60	0.74	5.43	-0.10	5.34	-0.01
RMSE				1.27		0.92		1.41		1.17		0.74		0.75
r²			0.35		0.68		0.27		0.41		0.71		0.68	

Table 5.14: Shapiro-Wilk normality test results of the parameter residuals from the validation of all models after removing outlier A04-36.

Model	Shapiro-Wilk results (N=17)	
	W	p-value
pls40sp-8fc-785ch	0.950	0.452
pls-40sp-6fc-169ch	0.948	0.425
pls-38sp-12fc-883ch	0.961	0.641
pls-37sp-8fc-948ch	0.973	0.867
pls-36sp-6fc-540ch	0.916	0.127
pls-34sp-7fc-297ch	0.948	0.421

Table 5.15: Summary of calibration and validation results of the different PLS models for Sotiel-Migollas.

	SET 1		SET 2			
	Full spectrum pls-40sp-8fc- 785ch	VNIR pls-40sp-6fc- 169ch	Full spectrum pls-38sp-12fc- 883ch	Full spectrum pls-37sp-8fc- 948ch	VNIR pls-36sp-6fc- 540ch	VNIR pls-34sp-7fc- 297ch
CALIBRATION						
Number of selected spectra (samples)	40	40	38	37	36	34
Linear regression equation	$Y=0.70x+1.13$	$Y=0.68x+1.21$	$Y=0.88x+0.45$	$Y=0.84x+0.63$	$Y=0.82x+0.65$	$Y=0.76x+0.86$
R ²	0.64	0.62	0.81	0.77	0.80	0.74
RMSE	1.08	1.11	0.75	0.82	0.70	0.71
SEC	1.09	1.13	0.76	0.84	0.71	0.72
REP (%)	28.04	28.97	20.28	21.87	19.09	19.54
VALIDATION						
Number of selected spectra (samples)	17	17	17	17	17	17
Linear regression equation	$Y=0.84x+1.12$	$Y=1.18x+0.15$	$y=0.81x+1.22$	$Y=0.90x+0.87$	$Y=1.03+0.25$	$Y=0.92x+0.69$
R ²	0.35	0.68	0.27	0.41	0.71	0.68
RMSE	1.27	0.92	1.41	1.17	0.74	0.75
SEP	1.31	0.95	1.46	1.21	0.77	0.78
REP (%)	38.17	27.67	42.30	35.05	22.29	22.55

5.4.4. Discussion

The REP (%) and SEP were estimated as part of the independent validation test, in addition to the r^2 and RMSE, whose results are included in table 5.15. When standard error rates of calibration and prediction (SEC and SEP) are similar, no over-fitting problems are observed, but when they present great differences then there are problems of imprecision in the modeling. Such case of discrepancy is observed for models pls-40sp-8fc-785ch, pls-38sp-12fc-883ch, and pls-37sp-8fc-948ch, where their SEP is larger than the corresponding SEC (table 5.15). On the other hand models pls-36sp-6fc-540ch and pls-34sp-7fc-297ch have similar values, thus no over-fitting should occur.

Relative errors of prediction percentage (REP%) are lower for models using a smaller number of factors (6 or 7) for the construction of the model. In the validation test, the REPs are lowest for models pls-36sp-6fc-540ch, pls-34sp-7fc-297ch, and pls-40sp-6fc-169ch, being respectively 22.29%, 22.55%, and 28.97%. When using more factors

the REP increases considerably, e.g. model pls-38sp-12fc-883ch with a REP of 42.30% for its validation, where 12 factors are used for the calibration.

The three calibration models created using the VNIR have r^2 consistent with that observed for the validation results (table 5.15) but a net improvement in the RMSE is seen in the set 2 models where parameter and/or spectral residuals outliers were removed prior to the calibration of the models. The set 2 VNIR models (pls-36sp-6fc-540 and pls-34sp-7fc-297ch) displayed similar validation results. Between these two models, pls-36sp-6fc-540ch is kept for further applications since it represents a larger population of samples in the calibration process and gives slightly better calibration and validation results.

This analysis suggests that the best calibration model results from the VNIR spectral range while removing the first parameter outliers detected and removing the bands with lower FRC values.

5.5. Application of the model to Hymap imagery

5.5.1. Results

The pH predictive model pls-36sp-6fc-540ch was applied to the 62 band VNIR Hymap imagery. This required resampling of the 540 model bands to the Hymap band resolution for each year of acquisition.

The pH results predicted for the imagery were assessed with the validation set of 17 samples that were collected at sites discernable on the images and not used for the calibration of the model. This validation set is the same as the one used to validate the calibration model. Appendix 5.8 lists the actual and predicted pH for sampling areas of the August 2004 and June 2005 field campaigns visible in the Hymap imagery of the corresponding year. A scatterplot of the predicted pH is shown on figure 5.10a and the best fit regression displays an r^2 of 0.46 with an RMSE of 0.60. These results are poorer

than that obtained from the laboratory validation data set. The model was built using the ASD spectrometer resolution, which contains more bands than available from Hymap imagery. Thus, when applying the model to imagery, a loss of spectral bands of significant importance occurs and reduces the quality of the results. Consequently, a new model was built using the calibration dataset but starting at a resampled resolution that corresponds to the 62 VNIR bands of Hymap.

As done during the development of models using the complete spectral data of the laboratory samples, a model was built with all 40 samples of the calibration set and the first detected parameter residuals outliers were removed (samples 14, 31, 36, 39, and 40, respectively J05-47, J05-20, J05-06, J05-10, and J05-41). These parameter outliers are the same as the ones identified in the laboratory models, except for outlier 14, which was identified as a spectral outlier. Bands with lowest FRC values were then removed until the best r^2 and RMSE were obtained, which were respectively, 0.77 and 0.73 leaving 28 bands (model pls-35sp-7fc-28ch). The validation results of this model are given in appendix 5.9 and are plotted in figure 5.10b. Applying this model to the imagery gave poor results – an r^2 of 0.01 and an RMSE of 4.90 (figure 5.10b). that the use of 28 bands thus appears not to be sufficient to predict pH from imagery.

Another model was built retaining all 62 VNIR bands and only removing the first detected parameter outliers which are the same as the same five outliers of the previous model (model pls-35sp-7fc-62ch). The calibration's r^2 and RMSE are respectively, 0.73 and 0.80. The predicted pH values are shown in appendix 5.10 and in figure 5.10c. The results are not much better than the previous model, having an r^2 of 0.05 and an RMSE of 1.76.

A final attempt to calibrate a model was performed with the full Hymap spectral range of 126 bands covering the VNIR and SWIR and by removing only parameter outliers. The final model kept all 126 bands and had 4 parameter outliers removed (21, 33, 38, and 39, respectively samples J05-21, A04-44, J05-52, and J05-10). The calibration results of this model (pls-36sp-8fc-126ch) gave an r^2 of 0.71 and RMSE of

0.83. The validation presents much improved results with an r^2 of 0.71 and RMSE of 0.77. The predicted pH values of this model are given in appendix 5.11 and plotted in figure 5.10d.

In summary, when fewer bands are available for modeling airborne imagery than available to model field or laboratory ASD data, it is best to keep all bands for the calibration of the pH model. A summary of the validation results is given in table 5.16.

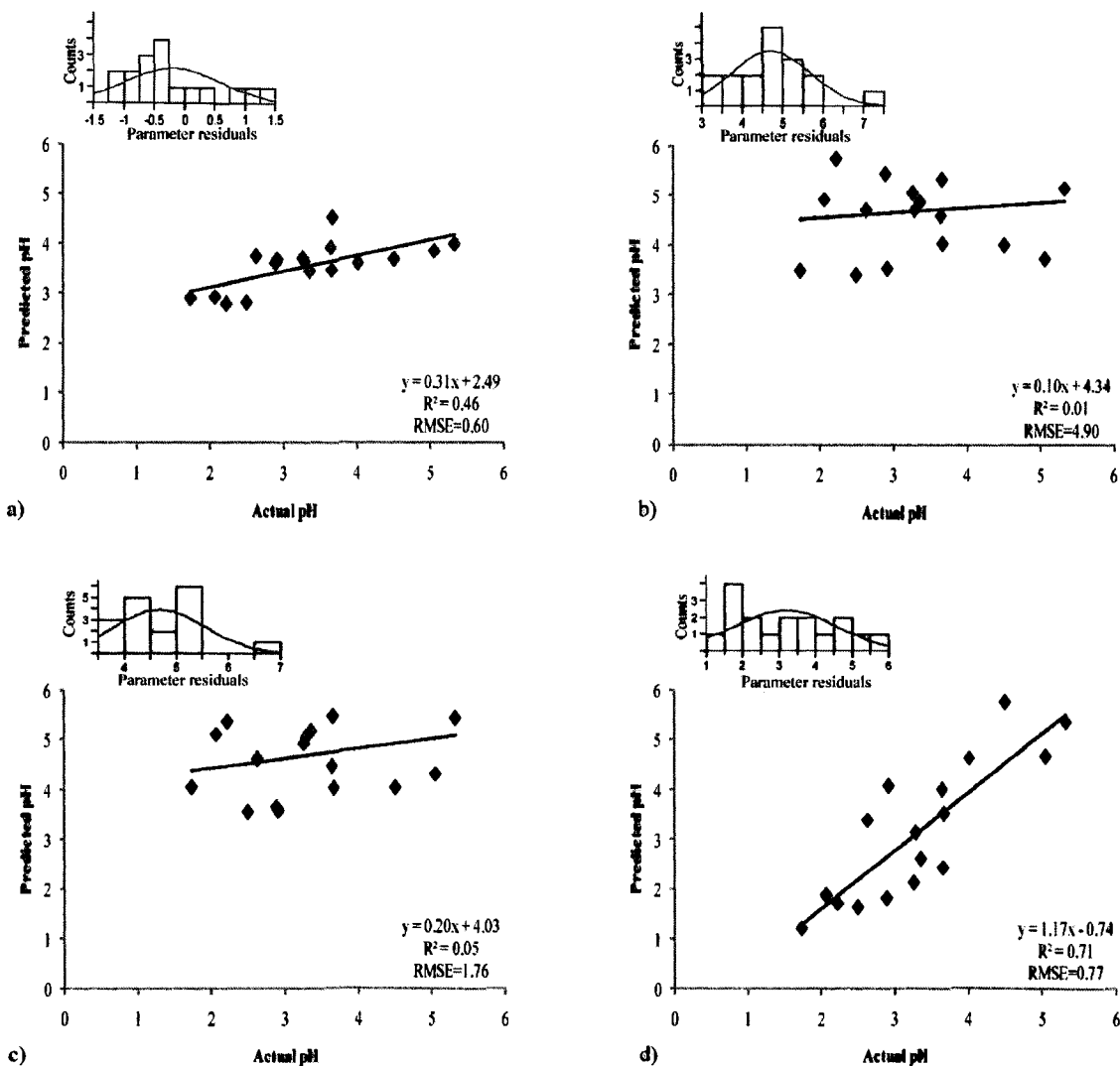


Figure 5.10: Results of the predicted pH versus actual pH when applying the models to the Hymap imagery of August 2004 and June 2005: a) pls-36sp-6fc-540ch; b) pls-35sp-7fc-28ch; c) pls-35sp-7fc-62ch; and d) pls-36ch-8fc-126ch. The red curve represents the Normal Fit Distribution of the data.

Table 5.16: Summary of the calibration and validation results of models applied to the Hymap imagery.

		Pls-36sp-6fc-540ch	Pls-35sp-7fc-28ch	Pls-35sp-7fc-62sp	Pls-36sp-8fc-126ch
	Spectral resolution and region	ASD resolution VNIR	Hymap resolution VNIR	Hymap resolution VNIR	Hymap resolution Full spectrum
CALIBRATION	Bands with low FRC values removed	Yes	Yes	No	No
	Parameter outliers removed	Yes	Yes	Yes	Yes
	R²	0.80	0.77	0.73	0.71
	RMSE	0.70	0.73	0.80	0.83
VALIDATION	R²	0.46	0.01	0.05	0.71
	RMSE	0.60	4.90	1.76	0.77

5.5.2. Predictive pH maps

Predictive pH maps obtained by applying model pls-36sp-8fc-126ch to Hymap imagery are shown in figures 5.11 to 5.16 for image subsets containing the mine tailings and areas affected by mine waste. The pH predictive maps show values ranging from 1.0 to 7.9 since values greater than 8 were not included in the calibration of the predictive pH model.

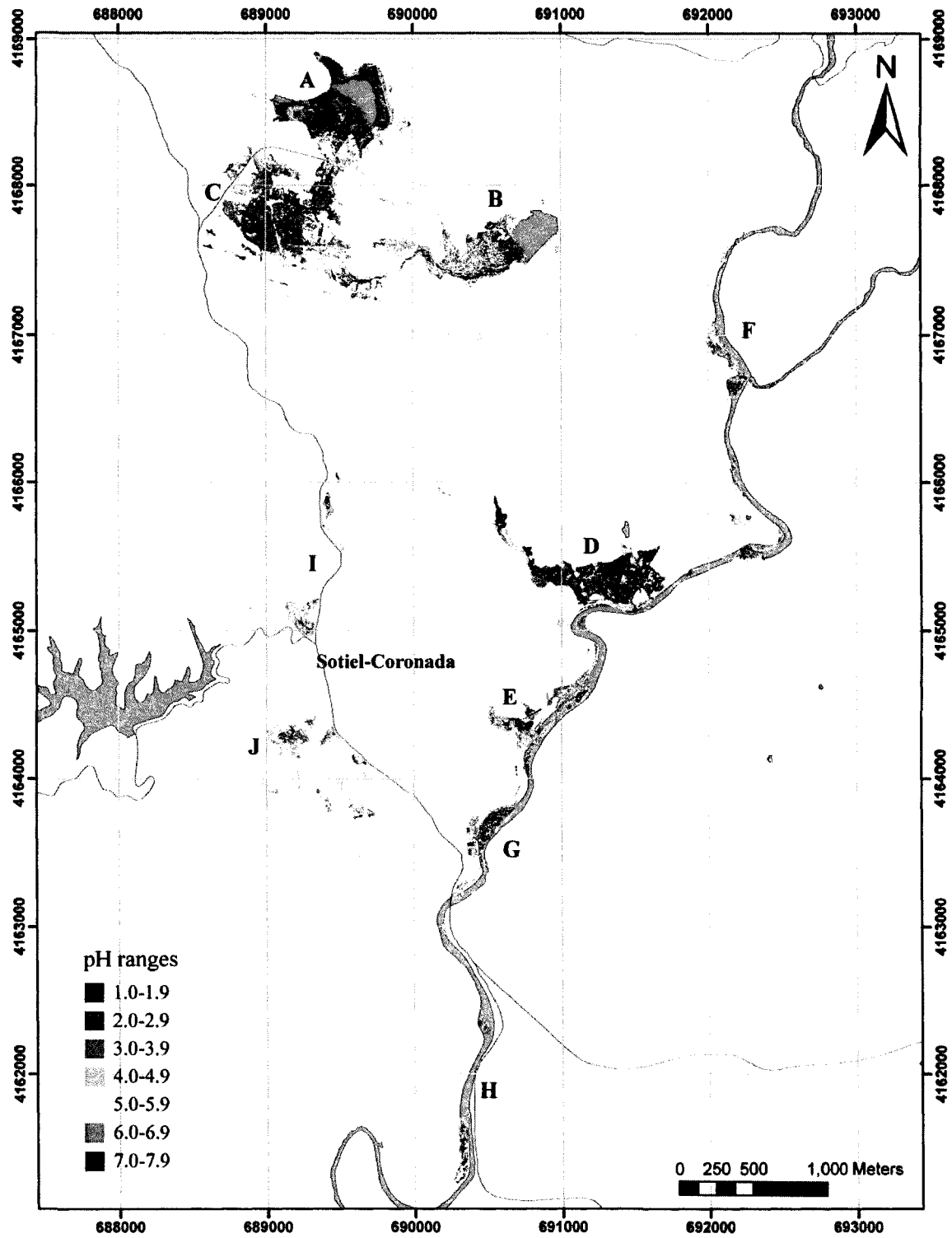


Figure 5.11: Overview of the pH predictive maps for the mine waste sites.

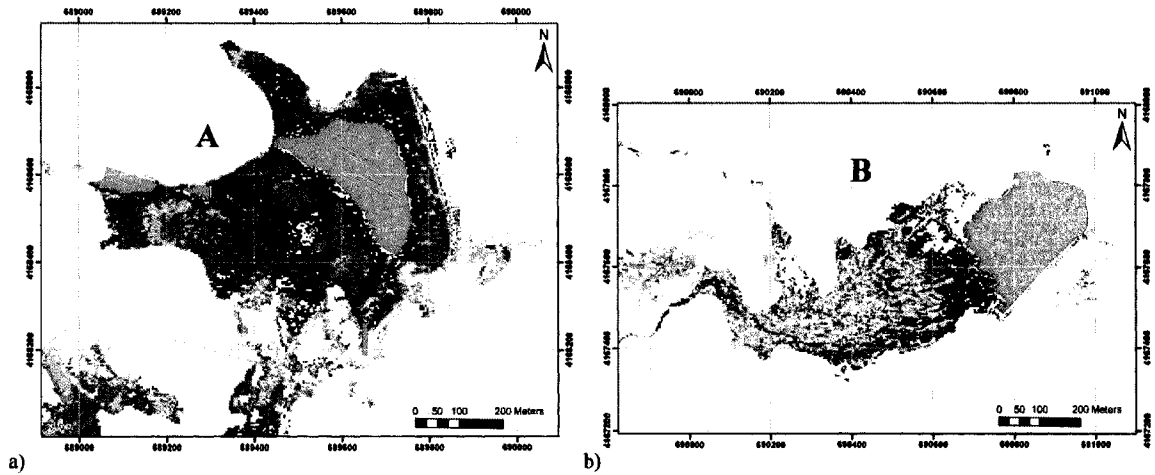


Figure 5.12: pH predictive map of tailings ponds: a) tailings pond northeast of the processing plant; b) tailings pond east of the processing plant. Colour table shown on figure 5.11.

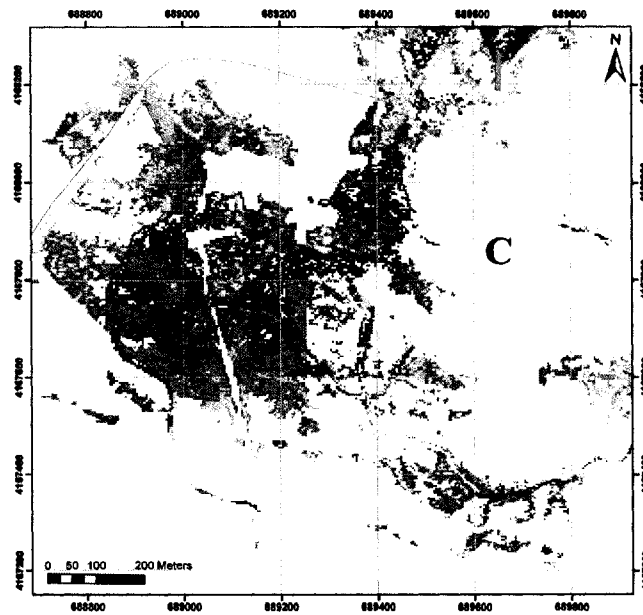


Figure 5.13: pH predictive map for the mine waste surrounding the processing plant. Colour table shown in figure 5.11.

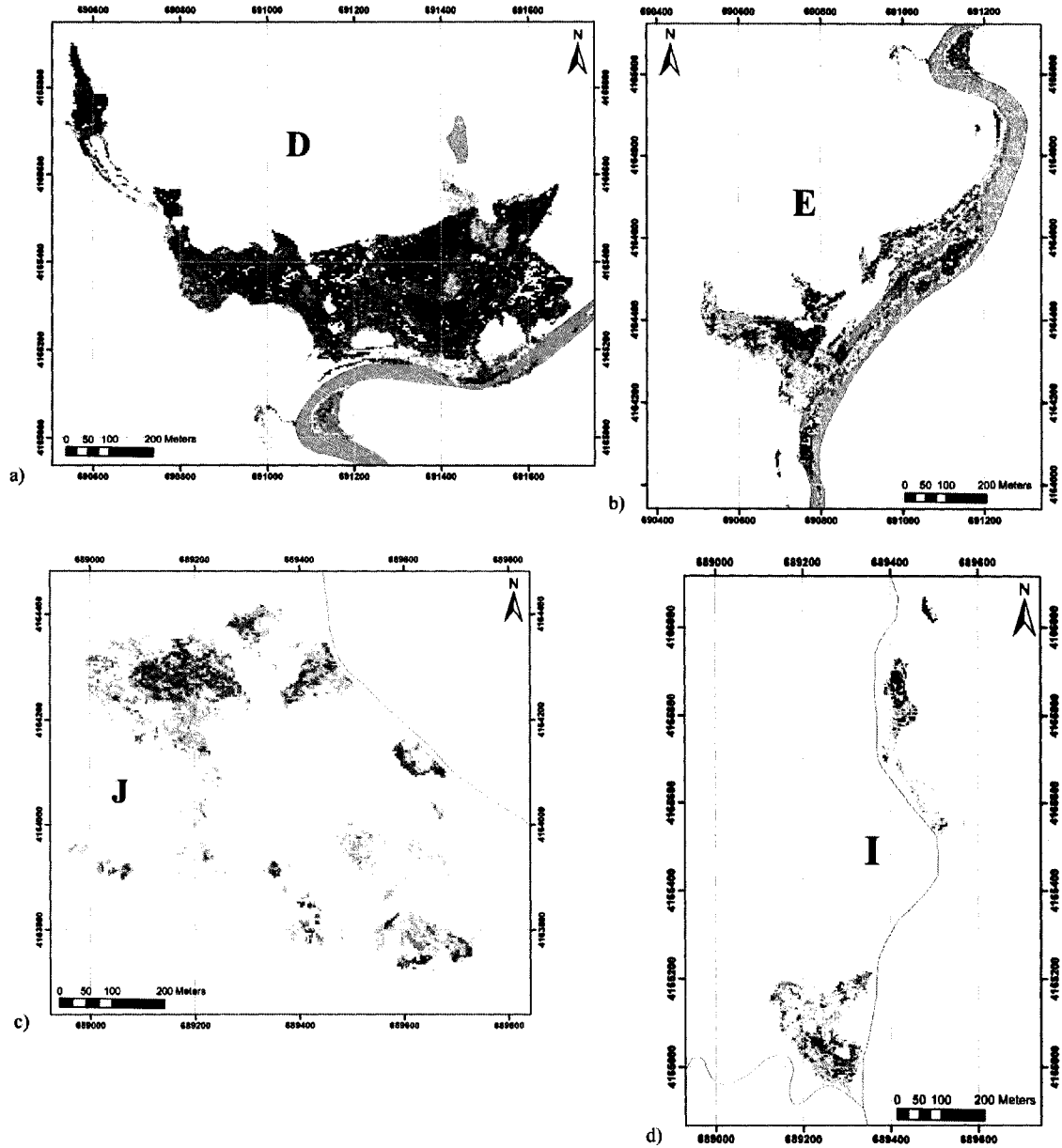


Figure 5.14: pH predictive maps of distal waste rock tailings: a) main mine waste tailings located southeast of the processing plant; b) mine waste tailings along the Odiel River, south of the main tailings; c) mine waste in Sotiel-Coronada; and d) mine waste at the Almagra S.A. Mines' Treatment Plant. Colour table shown in figure 5.11.

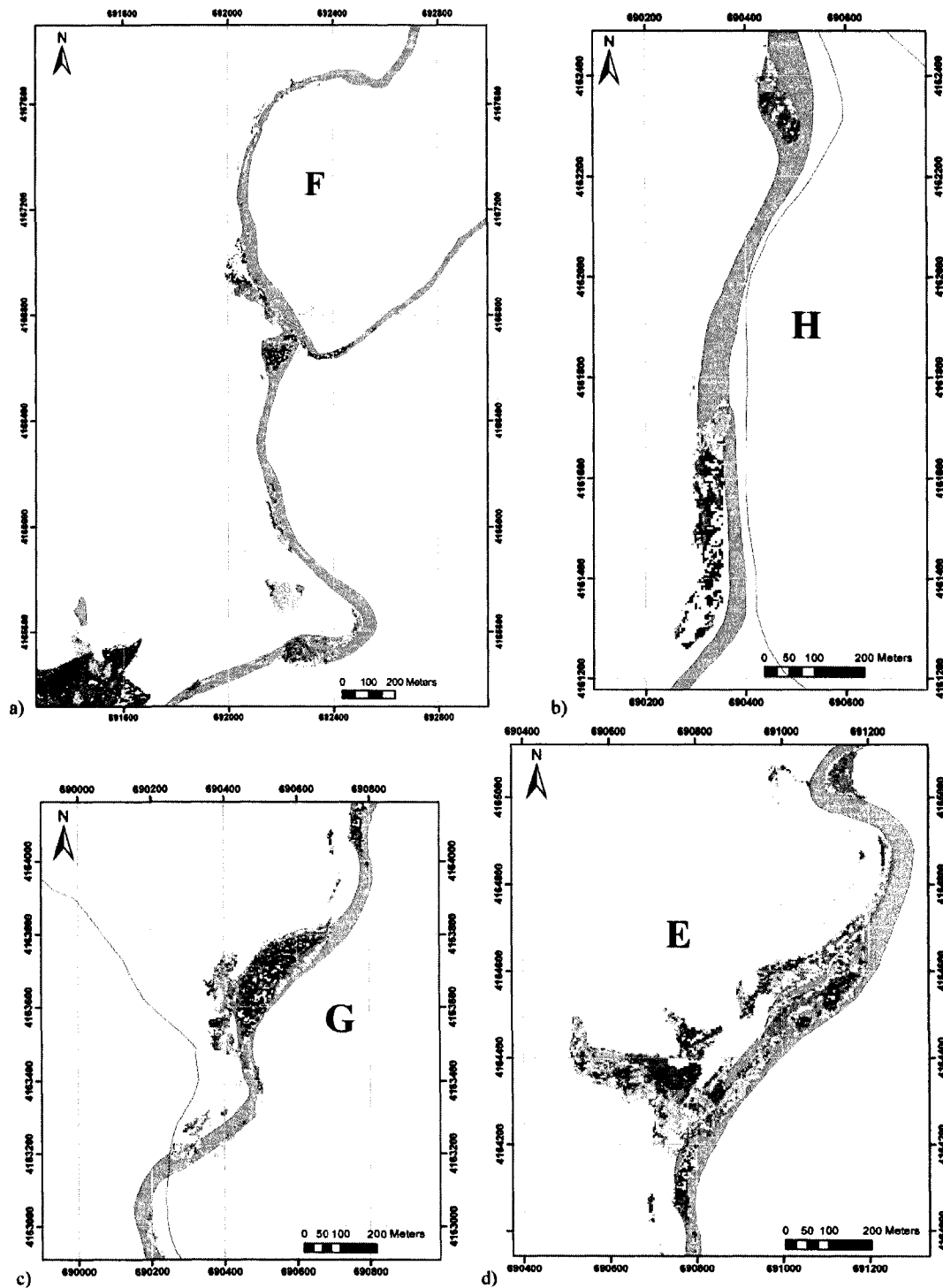


Figure 5.15: pH predictive maps of mine waste along the Odiel River: a) bed plains northeast of Sotiel-Coronada; b) bed plains south of Sotiel-Coronada; c) bed plains at Sotiel-Coronada; d) bed plains near the small waste-rock tailings by the Odiel River. Colour table shown in figure 5.11.

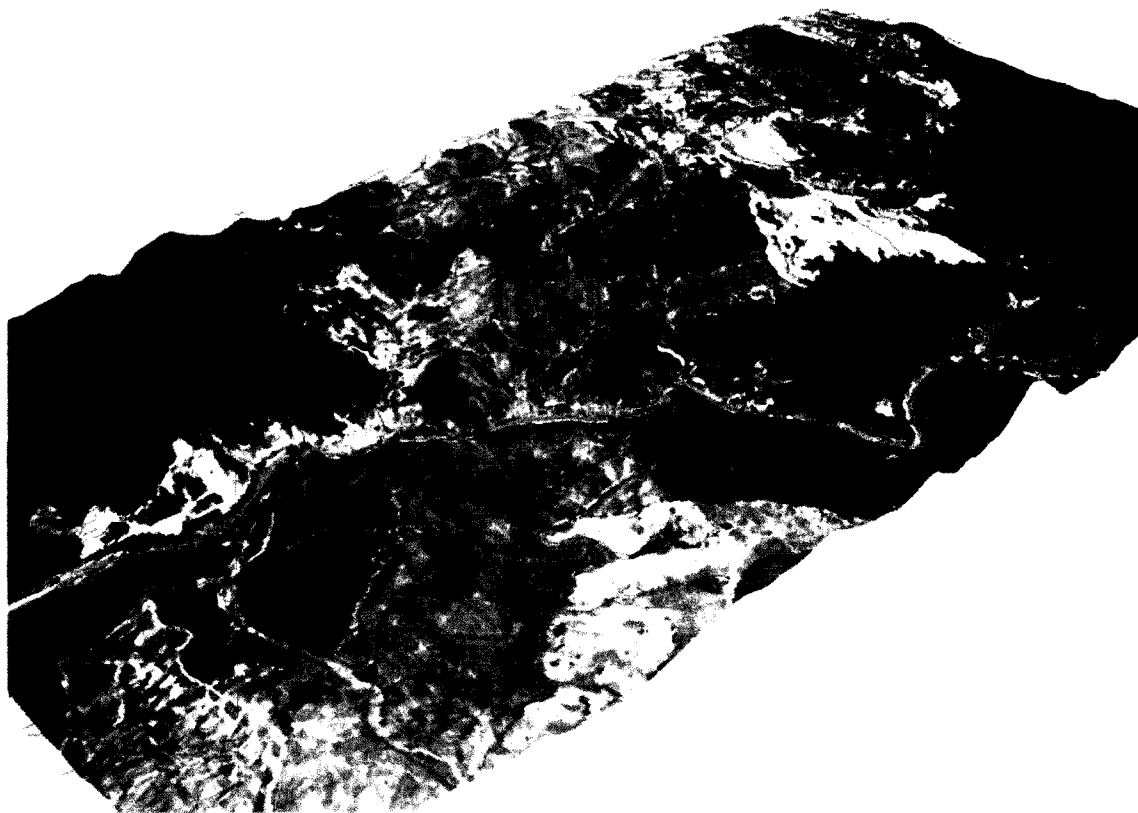


Figure 5.16: pH predictive maps of mine waste sites shown on figure 5.13 and draped over a digital elevation model. Backdrop image mosaic of Hymap strips 4, 5, and 6 (RGB bands, respectively 0.6335 μm , 0.5568 μm , and 0.4644 μm ; shown in black and white (stretch 0-255). Maximum relief, vertical exaggeration of 1.5. Colour table shown in figure 5.11.

5.5.3. Discussion and links with the mineral maps

A first glimpse at the predictive pH map (figure 5.11) for the tailings of the Sotiel-Migollas mine complex reveals very low pH values, especially in the tailing ponds northwest of the processing plant (A), at the tailings of the processing plant (C) and at the main waste rock tailings near the Odiel River (D). The tailing ponds near the processing plant (A) (figure 5.13a) are mainly composed of hematite, as seen from the mineral maps of chapter 4 (figure 4.3a), which can form in a wide range of pH. For areas where schwertmannite-jarosite (EM22) dominate on these pond tailings (figure 4.3a), the pH values are higher (e.g. 4.0-7.9), such as on the ridge of the wall of the dam and in a patch on the southeast of the tailings. In theory, schwertmannite should develop in a pH range between 3 and 4, whereas jarosite precipitates in very acidic conditions at a pH of 1.5 to 3. Thus, areas covered by endmember 22, schwertmannite-jarosite in this particular area,

have pH values that are overestimated. However, the other patch of schwertmannite-jarosite (south part of the tailings – figure 4.4a) has predicted values ranging from 2 to 5 and thus more consistent with expected values. The area dominated by halotrichite (figure 4.3a) for the same pond tailings (A) spans a pH range of 1-2. Halotrichite forms under very low pH conditions. According to Nordstrom et al. (1999), halotrichite can even form in negative-pH mine waters. Surrounding these pond tailings are patches dominated by goethite with a predicted pH of 4-5 . The pH level for the formation of goethite are theoretically lower than 6 (Bigam, 1994). Thus areas mapped as mixtures dominated by goethite appear to have well predicted pH levels.

The southeast pond tailings (B) (figure 5.13b) show finer spatial detail of pH patterns than seen on the mineral maps. These tailings are mainly dominated by rozenite, according to the classification, another efflorescent salt that forms under very low pH conditions. However the pond tailings show a large range of pH, from 1 to 8 where rozenite was mapped, suggesting that minerals with higher pH levels were not captured on the mineral maps, perhaps because their spectral features were masked by the dominance of rozenite. These tailings were not examined in the field due to their poor accessibility; thus the mineral and pH mapping of these tailings could not be validated. Where copiapite dominant endmembers 18 and 19 were mapped, the pH maps do not show predictions because the predicted values were beyond the 1.0 to 7.9 pH range of the model. Also, copiapite was not included in the calibration of the model. In order to improve the model, samples of copiapite are needed to complete the predictive model. From the same pond tailings, the patch mapped as endmember 22 (schwertmannite and jarosite mixture) corresponds to predicted pH values between 1 and 3, again in the expected pH range as mentioned in the previous paragraph.

At the processing plant (C), the pH values are very low. This site is mainly dominated by efflorescent salts that precipitate at very low pH levels and these minerals were mapped with predicted low values of pH. Areas that are composed of schwertmannite-jarosite or goethite-schwertmannite mixtures show predicted pH values of 3 and 4 which correspond to the expected pH range for these minerals.

The predicted pH values of the main waste-rock tailings (figure 5.14a) are very low, in the range of 1-4. Areas where the levels are slightly higher (e.g. pH=3-5) are patches that were dominated by goethite in accordance with expected pH levels. Hematite is predicted at pH levels of 1 and 2, as was seen in the hematite ponds tailings. The hematite dominant patch from the waste-rock tailings of figure 4.5b also has predicted pH levels of 1 and 2 (figure 5.14b). The pH conditions at which hematite precipitates can cover, in theory, a wide range of pH. In this study, the leachate pH measured in laboratory from samples containing mainly hematite gave low pH values, ranging from 1.4 to 3.0 (table 5.4). Precise values of pH at which hematite precipitates was not found in the literature. Thus, hematite patches can be considered as correctly predicted in regards to the leachate pH measured in the laboratory as opposed to the larger range of pH values over which hematite may precipitate in theory.

The waste-rock tailings presented in figures 5.14c and 5.14d show pH levels between 4 and 6. These areas were mapped as goethite rich sediments, again showing that the pH for areas of goethite is well predicted. In the lower elevations of tailings from figure 5.14c, many efflorescent salts were identified in the mineral maps and the corresponding pH values range from 1-4 again presenting a good pH prediction. However, efflorescent salts were not included in the calibration of the model. Thus the predicted pH obtained for these minerals are not reliable. Further improvement to the model would include these efflorescent salts.

Along the Odiel River the pH values are mainly in the neutral ranges of 5 to 8. These river beds were mapped mainly as goethite and schwertmannite with theoretical pH values ranging from 2.5 to 7.5 for goethite and 3-4 for schwertmannite. Tailings in the river bed with lower pH levels were mapped as goethite. Areas that presented a pH of 5.0 to 7.9 consist mainly of rocks with a thick coating of goethite. These surfaces are not exposed to the acidic waters of the river since they are above the river water level. Their thick coating of goethite likely remains stable at near neutral pHs.

Overall, the pH maps tend to give good pH predictions, especially for sediments dominated by goethite and schwertmannite-jarosite. The areas covered by hematite present very low predicted pH.

Few studies have tried to relate surface pH to mineralogy identified from imaging spectroscopy. Swayze et al. (2000) related a few minerals to laboratory leachate pH measurements (c.f. section 1.4.1). In the present study, the pH maps provided a larger set of minerals than that of Swayze et al. (2000). Ong et al. (2003) also used PLS analysis to predict pH from spectral measurements. However, limited data was available to validate their model and its applicability to Hymap imagery (as pointed out in section 1.4.1.). This study has a more robust methodology in that the sample data were statistically evaluated and the samples suites were balanced to have a calibration and a validation dataset that represented a normal distribution of the population. This aspect makes the model more reliable. Also, the model was validated with an independent suite of samples.

Improvements in the model could be examined by increasing the number of samples for both the calibration and the validation dataset, while encompassing all AMD related minerals including efflorescent salts, and all expected pH ranges. Further investigation could be performed with mid infrared (7-12 μ m) spectral data for the same samples to evaluate whether this spectral range can improve the quality of the prediction.

5.6. Comparison of the Brukunga and Sotiel-Migollas models

The site specific model for the Sotiel-Migollas mine complex provides the means for a comparison of results with that of the Brukunga predictive model.

Figure 5.17 gives the FRC values for models of Brukunga, at Hymap resolution, and Sotiel-Migollas, made from laboratory ASD spectral resolution, both showing the VNIR region. The models show high FRC values in several common spectral regions for the two models, but there are also discrepancies. The most significant spectral regions for the two models are presented in table 5.17. The common significant spectral regions

include: 0.44-0.51, 0.53-0.62, 0.70-0.86, 1.13-1.32, 2.01-2.19, 2.24-2.29, 2.29-2.41, and 2.45-2.48 μm . These spectral regions of high FRCs correlated with spectral features of the secondary iron bearing minerals of the study site (table 5.17).

Regions with high FRC values that are not common between both models include 0.50 μm , 0.63 μm , 0.68-0.73 μm , and 0.95-1.00 μm for Sotiel-Migollas, and 1.0-1.1 μm , 1.17-1.32 μm for Brukunga. As mentioned previously in table 5.3, the Brukunga model was calibrated principally with jarosite, schwertmannite, and goethite minerals, in addition to some soil spectra and one spectrum of pyrite and halotrichite. In contrast the Sotiel-Migollas model was calibrated with a majority of samples of hematite, goethite, and schwertmannite, and a few spectra of jarosite and ferrihydrite. Thus, the presence of higher FRC values at 0.50 μm for Sotiel-Migollas can be associated to the Fe^{3+} absorption feature from of hematite. The 0.63 μm feature is related to the shoulder position for ferrihydrite which is only found in the Sotiel-Migollas set. The higher FRC absolute values between 0.68 and 0.73 μm can be associated to the VIS peak reflectance of jarosite, but is not a unique observation since jarosite is present in both sets. The 0.95-1.00 μm region is attributed to the Fe^{3+} absorption band of schwertmannite, goethite, and ferrihydrite. This may explain the higher FRC values in the Sotiel-Migollas set because ferrihydrite is not found in the Brukunga set. Finally, the 1.17-1.32 μm region of higher FRC for Brukunga can be associated to the presence of halotrichite, which has an absorption feature at 1.18 μm related to Fe^{2+} .

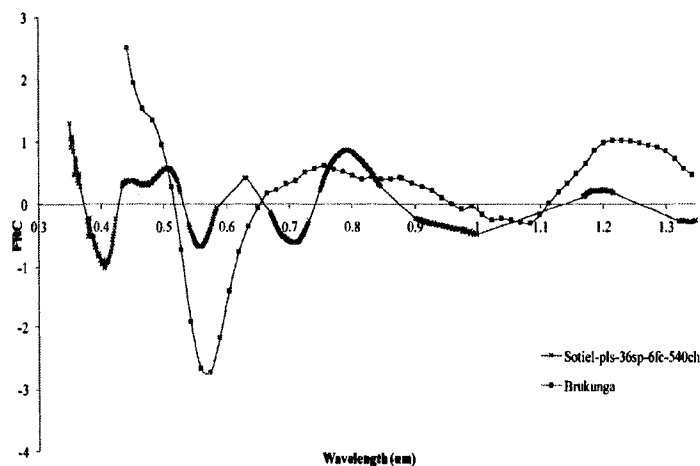


Figure 5.17: FRC for Brukunga model (resampled to Hymap resolution) and Sotiel-Migollas model using the ASD spectral resolution (Sotiel-pls-36sp-6fc-540ch).

Table 5.17: Spectral regions of high FRC values for Brukunga and Sotiel-Migollas models with a description of spectral features related to wavelength positions.

Brukung high FRC regions (µm)	Sotiel-Migollas ASD lab spectra model high FRC regions	Description of spectral features at wavelength positions
0.44-0.51	0.45	Absorption bands for Fe ³⁺ bearing sulphates – schwertmannite, goethite, and ferrihydrite
	0.50	Shoulder band position associated to Fe ³⁺ for schwertmannite and jarosite:
0.53-0.62	0.54-0.57	Absorption bands for Fe ³⁺ bearing sulphates – Goethite, ferrihydrite, and schwertmannite (0.60µm)
	0.63	Fe ³⁺ reflection shoulder of ferrihydrite
	0.68-0.73	VIS peak reflectance of jarosite (0.72µm)
0.70-0.80	0.76-0.83	VIS peak reflectance – ferrihydrite, hematite, goethite, and schwertmannite
	0.95-1.00	Absorption bands for Fe ³⁺ bearing sulphates – schwertmannite, goethite, and ferrihydrite
1.0-1.1		-
1.17-1.32		Absorption bands for Fe ²⁺ - Halotrichite (1.18µm)
	1.33-1.35	OH stretching overtones of copiapite and ferrihydrite

5.7. Summary

The main goal of the study was to verify the applicability of a predictive pH model built from an independent site. As demonstrated in this research, the model built from the Brukunga samples was not transferable to the Sotiel-Migollas mine site. The only explanation obtained in this regard was the disparity in mineralogy between both sites. In further investigations, it would be interesting to combine dataset from both sites to calibrate a new predictive pH model and test it on an independent site with a common mineralogy to see if any improvement may occur, since a greater dataset would be available with a greater diversity of minerals as well. But from this study one can only conclude that each site requires a site-specific pH predictive model.

This research also demonstrated the feasibility of non-invasively predicting pH by using a model built with partial least squares analysis. It was shown that the VNIR spectral region produced the best calibration and validation results then the overall VNIR and SWIR regions when using the complete laboratory ASD spectral data. The best

model produced during calibration had parameter residual outliers removed from the calibration set reducing the number of samples from 40 to 36. The optimal number of factor used for the calibration was 6 and was determined during the cross-validation procedure and corresponded to the lowest PRESS value. The total number of bands kept for the calibration was 540 out of the 1000 initial bands in the VNIR spectral range. The number of bands chosen was based on the higher FRC values when increasing the minimum threshold of FRC between each calibration test. Thus the calibration model pls-36sp-6fc-540ch presented the best r^2 and RMSE for the calibration and for the validation of the model on an independent dataset. For the calibration the r^2 was 0.80 with an RMSE of 0.70 and for the validation the r^2 was 0.71 with an RMSE of 0.74. To apply the model to the hyperspectral imagery (Hymap) a new model was built using the spectral resolution of the 126 bands of Hymap. It was found that when building a model with fewer bands (e.g 126 as opposed to 1000) better results were obtained without removing spectral bands.

Overall, the predicted pHs obtained from applying the model to the Hymap imagery gave results that are consistent with the expected pH ranges for each mineral. Also, the validation of this application gave an R^2 of 0.71 with an RMSE of 0.77 when comparing the predicted pH to their corresponding laboratory pH.

A key consideration for the creation of site-specific pH predictive models is to collect a large calibration set to cover the diversity of the mineralogy of the tailings. Even with the calibration and validation sample size of this study, it was possible to demonstrate the ability to predict pH values from the spectroscopy of iron bearing minerals derived from pyrite oxidation in mine tailings, but a more accurate model would likely result with a larger set of samples. It is important to carefully sample all the important minerals required in the pH maps. This aspect was partly deficient in this research. However, with the dataset collected, the predicted pH maps generally appear to have good accuracy. The most important consideration in the calibration of the pH model is to ensure that the pH measurements obtained in the laboratory are accurate and that the pHs from the samples correspond well to the theoretical pH ranges for each minerals.

There may be possible improvements in the methodology of the pH measurements conducted in the laboratory. In this study, the methodology used for the Brukunga model was followed for consistency since the objective was to examine the applicability of the Brukunga model to the Sotiel-Migollas site.

6. CONCLUSION

This thesis investigated the potential of high spatial-resolution hyperspectral Hymap data for detailed mine-tailing characterization and AMD detection through mineral maps and predicted pH maps of the Sotiel-Migollas mine complex. The intent was to develop tools to rapidly characterize the spatial distribution of the acid generating material and oxidizing tailings, which are likely associated with low pH values and high concentrations of heavy metals. Locating these acid generating areas play a key role in monitoring and remediation of mine tailings. With Spain being part of the European Union it now faces strict legislations and challenges to monitor the numerous abandon mine waste sites, and thus has great needs to use tools which could quickly characterize the sites. Providing predicted pH maps in addition to mineral maps can greatly help improve the characterization of the tailings in a rapid and cost-effective manner.

This work showed that hyperspectral remote sensing is an effective means of quantitatively and qualitatively pinpointing the sources of acidity. The mineral maps gave good classification maps which are consistent with field observation and sampling. They were produced using the iterative linear spectral unmixing analysis (ISMA). These maps provided a qualitative spatial distribution of the mineralogy affecting the environment, where spatial patterns have been observed and were found similar to other studies. Significant improvement in the details of the mapping was realized using the ISMA procedure over the Hourglass mapping method. In addition, the SSEE algorithm presented a faster and non-subjective method for endmember extraction as oppose to the Hourglass method. However, challenges remain in the labelling of mineral spectra due to the intimate mixtures.

The pH predictive model was created using field samples of the tailings, spectroscopy and partial least squares analysis. This research has shown that imaging spectroscopy data offers the ability to predict pH giving a full spatial distribution of pH values for mine waste tailings. In this work, it was determined that a pH predictive spectral model developed at an unrelated mine site could not be properly transferred to an

independent pyrite mine and led to the creation of a site-specific model for this study site. The application of the new model presented a positive significant correlation between the actual and predicted pHs. Future work can be pursued in regards to improving the predictive modeling of pH values, such as increasing the diversity of mineralogy and pH ranges found at the study site and include the efflorescent salts in the calibration of the model. Also, a new model could be created by merging both the Brukunga and Sotiel-Migollas datasets. This would give a representation of minerals found at different sites and possibly improve the transferability of the model to a new site.

Both types of maps have their own merits. The mineral maps provide a direct recognition of the variety of secondary minerals present in the tailings. The mineralogy context serves as indicator of the metal, sulphate, and pH levels of the AMD solution at the time the mineral precipitated. The mineral maps also provide important information on future development of minerals on the site when local conditions vary, e.g. temperature, humidity, heavy rainfalls, etc. Knowing the mineralogy present at the site, it may be possible to predict the consequential effects of the climate and weather variations on the development of subsequent minerals. For example, areas enriched in efflorescent salts may leach out waters with very high concentrations of heavy metals, higher content of SO_4^{2-} , higher acidity, thus the chemical reactions can be anticipated. It can determine what type of heavy metals may be released when dissolved during storms due to their high solubility. For instance, pickeringite ($\text{MgAl}_2(\text{SO}_4)_4 \cdot 22\text{H}_2\text{O}$) could release Mg and Al, and halotrichite ($\text{FeAl}_2(\text{SO}_4)_4 \cdot 22\text{H}_2\text{O}$) could release Al in the leachate. Also, the efflorescent salts can give an insight on details on the state of pyrite oxidation, i.e., hydrated or dehydrated conditions of the tailings. For example, melanterite is a heptahydrated ferrous sulphate that when exposed to air, may alter to a fine white powder composed mainly of rozenite and szomolnokite, indicating dehydration as melanterite loses hydration. The pH for these minerals may be the same, but pH maps will not show the hydrated state of the tailings.

The pH maps offer information on the pH conditions of the tailings thus giving an insight on the different types of oxidation reactions that may occur, e.g., in low pH

environments oxidation is often led by micro-organisms since the rate of ferrous iron oxidation is reduced in low pH conditions. Also, having pH maps can help direct the remediation efforts when wanting to neutralize the areas of lower pH. It may be useful to know the precise pH to evaluate the quantities and concentrations of neutralizing products needed to stabilize the soils and water pH. When only mineral maps are provided, the predicted pH values are estimated within a wide range of pH, e.g. goethite precipitates at pHs lower than 6 and hematite can precipitate over a wide range of pH. But when providing pH maps, then the predicted pH values are precise.

With the complexity of mine waste assessment and remediation processes, it is important to acquire the most information on the sites in order to evaluate the acidic conditions. Thus, providing both the mineral maps and the pH maps offers the ability to properly understand the chemistry of the disposal environment. With the information provided by the pH and mineral maps, one can estimate the geochemical consequences of various remediation scenarios for mine waste site with greater confidence. With the knowledge, quantitatively predicting pH values using spectroscopy data and PLS analysis, future investigations could be made in regards to predicting other physico-chemical properties of mine waste tailings, such as concentrations of heavy metals and sulphate, electric conductivity, etc. This information is of crucial importance in developing successful sulphide waste rock management. Predictive tests are the preferred choice in the characterization of the waste from an environmental and an economical standpoint.

7. BIBLIOGRAPHY

- Almodovar, G.R. et al., 1998. Geology and genesis of the Aznalcollar massive sulphide deposits, Iberian pyrite belt, Spain; Iberian Pyrite Belt thematic issue. *Mineralium Deposita*, 33(1-2): 111-136.
- Alpers, C.N., Blowes, D.W., Nordstrom, D.K. and Jambor, J.L., 1994. Secondary minerals and acid mine-water chemistry; Short course handbook on Environmental geochemistry of sulfide mine-wastes. Environmental geochemistry of sulfide mine-wastes, Waterloo, ON, Canada, May 1994, 22: 247-270.
- Analytical Spectral Devices, Inc., 2000. FieldSpec Pro® User's Guide, Boulder, CO
- Arnesen, R.-T., 1993. Water pollution from sulphide ore mines with discharge to freshwater (in Norwegian). O-67084/O-92204, Norsk Institutt for Vannforskning (NIVA), Oslo, Norway.
- Aye, F. and Picot, P., 1976. Sur les minéraux d'étain dans les amas sulfures massifs; découvertes récentes, inventaire, géologie. Tin minerals in massive sulfide ore bodies; recent discoveries, inventory, economic geology. *Comptes Rendus Hebdomadaires des Séances de l'Académie des Sciences, Série D: Sciences Naturelles*, 282(22): 1909-1912.
- Bachmann, M., 2007. Automated MESMA unmixing for fractional cover estimates. PhD. Dissertation Thesis, University of Würzburg, Würzburg, Germany.
- Bajwa, S.G. and Tian, L.F., 2005. Soil fertility characterization in agricultural fields using hyperspectral remote sensing. *Transactions of the ASAE*, 48(6): 2399-2406.
- Banks, D., Younger, P.L., Arnesen, R.-T., Iversen, E.R. and Banks, S.B., 1997. Mine-water chemistry; the good, the bad and the ugly. *Environmental Geology (Berlin)*, 32(3): 157-174.
- Barriga, F.J.A.S., Carvalho, D. and Ribeiro, A., 1997. Introduction to the Iberian Pyrite Belt. In: F.J.A.S. Barriga and D. Carvalho (Editors), SEG Neves Corvo Field Conference 1997, Guidebook Series Volume 27, pp. 20.
- Belzile, N., Chen, Y.-W., Cai, M.-F. and Li, Y., 2004. A review on pyrrhotite oxidation. *Journal of Geochemical Exploration*, 84(2): 65-76.
- Berk, A., Bernstein, L.S., Anderson, G.P., Acharya, P.K., Robertson, D.C., Chetwynd, J.H., Adler-Golden, S.M., 1998. MODTRAN cloud and multiple scattering upgrades with application to AVIRIS. *Remote Sensing of Environment*, 65: 367-375.
- Bigham, J.M., 1994. Mineralogy of ochre deposits formed by sulfide oxidation. In: J.L.J.a.D.W. Blowes (Editor), Environmental Geochemistry of Sulfide Mine-Wastes, Short Course Handbook. Mineral Association of Canada, pp. 103-132.

- Bigham, J.M., Schwertmann, U. and Pfab, G., 1996a. Influence of pH on mineral speciation in a bioreactor simulating acid mine drainage. *Applied Geochemistry*, 11: 845-849.
- Bigham, J.M., Schwertmann, U., Traina, S.J., Winland, R.L. and Wolf, M., 1996b. Schwertmannite and the chemical modeling of iron in acid sulfate waters. *Geochimica et Cosmochimica Acta*, 60(12): 2111-2121.
- Bishop, J.L. and Murad, E., 1996. Schwertmannite on Mars? Spectroscopic analyses of schwertmannite, its relationship to other ferric minerals, and its possible presence in the surface material on Mars. In: M.D. Dyar, McCammon, C. and Schaefer, M.W. (Editor), *Mineral Spectroscopy: A Tribute to Roger G. Burns* (Special Publication, No. 5). The Geochemical Society, Houston, TX, pp. 337-358.
- Blanco Freijero, A. and Rothenberg, B., 1981. *Exploración arqueometalúrgica de Huelva*, Barcelona, 312 pp.
- Boulter, C.A., 1993. Comparison of Rio Tinto, Spain, and Guaymas Basin, Gulf of California; an explanation of a supergiant massive sulfide deposit in an ancient sill-sediment complex. *Geology* (Boulder), 21(9): 801-804.
- Braungardt, C.B., Achterberg, E.P., Elbaz-Poulichet, F. and Morley, N.H., 2003. Metal geochemistry in a mine-polluted estuarine system in Spain. *Applied Geochemistry*, 18(11): 1757-1771.
- Briard, J., 1976. *L'age de bronze en Europe Barbare*. Hesperides Publications, Paris, pp. 81-86.
- Carvalho, D., Barriga, F.J.A.S. and Munha, J., 1999. Bimodal siliciclastic systems-the case of the Iberian Pyrite Belt. In: C.T. Barrie and M.D. Hannington (Editors), *Volcanic-associated Massive Sulfide Deposits: Processes and Examples in Modern and Ancient Settings: Reviews in Economic Geology*, SEG, Vol. 8, p. 375-408.
- Che, N., Price, J.C., 1992. Survey of radiometric calibration results and methods for visible and near infrared channels of NOAA-7, -9, and -11 AVHRRs. *Remote Sensing of Environment*, 41(1): 19-27.
- Clark, R.N. and Roush, T.L., 1984. Reflectance Spectroscopy: Quantitative Analysis Techniques for Remote Sensing Applications. *Journal of Geophysical Research*, 89: 6329-6340.
- Clark, R.N. and Swayze, G.A., 1995. Mapping minerals, amorphous materials, environmental materials, vegetation, water, ice, and snow, and other materials: The USGS Tricorder Algorithm, Summaries of the Fifth Annual JPL Airborne Earth Science Workshop, JPL Publication 95-1, p. 39-40.

- Clark, R.N. et al., 2003. Imaging spectroscopy - Earth and planetary remote sensing with the USGS Tetracorder and expert systems. *Journal of Geophysical Research*, 108, E12, 5131, doi: 10.1029/2002JE001847.
- Clark, R.N., 1999. Chapter 1: Spectroscopy of Rocks and Minerals, and Principles of Spectroscopy. In: A.N. Rencz (Editor), *Manual of Remote Sensing, Volume 3, Remote Sensing for the Earth Sciences*. John Wiley and Sons, New York, pp. 3-58
- Clark, R.N., Swayze, G.A. and Gallagher, A.J., 1992. Mapping the mineralogy and lithology of Canyonlands, Utah with imaging spectrometer data and multiple spectral feature mapping algorithm, *Summaries of the Third Annual JPL Airborne Geoscience Workshop, JPL Publication 92-14*, p. 11-13.
- Clark, R.N., Gallagher, A.J. and Swayze, G.A., 1990. Material absorption band depth mapping of imaging spectrometer data using the complete band shape least-squares algorithm simultaneously fit to multiple spectral features from multiple materials, *Proceedings of the Third Airborne Visible/Infrared Imaging Spectrometer (AVIRIS) Workshop, JPL Publication 90-54*, p. 176-186.
- Clark, R.N., King, T.V.V., Klejwa, M., Swayze, G.A. and Vergo, N., 1990. High spectral resolution reflectance spectroscopy of minerals. *Journal of Geophysical Research*, 95(B8): 12653-12680
- Clark, R.N., Swayze, G.A., Gallagher, A.J., Gorelick, N. and Kruse, F.A., 1991. Mapping with imaging spectrometer data using the complete band shape least-squares algorithm simultaneously fit to multiple spectral features from multiple materials, *Proceedings, 3rd Airborne Visible/Infrared Imaging Spectrometer (AVIRIS) workshop, JPL Publication 91-28*, p. 2-3.
- Clark, R.N., Swayze, G.A., Livo, E.K., Kokaly, R.F., King, T.V.V., Dalton, B.J., Vance, S.J., Rockwell, B.W., Hoefen, T., McDougal R.R., 2002. *Surface Reflectance Calibration of Terrestrial Imaging Spectroscopy Data: a Tutorial Using AVIRIS, 10th Airborne Earth Science Workshop. JPL Publication 02-1*.
- Cloutis, E.A. et al., 2006. Detection and discrimination of sulfate minerals using reflectance spectroscopy. *Icarus*, 184(1): 121-157.
- Cocks, T., Jenssen, R., Stewart, A., Wilson, I. and Shields, T., 1998. The Hymap TM airborne hyperspectral sensor: The system, calibration and performance. *First EARSEL workshop on Imaging Spectroscopy, Proceedings, Zurich, October*.
- Crosta, A.P. and Souza F., C.R., 1998. *Hyperspectral Data Processing For Mineral Mapping Using AVIRIS 1995 Data in Alto Paraiso de Goias, Central Brazil, Anais IX Simposio Brasileiro de Sensoriamento Remoto, Santos, Brazil, September 11-18, 1998, INPE. p 1357-1364*.
- Crowley, J.K. et al., 2003. Spectral reflectance properties (0.4-2.5 μm) of secondary Fe-oxide, Fe-hydroxide, and Fe-sulphate-hydrate minerals associated with sulphide-

- bearing mine wastes. *Geochemistry: Exploration, Environment, Analysis*, 3(3): 219-228.
- Dalton, J.B. et al., 2000. Distribution of Acid-Generating and Acid-Buffering Minerals in the Animas river Watershed as Determined by AVIRIS Spectroscopy, Proceedings of the ICARD 2000 Meeting, May 21-24, 2000, Denver, Colorado.
- Davis, M.B., 2001. Geology of the Iberian Pyrite Belt, southern Portugal and Spain, Selected Topics: Geology and Mineral Resources of the Iberian Pyrite Peninsula. GEO381R Regional Studies in Mineral Resources Geology. Department of Geological Sciences, University of Texas at Austin.
- Farrand, W.H. and Harsanyi, J.C., 1997. Mapping the Distribution of Mine Tailings in the Coeur d'Alene River Valley, Idaho, through the Use of a Constrained Energy Minimization Technique. *Remote Sensing of Environment*, 59: 64-76.
- Ferrero, M.D., 1988. Los conflictos de febrero de 1888 en Riotinto: distintas versiones de los hechos, *Huelva en su Historia*, pp. 603-624.
- Ferrier, G., 1999. Application of imaging spectrometer data in identifying environmental pollution caused by mining at Rodarquilar, Spain. *Remote Sensing of Environment*, 68: 125-137.
- Gonzalez, F., Moreno, C. and Santos, A., 2006. The massive sulphide event in the Iberian pyrite belt; confirmatory evidence from the Sotiel-Coronada Mine. *Geological Magazine*, 143(6): 821-827.
- Haaland, D.M. and Thomas, E.V., 1988. Partial Least-Squares Methods for Spectral Analyses. 1. Relation to Other Quantitative Calibration Methods and the Extraction of Qualitative Information. *Analytical Chemistry*, 60(11): 1193-1202.
- Hammarstrom, J.M., Seal II, R.R., Meier, A.L. and Kornfeld, J.M., 2005. Secondary sulfate minerals associated with acid drainage in the eastern US: recycling of metals and acidity in surficial environments. *Chemical Geology*, 215(1-4): 407-431.
- Harsanyi, J.C., 1993. Detection and classification of subpixel spectral signatures in hyperspectral image sequences. Ph.D. thesis, University of Maryland Baltimore County, 116 pp.
- Herzberg, G., 1945. *Molecular spectra and molecular structure. Volume 2: Infrared and Raman spectra of polyatomic molecules.* Van Nostrand Reinhold, New York, 632 pp.
- Hunt, G.R. and Ashley, R.P., 1979. Spectra of altered rocks in the visible and near infrared. *Economic geology*, 74(7): 1613-1629.
- Hunt, G.R. and Salisbury, J.W., 1970. Visible and Near-Infrared Spectra of Minerals and Rocks: I. Silicate Minerals. *Modern Geology*, 1: 283-300.

- Johnson, D.B. and Hallberg, K.B., 2003. The microbiology of acidic mine waters. *Research in Microbiology*, 154(7): 466-473.
- Kemper, T. and Sommer, S., 2002. Use of Field and Airborne Hyperspectral Data to Assess Residual Heavy Metal Contamination and Acidification Risk in the Guadiamar Floodplain after the Aznalcollar Mining Accident (Andalusia, Spain), Powerpoint presentation, 2nd MINEO Workshop 11-13 December, 2002.
- Kemper, T., Haro, J.G., Preissler, H., Mehl, W. and Sommer, S., 2000. A Multiple Endmember Unmixing Approach for Mapping Heavy Metal Contamination After the Donana Mining Accident (Sevilla, Spain), 2nd EARSeL Workshop on Imaging Spectroscopy, 2002.
- King, T.V.V., R.N., C., Anger, C. and Swayze, G.A., 1995. Remote mineral mapping using AVIRIS data at Summitville, Colorado and the adjacent San Juan Mountains. In: H.H. Posey, J.A. Pendelton and D. Van Zyl (Editors), *Proceedings: Summitville Forum '95*. Colorado Geological Survey Special Publication 38, p.59-63.
- Kleinmann, R.L.P., Crerar, D.A. and Pacelli, R.R., 1981. Biogeochemistry of acid mine drainage and a method to control acid formation. *Mining Engineering*, 33(3): 300-305.
- Kruse, F.A. et al., 1993. The spectral image processing system (SIPS). Interactive visualisation and analysis of imaging spectrometer data. *Remote Sensing of Environment*, 44: 145-163.
- Lapakko, K., 2002. *Metal Mine Rock and Waste Characterization Tools: An Overview*, International Institute for Environment and Development.
- Leistel, J.M. et al., 1998. The volcanic-hosted massive sulphide deposits of the Iberian pyrite belt; review and preface to the thematic issue; Iberian Pyrite Belt thematic issue. *Mineralium Deposita*, 33(1-2): 2-30.
- Lopez-Pamo, E. et al., 1999. The extent of the Aznalcollar pyritic sludge spill and its effects on soils. *The Science of the total environment*, 242(1): 57-88.
- Martens, H., Naes, T., 1989. *Multivariate Calibration*. Wiley, New York, 419 pp.
- Mason, P., 1998. *XSPECTRA*. CSIRO, Division of Exploration and Mining, North Ryle.
- McCubbin, I. and Lang, H., 1999. *Mapping Environmental Contaminants at Ray Mine, AZ*. JPL Publication, USA. <http://hdl.handle.net/2014/18319>.
- Mitsuno, C. et al., 1988. Geological studies of the "Iberian Pyrite Belt" with special reference to its genetical correlation of the Yanahara ore deposits and others in the inner zone of southwest Japan. University of Okayama, Japan.
- Montero S., I.C., Brimhall, G.H., Alpers, C.N. and Swayze, G.A., 2005. Characterization of waste rock associated with acid drainage at the Penn Mine, California, by

ground-based visible to short-wave infrared reflectance spectroscopy assisted by digital mapping; Geochemistry of sulfate minerals in high and low temperature environments; a tribute to Robert O. Rye. Geological Society of America, 2000 annual meeting, Reno, NV, United States, Nov. 9-18, 2000, 215(1-4): 453-472.

- Morales, J.R., 1999. Present Status of IPB Activity: A Case of Re-emergence of Mining Activity in Europe?, Mining Development Strategies With a Focus on the Case of the Iberian Pyrite Belt. Technical Journey 25th September 1998, Lisbon, Portugal.
- Moreno, C., 1993. Postvolcanic Paleozoic of the Iberian pyrite belt; an example of basin morphologic control on sediment distribution in a turbidite basin. *Journal of Sedimentary Petrology*, 63(6): 1118-1128.
- Moreno, C., Sierra, S. and Saez, R., 1996. Evidence for catastrophism at the Famennian-Dinantian boundary in the Iberian pyrite belt; Recent advances in Lower Carboniferous geology. *Geological Society Special Publications*, 107: 153-162.
- Munha, J., Barriga, F.J.A.S. and Kerrich, R., 1986. High (super 18) O ore-forming fluids in volcanic-hosted base metal massive sulfide deposits; geologic, (super 18) O/ (super 16) O, and D/H evidence from the Iberian pyrite belt; Crandon, Wisconsin; and Blue Hill, Maine. *Economic Geology and the Bulletin of the Society of Economic Geologists*, 81(3): 530-552.
- Murad, E. and Rojik, P., 2003. Iron-rich precipitates in a mine drainage environment; influence of pH on mineralogy; Environmental mineralogy. *American Mineralogist*, 88(11-12, Part 2): 1915-1918.
- Nash, E.B. and Conel, J.E., 1974. Spectral reflectance systematics for mixtures of powdered hyersthene, labradorite, and ilmentite. *Journal of Geophysical Research*, 79: 1615-1621.
- Nordstrom, D.K. and Southam, G., 1997. Geomicrobiology; interactions between microbes and minerals. *Reviews in Mineralogy*, 35: 448.
- Nordstrom, D.K., Alpers, C.N. and Smith, J.V., 1999. Negative pH, efflorescent mineralogy, and consequences for environmental restoration at the Iron Mountain Superfund site, California; Papers from a National Academy of Sciences colloquium on Geology, mineralogy, and human welfare. 96, National Academy of Sciences, Washington, DC, United States (USA), United States (USA).
- Nordstrom, D.K., Jenne, E.A. and Ball, J.W., 1978. Redox equilibria of iron in acid mine waters. In: E.A. Jenne (Editor), *Chemical Modeling in Aqueous Systems: Speciation, Sorption, Solubility, and Kinetics*. ACS Symposium Series, Washington, DC, pp. 51-79.
- Olías, M., Nieto, J.M., Sarmiento, A.M., Cerón, J.C. and Cánovas, C.R., 2004. Seasonal water quality variations in a river affected by acid mine drainage: the Odiel River (South West Spain). *Science of The Total Environment*, 333(1-3): 267-281.

- Ong, C. and Cudahy, T.J., 2002. Deriving quantitative monitoring data related to acid drainage using multi-temporal hyperspectral data, 2nd EARSEL Workshop on Imaging Spectroscopy. EARSEL.
- Ong, C., Cudahy, T.J. and Swayze, G., 2003a. Predicting Acid Drainage Related Physicochemical Measurements Using Hyperspectral Data, 3rd EARSEL Workshop on Imaging Spectroscopy, 13-16 May 2003, Herrsching, pp. 363-373.
- Ong, C., G. Swayze, and R. Clark, 2003b, An investigation of the use of the Tetracorder expert system for multi-temporal mapping of acid drainage-related minerals using airborne hyperspectral data: Proceedings of the 3rd EARSEL Workshop on Imaging Spectroscopy, May 13-16, 2003, Herrsching, Germany, p. 357-362.
- Pauwels, H. et al., 2002. Chemical characteristics of groundwater around two massive sulphide deposits in an area of previous mining contamination, Iberian pyrite belt, Spain. *Journal of Geochemical Exploration*, 75(1-3): 17-41.
- Reimann, C. and Filzmoser, P., 1999. Normal and lognormal data distribution in geochemistry: death of a myth. Consequences for the statistical treatment of geochemical and environmental data. *Environmental Geology*, 9: 1001-1014.
- Richter, R., Schlaepfer, D., 2002. Geo-atmospheric processing of airborne imaging spectrometry data. Part 2: atmospheric/topographic correction. *International Journal of Remote Sensing*, 23(13): 2631-2649.
- Rockwell, B.W. et al., 1999. Preliminary materials mapping in the Park City region for the Utah USGS-EPA Imaging Spectroscopy Project using both high and low altitude AVIRIS data. In: R.O. Green (Editor), *Summaries of the Eighth Annual JPL Airborne Earth Science Workshop, NASA JPL AVIRIS Workshop*. February 8-11: JPL Publication 99-17, Pasadena, California, USA, pp. 365-375.
- Rockwell, B.W. et al., 2000. Mineral mapping in the Marysvale volcanic field, Utah using AVIRIS data. In: R.O. Green (Editor), *Summaries of the Ninth Annual JPL Airborne Earth Science Workshop, NASA JPL AVIRIS Workshop*. February 23-25: JPL Publication 00-18, Pasadena, California, USA, pp. 407-417.
- Rockwell, B.W., McDougal, R.R. and Gent, C.A., 2005. *Remote Sensing for Environmental Site Screening and Watershed Evaluation in Utah Mine Lands—East Tintic Mountains, Oquirrh Mountains, and Tushar Mountains*. Scientific Investigations Report 2004-5241, U.S. Geological Survey.
- Rogge, D.M. et al., 2007. Integration of spatial-spectral information for the improved extraction of endmembers. *Remote Sensing of Environment*, 110(3): 287-303.
- Rogge, D.M., Rivard, B., Zhang, J. and Feng, J., 2006. Iterative Spectral Unmixing for Optimizing Per-Pixel Endmember Sets. *Geoscience and Remote Sensing, IEEE Transactions on*, 44(12): 3725-3736.

- Rothenberg, B. and Blanco Freijero, A., 1980. Scientific Studies in early Mining and Extractive Metallurgy. In: Craddock (Editor), British Museum Occasion, 20, pp. 41-56.
- Routhier, P., 1980. La ceinture sud-iberique a amas sulfures dans sa partie espagnole mediane; Tableau geologique et metallogenique; Synthese sur le type amas sulfures volcano-sedimentaires. The South Iberian Belt with massive sulfide deposits in its central Spanish section; geology and metallogeny; summary of volcano-sedimentary massive sulfide deposits, Memoires du B.R.G.M., no.94, 265 pp. Bureau de Recherches Geologiques et Minieres, (BRGM), Paris, France (FRA), France (FRA).
- Ruiz, F. et al., 1998. Stratigraphic sequence, elemental concentrations and heavy metal pollution in Holocene sediments from the Tinto-Odiel Estuary, southwestern Spain. *Environmental Geology*, 34(4): 270-278.
- Saez, R., Pascual, E., Toscano, M. and Almodova, G.R., 1999. The Iberian type of volcano-sedimentary massive sulphide deposits. *Mineralium Deposita*, 34(5-6): 549-570.
- Sainz, A., Grande, J.A. and de la Torre, M.L., 2003. Odiel River, acid mine drainage and current characterisation by means of univariate analysis. *Environment international*, 29(1): 51-59.
- Salomons, W., 1995. Environmental impact of metals derived from mining activities: Processes, predictions, prevention. *Journal of Geochemical Exploration*, 52(1-2): 5-23.
- Santos, A., Prada, J.M. and Rosales, F., 1993. Aspectos geologicos y geofisicos del yacimiento de Migollas. Symposium on the polymetallic sulphides of the Iberian Pyrite Belt, Evora. *Apimineral*, 1: 8-20.
- Sares, M.A. et al., 2004. Characterizing Sources of Acid Rock Drainage and Resulting Water Quality Impacts Using Hyperspectral Remote Sensing - Examples from the Upper Arkansas River Basin, Colorado, 2004 Advanced Integration of Geospatial Technologies in Mining and Reclamation, Dec. 7-9, 2004, Atlanta, GA.
- Schermerhorn, L.J.G., 1971. An outline stratigraphy of the Iberian pyrite belt. *Boletin Geologico y Minero*, 82(3-4): 23-52.
- Schlaepfer, D., Richter, R., 2002. Geo-atmospheric processing of airborne imaging spectrometry data. Part 1: parametric orthorectification. *International Journal of Remote Sensing*, 23(13): 2609-2630.
- Shang, J. et al., 2002. Mine tailings characterization using PROBE data (preliminary results); Remote sensing; integrating our view of the planet; proceedings. 24th Canadian symposium on Remote Sensing, Toronto, ON, Canada, June 24-28, 2002: 2921-2923.

- Sierra, J., 1984. Geologia, mineralogia y metalogenia del yacimiento de Azualcollar; Segunda parte, Mineralogia y sucesion mineral. Geology, mineralogy and metallogeny of the Azualcollar Deposit; Part 2, Mineralogy and mineral succession. *Boletin Geologico y Minero*, 95(6): 553-568.
- Silverman, M.P. and Ehrlich, H.L., 1964. Microbial formation and degradation of minerals. *Adv. Appl. Microbiol.* ; Vol/Issue: 6: Pages: 153-206.
- Singer, P.C. and Stumm, W., 1970. Acidic Mine Drainage: The Rate-Determining Step. *Science*, 167(3921): 1121-1123.
- Singer, R.B., 1981. Near-infrared spectral reflectance of mineral mixtures: Systematic combinations of pyroxenes, olivine, and iron oxides. *Journal of Geophysical Research*, 86: 7967-7982.
- Strauss, G.K. and Madel, J., 1974. Geology of massive sulphide deposits in the Spanish-Portuguese Pyrite Belt. *Geologische Rundschau*, 63(1): 191-211.
- Strauss, G.K., 1970. Sobre la Geologia de la provincia piritifera del Suroeste de la Peninsula Iberica y de sus yacimientos, en especial sobre la mina de piritita do Lousal (Portugal). The geology of the pyrite province of the southwestern Iberian Peninsula and its deposits, especially the pyrite mine at Lousal, Portugal. *Memorias del Instituto Geologico y Minero de Espana*, 77: 266.
- Strauss, G.K., Madel, J., Fernandez Alonso, F., Klemm, D.D. and Schneider, H.J., 1977. Exploration practice for strata-bound volcanogenic sulphide deposits in the Spanish-Portuguese Pyrite Belt; geology, geophysics, and geochemistry. In: Anonymous (Editor), *Time- and strata-bound ore deposits*. Springer-Verlag, Berlin, Federal Republic of Germany (DEU).
- Stumm, W. and Morgan, J.J., 1981. *Aquatic Chemistry: An Introduction Emphasizing Chemical Equilibria in Natural Waters*. J. Wiley, New York.
- Swayze, G.A. et al., 2000. Using Imaging Spectroscopy to Map Acidic Mine Waste. *Environmental Science and Technology*, 34: 47-54.
- Swayze, G.A., Clark, R.N., Pearson, R.M. and Livo, K.E., 1996. Mapping Acid-Generating Minerals at the California Gulch Superfund Site in Leadville, Colorado using Imaging Spectroscopy, *Summaries of the 6th Annual JPL Airborne Earth Science Workshop*. JPL Publication.
- Thieblemont, D., Pascual, E. and Stein, G., 1998. Magmatism in the Iberian pyrite belt; petrological constraints on a metallogenic model; Iberian Pyrite Belt thematic issue. *Mineralium Deposita*, 33(1-2): 98-110.
- Tornos, F., 2006. Environment of formation and styles of volcanogenic massive sulfides: The Iberian Pyrite Belt. *Ore Geology Reviews*, 28(3): 259-307.
- van den Boogaard, M., 1967. *Geology of the Pomarao region (southern Portugal)*, Rotterdam, 113 pp.

- van Geen, A., Adkins, J.F., Boyle, E.A., Nelson, C.H. and Palanques, A., 1997. A 120 yr record of widespread contamination from mining of the Iberian pyrite belt. *Geology (Boulder)*, 25(4): 291-294.
- Williams, D.J. et al., 2002. Assessing mine drainage pH from the color and spectral reflectance of chemical precipitates. *Applied Geochemistry*, 17(10): 1273-1286.
- Wold, S., 1978. Cross-Validatory Estimation of the Number of Components in Factor and Principal Components Models. *Technometrics*, 20(4): 397-405.

8. APPENDICES

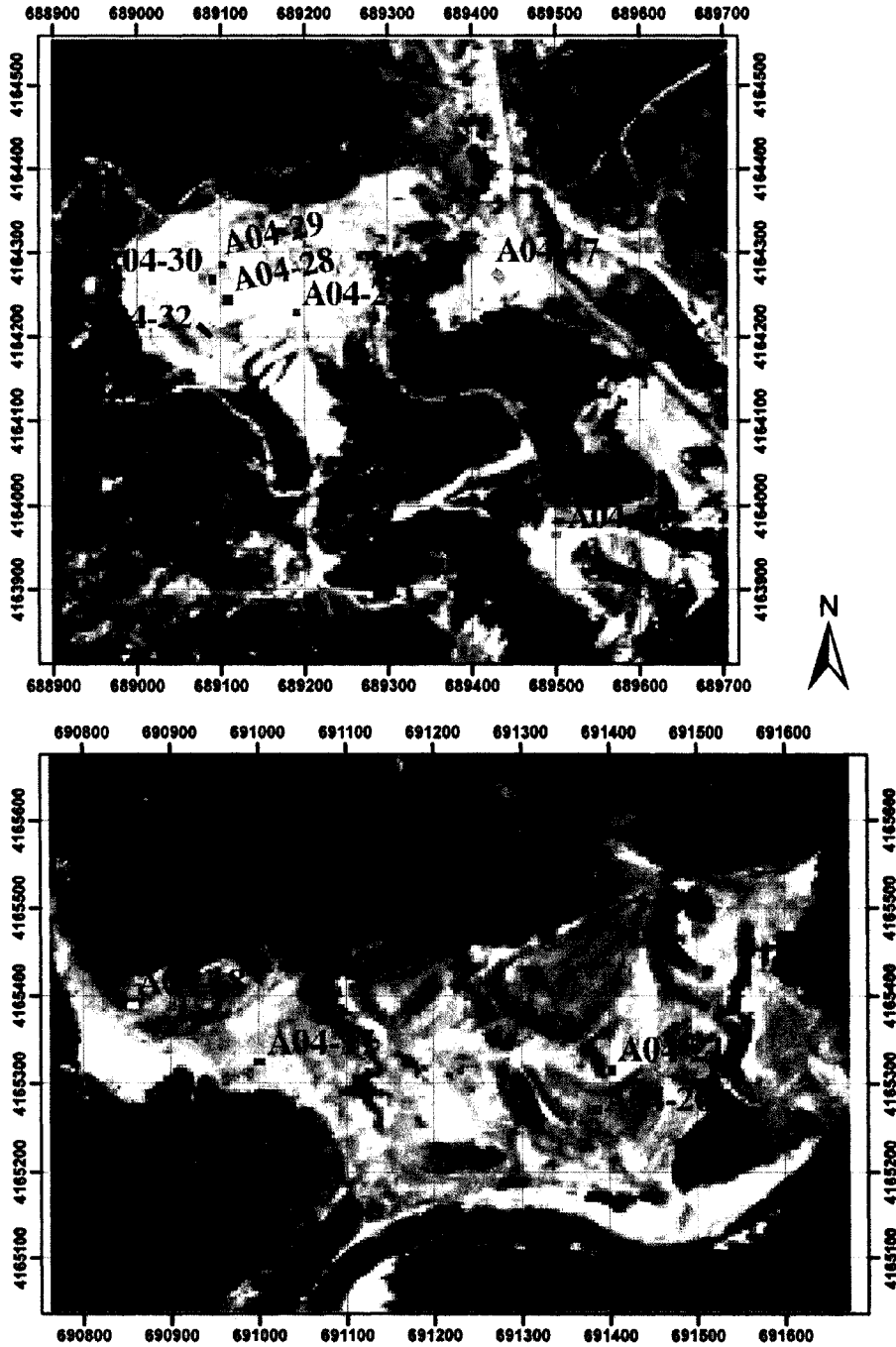
Appendix 3.1: UTM location of AMD mineral soil sampling sites.

Sample ID	X	Y	Mineral category	Sample ID	X	Y	Mineral category
A04-01	686207	4163061	Other	J05-01	689547	4168327	AMD
A04-06	689242	4165122	Other	J05-02	689496	4168305	AMD
A04-07	690430	4163497	AMD	J05-02a	689496	4168305	Eff
A04-08	690438	4163624	AMD	J05-02b	689496	4168305	Eff
A04-09	690393	4163500	AMD	J05-04	690654	4163780	AMD
A04-11	690171	4163407	Other	J05-05	690561	4163672	Other
A04-12	690166	4163414	Other	J05-06	690415	4163623	AMD
A04-13	690940	4162067	Other	J05-08	690415	4163623	AMD
A04-14	690581	4163860	AMD	J05-09	690423	4163622	AMD
A04-15	690759	4164486	Other	J05-10	688922	4168162	AMD
A04-16	691009	4165332	Eff	J05-11	691038	4167773	Other
A04-17	691008	4165320	Eff	J05-12	690217	4167676	Eff
A04-18	690857	4165394	AMD	J05-13	690217	4167676	Eff
A04-19	690935	4165409	Eff	J05-14	690217	4167676	AMD
A04-20	691379	4165277	AMD	J05-15	690227	4167601	AMD
A04-21	691396	4165316	AMD	J05-16	690227	4167601	Other
A04-22	691619	4165350	AMD	J05-18	690414	4162414	Other
A04-23	691627	4165412	AMD	J05-19	689752	4168431	AMD
A04-24	691480	4165369	Eff	J05-20	689758	4168402	AMD
A04-25	689187	4164264	Eff	J05-21	689799	4168474	AMD
A04-26	689187	4164244	Eff	J05-22	689800	4168445	AMD
A04-27	689193	4164239	AMD	J05-23	689848	4168472	AMD
A04-28	689101	4164252	Other	J05-24	689837	4168540	AMD
A04-29	689107	4164280	AMD	J05-25	689837	4168555	AMD
A04-30	689093	4164279	Eff	J05-26	689297	4167889	Eff
A04-31	689079	4164259	AMD	J05-27	690942	4167538	Eff
A04-32	689074	4164226	Other	J05-27b	689171	4164260	Eff
A04-33	689016	4164253	AMD	J05-28	689167	4164263	Eff
A04-34	689505	4163961	AMD	J05-29	689161	4164261	Eff
A04-35	690253	4163293	Other	J05-30	689186	4164250	AMD
A04-36	690452	4162339	AMD	J05-31	689170	4164249	Eff
A04-37	690449	4162386	AMD	J05-32	689177	4164230	AMD
A04-38	690426	4162401	Other	J05-33	689170	4164249	Eff
A04-40	690307	4161629	Other	J05-34	689174	4164217	Other
A04-41	686407	4167147	Other	J05-35	689100	4164266	AMD
A04-42	686216	4167087	Other	J05-36	687960	4167284	AMD
A04-43	686047	4166665	Other	J05-37	690512	4164409	AMD
A04-44	686190	4166273	Other	J05-38	690726	4164358	AMD
A04-45	686240	4166144	Other	J05-39	690769	4164337	AMD
A04-46	686253	4166200	Other	J05-40	690845	4164313	AMD
A04-47	689433	4164285	Other	J05-41	690906	4164359	AMD
				J05-42	690785	4164368	AMD
				J05-43	690891	4165303	AMD
				J05-44	690838	4165416	AMD
				J05-45	690882	4165374	AMD
				J05-46	690965	4165339	AMD
				J05-47	690983	4165372	AMD
				J05-48	690987	4165321	Eff
				J05-49	690807	4165427	AMD
				J05-50	689139	4164297	Eff
				J05-51	689277	4164963	AMD
				J05-52	689117	4167626	AMD
				J05-53	691152	4165399	AMD
				J05-54	691184	4165401	AMD
				J05-55	691279	4165454	AMD
				J05-56	691389	4165360	AMD

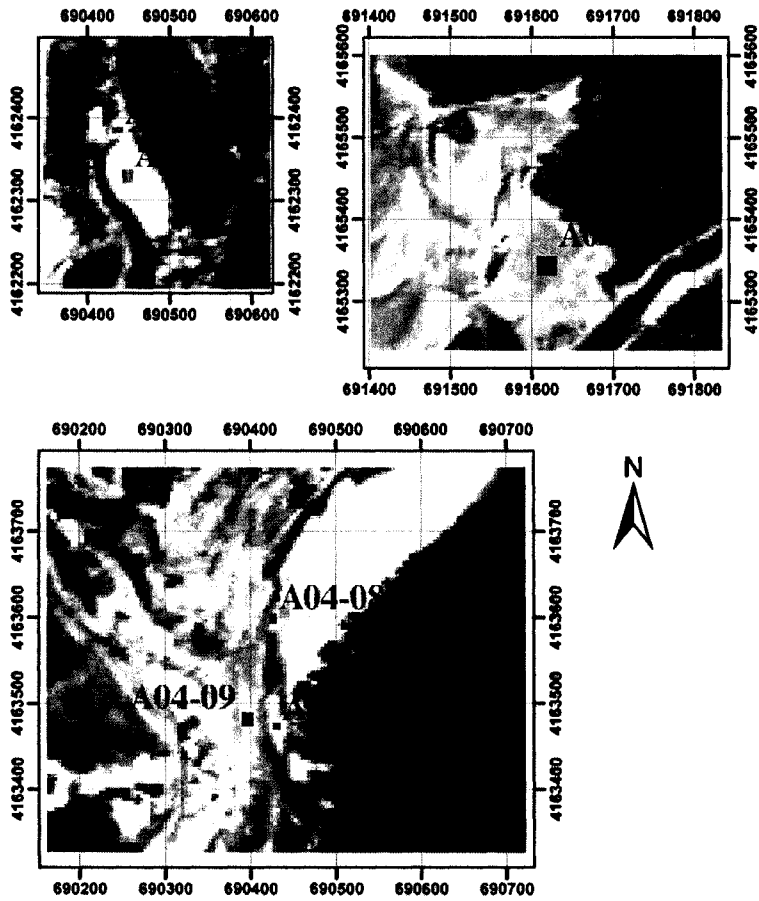
X-Y coordinates in UTM European Mean 1950 z29N

Appendix 3.2: Maps of the location and area of the sampling sites.

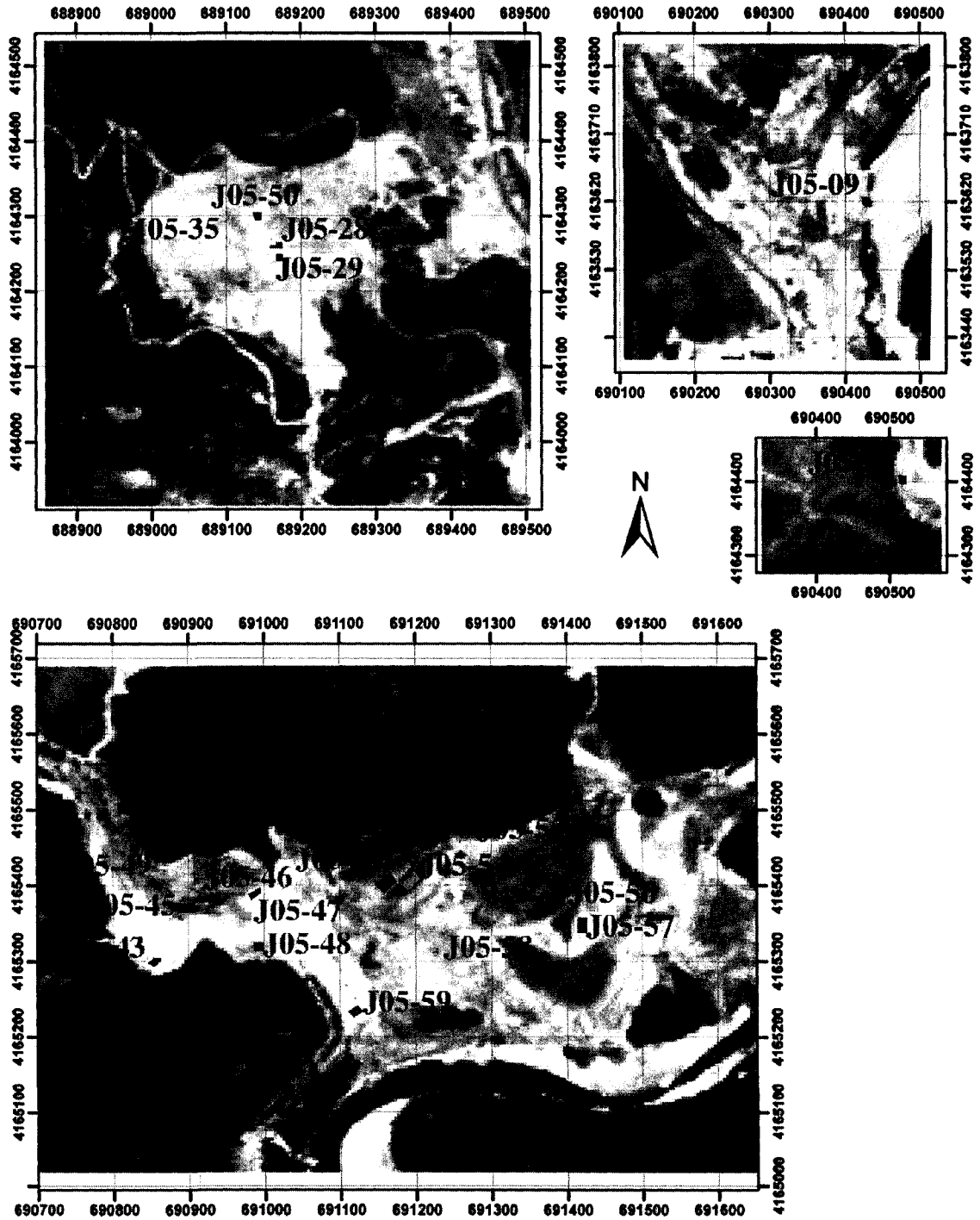
a) Sampling sites of August 2004 field campaign:



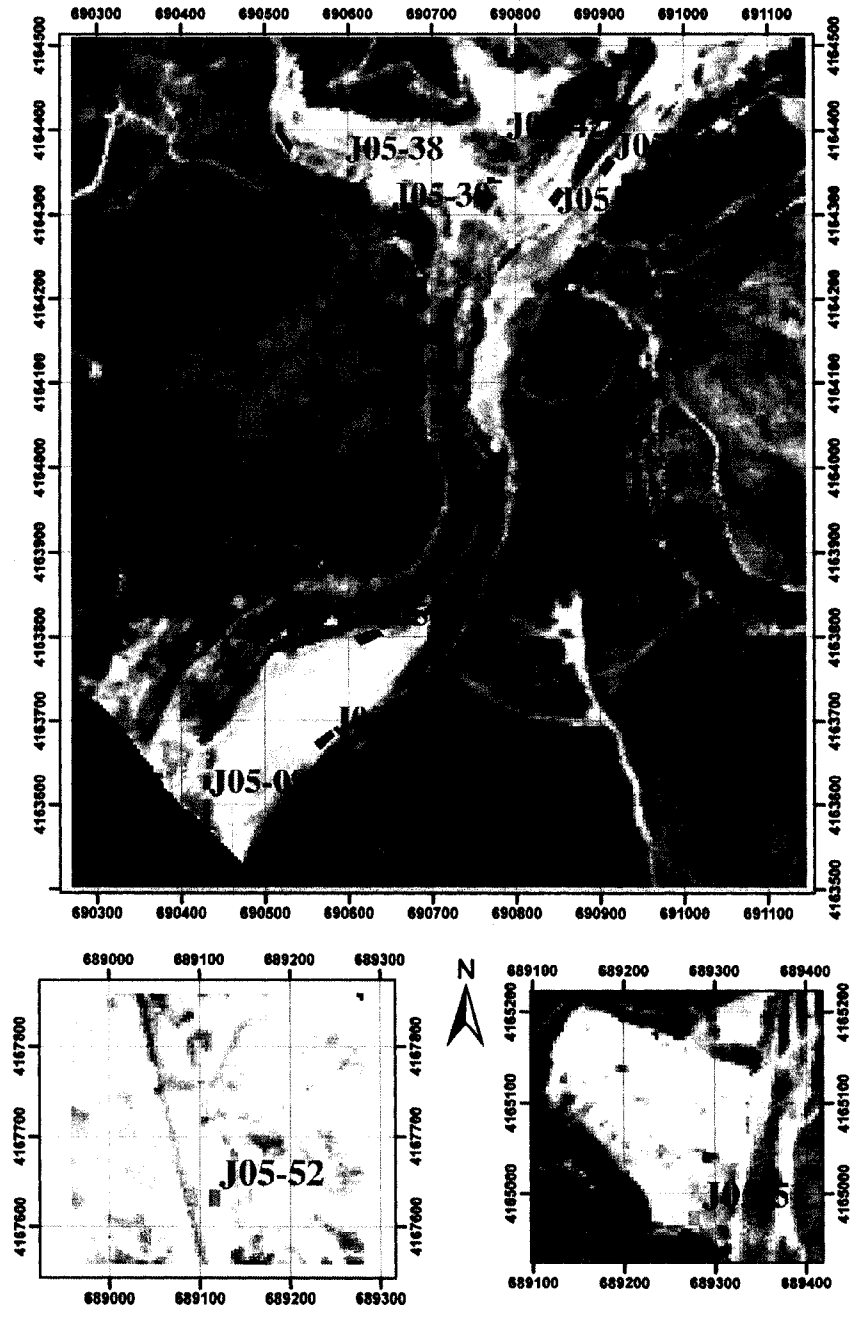
Appendix 3.2 (a) continued.

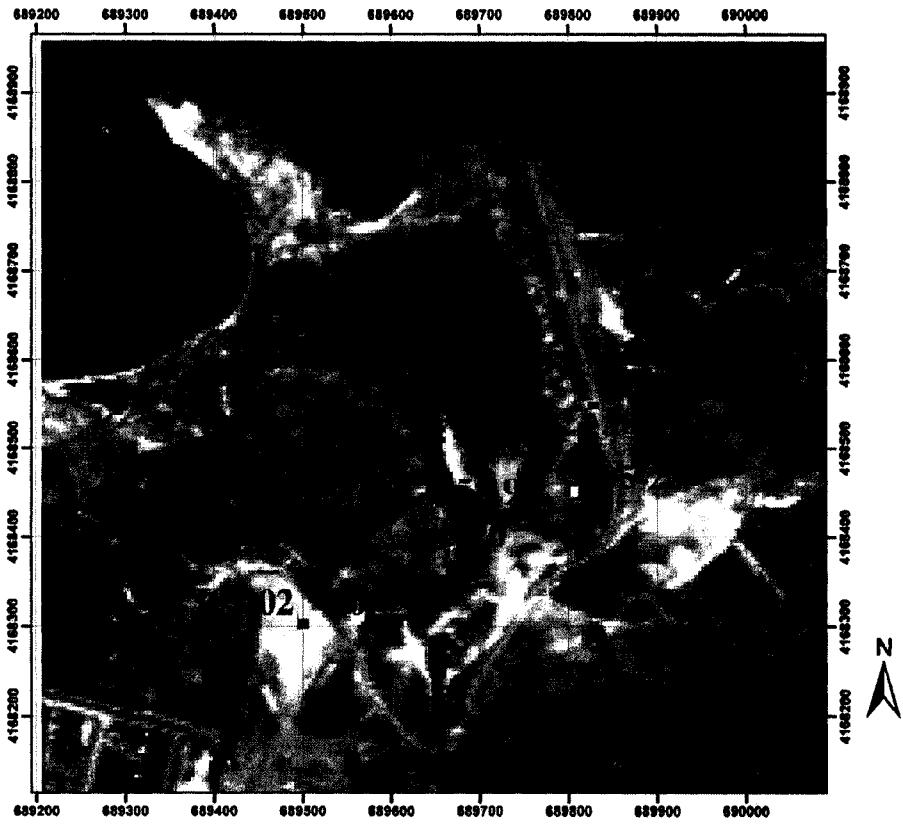


b) Sampling sites of June 2005 field campaign:



Appendix 3.2 (b) continued.





Appendix 3.3: Calculation of Absolute Reflectance for field spectral measurements.

Calculation of Absolute Reflectance:

Absolute Reflectance Calculation for 2005 Field Spectra

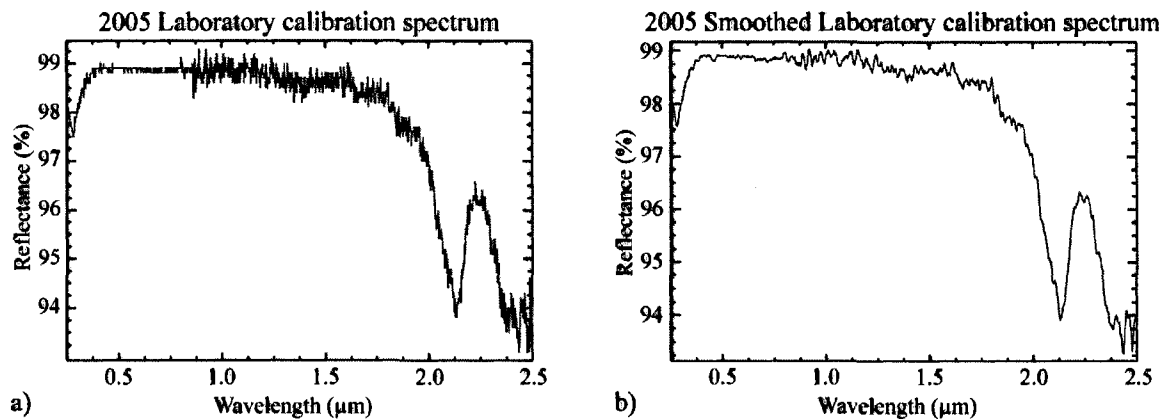
$$R_{\text{absolute 2005}} = R_{\text{relative of target}} * \text{laboratory calibration spectrum 2005}$$

Where:

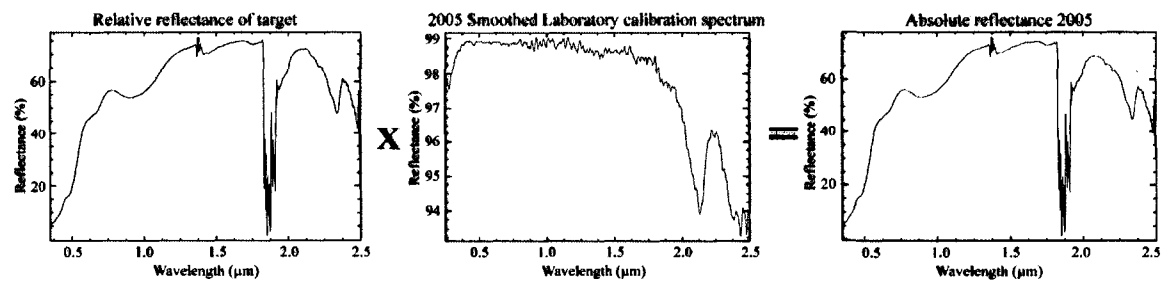
$$R_{\text{relative of target}} = (I_{\text{target}} / I_{\text{reference standard 2005}})$$

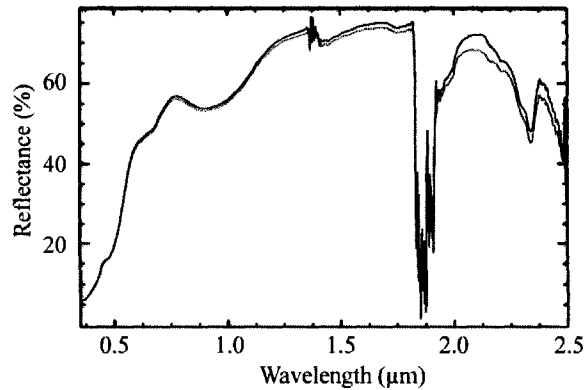
$$\text{Laboratory calibration spectrum 2005} = (I_{\text{field reference standard 2005}} / I_{\text{laboratory reference standard}})$$

The 2005 laboratory calibration spectrum (a) was provided by DFD-DLR and was noisy. Therefore, a Savitzky-Golay filter was applied to the 2005 spectralon calibration factor to reduce noise in the spectrum with a window size of 25 at 3 degree was used (b).



Then the 2005 smoothed spectralon calibration factor was multiplied with the 2005 field relative reflectance spectra of the target to give the absolute reflectance.





Comparison of the relative reflectance spectrum (blue) of the football field in 2005 versus the absolute reflectance (green) for the same target.

Absolute Reflectance Calculation for 2004 Field Spectra

$$R_{\text{absolute 2004}} = R_{\text{relative of target}} * \text{laboratory calibration spectrum 2004}$$

Where:

$$R_{\text{relative of target}} = (I_{\text{target}} / I_{\text{reference standard 2004}})$$

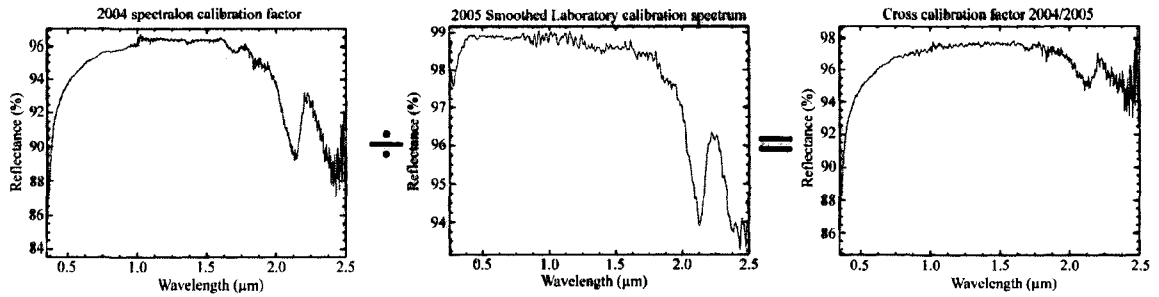
and

$$\text{Laboratory calibration spectrum 2004} = (I_{\text{field reference standard 2005}} / I_{\text{laboratory reference standard}}) / \text{Cross calibration factor}$$

The Cross calibration factor is the difference between the laboratory calibration spectrum of 2004 and 2005:

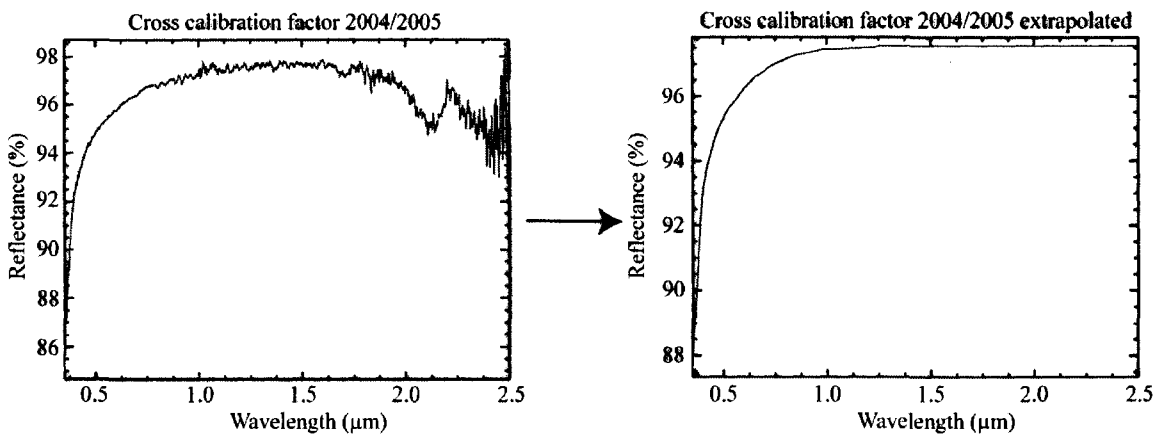
$$\text{Cross calibration factor} = \text{laboratory calibration spectrum 2004} / \text{laboratory calibration spectrum 2005}$$

The 2004 spectralon calibration factor was provided by IMF-DLR. This calibration factor was too noisy. So to correct the 2004 field spectra to absolute reflectance, it was necessary to correct the 2004 data to the 2005 data by applying a cross calibration factor between 2004 and 2005.

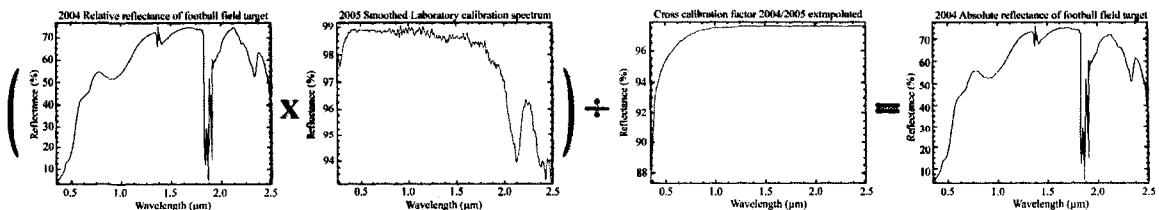


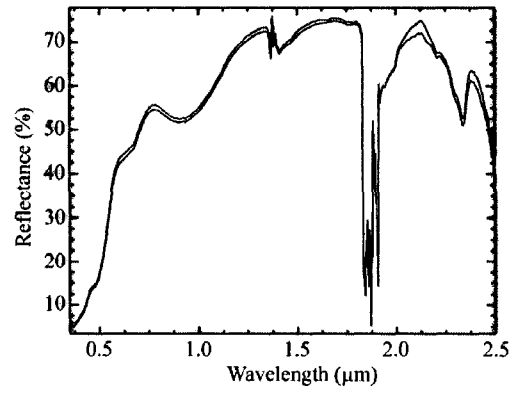
Cross calibration factor: This factor is the difference between the 2004 spectralon calibration factor and the 2005 spectralon calibration factor: 2004/2005

The Cross calibration factor was extrapolated to a straight line in the SWIR. This extrapolated cross calibration factor between 2004 and 2005 is used to correct the 2004 field spectra to absolute reflectance.



Example of calculation to absolute reflectance of 2004 field target spectra:





Comparison of the relative reflectance spectra of the football field in 2004 versus the absolute reflectance for the same target.

Appendix 3.4: Hymap flight lines information.

	Time UTC	Image samples	Image lines	Nb bands	Pixel size	Latitude	Longitude	Flight elevation (above sea level) (m)	Mean ground elevation (m)	Flight heading	Solar azimuth	Solar Zenith
May 6, 1999												
Line 1	13:14:25	512	1421	128	5 m	37°	-6°	3577	200	313°		
Line 2		512	1659	128	5 m	37°	-6°		200			
Line 3	12:58:51	512	1664	128	5 m	37.61°	-6.85°	3562	200	314.1°	202.6	22.4
Line 4	12:43:53	512	1647	128	5 m	37.62°	-6.84°	3602	200	313.9°	193.3	21.5
Line 5	12:28:48	512	1651	128	5 m	37.63°	-6.84°	3586	200	314.1°	215.0°	17.1°
May 19, 2004												
Line 1	10:05:55	512	3026	126	4 m	37.55°	-6.88°	2218	208	319.8°	111.3°	34.6°
Line 2	10:50:48	512	2056	126	4 m	37.53°	-6.82°	2220	218	317.9°	125.0°	26.8°
Line 3	10:14:45	512	2520	126	4 m	37.59°	-6.87°	2219	208	134.1°	113.7°	32.9°
Line 4	10:42:47	512	3240	126	4 m	37.65°	-6.86°	2217	231	130.9°	128.2°	25.6°
Line 5	11:01:22	512	3026	126	4 m	37.61°	-6.87°	2219	250	131.9°	129.1°	25.2°
Line 6	10:21:54	512	2475	126	4 m	37.59°	-6.87°	2218	260	319.7°	115.5°	31.8°
August 14, 2004												
Line 1	08:02:13	512	3686	126	4 m	37.55°	-6.87°	2188	214	312.3°	91.9°	63.7°
Line 2	08:28:03	512	3685	126	4 m	37.57°	-6.87°	2191	211	135.4°	96.0°	58.5°
Line 3	08:11:09	512	3131	126	4 m	37.59°	-6.88°	2191	216	135.7°	93.3°	61.9°
Line 4	08:36:04	512	3132	126	4 m	37.60°	-6.85°	2192	230	313.6°	97.34°	57.0°
Line 5	08:19:18	512	3073	126	4 m	37.61°	-6.84°	2189	253	313.3°	94.6°	60.3°
Line 6	08:45:03	512	3061	126	4 m	37.64°	-6.86°	2194	266	136.9°	99.0°	55.2°
June 17, 2005												
Line 1	11:50:58	512	3634	126	4 m	37.50°	-6.812°	2227	215	315.3°	148.7°	16.1°
Line 2	12:35:05	512	3079	126	4 m	37.62°	-6.939°	2223	210	133.8°	187.3°	14.3°
Line 3	12:00:09	512	3057	126	4 m	37.64°	-6.930°	2218	215	134.3°	155.8°	15.3°
Line 4	12:26:32	512	3077	126	4 m	37.56°	-6.798°	2223	230	315.5°	179.9°	14.2°
Line 5	12:09:00	512	3057	126	4 m	37.57°	-6.791°	2227	254	311.7°	163.5°	14.7°
Line 6	12:17:46	512		126	4 m	37.68°	-6.899°	2238	263	136.0°	171.6°	14.4°

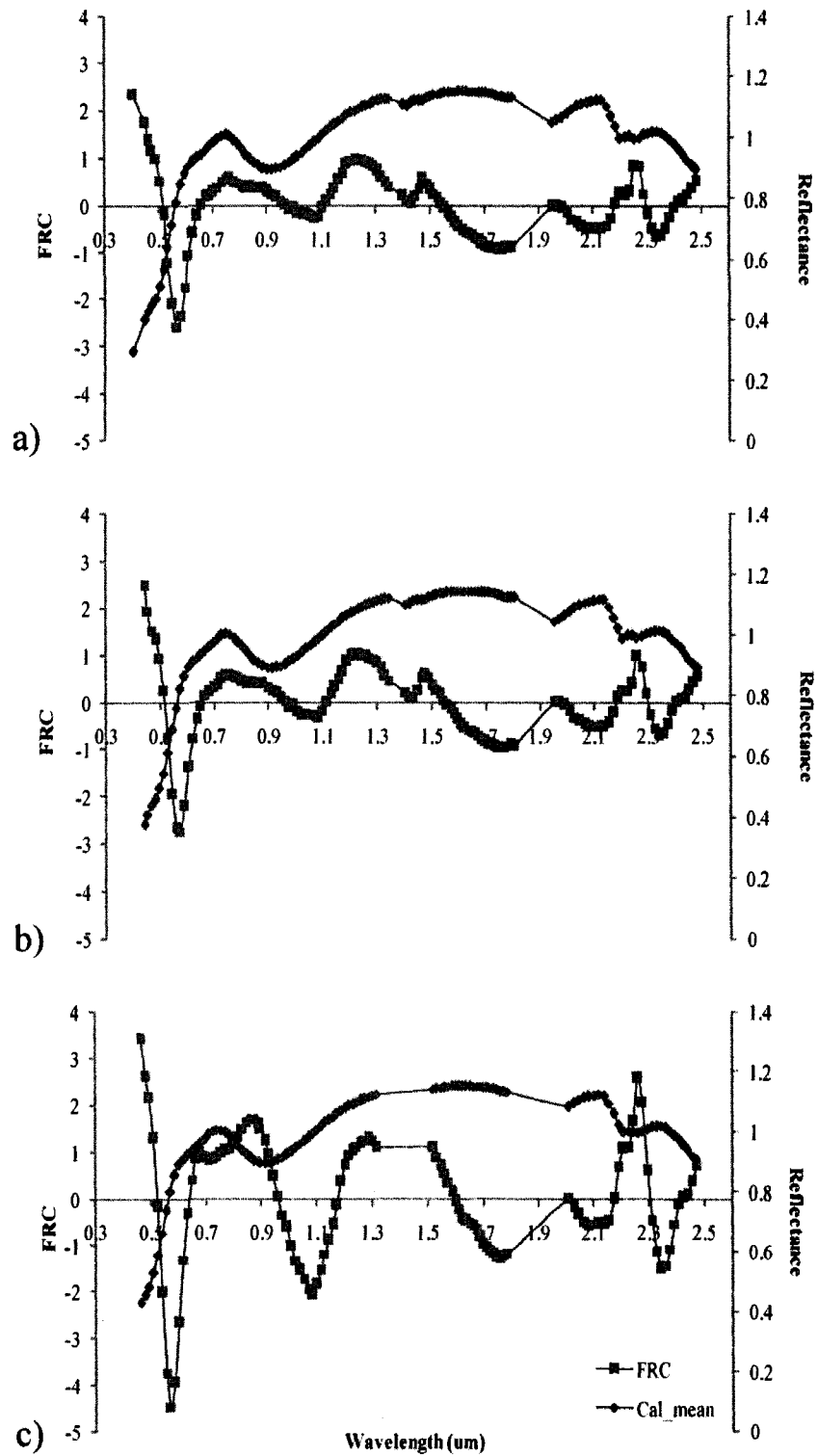
Appendix 3.5: XRD results for samples used in this study

Sample	Minerals Identified by XRD analysis	Sample	Minerals Identified by XRD analysis
A04-07	Quartz, syn (SiO ₂)	A04-36	Quartz, syn (SiO ₂)
	Goethite (Fe+3O(OH))		Albite, calcian, ordered ((Na,Ca)Al(Si,Al)3O8)
	Muscovite-2M1 (KAl ₂ (Si ₃ Al)O ₁₀ (OH,F)2)		Orthoclase (KAlSi ₃ O ₈)
A04-08	Gypsum, syn (CaSO ₄ ·2H ₂ O)	A04-37	Quartz, syn (SiO ₂)
	Kalolinite-1A (Al ₂ Si ₂ O ₅ (OH)4)		Clinocllore-1Mllb ((Mg ₅ Al)(Si,Al)4O ₁₀ (OH)8)
	Quartz, syn (SiO ₂)		Muscovite-3T ((K,Na)(Al,Mg,Fe)2(Si ₃ .1Al _{0.9})O ₁₀ (OH)2)
A04-09	Hematite, syn (Fe ₂ O ₃)	A04-43	Sekaninaite, syn (Fe ₂ Al ₄ Si ₅ O ₁₈)
	Goethite (Fe+3O(OH))		Albite, disordered (Na(Si ₃ Al)O ₈)
	Quartz, syn (SiO ₂)		Muscovite-2M1 (KAl ₂ (Si ₃ Al)O ₁₀ (OH,F)2)
A04-14	Chlorite-serpentine ((Mg,Al)6(Si,Al)4O ₁₀ (OH)8)	A04-44	Quartz, syn (SiO ₂)
	Jarosite, hydronian ((K, H ₃ O)Fe ₃ (SO ₄) ₂ (OH)6)		Kalolinite-1A (Al ₂ Si ₂ O ₅ (OH)4)
	Muscovite-2M1 (KAl ₂ (Si ₃ Al)O ₁₀ (OH,F)2)		Hematite, syn (Fe ₂ O ₃)
A04-18	Rutile, syn (TiO ₂)	A04-47	Rutile, syn (TiO ₂)
	Quartz, syn (SiO ₂)		Muscovite-2M1 (KAl ₂ (Si ₃ Al)O ₁₀ (OH,F)2)
	Muscovite-2M1 (KAl ₂ (Si ₃ Al)O ₁₀ (OH,F)2)		Clinocllore-1Mla, ferroan ((Mg,Fe,Al)6(Si,Al)4O ₁₀ (OH)8)
A04-20	Clinocllore-1Mllb, ferroan ((Mg,Fe)6(Si,Al)4O ₁₀ (OH)8)	J05-01	Quartz, syn (SiO ₂)
	Goethite (Fe+3O(OH))		Clinocllore-1Mllb ((Mg ₅ Al)(Si,Al)4O ₁₀ (OH)8)
	Anorthoclase, disordered ((Na,K)(Si ₃ Al)O ₈)		Albite, calcian, ordered ((Na,Ca)Al(Si,Al)3O8)
A04-21	Hematite, syn (Fe ₂ O ₃)	J05-02	Paragonite-2M1 (NaAl ₂ (AlSi ₃)O ₁₀ (OH)2)
	Quartz, syn (SiO ₂)		Muscovite-2M1 (KAl ₂ (Si ₃ Al)O ₁₀ (OH,F)2)
	Jarosite, hydronian ((K, H ₃ O)Fe ₃ (SO ₄) ₂ (OH)6)		Quartz, syn (SiO ₂)
A04-22	Muscovite-2M2, calcian (K,Ca,Na)(Al,Mg,Fe)2(Si,Al)4O ₁₀ (OH)2	J05-04	Chlorite-serpentine (Mg,Al)6(Si,Al)4O ₁₀ (OH)8)
	Hematite, syn (Fe ₂ O ₃)		Jarosite, hydronian ((K, H ₃ O)Fe ₃ (SO ₄) ₂ (OH)6)
	Quartz, syn (SiO ₂)		Muscovite-2M1 (KAl ₂ (Si ₃ Al)O ₁₀ (OH,F)2)
A04-27	Jarosite, hydronian ((K, H ₃ O)Fe ₃ (SO ₄) ₂ (OH)6)	J05-05	Rutile, syn (TiO ₂)
	Muscovite-2M1 (KAl ₂ (Si ₃ Al)O ₁₀ (OH,F)2)		Pyrite (FeS ₂)
	Rutile, syn (TiO ₂)		Richterite, potassian, syn (Na(CaK)Mg ₅ Si ₈ O ₂₂ (OH)2)
A04-29	Muscovite-2M1 (KAl ₂ (Si ₃ Al)O ₁₀ (OH,F)2)	A04-31	Chlorite-serpentine (Mg,Al)6(Si,Al)4O ₁₀ (OH)8)
	Jarosite, hydronian ((K, H ₃ O)Fe ₃ (SO ₄) ₂ (OH)6)		Albite, ordered (NaAlSi ₃ O ₈)
	Muscovite-2M1 (KAl ₂ (Si ₃ Al)O ₁₀ (OH,F)2)		Actinolite (Ca ₂ (Mg,Fe+2) ₅ Si ₈ O ₂₂ (OH)2)
A04-33	Gypsum, syn (CaSO ₄ ·2H ₂ O)	A04-34	Muscovite-1M, syn (KAl ₂ Si ₃ AlO ₁₀ (OH)2)
	Rutile, syn (TiO ₂)		Quartz, syn (SiO ₂)
	Kalolinite-1A (Al ₂ Si ₂ O ₅ (OH)4)		Albite, low (Na(AlSi ₃ O ₈))
A04-34	Kalolinite-1A (Al ₂ Si ₂ O ₅ (OH)4)	A04-33	Muscovite-2M1, vanadian (K(Al,V)2(Si,Al)4O ₁₀ (OH)2)
	Rutile, syn (TiO ₂)		Clinocllore-1Mllb ((Mg ₅ Al)(Si,Al)4O ₁₀ (OH)8)
	Pyrite (FeS ₂)		Pyrite (FeS ₂)
A04-31	Quartz, syn (SiO ₂)	A04-33	Muscovite-1M, syn (KAl ₂ Si ₃ AlO ₁₀ (OH)2)
	Muscovite-2M1 (KAl ₂ (Si ₃ Al)O ₁₀ (OH,F)2)		Chlorite-serpentine (Mg,Al)6(Si,Al)4O ₁₀ (OH)8)
	Rutile, syn (TiO ₂)		Albite, ordered (NaAlSi ₃ O ₈)
A04-33	Clinocllore-1Mllb ((Mg ₅ Al)(Si,Al)4O ₁₀ (OH)8)	A04-33	Actinolite (Ca ₂ (Mg,Fe+2) ₅ Si ₈ O ₂₂ (OH)2)
	Quartz, syn (SiO ₂)		Muscovite-1M, syn (KAl ₂ Si ₃ AlO ₁₀ (OH)2)
	Clinocllore-1Mllb, ferroan ((Mg,Fe)6(Si,Al)4O ₁₀ (OH)8)		
A04-34	Muscovite-2M1 (KAl ₂ (Si ₃ Al)O ₁₀ (OH,F)2)		
	Quartz, syn (SiO ₂)		
	Muscovite-2M1 (KAl ₂ (Si ₃ Al)O ₁₀ (OH,F)2)		

Sample	Minerals identified by XRD analysis	Sample	Minerals identified by XRD analysis
J05-06	Gypsum, syn (CaSO4·2H2O)	J05-25	Clinocllore-1Mllb ((Mg5Al)(Si,Al)4O10(OH)8)
	Hexahydrite, syn (MgSO4·6H2O)		Albite, ordered (NaAlSi3O8)
	Pickeringite (MgAl2(SO4)4·22H2O)		Dolomite (CaMg(CO3)2)
	Quartz, syn (SiO2)		Hastingsite, chlorian potassiau ((K,Na)Ca2(Fe,Mg)5(Si,Al)8O22C12)
	Jarosite, syn (KFe3(SO4)2(OH)6)		Quartz, syn (SiO2)
J05-08	Goethite (Fe+3O(OH))	J05-28	Melanterite, syn (Fe+2SO4·7H2O)
	Muscovite-2M1 (KAl2(Si3Al)O10(OH,F)2)		Montroyalite (Si4Al8(CO3)3[(OH,F)]26·11H2O)
	Quartz, syn (SiO2)		Alumohydrocalcite (CaAl2(CO3)2(OH)4·3H2O)
Clinocllore-1Mllb ((Mg5Al)(Si,Al)4O10(OH)8)	Silinaite (LiNaSi2O5·2H2O)		
	Quartz, syn (SiO2)		Koninckite (Fe+3PO4·3H2O)
J05-09	Albite, ordered (NaAlSi3O8)		Pargasite, potassiau (Na,K)Ca2(Mg,Fe)4Al(Si6Al2)O23)
	Muscovite-2M1 (KAl2(Si3Al)O10(OH,F)2)		Calkinsite-(Ce) ((Ce,La)2(CO3)3·4H2O)
	Orthoclase (KAlSi3O8)		Sigloite (FeAl2(PO4)2(O,OH)2·8H2O)
	Quartz, syn (SiO2)	J05-29	Szomohokite, syn (FeSO4·H2O)
Albite, ordered (NaAlSi3O8)			Zirkelite, syn (CaZrTi2O7)
Clinocllore-1Mllb ((Mg5Al)(Si,Al)4O10(OH)8)			Kalolinite-1A (Al2Si2O5(OH)4)
Muscovite-2M1 (KAl2(Si3Al)O10(OH,F)2)			Peisleyite (Na3Al16(SO4)2(PO4)10(OH)17·20H2O)
J05-14	Gypsum, syn (CaSO4·2H2O)		Magnesiocarpholite, syn (MgAl2Si2O6(OH)4)
	Quartz, syn (SiO2)		Petalite-1M (LiAlSi4O10)
	Starkeyite, syn (MgSO4·4H2O)		Analcime M (NaAlSi2O6·xH2O)
	Natrojarosite, syn (NaFe3(SO4)2(OH)6)	J05-30	Quartz, syn (SiO2)
	Pyrite (FeS2)		Muscovite-2M1 (KAl2(Si3Al)O10(OH,F)2)
	Albite, disordered (Na(Si3Al)O8)		Clinocllore-1Mllb, ferroan ((Mg,Fe)6(Si,Al)4O10(OH)8)
	Potassiumalum, syn (KAl(SO4)2·12H2O)	J05-32	Quartz, syn (SiO2)
	Gypsum, syn (CaSO4·2H2O)		Muscovite-2M1 (KAl2(Si3Al)O10(OH,F)2)
	Quartz, syn (SiO2)		Kalolinite-1A (Al2Si2O5(OH)4)
J05-15	Starkeyite, syn (MgSO4·4H2O)		Goethite (Fe+3O(OH))
	Natrojarosite, syn (NaFe3(SO4)2(OH)6)		Rutile, syn (TiO2)
	Albite, ordered (NaAlSi3O8)	J05-35	Quartz, syn (SiO2)
	Chlorite-serpentine (Mg,Al)6(Si,Al)4O10(OH)8)		
	Muscovite-2M1 (KAl2(Si3Al)O10(OH,F)2)		
	Goethite (Fe+3O(OH))		
J05-19	Hematite, syn (Fe2O3)		Kalolinite-1A (Al2Si2O5(OH)4)
	Franklinite, syn (ZnFe2O4)		Jarosite, hydronian ((K, H3O)Fe3(SO4)2(OH)6)
	Gypsum, syn (CaSO4·2H2O)	J05-37	Quartz, syn (SiO2)
	Maghemite-Q, syn (Fe2O3)		Illite-2M1 ((K,H3O)Al2Si3AlO10(OH)2)
	Quartz, syn (SiO2)		Kalolinite-1A (Al2Si2O5(OH)4)
	Hexahydrite, syn (MgSO4·6H2O)		Goethite (Fe+3O(OH))
	Jarosite, syn (KFe3(SO4)2(OH)6)		
	Clinocllore-1Mllb, ferroan ((Mg,Fe)6(Si,Al)4O10(OH)8)		
	Albite, disordered (Na(Si3Al)O8)		Obertiite (Na3(Mg3Fe+3Ti+4)Si8O22O2)
J05-20	Polyhalite (K2Ca2Mg(SO4)4·2H2O)		Muscovite-2M1 (KAl2(Si3Al)O10(OH,F)2)
	Kalolinite-1A (Al2Si2O5(OH)4)		Dolomite (CaMg(CO3)2)
	Albite, ordered (NaAlSi3O8)	J05-38	Chlorite-serpentine (Mg,Al)6(Si,Al)4O10(OH)8)
	Brushite, syn (CaPO3(OH)·2H2O)		Quartz, syn (SiO2)
	Jarosite, syn (KFe3(SO4)2(OH)6)		Illite-2M1 ((K, H3O)Al2Si3AlO10(OH)2)
	Edenite (NaCa2Mg5AlSi7O22(OH)2)		Hematite, syn (Fe2O3)
	Clinocllore-1Mlla, ferroan ((Mg,Fe,Al)6(Si,Al)4O10(OH)8)		Jarosite, syn (KFe3(SO4)2(OH)6)
			Rutile, syn (TiO2)
		Muscovite-2M1 (KAl2(Si3Al)O10(OH,F)2)	
		Muscovite-2M1, ammonian ((K,NH4,Na)Al2(Si,Al)4O10(OH)2)	
J05-23	Hematite, syn (Fe2O3)		Ojuelait (ZnFe2+3(AsO4)2(OH)2·4H2O)
	Maghemite-C, syn (Fe2O3)		Orthoclase (KAlSi3O8)
	Gunningite, syn (ZnSO4·H2O)		
	Jarosite, syn (KFe3(SO4)2(OH)6)		
	Quartz, syn (SiO2)		
J05-24	Hematite, syn (Fe2O3)		
	Maghemite-C, syn (Fe2O3)		
	Gunningite, syn (ZnSO4·H2O)		
	Jarosite, hydronian ((K, H3O)Fe3(SO4)2(OH)6)		
	Gypsum, syn (CaSO4·2H2O)		

Sample	Minerals Identified by XRD analysis	Sample	Minerals Identified by XRD analysis
J05-39	Quartz, syn (SiO ₂)	J05-50	Rozenite (FeSO ₄ ·4H ₂ O)
	Chlorite-serpentine ((Mg,Al) ₆ (Si,Al) ₄ O ₁₀ (OH) ₈)		Quartz, syn (SiO ₂)
	Hematite, syn (Fe ₂ O ₃)		Starkeyite, syn (MgSO ₄ ·4H ₂ O)
	Illite-2M1 ((K,H ₃ O)Al ₂ Si ₃ AlO ₁₀ (OH) ₂)		Pyrite (FeS ₂)
	Ferrihydrite, syn (Fe ₅ O ₇ (OH)·4H ₂ O)		Meixnerite ((Mg ₅ Al ₃ (OH) ₁₆)((OH) ₃ (H ₂ O) ₄))
	Anhydrite, syn (CaSO ₄)		Szomolnokite, syn (FeSO ₄ ·H ₂ O)
J05-40	Anatase, syn (TiO ₂)	J05-51	Copiapite (FeFe ₄ (SO ₄) ₆ (OH) ₂ ·2H ₂ O)
	Rutile, syn (TiO ₂)		Polythionite-1M, ferroan (K(AlFeLi)(Si ₃ Al)O ₁₀ (OH)F)
	Gypsum, syn (CaSO ₄ ·2H ₂ O)		Quartz, syn (SiO ₂)
	Hexahydrate, syn (MgSO ₄ ·6H ₂ O)		Chlorite-serpentine ((Mg,Al) ₆ (Si,Al) ₄ O ₁₀ (OH) ₈)
J04-41	Quartz, syn (SiO ₂)	J05-52	Muscovite-2M1 (KAl ₂ (Si ₃ Al)O ₁₀ (OH,F) ₂)
	Clinocllore-1Mllb ((Mg ₅ Al)(Si,Al) ₄ O ₁₀ (OH) ₈)		Brushite, syn (CaPO ₃ (OH)·2H ₂ O)
	Albite disordered (Na(Si ₃ Al)O ₈)		Quartz, syn (SiO ₂)
	Dolomite (CaMg(CO ₃) ₂)		Muscovite-2M1 (KAl ₂ (Si ₃ Al)O ₁₀ (OH,F) ₂)
J05-42	Magnesiolarvedsonite ((Na,K) ₃ (Fe,Mg,Al) ₅ Si ₈ O ₂₂ (F,OH) ₂)	J05-53	Clinocllore-1Mllb ((Mg ₅ Al)(Si,Al) ₄ O ₁₀ (OH) ₈)
	Hematite, syn (Fe ₂ O ₃)		Quartz, syn (SiO ₂)
	Quartz, syn (SiO ₂)		Muscovite-2M1 (KAl ₂ (Si ₃ Al)O ₁₀ (OH,F) ₂)
	Jarosite, hydronian ((K, H ₃ O)Fe ₃ (SO ₄) ₂ (OH) ₆)		Anandite-2M1 (BaFe ₃ +2(Si,Fe) ₄ (O,OH) ₁₀ (OH) ₅)
J05-43	Illite-2M2 (KAl ₂ (Si ₃ Al)O ₁₀ (OH) ₂)	J05-54	Jarosite, hydronian ((K, H ₃ O)Fe ₃ (SO ₄) ₂ (OH) ₆)
	Quartz, syn (SiO ₂)		Clinocllore-1Mllb, ferroan ((Mg,Fe) ₆ (Si,Al) ₄ O ₁₀ (OH) ₈)
	Muscovite-3T ((K,Na)(Al,Mg,Fe) ₂ (Si ₃ Al _{0.9})O ₁₀ (OH) ₂)		Quartz, syn (SiO ₂)
	Jarosite, syn (KFe ₃ (SO ₄) ₂ (OH) ₆)		Hematite, syn (Fe ₂ O ₃)
J05-44	Goethite (Fe ₃ O(OH))	J05-55	Natrojarosite, syn (NaFe ₃ (SO ₄) ₂ (OH) ₆)
	Hematite, syn (Fe ₂ O ₃)		Moutmorillonite-18A (Na _{0.3} (AlMg) ₂ Si ₄ O ₁₀ H ₂ ·6H ₂ O)
	Quartz, syn (SiO ₂)		Nonisilite-1M (KMn ₂ +3LiSi ₄ O ₁₂)
	Ferriccopiapite (Fe ₄ .67(SO ₄) ₆ (OH) ₂ ·2H ₂ O)		Kintoreite (PbFe ₃ (PO ₄) ₂ (OH) ₂ (H ₂ O) ₆)
J05-45	Jarosite, hydronian ((K, H ₃ O)Fe ₃ (SO ₄) ₂ (OH) ₆)	J05-56	Gedrite ((Fe,Mg,Al) ₇ Al ₂ Si ₆ O ₂₂ (OH) ₂)
	Plumbojarosite (PbFe ₆ (SO ₄) ₄ (OH) ₁₂)		Siderite (FeSO ₄ ·5H ₂ O)
	Hematite, syn (Fe ₂ O ₃)		Quartz, syn (SiO ₂)
	Quartz, syn (SiO ₂)		Muscovite-1M, syn (KAl ₂ Si ₃ AlO ₁₀ (OH) ₂)
J05-46	Vajdakite (((Mo+6O ₂) ₂ As ₂ +3) ₅ (H ₂ O) ₂):H ₂ O)	J05-57	Plumbojarosite (PbFe ₆ (SO ₄) ₄ (OH) ₁₂)
	Aluminocopiapite ((Mg,Al)(Fe+3,Al) ₄ (SO ₄) ₆ (OH) ₂ ·2H ₂ O)		Hematite, syn (Fe ₂ O ₃)
	Strunzite (MnFe ₂ (PO ₄) ₂ (OH) ₂ ·6H ₂ O)		Illite-2M1 ((K,H ₃ O)Al ₂ Si ₃ AlO ₁₀ (OH) ₂)
	Quartz, syn (SiO ₂)		Hematite, syn (Fe ₂ O ₃)
J05-47	Hematite, syn (Fe ₂ O ₃)	J05-58	Quartz, syn (SiO ₂)
	Magnesiocopiapite (MgFe ₄ +3(SO ₄) ₆ (OH) ₂ ·2H ₂ O)		Pyrite (FeS ₂)
	Glaucophane (Na ₂ Mg ₃ Al ₂ Si ₈ O ₂₂ (OH) ₂)		Clinocllore-1Mllb, ferroan ((Mg,Fe) ₆ (Si,Al) ₄ O ₁₀ (OH) ₈)
	Jarosite, syn (KFe ₃ (SO ₄) ₂ (OH) ₆)		Muscovite-3T ((K,Na)(Al,Mg,Fe) ₂ (Si ₃ Al _{0.9})O ₁₀ (OH) ₂)
J05-48	Muscovite-2M1 (KAl ₂ (Si ₃ Al)O ₁₀ (OH,F) ₂)	J05-59	Gismondine (CaAl ₂ Si ₂ O ₈ ·4H ₂ O)
	Quartz, syn (SiO ₂)		Illite-2M1 ((K,H ₃ O)Al ₂ Si ₃ AlO ₁₀ (OH) ₂)
	Chlorite-serpentine ((Mg,Al) ₆ (Si,Al) ₄ O ₁₀ (OH) ₈)		Rutile, syn (TiO ₂)
	Muscovite-2M1 (KAl ₂ (Si ₃ Al)O ₁₀ (OH,F) ₂)		Quartz, syn (SiO ₂)
J04-49	Hematite, syn (Fe ₂ O ₃)	J05-59	Hematite, syn (Fe ₂ O ₃)
	Jarosite, syn (KFe ₃ (SO ₄) ₂ (OH) ₆)		Anglesite, syn (PbSO ₄)
	Pyrite (FeS ₂)		Ferriccopiapite (Fe ₄ .67(SO ₄) ₆ (OH) ₂ ·2H ₂ O)
	Quartz, syn (SiO ₂)		Natrojarosite, syn (NaFe ₃ (SO ₄) ₂ (OH) ₆)
J05-49	Anglesite, syn (PbSO ₄)	J05-59	Cocumbite (Fe ₂ +3(SO ₄) ₃ ·9H ₂ O)
	Sulfur, syn (S)		Szomolnokite, syn (FeSO ₄ ·H ₂ O)
	Rhombochlore, syn (FeH(SO ₄) ₂ ·4H ₂ O)		Spencerite (Zn ₄ (PO ₄) ₂ (OH) ₂ ·3H ₂ O)
	Hematite, syn (Fe ₂ O ₃)		Alunogen (Al ₂ (SO ₄) ₃ ·17H ₂ O)
J04-49	Jarosite, hydronian ((K, H ₃ O)Fe ₃ (SO ₄) ₂ (OH) ₆)	J05-59	Penkviksite-2O (Na ₄ Ti ₂ Si ₈ O ₂₂ ·4H ₂ O)
	Gypsum, syn (CaSO ₄ ·2H ₂ O)		Howieite (Na(Fe+2,Mn) ₁₀ (Fe+3,Al) ₂ Si ₁₂ O ₃₁ (OH) ₁₃)
	Muscovite-2M1 (KAl ₂ (Si ₃ Al)O ₁₀ (OH,F) ₂)		
	Quartz, syn (SiO ₂)		

Appendix 5.1: FRC and spectral reflectance of the mean calibration spectrum for the Brukunga model resampled to Hymap resolutions of Sotiel-Migollas imagery: a) 1999; b) 2004; c) 2005.



Appendix 5.2: Calibration models using the full spectrum of all 40 samples (Set 1 – group 1).

Calibration - Normalization MEAN=1 ASD resolution, 40 spectra samples Full spectrum, No H2O vapor bands														
Number of selected spectra (samples)	Number of channels	CV Number of factors after AUTO	Optimal #factor after running CV	F prob	Outlier F prob	Removed Outlier samples	Minimum FRC	Measured vs predicted Correl. (R)	Measured vs predicted RMS error	Param Outliers detected	Spec Outliers detected	score scatterplots RAW data outliers	score scatterplots Mahalanobis distance outliers	PLS file name
40	1869	39	9	0.25	0.9	-	-	0.758439	1.1898	32, 39	14	none	none	pls-40sp-9fc-1869ch.pls
40	1635	39	8	0.25	0.9	-	0.025	0.730296	1.23366	13, 32, 39	33	none	none	pls-40sp-8fc-1635ch.pls
40	1635	39	9	4.77E-14	0.9	-	-	0.757937	1.19266	32, 39	14	none	none	pls-40sp-9fc-1635ch.pls
40	1452	39	9	4.77E-14	0.9	-	0.05	0.765327	1.17676	32, 39	3, 14, 40	none	none	pls-40sp-9fc-1452ch.pls
40	1312	39	9	4.77E-14	0.9	-	0.075	0.769354	1.16621	32, 39	14, 40	none	none	pls-40sp-9fc-1312ch.pls
40	1123	39	8	4.77E-14	0.9	-	0.1	0.770296	1.1453	32, 39	13	none	none	pls-40sp-8fc-1123ch.pls
40	1123	39	9	0.0311258	0.9	-	-	0.774264	1.15243	32, 39	14, 40	none	none	pls-40sp-9fc-1123ch.pls
40	1039	39	8	4.77E-14	0.9	-	0.075	0.775162	1.13354	39	1, 13, 14	none	none	pls-40sp-8fc-1039ch.pls
40	986	39	8	4.77E-14	0.9	-	0.1	0.783428	1.11461	32, 39	1, 13, 14	none	none	pls-40sp-8fc-986ch.pls
40	862	39	8	4.77E-14	0.9	-	0.125	0.793023	1.09329	10, 32, 39	1, 14	none	none	pls-40sp-8fc-862ch.pls
40	785	39	8	4.77E-14	0.9	-	0.15	0.800517	1.07673	10, 32, 39	1, 14, 33	none	none	pls-40sp-8fc-785ch.pls
40	690	39	10	4.77E-14	0.9	-	0.175	0.797602	1.08464	10, 32, 33, 39, 40	20	25	25	pls-40sp-10fc-690ch.pls
40	690	39	8	0.275683	0.9	-	-	0.7718	1.14727	32, 33, 39	33	25	25	pls-40sp-8fc-690ch.pls

Appendix 5.3: Calibration models using the VNIR of all 40 samples (Set 1 – group 2).

ASD resolution, 40 spectra samples VNIR, No H2O vapor bands - VNIR Bands 1 to 1000														
Calibration - Normalization MEAN=1														
Nb of selected spectra (samples)	Nb of channels	CV Number of factors after	Optimal #factor after running CV	F prob	Outlier F prob	Removed Outlier samples	Minimum FRC	Measured vs predicted Correl. (R)	Measured vs predicted RMS error	Param Outliers detected	Spec Outliers detected	score scatterplots RAW data outliers	score scatterplots Mahalanobis distance outliers	PLS File name
40	1000	26	7	0.25	0.9	-	-	0.712176	1.26211	31, 36, 39, 40	13, 14	none	none	pls-40sp-7fc-1000ch.pls
40	945	27	7	2.50E-01	0.9	-	0.025	0.714814	1.25707	31, 36, 39, 40	13, 14	none	none	pls-40sp-7fc-945ch.pls
40	892	26	7	2.50E-01	0.9	-	0.05	0.71713	1.25265	31, 36, 39, 40	13, 14	none	none	pls-40sp-7fc-892ch.pls
40	810	26	7	2.50E-01	0.9	-	0.075	0.722672	1.24204	31, 36, 39, 40	13, 14, 21	15	15	pls-40sp-7fc-810ch.pls
40	758	27	7	2.50E-01	0.9	-	0.1	0.726806	1.23398	31, 36, 39, 40	13, 14, 21	15	15	pls-40sp-7fc-758ch.pls
40	682	26	7	2.50E-01	0.9	-	0.125	0.735085	1.2181	31, 36, 39, 40	13, 14, 21	15	15	pls-40sp-7fc-682ch.pls
40	574	27	7	2.50E-01	0.9	-	0.15	0.759207	1.17055	31, 36, 39, 40	14, 15, 21	15	15	pls-40sp-7fc-574ch.pls
40	505	27	6	2.50E-01	0.9	-	0.15	0.753195	1.18266	31, 36, 39, 40	14, 15, 35	19	19	pls-40sp-6fc-505ch.pls
40	505	27	7	4.77E-14	0.9	-	-	0.761204	1.17	31, 36, 39, 40	15, 19, 21	19	19	pls-40sp-7fc-505ch.pls
40	471	26	7	4.77E-14	0.9	-	0.175	0.76546	1.16165	31, 36, 39, 40	14, 19, 21	19	19	pls-40sp-7fc-471ch.pls
40	444	26	7	4.77E-14	0.9	-	0.2	0.769361	1.15519	31, 36, 39, 40	14, 19, 21	19	19	pls-40sp-7fc-444ch.pls
40	425	26	7	4.77E-14	0.9	-	0.225	0.778639	1.13487	31, 36, 39, 40	14, 21, 38	19	19	pls-40sp-7fc-425ch.pls
40	382	24	6	4.77E-14	0.9	-	0.25	0.77434	1.13694	31, 36, 39, 40	14	19	pls-40sp-6fc-382ch.pls	
40	346	25	6	4.77E-14	0.9	-	0.25	0.778609	1.12727	31, 36, 39, 40	14, 15	19	19	pls-40sp-6fc-346ch.pls
40	339	23	6	4.77E-14	0.9	-	0.25	0.780495	1.12287	31, 36, 39, 40	14, 15	19	19	pls-40sp-6fc-339ch.pls
40	324	24	7	4.77E-14	0.9	-	0.3	0.782761	1.12177	31, 36, 39, 40	14, 21, 31	19	19	pls-40sp-7fc-324ch.pls
40	324	24	6	0.003875	0.9	-	0.325	0.780636	1.12264	31, 36, 39, 40	14, 15	19	19	pls-40sp-6fc-324ch.pls
40	304	22	6	0.003875	0.9	-	0.35	0.781857	1.11989	31, 36, 39, 40	14, 15	19	19	pls-40sp-6fc-304ch.pls
40	298	23	6	0.007517	0.9	-	0.375	0.782337	1.11886	31, 36, 39, 40	14, 15	19	19	pls-40sp-6fc-298ch.pls
40	282	21	6	0.003875	0.9	-	0.4	0.781953	1.11988	31, 36, 39, 40	14, 15	19	19	pls-40sp-6fc-282ch.pls
40	273	21	6	0.003875	0.9	-	0.425	0.782799	1.11809	31, 36, 39, 40	14, 15	19	19	pls-40sp-6fc-273ch.pls
40	261	21	6	0.003875	0.9	-	0.475	0.783324	1.11698	31, 36, 39, 40	14, 15	19	19	pls-40sp-6fc-261ch.pls
40	253	21	6	0.003875	0.9	-	0.5	0.782281	1.11955	31, 36, 39, 40	14, 15	19	19	pls-40sp-6fc-253ch.pls
40	234	21	6	0.003875	0.9	-	0.525	0.783255	1.11743	31, 36, 39, 40	14, 15	19	19	pls-40sp-6fc-234ch.pls
40	224	21	6	0.003875	0.9	-	0.55	0.784027	1.1157	31, 36, 39, 40	14, 15	19	19	pls-40sp-6fc-224ch.pls
40	214	20	6	0.003875	0.9	-	0.6	0.783005	1.11819	31, 36, 39, 40	14, 15	19	19	pls-40sp-6fc-214ch.pls
40	203	20	6	0.003875	0.9	-	0.625	0.784459	1.11486	31, 36, 39, 40	14, 15	19	19	pls-40sp-6fc-203ch.pls
40	193	18	6	0.003875	0.9	-	0.65	0.785111	1.11328	31, 36, 39, 40	14, 15	19	19	pls-40sp-6fc-193ch.pls
40	184	19	6	0.003875	0.9	-	0.7	0.784695	1.11428	31, 36, 39, 40	14, 15	19	19	pls-40sp-6fc-184ch.pls
40	176	18	6	0.003875	0.9	-	0.725	0.785047	1.11348	31, 36, 39, 40	14, 15	19	19	pls-40sp-6fc-176ch.pls
40	171	18	6	0.003875	0.9	-	0.75	0.785443	1.11227	31, 36, 39, 40	14, 15	19	19	pls-40sp-6fc-171ch.pls
40	169	18	6	0.003875	0.9	-	0.775	0.78291	1.11846	31, 36, 39, 40	14, 15	19	19	pls-40sp-6fc-169ch.pls
40	152	19	6	0.003875	0.9	-	0.775	0.78523	1.11261	31, 36, 39, 40	12, 14, 15	19	19	pls-40sp-6fc-152ch.pls
40	146	18	6	0.003875	0.9	-	0.775	0.785847	1.11117	31, 36, 39, 40	12, 14, 15, 19	19	19	pls-40sp-6fc-146ch.pls

Appendix 5.4: Calibration models using the full spectrum and removing parameter outliers from the first model (Set 2 – group 1).

Calibration - Normalization MEAN=1 ASD resolution, 40 spectra samples Full spectrum, No H2O vapor bands														
Number of selected spectra (samples)	Number of channels	CV Number of factors After AUTO	Optimal #factor after running CV	F prob	Outlier F prob	Removed Outlier samples	Minimum FRC	Measured vs predicted Correl. (R)	Measured vs predicted RMS error	Param Outliers detected	Spec Outliers detected	score scatterplots - RAW data outliers	score scatterplots - Mahalanobis distance outliers	PLS file name
40	1869	39	9	0.25	0.9	-	-	0.758439	1.1898	32, 39	14	none	none	pls-40sp-9fc-1869ch.pls
38	1869	37	9	0.25	0.9	32, 39	-	0.854495	0.895044	9, 10, 13, 34	14	none	none	pls-38sp-9fc-1869ch.pls
38	1712	37	9	0.25	0.9	32, 39	0.01	0.866574	0.869741	9, 10, 13, 34	14, 33	none	none	pls-38sp-9fc-1712ch.pls
38	1643	37	9	0.25	0.9	32, 39	0.02	0.861096	0.879503	9, 10, 13, 34	13, 14	none	none	pls-38sp-9fc-1643ch.pls
38	1577	37	8	0.25	0.9	32, 39	0.03	0.854052	0.893505	10, 13, 34	1	none	none	pls-38sp-8fc-1577ch.pls
38	1436	37	8	0.25	0.9	32, 39	0.03	0.860678	0.876081	6, 10, 13, 15, 34	1	none	none	pls-38sp-8fc-1436ch.pls
38	1400	37	9	0.25	0.9	32, 39	0.04	0.869391	0.862831	1, 10, 13, 34	13, 14, 40	none	none	pls-38sp-9fc-1400ch.pls
38	1349	37	8	0.25	0.9	32, 39	0.04	0.868046	0.852374	6, 10, 13, 15, 34	1, 14	none	none	pls-38sp-8fc-1349ch.pls
38	1309	37	8	0.25	0.9	32, 39	0.05	0.86781	0.854664	6, 10, 13, 15, 34	1, 14	none	none	pls-38sp-8fc-1309ch.pls
38	1205	37	11	0.25	0.9	32, 39	0.06	0.870141	0.85012	10, 34, 36	14, 25	none	none	pls-38sp-11fc-1205ch.pls
38	1018	37	8	0.25	0.9	32, 39	0.06	0.878046	0.818752	6, 9, 10, 13, 34	1, 14	none	none	pls-38sp-8fc-1018ch.pls
38	996	37	8	0.25	0.9	32, 39	0.07	0.87798	0.817688	6, 9, 10, 13, 34	1, 13, 14	none	none	pls-38sp-8fc-996ch.pls
38	980	37	9	0.25	0.9	32, 39	0.09	0.882584	0.816194	1, 6, 9, 10, 13, 34	14, 40	none	none	pls-38sp-9fc-980ch.pls
38	945	37	8	0.25	0.9	32, 39	0.1	0.882704	0.803614	6, 9, 10, 13, 36	1, 13, 14	none	none	pls-38sp-8fc-945ch.pls
38	918	37	9	0.25	0.9	32, 39	0.1	0.883057	0.818308	1, 9, 10, 13, 34	14, 40	none	none	pls-38sp-9fc-918ch.pls
38	900	37	9	0.25	0.9	32, 39	0.11	0.886443	0.804878	1, 9, 10, 13, 34	14	none	none	pls-38sp-9fc-900ch.pls
38	883	37	12	0.25	0.9	32, 39	0.12	0.900001	0.752537	10, 11, 34, 36	20, 33	none	none	pls-38sp-12fc-883ch.pls
38	673	37	8	0.25	0.9	32, 39	0.12	0.891493	0.775488	9, 10, 13, 33, 34	1, 14, 25, 33	none	none	pls-38sp-8fc-673ch.pls
38	667	37	8	0.25	0.9	32, 39	0.12	0.896099	0.755514	9, 10, 13, 34	1, 14, 33	none	none	pls-38sp-8fc-667ch.pls
38	664	37	8	0.25	0.9	32, 39	0.13	0.895753	0.757016	9, 10, 13, 34	1, 14, 33	none	none	pls-38sp-8fc-664ch.pls
38	657	37	8	0.25	0.9	32, 39	0.14	0.89761	0.74946	9, 10, 13, 34	1, 14, 33	none	none	pls-28sp-8fc-657ch.pls
38	653	37	7	0.25	0.9	32, 39	0.15	0.884277	0.793065	9, 10, 11, 13, 34	33, 40	none	none	pls-38sp-7fc-653ch.pls
38	627	37	7	0.25	0.9	32, 39	0.15	0.882763	0.798077	9, 10, 11, 13, 34	33, 40	none	none	pls-38sp-7fc-627ch.pls
38	621	37	7	0.25	0.9	32, 39	0.16	0.883542	0.795644	9, 10, 11, 13, 34	33, 40	none	none	pls-38sp-7fc-621ch.pls

Appendix 5.5: Calibration models using the full spectrum and removing parameter and spectral outliers from the first model (Set 2 – group 2).

Calibration - Normalization MEAN=1 ASD resolution, 40 spectra samples Full spectrum, No H2O vapor bands														
Number of selected spectra (samples)	Number of channels	CV Number of factors After AUTO	Optimal #factor after running CV	F prob	Outlier F prob	Removed Outlier samples	Minimum FRC	Measured vs predicted Correl. (R)	Measured vs predicted RMS error	Param Outliers detected	Spec Outliers detected	score scatterplots RAW data outliers	score scatterplots Mahalanobis distance outliers	PLS file name
40	1869	39	9	0.25	0.9	-	-	0.758439	1.1898	32, 39	14	none	none	pls-40sp-9fc-1869ch.pls
37	1869	36	9	0.25	0.9	14, 32,39	-	0.84433	0.917157	9, 10, 13, 34	1, 28	none	none	pls-37sp-9fc-1869ch.pls
37	1763	36	9	0.25	0.9	14, 32,39	0.01	0.848254	0.907409	9, 10, 13, 34	1, 28	25	25	pls-37sp-9fc-1763ch.pls
37	1643	36	8	0.25	0.9	14, 32,39	0.02	0.842704	0.923059	10,13, 34	1, 33	25	25	pls-37sp-8fc-1643ch.pls
37	1549	36	8	0.25	0.9	14, 32,39	0.02	0.841513	0.924935	10, 13, 15, 34	1, 33	25	25	pls-37sp-8fc-1549ch.pls
37	1497	36	8	0.25	0.9	14, 32,39	0.03	0.84173	0.923237	10, 13, 15, 34	1, 33	25	25	pls-37sp-8fc-1497ch.pls
37	1438	36	8	0.25	0.9	14, 32,39	0.04	0.841804	0.923291	10, 13, 15, 34	1, 33	25	25	pls-37sp-8fc-1438ch.pls
37	1363	36	8	0.25	0.9	14, 32,39	0.05	0.847402	0.905234	10, 13, 15, 34	1, 33	25	25	pls-37sp-8fc-1363ch.pls
37	1305	36	8	0.25	0.9	14, 32,39	0.06	0.8503	0.900497	10, 13, 15, 34	1, 33	25	25	pls-37sp-8fc-1305ch.pls
37	1234	36	8	0.25	0.9	14, 32,39	0.07	0.85571	0.885261	10, 13, 34	1	25	25	pls-37sp-8fc-1234ch.pls
37	1183	36	8	0.25	0.9	14, 32,39	0.08	0.862031	0.864022	10, 13, 15, 34	1	25	25	pls-37sp-8fc-1183ch.pls
37	1132	36	8	0.25	0.9	14, 32,39	0.09	0.864774	0.856008	10,13, 34	1	25	25	pls-37sp-8fc-1132ch.pls
37	1092	36	8	0.25	0.9	14, 32,39	0.1	0.868932	0.842694	10,13, 34	1	25	25	pls-37sp-8fc-1092ch.pls
37	1061	36	8	0.25	0.9	14, 32,39	0.11	0.870725	0.870725	6, 9, 10, 13, 34	1, 33	25	25	pls-37sp-8fc-1061ch.pls
37	1006	36	8	0.25	0.9	14, 32,39	0.12	0.872776	0.832063	6, 9, 10, 13, 34	1, 25, 33	25	25	pls-37sp-8fc-1006ch.pls
37	977	36	8	0.25	0.9	14, 32,39	0.13	0.874308	0.825728	9, 10, 13, 34	1, 25, 33	25	25	pls-37sp-8fc-977ch.pls
37	948	36	8	0.25	0.9	14, 32,39	0.14	0.874915	0.824442	6, 9, 10, 13, 34	1, 25, 33	25	25	pls-37sp-8fc-948ch.pls
37	911	36	7	0.25	0.9	14, 32,39	0.15	0.857654	0.86602	10, 13, 34	1, 40	25	25	pls-37sp-7fc-911ch.pls
37	733	36	7	0.25	0.9	14, 32,39	0.15	0.857767	0.86425	10, 13, 34	1, 33, 40	25	25	pls-37sp-7fc-733ch.pls
37	713	36	7	0.25	0.9	14, 32,39	0.15	0.859647	0.859164	9, 10, 13, 34	1, 33, 40	25	25	pls-37sp-7fc-713ch.pls

Appendix 5.6: Calibration model using the VNIR and removing parameter outliers from the first model (Set 2 – group 3).

Calibration - Normalization MEAN=1														
ASD resolution, 40 spectra samples VNIR, No H2O vapor bands - VNIR Bands 1 to 1000														
number of selected spectra (samples)	Number of channels	CV Number of factors after AUTO	Optimal #factor after running CV	F prob	Outlier F prob	Removed Outlier samples	Minimum FRC	Measured vs predicted Correl. (R)	Measured vs predicted RMS error	Param Outliers detected	Spec Outliers detected	score scatterplots RAW data outliers	score scatterplots Mahalanobis distance outliers	PLS file name
40	1000	26	7	0.25	0.9	-	-	0.712176	1.26211	31, 36, 39, 40	13, 14	none	none	pls-40sp-7fc-1000ch.pls
36	1000	26	8	0.25	0.9	31, 36, 39, 40	-	0.880883	0.742051	9, 14, 32, 33, 34	14, 33	none	none	pls-36sp-8fc-1000ch.pls
36	966	26	8	0.25	0.9	31, 36, 39, 40	0.25	0.881835	0.73921	9, 14, 32, 33, 34	14, 33	none	none	pls-36sp-8fc-966ch.pls
36	931	26	8	0.25	0.9	31, 36, 39, 40	0.5	0.882331	0.737717	9, 32, 33, 34	14, 33	none	none	pls-36sp-8fc-931ch.pls
36	889	26	8	0.25	0.9	31, 36, 39, 40	0.75	0.883678	0.733693	9, 32, 33, 34	14, 33	none	none	pls-36sp-8fc-889ch.pls
36	822	25	8	0.25	0.9	31, 36, 39, 40	0.1	0.884727	0.730583	9, 32, 33, 34	14, 33	none	none	pls-36sp-8fc-822ch.pls
36	784	26	8	0.25	0.9	31, 36, 39, 40	0.125	0.885804	0.727349	9, 32, 33, 34	14, 33	none	none	pls-36sp-8fc-784ch.pls
36	705	26	8	0.25	0.9	31, 36, 39, 40	0.15	0.888077	0.720543	9, 32, 33, 34	14, 33	none	none	pls-36sp-8fc-705ch.pls
36	659	26	8	0.25	0.9	31, 36, 39, 40	0.175	0.889749	0.715483	9, 10, 32, 33, 34	14, 33	none	none	pls-36sp-8fc-659ch.pls
36	630	27	8	0.25	0.9	31, 36, 39, 40	0.2	0.890994	0.711812	9, 10, 32, 33, 34	14, 33	none	none	pls-36sp-8fc-630ch.pls
36	540	26	8	0.25	0.9	31, 36, 39, 40	0.225	0.894655	0.700676	9, 10, 32, 33, 34	3, 33	15	15	pls-36sp-8fc-540ch.pls
36	464	25	7	0.25	0.9	31, 36, 39, 40	0.25	0.879617	0.745195	9, 10, 32	14, 33	15	15	pls-36sp-7fc-464ch.pls
36	393	25	6	0.25	0.9	31, 36, 39, 40	0.25	0.87852	0.748508	9, 10, 14, 32	14, 33	33	33	pls-36sp-6fc-393ch.pls
36	375	24	6	0.25	0.9	31, 36, 39, 40	0.275	0.878276	0.74183	9, 10, 14, 32	14, 33	33	33	pls-36sp-6fc-375ch.pls
36	366	23	6	0.25	0.9	31, 36, 39, 40	0.3	0.877111	0.752449	9, 10, 14, 32	14, 33	33	33	pls-36sp-6fc-366ch.pls
36	350	23	6	0.25	0.9	31, 36, 39, 40	0.325	0.87909	0.746687	9, 10, 14, 32	14, 33	33	33	pls-36sp-6fc-350ch.pls
36	339	24	6	0.25	0.9	31, 36, 39, 40	0.35	0.879662	0.745006	9, 10, 14, 32	14, 33	33	33	pls-36sp-6fc-339ch.pls
36	321	23	6	0.25	0.9	31, 36, 39, 40	0.375	0.879199	0.746333	9, 10, 14, 32	14, 33	none	none	pls-36sp-6fc-321ch.pls
36	305	23	6	0.25	0.9	31, 36, 39, 40	0.4	0.879799	0.74458	9, 10, 32	14, 33	none	none	pls-36sp-6fc-305ch.pls
36	287	23	6	0.25	0.9	31, 36, 39, 40	0.425	0.879479	0.7455	9, 10, 32	14, 33	none	none	pls-36sp-6fc-287ch.pls
36	279	23	6	0.25	0.9	31, 36, 39, 40	0.45	0.880386	0.742862	9, 10, 32	14, 33	none	none	pls-36sp-6fc-279ch.pls
36	264	23	6	0.25	0.9	31, 36, 39, 40	0.475	0.88057	0.742338	9, 10, 32	14, 33	none	none	pls-36sp-6fc-264ch.pls
36	259	23	6	0.25	0.9	31, 36, 39, 40	0.5	0.88123	0.740403	9, 10, 32	14, 33	none	none	pls-36sp-6fc-259ch.pls
36	242	22	6	0.25	0.9	31, 36, 39, 40	0.525	0.879801	0.744609	9, 10, 13, 32	14, 15, 33	none	none	pls-36sp-6fc-242ch.pls
36	239	22	6	0.25	0.9	31, 36, 39, 40	0.55	0.880484	0.742614	9, 10, 13, 32	14, 15, 33	none	none	pls-36sp-6fc-239ch.pls
36	191	20	6	0.25	0.9	31, 36, 39, 40	0.6	0.880595	0.743621	9,10, 32	14, 33	none	none	pls-36sp-6fc-191ch.pls

Appendix 5.7: Calibration model using the VNIR and removing parameter and spectral outliers from the first model (Set 2 – group4).

Calibration - Normalization MEAN=1														
ASD resolution, 34 spectra samples VNIR, No H2O vapor bands - VNIR Bands 1 to 1000														
Number of selected spectra (samples)	Number of channels	CV Number of factors after AUTO	Optimal #factor after running CV	F prob	Outlier F prob	Removed Outlier samples	Minimum FRC	Measured vs predicted Correl. (R)	Measured vs predicted RMS error	Param Outliers detected	Spec Outliers detected	score scatterplots RAW data outliers	score scatterplots Mahalanobis distance outliers	PLS file name
40	1000	26	7	0.25	0.9	-	-	0.712176	1.26211	31, 36, 39, 40	13, 14	none	none	pls-40sp-7fc-1000ch.pls
36	1000	26	8	0.25	0.9	31, 36, 39, 40	-	0.880883	0.742051	9, 14, 32, 33, 34	14, 33	none	none	pls-36sp-8fc-1000ch.pls
34	1000	23	8	0.25	0.9	13, 14, 31, 36, 39, 40	-	0.812516	0.809672	28, 32, 33, 34	1, 28	none	none	pls-34sp-8fc-1000ch.pls
34	969	25	8	0.25	0.9	13, 14, 31, 36, 39, 40	0.025	0.815538	0.803787	28, 32, 33, 34	1, 28	none	none	pls-34sp-8fc-969ch.pls
34	922	24	8	0.25	0.9	13, 14, 31, 36, 39, 40	0.05	0.818769	0.797435	28, 32, 33, 34	1, 28	none	none	pls-34sp-8fc-922ch.pls
34	849	25	8	0.25	0.9	13, 14, 31, 36, 39, 40	0.075	0.8222606	0.789343	28, 32, 33, 34	28	15	15	pls-34sp-8fc-849ch.pls
34	794	25	8	0.25	0.9	13, 14, 31, 36, 39, 40	0.1	0.82646	0.781311	28, 32, 33, 34	28, 33	15	15	pls-34sp-8fc-794ch.pls
34	729	25	8	0.25	0.9	13, 14, 31, 36, 39, 40	0.125	0.831163	0.771279	32, 33, 34	28, 33	15	15	pls-34sp-8fc-729ch.pls
34	648	25	7	0.25	0.9	13, 14, 31, 36, 39, 40	0.15	0.825055	0.781071	9, 10, 12, 34	21, 28, 33	15	15	pls-34sp-7fc-648ch.pls
34	598	22	7	0.25	0.9	13, 14, 31, 36, 39, 40	0.15	0.827005	0.777272	9, 10, 12, 32, 34	21, 28	15	15	pls-34sp-7fc-598ch.pls
34	592	22	7	0.25	0.9	13, 14, 31, 36, 39, 40	0.175	0.827197	0.776902	9, 10, 12, 34	21, 28	15	15	pls-34sp-7fc-592ch.pls
34	565	22	7	0.25	0.9	13, 14, 31, 36, 39, 40	0.2	0.829533	0.772134	9, 10, 12, 34	21, 28	15	15	pls-34sp-7fc-565ch.pls
34	537	23	7	0.25	0.9	13, 14, 31, 36, 39, 40	0.225	0.832901	0.765059	9, 10, 12, 34	21, 28	15	15	pls-34sp-7fc-537ch.pls
34	503	22	7	0.25	0.9	13, 14, 31, 36, 39, 40	0.25	0.838102	0.753982	9, 10, 12, 32, 33, 34	21, 28	15	15	pls-34sp-7fc-503ch.pls
34	449	20	7	0.25	0.9	13, 14, 31, 36, 39, 40	0.275	0.843829	0.741692	9, 10, 12, 32, 33, 34	21, 28	15	15	pls-34sp-7fc-449ch.pls
34	435	20	7	0.25	0.9	13, 14, 31, 36, 39, 40	0.3	0.845208	0.738673	9, 10, 12, 32, 33, 34	21, 28	15	15	pls-34sp-7fc-435ch.pls
34	403	21	7	0.25	0.9	13, 14, 31, 36, 39, 40	0.325	0.854308	0.718532	7, 9, 10, 32, 33, 34	15, 28	15	15	pls-34sp-7fc-403ch.pls
34	374	20	7	0.25	0.9	13, 14, 31, 36, 39, 40	0.35	0.857015	0.712444	7, 9, 10, 32, 33, 34	15, 28	15	15	pls-34sp-7fc-374ch.pls
34	363	18	7	0.25	0.9	13, 14, 31, 36, 39, 40	0.375	0.856037	0.714704	7, 9, 10, 32, 33, 34	15, 28	15	15	pls-34sp-7fc-363ch.pls
34	356	19	7	0.25	0.9	13, 14, 31, 36, 39, 40	0.4	0.856572	0.713482	7, 9, 10, 32, 33, 34	15, 28	15	15	pls-34sp-7fc-356ch.pls
34	336	19	7	0.25	0.9	13, 14, 31, 36, 39, 40	0.425	0.85781	0.710646	7, 9, 10, 32, 33, 34	15, 28	15	15	pls-34sp-7fc-336ch.pls
34	324	19	7	0.25	0.9	13, 14, 31, 36, 39, 40	0.45	0.858945	0.7081	7, 9, 10, 32, 33, 34	15, 28	15	15	pls-34sp-7fc-324ch.pls
34	312	19	7	0.25	0.9	13, 14, 31, 36, 39, 40	0.475	0.859104	0.707736	7, 9, 10, 32, 33, 34	15, 28	15	15	pls-34sp-7fc-312ch.pls
34	297	20	7	0.25	0.9	13, 14, 31, 36, 39, 40	0.5	0.860209	0.705197	7, 9, 10, 32, 33, 34	15, 28	15	15	pls-34sp-7fc-297ch.pls
34	276	19	7	0.25	0.9	13, 14, 31, 36, 39, 40	0.525	0.848957	0.73625	10, 32, 33	21, 28	none	none	pls-34sp-7fc-276ch.pls
34	203	17	5	0.25	0.9	13, 14, 31, 36, 39, 40	0.525	0.854634	0.717544	9, 10, 12, 32	33	none	none	pls-34sp-5fc-203ch.pls
34	140	17	5	0.25	0.9	13, 14, 31, 36, 39, 40	0.525	0.847147	0.734339	9, 10, 12, 32	21, 28	none	none	pls-34sp-5fc-140ch.pls

Appendix 5.8: Actual pH and predicted pH when applying model pls-36sp-6fc-540ch to the Hymap imagery

Sample site	Actual pH	Predicted pH from Hymap imagery	
		Hymap August 2004	Hymap June 2005
J05-02	3.26	-	3.68
A04-43	5.06	3.84	-
A04-21	2.92	3.66	-
J05-37	3.64	-	3.91
J05-57	4.01	-	3.59
A04-08	4.51	3.66	-
J05-45	1.73	-	2.90
J05-58	2.07	-	2.92
J05-42	2.22	-	2.77
J05-19	2.50	-	2.79
A04-18	2.63	3.74	-
J05-39	3.28	-	3.63
J05-47	2.89	-	3.60
J05-43	3.67	-	4.51
J05-55	3.36	-	3.44
J05-53	3.66	-	3.46
A04-34	5.33	3.97	-

Appendix 5.9: Actual pH and predicted pH when applying model pls-35sp-7fc-28ch to the Hymap imagery

Sample site	Actual pH	Predicted pH from Hymap imagery	
		Hymap August 2004	Hymap June 2005
J05-02	3.26	-	5.05
A04-43	5.06	3.71	-
A04-21	2.92	3.52	-
J05-37	3.64	-	4.59
J05-57	4.01	-	7.07
A04-08	4.51	4.00	-
J05-45	1.73	-	3.48
J05-58	2.07	-	4.92
J05-42	2.22	-	5.74
J05-19	2.50	-	3.39
A04-18	2.63	4.70	-
J05-39	3.28	-	4.71
J05-47	2.89	-	5.43
J05-43	3.67	-	4.01
J05-55	3.36	-	4.86
J05-53	3.66	-	5.31
A04-34	5.33	5.16	-

Appendix 5.10: Actual pH and predicted pH when applying model pls-35sp-7fc-62ch to the Hymap imagery

Sample site	Actual pH	Predicted pH from Hymap imagery	
		Hymap August 2004	Hymap June 2005
J05-02	3.26	-	4.92
A04-43	5.06	4.31	-
A04-21	2.92	3.58	-
J05-37	3.64	-	4.46
J05-57	4.01	-	6.87
A04-08	4.51	4.04	-
J05-45	1.73	-	4.04
J05-58	2.07	-	5.11
J05-42	2.22	-	5.36
J05-19	2.50	-	3.55
A04-18	2.63	4.60	-
J05-39	3.28	-	5.03
J05-47	2.89	-	3.64
J05-43	3.67	-	4.04
J05-55	3.36	-	5.17
J05-53	3.66	-	5.48
A04-34	5.33	5.42	-

Appendix 5.11: Actual pH and predicted pH when applying model pls-36sp-8fc-126ch to the Hymap imagery

Sample site	Actual pH	Predicted pH from Hymap imagery	
		Hymap August 2004	Hymap June 2005
J05-02	3.26	-	2.11
A04-43	5.06	4.65	-
A04-21	2.92	4.07	-
J05-37	3.64	-	3.99
J05-57	4.01	-	4.64
A04-08	4.51	5.75	-
J05-45	1.73	-	1.23
J05-58	2.07	-	1.87
J05-42	2.22	-	1.72
J05-19	2.50	-	1.64
A04-18	2.63	3.39	-
J05-39	3.28	-	3.14
J05-47	2.89	-	1.8
J05-43	3.67	-	3.52
J05-55	3.36	-	2.6
J05-53	3.66	-	2.41
A04-34	5.33	5.35	-